frontiers | Research Topics

Advanced MR imaging techniques in the musculoskeletal system

Edited by
Yajun Ma, Shaolin Li and Bing Wu

Published in
Frontiers in Endocrinology

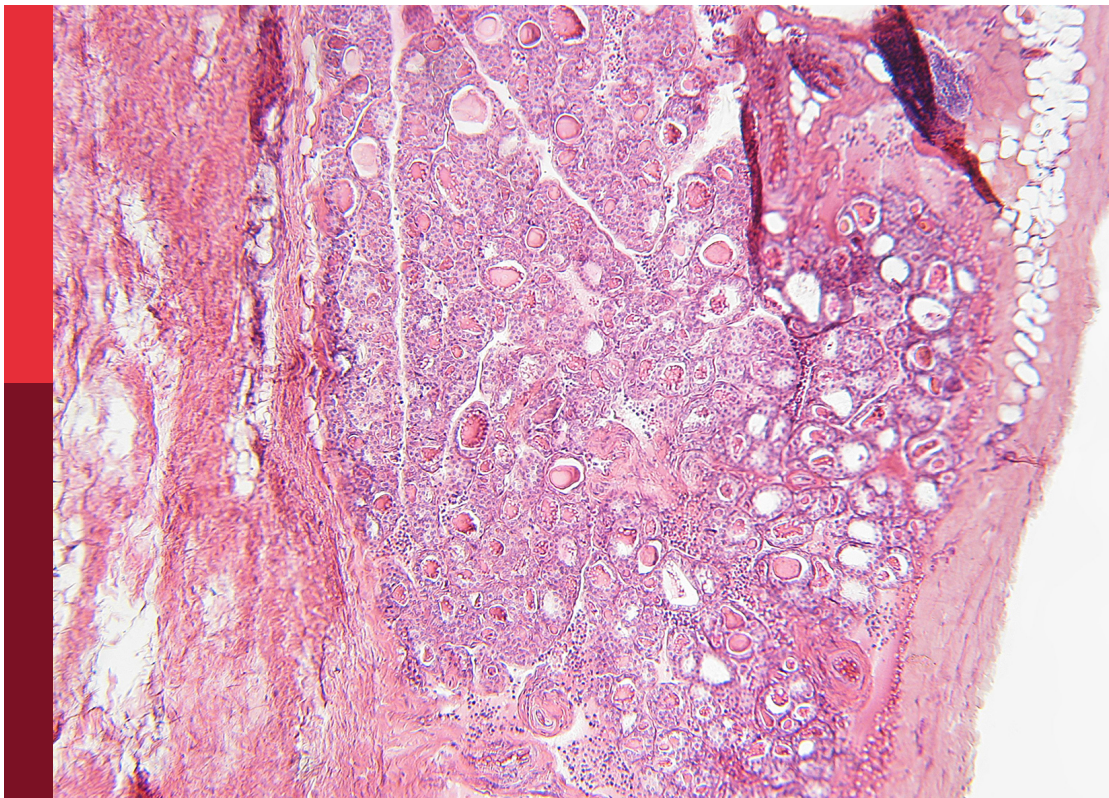

ISSN 1664-8714
ISBN 978-2-83251-501-3
DOI 10.3389/978-2-83251-501-3

About Frontiers

Frontiers is more than just an open access publisher of scholarly articles: it is a pioneering approach to the world of academia, radically improving the way scholarly research is managed. The grand vision of Frontiers is a world where all people have an equal opportunity to seek, share and generate knowledge. Frontiers provides immediate and permanent online open access to all its publications, but this alone is not enough to realize our grand goals.

Frontiers journal series

The Frontiers journal series is a multi-tier and interdisciplinary set of open-access, online journals, promising a paradigm shift from the current review, selection and dissemination processes in academic publishing. All Frontiers journals are driven by researchers for researchers; therefore, they constitute a service to the scholarly community. At the same time, the *Frontiers journal series* operates on a revolutionary invention, the tiered publishing system, initially addressing specific communities of scholars, and gradually climbing up to broader public understanding, thus serving the interests of the lay society, too.

Dedication to quality

Each Frontiers article is a landmark of the highest quality, thanks to genuinely collaborative interactions between authors and review editors, who include some of the world's best academicians. Research must be certified by peers before entering a stream of knowledge that may eventually reach the public - and shape society; therefore, Frontiers only applies the most rigorous and unbiased reviews. Frontiers revolutionizes research publishing by freely delivering the most outstanding research, evaluated with no bias from both the academic and social point of view. By applying the most advanced information technologies, Frontiers is catapulting scholarly publishing into a new generation.

What are Frontiers Research Topics?

Frontiers Research Topics are very popular trademarks of the *Frontiers journals series*: they are collections of at least ten articles, all centered on a particular subject. With their unique mix of varied contributions from Original Research to Review Articles, Frontiers Research Topics unify the most influential researchers, the latest key findings and historical advances in a hot research area.

Find out more on how to host your own Frontiers Research Topic or contribute to one as an author by contacting the Frontiers editorial office: frontiersin.org/about/contact

Advanced MR imaging techniques in the musculoskeletal system

Topic editors

Yajun Ma — University of California, United States

Shaolin Li — The Fifth Affiliated Hospital of Sun Yat-sen University, China

Bing Wu — GE Healthcare, China

Citation

Ma, Y., Li, S., Wu, B., eds. (2023). *Advanced MR imaging techniques in the musculoskeletal system*. Lausanne: Frontiers Media SA.

doi: 10.3389/978-2-83251-501-3

Table of contents

frontiers in Endocrinology

ORIGINAL RESEARCH
published: 05 November 2021
doi: 10.3389/fendo.2021.775066

CKD Stages, Bone Metabolism Markers, and Cortical Porosity Index: Associations and Mediation Effects Analysis

Yan Xiong[1], Tongxiang He[1], Yanan Wang[1], Weiyin Vivian Liu[2], Shuang Hu[1], Yao Zhang[1], Donglin Wen[1], Bowen Hou[1], Yitong Li[1], Peisen Zhang[3], Jianyi Liu[4], Fan He[5] and Xiaoming Li[1]**

[1] Department of Radiology, Tongji Hospital, Tongji Medical College, Huazhong University of Science and Technology, Wuhan, China, [2] MR Research, GE Healthcare, Beijing, China, [3] Department of Rehabilitation Medicine, School of Medicine, Guangzhou First People's Hospital, South China University of Technology, Guangzhou, China, [4] Renhe Shijia, Wuhan, China, [5] Department of Nephrology, Tongji Hospital, Tongji Medical College, Huazhong University of Science and Technology, Wuhan, China

OPEN ACCESS

Edited by:
Bing Wu,
GE Healthcare, China

Reviewed by:
Hongjiang Wei,
Shanghai Jiao Tong University, China
Niu Jinliang,
Second Hospital of Shanxi Medical University, China

***Correspondence:**
Fan He
fhe@tjh.tjmu.edu.cn
Xiaoming Li
lilyboston2002@sina.com

Specialty section:
This article was submitted to Bone Research, a section of the journal Frontiers in Endocrinology

Received: 13 September 2021
Accepted: 20 October 2021
Published: 05 November 2021

Citation:
Xiong Y, He T, Wang Y, Liu WV, Hu S, Zhang Y, Wen D, Hou B, Li Y, Zhang P, Liu J, He F and Li X (2021) CKD Stages, Bone Metabolism Markers, and Cortical Porosity Index: Associations and Mediation Effects Analysis. Front. Endocrinol. 12:775066. doi: 10.3389/fendo.2021.775066

Chronic kidney disease (CKD) has a significant negative impact on bone health. However, the mechanisms of cortical bone deterioration and cortical porosity enlargement caused by CKD have not been fully described. We therefore examined the association of CKD stages with cortical porosity index (PI), and explored potential mediators of this association. Double-echo ultrashort echo-time magnetic resonance imaging (UTE MRI) provides the possibility of quantifying cortical porosity *in vivo*. A total of 95 patients with CKD stages 2-5 underwent 3D double-echo UTE-Cones MRI (3.0T) of the midshaft tibia to obtain the PI. PI was defined as the ratio of the image signal intensity of a sufficiently long echo time (TE) to the shortest achievable TE. Parathyroid hormone (PTH), β-CrossLaps (β-CTX), total procollagen type I amino-terminal propeptide (T-P1NP), osteocalcin (OC), 25-hydroxyvitamin D (25OHD), and lumbar bone mineral density (BMD) were measured within one week of the MRI. Partial correlation analysis was performed to address associations between PI, eGFR and potential mediators (PTH, β-CTX, T-P1NP, OC, 25OHD, BMD, and T-score). Multiple linear regression models were used to assess the association between CKD stages and PI value. Then, a separate exploratory mediation analysis was carried out to explore the impact of CKD stages and mediators on the PI value. The increasing CKD stages were associated with a higher PI value ($P_{trend} < 0.001$). The association of CKD stages and PI mediated 34.4% and 30.8% of the total effect by increased PTH and β-CTX, respectively. Our study provides a new idea to monitor bone health in patients with CKD, and reveals the internal mechanism of bone deterioration caused by CKD to some extent.

Keywords: chronic kidney disease, CKD-MBD, Ultrashort TE, porosity index, cortical porosity, mediation analysis, bone metabolism markers

INTRODUCTION

Chronic kidney disease (CKD) has become a recognized global public health problem, which affects approximately 0.75 billion human beings worldwide (1). CKD has a significant negative impact on bone health (2, 3), which results in a two-fourfold higher risk of fracture in CKD patients compared with general population, and the occurrence of fractures is associated with increased mortality (4, 5). Cortical bone is the main factor that determines the overall bone strength, accounting for more than 80% of the total bone (6). Cortical porosity is the main factor that determines the strength of cortical bone, and the development of cortical pores leads to an increase in bone fragility, which increases the fracture (7). A study by Nickolas et al. (8) found that hemodialysis has an independent effect on the increase in cortical porosity, which suggests that cortical porosity may increase as CKD progresses.

CKD-mineral and bone disorder (CKD-MBD), a disease of bone metabolism that manifests as systemic mineral and bone metabolism disorders, is the main complication of CKD and affects most patients with moderate to severe CKD (9). Elevated parathyroid hormone (PTH) is a potential mediator for patients with MBD, and it is also the most widely studied and most recognized bone metabolism marker for predicting bone turnover in CKD patients (10). In terms of the mechanism, with the progression of CKD and calcium and phosphorus metabolism disorders, patients develop secondary hyperparathyroidism to varying degrees, and increased PTH has a catabolic effect on cortical bone (11). Cortical porosity in patients with CKD showed highly positive correlation with PTH ($r = 0.62$; $P = 0.021$) (3). In addition, tartrate-resistant acid phosphatase 5b (TRAP5b) and bone-specific alkaline phosphatase (BSAP) are less affected by renal clearance and can more accurately assess MBD (12), but these two indicators are not as widely used in clinical practice as PTH. The application of other bone metabolism markers (e.g., β-CrossLaps (β-CTX), total procollagen type I amino-terminal propeptide (T-P1NP), osteocalcin (OC), and 25-hydroxyvitamin D (25OHD), etc.) in CKD is controversial, and there are few related studies. These bone metabolism markers are relatively common in the study of osteoporosis. In this study, we wanted to explore which metabolic markers influenced the relationship between CKD and cortical porosity, and therefore some of these metabolic markers were included.

Early imaging studies on CKD-MBD mainly focused on trabecular bone (13). However, recent research has shown that cortical bone plays a more crucial part than trabecular bone in the bone health of CKD-MBD patients (14). In patients with CKD, the loss of cortical bone is associated with increased cortical porosity and decreased cortical thickness (8). Nevertheless, cortical bone is not taken as a key parameter in the "turnover, mineralization, volume" classification of CKD-MBD (3).

At present, information on the porosity of human cortical bone *in vivo* is mainly obtained through high-resolution peripheral quantitative computed tomography (HR-pQCT) and bone biopsy (15). However, HR-pQCT involves radiation, and its limited resolution underestimates porosity (16). And bone biopsy is expensive and invasive and requires professional knowledge to perform, process, and interpret; thus, only a few laboratories worldwide carry out this test (15). With the development of magnetic resonance technology, the adoption of ultrashort echo time (UTE) *in vivo* has proven to be feasible for quantitative assessment of cortical pore information (17). Magnetic resonance quantification of bone tissue has always been a difficult problem in the field of magnetic resonance research. UTE magnetic resonance imaging (MRI) is an advanced and promising method. Its echo time is very short, which solves the difficult problem of the inability of conventional MRI sequences to obtain bone signals. At present, this sequence has been used for the quantitative and qualitative assessment of cortical bone pore water (e.g., bicomponent analysis, tricomponent analysis, single/double adiabatic inversion of UTE technology, etc.) (18), and increased pore water content has been confirmed to be related to increase in cortical porosity and decrease in mechanical properties (19). However, these methods are complicated, the scanning time is very long, and the postprocessing technology requirements are very strict, so they are hardly used in clinical research. Rajapakse et al. (20) evaluated cortical bone porosity using a novel double-echo UTE MR sequence recently. The porosity index (PI) was defined as the ratio of the image signal intensity of a sufficiently long echo time (TE) (mainly from the pore water signal) to the shortest achievable TE (from all water signals), representing the fraction of pore-water. The selection of TE value needs to consider the T2* value of bound water (0.3-0.4 ms) and pore water (> 1 ms) (20, 21). The researchers found that the PI measured by this method exhibits highly positive correlation with cortical porosity measured by micro-CT ($R^2 = 0.79$). Furthermore, this means showed high repeatability when measuring vivo tibial PI (with a variation of 2.2% in between-day coefficient). Thus, it is reasonable for us to conclude that PI can reflect porosity to a large extent. This method, which is noninvasive and does not involve radiation, has a short scanning time and a simple processing protocol, which results in a high potential for application in clinical practice. Chen et al. (22) applied this method to healthy volunteers. However, there are almost no relevant studies on applying this method to various metabolic bone diseases, including CKD-MBD.

The mediators selected in this study are currently the most recognized mediators in bone metabolism, and their application in CKD-MBD needs to be further studied. Therefore, the aim of this research is to (1) explore the association between the increasing stages of CKD and the development of cortical PI; (2) judge the mediation effect of several bone metabolism markers (i.e., PTH, β-CTX, T-P1NP, OC, and 25OHD) and dual-energy X-ray absorptiometry (DXA) lumbar spine bone mineral density (BMD) on this association.

MATERIALS AND METHODS

Subjects

This cross-sectional cohort study was prospective, which was approved by Medical Ethics Committee of Tongji Hospital of

Huazhong University of Science and Technology, TJ-IRB20210108. We obtained written informed consent from every participant before the research. This trial was registered with ClinicalTrials.gov as NCT04564924. The subjects were recruited from September 1, 2020, to April 11, 2021. We recruited one hundred patients from the Department of Nephrology of Tongji Hospital. Three initially collected patients were excluded as a result of the replacement of coils, one patient was excluded because the tibia cortex was too thin to draw the ROI, and one patient was excluded due to poor image quality. The remaining 95 patients were included. All participants were over 18 years old and ambulatory. The specific diagnostic criteria for CKD are: (1) any evidence of kidney damage (pathological abnormalities, abnormal blood or urine components, or abnormal imaging tests.) or (2) eGFR < 60 mL/min/1.73m^2 longer than 3 months. The inclusion criteria were hospitalized patients diagnosed with CKD stage 2-5. The reason why we did not include CKD stage 1 (eGFR > 90 mL/min/1.73m^2) is (1) The onset of CKD is insidious in the ultra-early stage, and the clinical symptoms of CKD stage 1 patients are atypical and cannot be firmly diagnosed by eGFR alone. The evidence of kidney damage should be acquired. Fewer than 5% of early-stage CKD patients are aware of their disease (23). Therefore, there are few such patients in clinical practice; (2) In the process of recruiting patients, we hardly recruited patients with CKD stage 1; (3) Almost none studies on CKD-MBD in last decades have included CKD stage 1 patients (8, 15, 24, 25). Key exclusion criteria included any disease known to affect bone metabolism (e.g., diabetes, hyperthyroidism, rickets, osteomalacia, Paget's disease, acromegaly, scurvy (vitamin C deficiency), history of malignant tumors, treatment with radiotherapy or chemotherapy, fractures within 6 months, lumbar or calf trauma surgery, rheumatic immunity disease, scoliosis, anorexia nervosa, and motor neuron disease); use of medications known to influence bone metabolism (e.g., bisphosphonates, oral glucocorticoids, steroid hormones, and salmon calcitonin); and general contraindications to MRI exam (e.g., IUD, pacemaker, cochlear implant, and claustrophobia).

MRI Scanning

Studies were conducted on a 3 Tesla (T) clinical scanner (Signa Pioneer, GE Healthcare, USA) using a medium soft coil, and the dominant leg was scanned. A 3D double-echo UTE-Cones sequence (TR/TE_1/TE_2, 11.5/0.032/4.4 ms; FOV, 16 cm; slice thickness, 3 mm; flip angle, 9°; bandwidth, 62.5 kHz; in-plane spatial resolution, 0.89mm*0.89mm; 12 axial images; and scan time, 54 s) was adopted to get tibial images. To locate the thickest part of the tibial cortex, in the positioning phase, the spine coil was used to image the full length of the tibia and was then positioned at the thickest plane (approximately in a 38% place of the tibial length close to the lateral malleolus) of the tibia in the coronal and sagittal planes.

The reason for tibial cortex used for our study is mainly due to two reasons: (1) In the study of bone pore water, the tibial cortex and the femoral neck cortex are often selected parts (8, 20, 22, 26, 27). (2) According to other research and our pre-experiment, compared with the femoral neck cortex, the tibial cortex is very thick, and the boundary with the bone marrow is very clear, which is more beneficial to accurately draw the ROI of bone cortex.

Image Processing

All images were processed with ImageJ (National Institutes of Health). Two experienced musculoskeletal radiologists (one had three years of experience and one had five years of experience), who were blinded to the subjects' clinical data, independently drew the ROI. The ROI was drawn on TE_1 and then copied to TE_2. PI = $TE_{4.4}$intensity/$TE_{0.032}$intensity. The ROI was limited to a compacting cortex in appearance, and the trabecularized transition zone was not included, because most UTE signals in these parts were derived from adipose tissue, interfering with water signal of the cortical, thereby interfering with the measurement of PI. The tibial cortex was analyzed on the middle 5 layers of the 12 axial images. Subsequently, the PI value of each layer was calculated separately, and then the average value of PI was obtained. **Figure 1** shows examples of the ROI.

Kidney Function

All subjects completed the kidney function examination within one week of the MRI examination. We used serum creatinine level to obtain the estimated glomerular filtration rate (eGFR) through the CKD-EPI formula (28). The stages of CKD were based on the eGFR.

Bone Metabolism Markers

Bone metabolism markers, namely, PTH, β-CTX, T-P1NP, OC, and 25OHD, were assessed within one week of the MRI examination.

Dual-Energy X-Ray Absorptiometry

A Prodigy Lunar scanner (GE Healthcare, Waukesha, WI, USA) was used to evaluate the areal BMD and T-score of the lumbar spine (from L1 to L4).

Statistical Analysis

We summarized continuous variables as the mean ± SD, and categorical variables as frequency and percentage. Based on eGFR, patients were divided into four stages. The baseline characteristics between the four stages were compared for linear trends using one-way analysis of variance (ANOVA) for continuous variables and Chi-squared statistics for categorical variables. Partial correlation analysis was performed to address associations between PI, eGFR and potential mediators, controlling for age and BMI. Multiple linear regression models were used to assess the association between CKD stages and PI value. Crude effects were tested in an unadjusted model. Next model, we adjusted for age, sex, and BMI. In the final model, we introduced the potential mediators that were correlated with PI value in partial correlation analysis as well as the mediators' interactions with CKD stages. We calculated *P* for the linear trend by analyzing CKD stages as a continuous instead of an ordinal variable. Then, a separate exploratory mediation analysis was carried out for each metabolic indicator to explore the

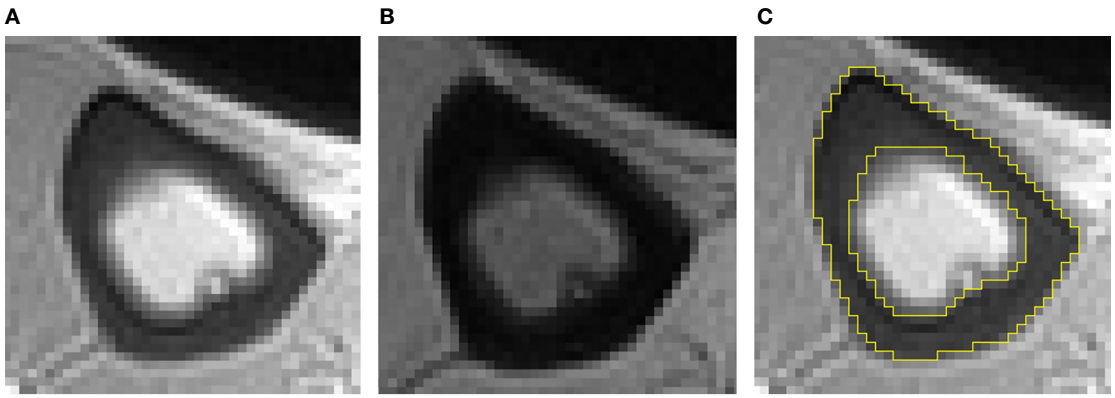

FIGURE 1 | Typical double-echo UTE images and ROI of the tibia **(A–C)**. **(A)** The image of first echo; **(B)** the image of second echo; **(C)** example of ROI.

impact of CKD stages and mediators on the PI value. The mediation R package (29) was used for mediation analysis. In this analysis, statistical models were simplified by treating CKD stages as interval variables. *P*-values and nonparametric bootstrap confidence intervals were estimated from one thousand simulations. **Figure 2** shows the tested hypothesized pathways in this study, which is the underlying model of this analysis. The model assumes that there is a causal relationship between the selected bone metabolism markers and the progression of CKD and cortical bone PI. The model includes age, sex, and BMI to adjust for potential confounding factors. Direct and indirect effects are obtained from multiple linear regression. The interobserver variability of PI was assessed between two independent raters using intraclass correlation coefficients (ICCs). The ICCs were computed by using the two-way mixed model for absolute agreement and single measures. An ICC value greater than 0.90 was considered excellent, and a value between 0.75 and 0.90 was considered good. All statistical analyses were performed in R v4.0.3. We set the statistical significance at $P < 0.05$.

RESULTS

Baseline Characteristics

Table 1 reports the baseline characteristics for the four CKD stages (12 people in stage 2, 23 people in stage 3, 20 people in stage 4, and 40 people in stage 5). The mean age, sex and BMI distributions were comparable across all four groups. Patients with more severe CKD had significantly higher intact PTH, β-CTX, T-P1NP, OC and PI values. No difference could be observed in 25OHD or BMD.

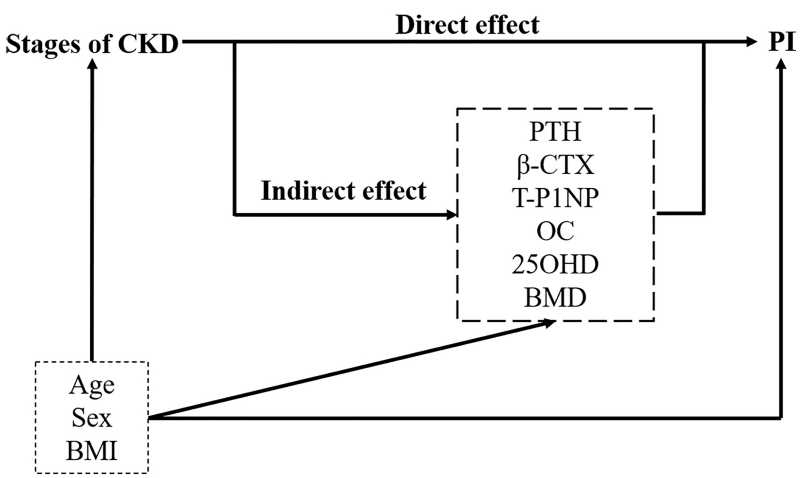

FIGURE 2 | Path diagram of the mediation relationship between grouping (the stages of CKD), mediators (bone metabolism markers and lumbar BMD) and outcome (PI). Adjusting for confounders: age, sex, and BMI. Direct and indirect effects are obtained from multiple linear regression. PTH, parathyroid hormone; β-CTX, β-CrossLaps; T-P1NP, total procollagen type I amino-terminal propeptide; OC, osteocalcin; 25OHD, 25-hydroxyvitamin D; BMD, bone mineral density; PI, porosity index.

TABLE 1 | Baseline characteristics by the stages of CKD.

	Total	Stages of CKD				P_{trend}
		2	3	4	5	
n	95	12 (12.6)	23 (24.2)	20 (21.1)	40 (42.1)	na
Males (%)	48 (50.5)	9 (75)	10 (43.5)	12 (60)	17 (42.5)	0.158
Age (years)	49.7 (12.5)	52.9 (8.1)	49.8 (12.8)	49.5 (13.8)	48.7 (13.0)	0.360
BMI (kg/m^2)	23.2 (3.4)	24.3 (4.2)	22.5 (3.3)	23.8 (3.7)	22.9 (2.9)	0.542
eGFR (mL/min/1.73m^2)	27.2 (22.0)	71.0 (5.7)	41.1 (9.0)	23.3 (4.1)	8.1 (3.5)	**< 0.001**
intact PTH (pg/mL)	150.2 (124.7)	64.9 (51.2)	84.9 (54.5)	139.9 (81.5)	218.4 (149.2)	**< 0.001**
β-CTX (ng/mL)	1.23 (1.00)	0.58 (0.39)	0.75 (0.47)	0.91 (0.54)	1.86 (1.18)	**< 0.001**
T-P1NP (ng/mL)	122.7 (140.2)	29.8 (19.9)	40.6 (49.9)	88.6 (74.9)	214.9 (164.8)	**< 0.001**
OC (ng/mL)	73.9 (66.3)	27.2 (19.2)	30.4 (24.2)	58.6 (39.6)	120.5 (72.5)	**< 0.001**
25OHD (ng/mL)	18.5 (8.5)	21.9 (8.2)	19.8 (8.5)	16.8 (7.7)	17.6 (8.8)	0.102
L1-L4 BMD (g/cm^2)	1.11 (0.16)	1.17 (0.14)	1.14 (0.17)	1.07 (0.15)	1.10 (0.16)	0.120
L1-L4 T-score	-0.83 (1.23)	-0.45 (1.07)	-0.59 (1.40)	-1.11 (1.02)	-0.93 (1.25)	0.151
PI (%)	20.2 (2.4)	18.2 (1.8)	19.8 (2.0)	20.2 (2.1)	21.1 (2.4)	**< 0.001**

Data are presented as means (standard deviation) and numbers (%). In Appropriate time, one-way ANOVA and Chi-square are used. Bold P_{trend} indicates statistical significance.

Partial Correlation Between PI, eGFR and Potential Mediators

Significant correlations were revealed between the PI value and different bone metabolism markers (PTH: r = 0.381, $P < 0.001$; β-CTX: r = 0.375, $P < 0.001$; T-P1NP: r = 0.327, $P = 0.001$; OC: r = 0.357, $P < 0.001$). Similarly, significant correlations were revealed between the eGFR and different bone metabolism markers (PTH: r = -0.499, $P < 0.001$; β-CTX: r = -0.470, $P < 0.001$; T-P1NP: r = -0.512, $P < 0.001$; OC: r = -0.538, $P < 0.001$) (**Table 2**).

Multiple Linear Regression Analysis

In the crude model (model 1), we observed a positive association of CKD stages with PI, again with a significant gradient [stage 3 versus 2: β (95% CI) 1.58 (0.02, 3.14), stage 4 versus 2: β (95% CI) 2.01 (0.41, 3.61), stage 5 versus 2: β (95% CI) 2.93 (1.48, 4.37), $P_{trend} < 0.001$; In model 2, after adjusting for age, sex and BMI, the association was attenuated, but significance remained [stage 4 versus 2: β (95% CI) 1.96 (0.32, 3.59), stage 5 versus 2: β (95% CI) 2.83 (1.32, 4.33), $P_{trend} < 0.001$]. In model 3, after introducing all potential mediators (PTH, β-CTX, T-P1NP, and OC) that were correlated with PI value in partial correlation analysis as well as the mediators' interactions with CKD stages, we found that the association between CKD stages and PI were no longer significant. (**Table 3**).

Mediation Analysis

According to model 3, we found that the potential mediators were in the four bone metabolism markers (PTH, β-CTX, T-P1NP, and OC). At the same time, due to the multicollinearity between these four markers and their correlation with eGFR, in order to explore the impact of CKD stages and these four markers on PI value, we conducted simple causal mediation analysis for these four markers respectively. The main effects of PTH and β-CTX were significant (**Table S2**). We tested interactions of the stages of CKD with each potential mediator respectively (adjusted for age, sex and BMI); none of them was significant ($P > 0.05$). The association of CKD stages and PI mediated 34.4% ($P = 0.012$) and 30.8% ($P = 0.024$) of the total effect by increased PTH and β-CTX, respectively. No significant mediation was observed by T-P1NP and OC, 25(OH) vitamin D or BMD (**Table 4**). The results of mediation analysis of PTH and β-CTX were shown in **Figure 3**. After adjusting for confounding factors, one increase in CKD stage was associated with an increase of 58.87 pg/mL (95% CI: 38.00, 79.73) in PTH, and associated with an increase of 0.545% (95% CI: 0.096, 1.027) in PI; for every 1 pg/mL increase in PTH was associated with an increase of 0.005% (95% CI: 0.001, 0.009) in PI; the increased PTH mediated 34.4% of the total effect of CKD stages on PI. Similarly, one increase in CKD stage was associated with an increase of 0.47 ng/mL (95% CI: 0.30, 0.63) in β-CTX, and associated with an increase of 0.575% (95% CI: 0.099, 1.058) in PI; for every 1 ng/mL increase in β-CTX was associated with an increase of 0.549% (95% CI: 0.027, 1.071) in PI; the increased β-CTX mediated 30.8% of the total effect of CKD stages on PI. The association of CKD stages with potential mediators was shown in **Table S1**. The main effect of potential mediators was shown in **Table S2**.

TABLE 2 | Adjusted correlation coefficients between PI, eGFR and potential mediators.

	PI	eGFR
PTH	**0.381 (<0.001)**	**-0.499 (<0.001)**
β-CTX	**0.375 (<0.001)**	**-0.470 (<0.001)**
T-P1NP	**0.327 (0.001)**	**-0.512 (<0.001)**
OC	**0.357 (<0.001)**	**-0.538 (<0.001)**
25OHD	0.058 (0.578)	0.171 (0.101)
L1-L4 BMD	-0.139 (0.183)	0.227 (0.029)
L1-L4 T-score	-0.135 (0.198)	0.215 (0.039)

Partial correlation coefficients adjusted by age, and eGFR. Data are presented as means (P-value). The bold part indicates significant meaning.

TABLE 3 | Association of the stages of CKD with PI.

Outcome	Stages of CKD				P_{trend}
	2	3	4	5	
Model 1	(ref.)	**1.58 (0.02, 3.14)**	**2.01 (0.41, 3.61)**	**2.93 (1.48, 4.37)**	**<0.001**
Model 2	(ref.)	1.49 (-0.13, 3.11)	**1.96 (0.32, 3.59)**	**2.83 (1.32, 4.33)**	**<0.001**
Model 3	(ref.)	1.35 (-0.25, 2.96)	1.53 (-0.12, 3.18)	1.73 (-0.02, 3.49)	0.084

Data are presented as regression coefficient (95% CI). The bold part indicates significant meaning.
Model 1: crude stages of CKD (Stage 2 is reference category).
Model 2: Model 1 + age, sex, and BMI.
Model 3: Model 2 + potential mediators (PTH, β-CTX, T-P1NP, and OC) (and their interactions with CKD stages).

Interobserver Variability

The ICC was 0.85 (95% CI: 0.430, 0.942).

DISCUSSION

We examined the associations of CKD stages with the PI of the tibial cortex. More severe CKD is associated with higher PI values, independent of age, sex and BMI, while dependent of potential mediators. It was suggested that the association between CKD stages and tibial PI was partly due to PTH and β-CTX through exploratory mediation analysis.

Although the importance of cortical porosity for bone biomechanics has been increasingly appreciated (7, 30, 31), almost no one has assessed it noninvasively *in vivo*. Through PI measurements, we evaluated cortical porosity of the tibia by using double-echo UTE MRI sequences. The mean PI value of all subjects measured in our study was 20.2% ± 2.4%, which is consistent with the tibial cortical PI value of 20% ± 3.8% (range, 15%-31%) of 34 old menopausal women aged 55-80 years (20). This method can quantify the changes in cortical PI in CKD patients, providing a new choice to monitor and detect the deterioration of cortical bone microarchitecture in CKD patients.

The mechanisms underlying the association between CKD stages and cortical porosity are not completely clear, and few related studies have been conducted. Nickolas et al. (8) performed HR-pQCT scans on the distal tibia and distal radius. They found that dialysis was an independent factor in the increase in cortical porosity. On the basis of this research, our study further covered more complete CKD stages, supplemented the current evidence, and further showed that the progression of CKD is closely associated with increased cortical porosity. Nevertheless, we should not assume that more severe CKD necessarily corresponds to greater PI values, because the actual mechanism by which CKD drives cortical pore enlargement is still largely unknown (32). The factors leading to bone deterioration in patients with CKD are very complex and include the severity of hyperparathyroidism, the level of various bone metabolism markers, the degree of bone turnover and the impact of CKD itself on the bones, and these factors are interrelated (33–35). Consequently, we further conducted an exploratory mediation analysis. We tested each mediator separately with corrected age, sex and BMI to prevent overadjustment.

Among the indicators included in this study, high PTH was the strongest mediator. PTH can directly stimulate osteocytes to release receptor activator of nuclear factor κB ligand (RANKL), which results in increased osteoclast generation (36). In a study of CKD mice, Metzger et al. (37) found that PTH and cortical porosity increased with time, meanwhile RANKL increased and osteocyte apoptosis decreased. Therefore, they speculated that high PTH could prolong the life of osteocytes and lead to sustained RANKL and thus osteoclastic bone resorption in the cortex, promoting the cortical porosity formation. At present, PTH is still the most commonly used diagnostic aid for MBD. On the basis of the 2017 Kidney Disease: Improving Global Outcomes (KDIGO) guidelines, the level of bone turnover can be classified according to the level of PTH (2). Recently, some studies have shown that increased porosity is associated with increased PTH (3, 8, 26, 37, 38), which is consistent with our results. At the same time, our study also found that the increase in cortical porosity in people at different CKD stages is partly due to higher PTH.

Second, our research found that β-CTX was also a mediator. β-CTX is a marker of bone resorption, which can reflect osteocyte activity (39). At present, there is no consensus on the application of β-CTX in MBD. Some studies indicate that β-CTX

TABLE 4 | Mediators of the association between CKD stages and PI.

Mediators	IDE	*P*	DE	*P*	Proportion mediated	*P*
PTH	0.286 (0.051, 0.518)	**0.012**	0.545 (0.096, 1.027)	**0.012**	0.344 (0.051, 0.824)	**0.012**
β-CTX	0.256 (0.040, 0.499)	**0.024**	0.575 (0.099, 1.058)	**0.020**	0.308 (0.038, 0.795)	**0.024**
T-P1NP	0.198 (-0.064, 0.477)	0.140	0.633 (0.096, 1.191)	**0.022**	0.238 (-0.079, 0.794)	0.140
OC	0.242 (-0.081, 0.529)	0.114	0.589 (0.067, 1.168)	**0.024**	0.292 (-0.083, 0.862)	0.114

Data are presented as means (95% CI). Nonparametric bootstrap Confidence Intervals are estimated from 1000 simulations adjusted for age, sex, and BMI. Bold P-values indicate statistical significance. IDE, indirect effect; DE, direct effect.

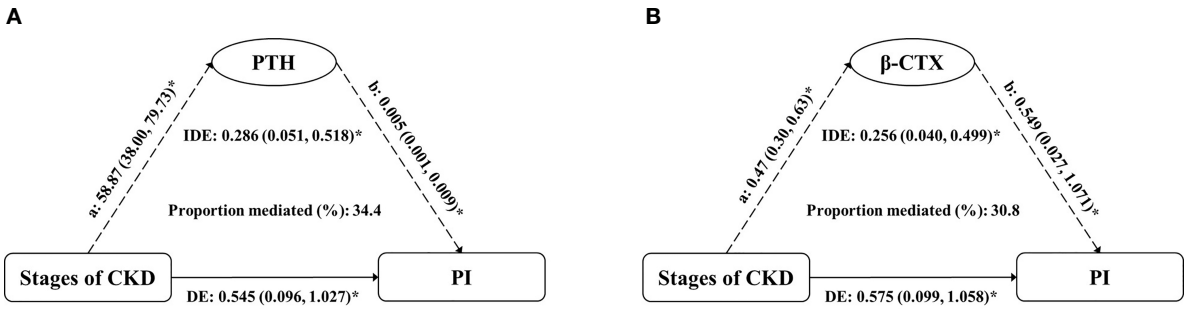

FIGURE 3 | Estimates of the mediation effect of **(A)** PTH and **(B)** β-CTX about the association between the stages of CKD and PI value, after adjusting for age, sex and BMI. Note: **(A)** the effect of grouping on mediator; **(B)** the main effect of mediator on PI; IDE, indirect effect (Stages of CKD→PTH/β-CTX→PI); DE, direct effect (Stages of CKD→PI); PTH, parathyroid hormone; β-CTX, β-CrossLaps; PI, porosity index. *P < 0.05.

is a bone turnover biomarker which exists direct release during bone resorption and could be used to more accurately assess the bone turnover in CKD (12). At the same time, Nishiyama et al. (24) found that higher levels of β-CTX and worsening cortical porosity have a linear dose-response relationship, which suggested that β-CTX could predict cortical deterioration. However, some studies suggested that β-CTX was not suitable as a diagnostic aid for MBD due to the influence of renal function (40). The role of this indicator in CKD-MBD needs further study. T-P1NP and OC did not show mediation effects in this study, possibly because these two indicators were greatly affected by renal clearance and could not accurately reflect bone deterioration in patients with CKD. There was also no mediation effect of 25OHD, which may due to supplement with vitamin D for the most patients with end-stage CKD, so that the 25OHD level in end-stage patients was higher than that in patients at earlier stages in our study. Due to the analytical and biological variability of these serum markers, there are few studies on bone metabolism markers other than PTH in CKD, and the clinical applications of these indicators are limited. The results of this study could provide some hints for further research in the future.

Interestingly, we did not observe a mediation effect of lumbar BMD measured by DXA, and we found that as CKD progressed, BMD did not continue to decrease. It might be that the BMD measured by DXA was a real BMD, which is not distinguishable between trabecular and cortical bone (11, 41), or that BMD itself has a small contribution to porosity. Because cortical and trabecular bone behave differently in answer to increased parathyroid activity (decrease and increase, respectively) and larger trabecular BMD can mask the loss of cortical bone, BMD measured by DXA in CKD patients may be higher, equal to or lower than that in healthy controls (13). Some studies were consistent with our study. Rajapakse et al. (20) showed that the femur and spine BMD measured by DXA had no significant correlation with PI. They also found that the cortical BMD obtained using pQCT imaging in bone specimens can merely partially explain the change in porosity, highlighting the need to estimate porosity without the dependence of BMD. Similarly, Carvalho et al. (42) found that there was no significant correlation between DXA parameters and cortical porosity for either internal cortical bone or external cortical bone.

The advantages of this study include: (1) The assessment of relatively complete indicators related to bone deterioration. (2) There is currently little evidence for indicators other than PTH in CKD, and this study can be used as a supplement to some extent. (3) We prospectively included CKD stages 2-5 patients in strict accordance with the inclusion criteria and exclusion criteria that may affect bone metabolism. (4) We also explored the mediation effect of a series of potential mediators, which can reflect the inherent causal relationship between CKD progress and the changes in PI values, which is not seen in the current CKD-MBD research. At the same time, this study has some limitations: (1) Many drugs and diseases can affect bone metabolism, so we excluded diseases and drugs that are known to affect bone metabolism as much as possible based on relevant research. Dialysis has been proved to be an independent factor of PI increase (8), but this study did not include dialysis patients. Our follow-up study will take dialysis patients as a separate group for further study. (2) Due to the limited detection level, we did not include TRAP5b or BSAP, two markers of bone metabolism that are considered to be independent of glomerular filtration rate.

In conclusion, the progression of CKD is associated with increased cortical PI values, and this association may be partly mediated by increased PTH and β-CTX. Our study provides a new idea to monitor bone health in patients with CKD, and reveal the internal mechanism of bone deterioration caused by CKD to some extent. Further work needs to be done to study other deep possible mechanisms about the association.

DATA AVAILABILITY STATEMENT

The raw data supporting the conclusions of this article will be made available by the authors, without undue reservation.

ETHICS STATEMENT

The studies involving human participants were reviewed and approved by Medical Ethics Committee of Tongji Hospital, Tongji Medical College, Huazhong University of Science and Technology. The patients/participants provided their written informed consent to participate in this study.

AUTHOR CONTRIBUTIONS

FH and XL concept and design. DW, BH, and YL devised the outline of the manuscript. YX and TH designed the study and evaluated the data. YW, SH, and YZ collected the information and analyzed the data. YX wrote the manuscript. PZ and JL created the figures for the manuscript. WL and XL critically revised the manuscript. All authors contributed to the article and approved the submitted version.

FUNDING

This study was supported by the National Natural Science Foundation of China (NSFC) (No. 31630025 and 81930045).

SUPPLEMENTARY MATERIAL

The Supplementary Material for this article can be found online at: https://www.frontiersin.org/articles/10.3389/fendo.2021.775066/full#supplementary-material

REFERENCES

1. Khairallah P, Nickolas TL. Updates in CKD-Associated Osteoporosis. *Curr Osteoporos Rep* (2018) 16(6):712–23. doi: 10.1007/s11914-018-0491-3
2. Kidney Disease: Improving Global Outcomes (KDIGO) CKD-MBD Update Work Group. KDIGO 2017 Clinical Practice Guideline Update for the Diagnosis, Evaluation, Prevention, and Treatment of Chronic Kidney Disease-Mineral and Bone Disorder (CKD-MBD). *Kidney Int Suppl (2011)* (2017) 7(1):1–59. doi: 10.1016/j.kisu.2017.04.001
3. Sharma AK, Toussaint ND, Masterson R, Holt SG, Rajapakse CS, Ebeling PR, et al. Deterioration of Cortical Bone Microarchitecture: Critical Component of Renal Osteodystrophy Evaluation. *Am J Nephrol* (2018) 47(6):376–84. doi: 10.1159/000489671
4. Pimentel A, Ureña-Torres P, Zillikens MC, Bover J, Cohen-Solal M. Fractures in Patients With CKD-Diagnosis, Treatment, and Prevention: A Review by Members of the European Calcified Tissue Society and the European Renal Association of Nephrology Dialysis and Transplantation. *Kidney Int* (2017) 92(6):1343–55. doi: 10.1016/j.kint.2017.07.021
5. Moorthi RN, Fadel W, Eckert GJ, Ponsler-Sipes K, Moe SM, Lin C, et al. Bone Marrow Fat Is Increased in Chronic Kidney Disease by Magnetic Resonance Spectroscopy. *Osteoporos Int* (2015) 26(6):1801–7. doi: 10.1007/s00198-015-3064-7
6. Clarke B. Normal Bone Anatomy and Physiology. *Clin J Am Soc Nephrol* (2008) 3 Suppl 3(Suppl 3):S131–9. doi: 10.2215/CJN.04151206
7. Morgan EF, Unnikrisnan GU, Hussein AI. Bone Mechanical Properties in Healthy and Diseased States. *Annu Rev BioMed Eng* (2018) 20:119–43. doi: 10.1146/annurev-bioeng-062117-121139
8. Nickolas TL, Stein EM, Dworakowski E, Nishiyama KK, Komandah-Kosseh M, Zhang CA, et al. Rapid Cortical Bone Loss in Patients With Chronic Kidney Disease. *J Bone Miner Res* (2013) 28(8):1811–20. doi: 10.1002/jbmr.1916
9. Nickolas TL, Leonard MB, Shane E. Chronic Kidney Disease and Bone Fracture: A Growing Concern. *Kidney Int* (2008) 74(6):721–31. doi: 10.1038/ki.2008.264
10. Evenepoel P, Cavalier E, D'Haese PC. Biomarkers Predicting Bone Turnover in the Setting of CKD. *Curr Osteoporos Rep* (2017) 15(3):178–86. doi: 10.1007/s11914-017-0362-3
11. Silva BC, Costa AG, Cusano NE, Kousteni S, Bilezikian JP. Catabolic and Anabolic Actions of Parathyroid Hormone on the Skeleton. *J Endocrinol Invest* (2011) 34(10):801–10. doi: 10.3275/7925
12. Salam S, Gallagher O, Gossiel F, Paggiosi M, Khwaja A, Eastell R. Diagnostic Accuracy of Biomarkers and Imaging for Bone Turnover in Renal Osteodystrophy. *J Am Soc Nephrol* (2018) 29(5):1557–65. doi: 10.1681/ASN.2017050584
13. Leonard MB. A Structural Approach to Skeletal Fragility in Chronic Kidney Disease. *Semin Nephrol* (2009) 29(2):133–43. doi: 10.1016/j.semnephrol.2009.01.006
14. Moe SM, Chen NX, Newman CL, Gattone VH2nd, Organ JM, Chen X, et al. A Comparison of Calcium to Zoledronic Acid for Improvement of Cortical Bone in an Animal Model of CKD. *J Bone Miner Res* (2014) 29(4):902–10. doi: 10.1002/jbmr.2089
15. Marques ID, Araújo MJ, Graciolli FG, Reis LM, Pereira RM, Custódio MR, et al. Biopsy vs. Peripheral Computed Tomography to Assess Bone Disease in CKD Patients On Dialysis: Differences and Similarities. *Osteoporos Int* (2017) 28(5):1675–83. doi: 10.1007/s00198-017-3956-9
16. Link TM. Osteoporosis Imaging: State of the Art and Advanced Imaging. *Radiology* (2012) 263(1):3–17. doi: 10.1148/radiol.2631201201
17. Manhard MK, Nyman JS, Does MD. Advances in Imaging Approaches to Fracture Risk Evaluation. *Transl Res* (2017) 181:1–14. doi: 10.1016/j.trsl.2016.09.006
18. Chang EY, Du J, Chung CB. UTE Imaging in the Musculoskeletal System. *J Magn Reson Imaging* (2015) 41(4):870–83. doi: 10.1002/jmri.24713
19. Jerban S, Lu X, Dorthe EW, Alenezi S, Ma Y, Kakos L, et al. Correlations of Cortical Bone Microstructural and Mechanical Properties With Water Proton Fractions Obtained From Ultrashort Echo Time (UTE) MRI Tricomponent T2* Model. *NMR BioMed* (2020) 33(3):e4233. doi: 10.1002/nbm.4233
20. Rajapakse CS, Bashoor-Zadeh M, Li C, Sun W, Wright AC, Wehrli FW. Volumetric Cortical Bone Porosity Assessment With MR Imaging: Validation and Clinical Feasibility. *Radiology* (2015) 276(2):526–35. doi: 10.1148/radiol.15141850
21. Seifert AC, Wehrli SL, Wehrli FW. Bi-Component T2 Analysis of Bound and Pore Bone Water Fractions Fails at High Field Strengths. *NMR BioMed* (2015) 28(7):861–72. doi: 10.1002/nbm.3305
22. Chen M, Yuan H. Assessment of Porosity Index of the Femoral Neck and Tibia by 3D Ultra-Short Echo-Time MRI. *J Magn Reson Imaging* (2018) 47(3):820–8. doi: 10.1002/jmri.25782
23. Chen TK, Knicely DH, Grams ME. Chronic Kidney Disease Diagnosis and Management: A Review. *JAMA* (2019) 322(13):1294–304. doi: 10.1001/jama.2019.14745
24. Nishiyama KK, Pauchard Y, Nikkel LE, Iyer S, Zhang C, McMahon DJ, et al. Longitudinal HR-pQCT and Image Registration Detects Endocortical Bone Loss in Kidney Transplantation Patients. *J Bone Miner Res* (2015) 30(3):554–61. doi: 10.1002/jbmr.2358
25. Woods GN, Ewing SK, Sigurdsson S, Kado DM, Ix JH, Hue TF, et al. Chronic Kidney Disease Is Associated With Greater Bone Marrow Adiposity. *J Bone Miner Res* (2018) 33(12):2158–64. doi: 10.1002/jbmr.3562
26. Trombetti A, Stoermann C, Chevalley T, Van Rietbergen B, Herrmann FR, Martin PY, et al. Alterations of Bone Microstructure and Strength in End-Stage Renal Failure. *Osteoporos Int* (2013) 24(5):1721–32. doi: 10.1007/s00198-012-2133-4
27. Lu X, Jerban S, Wan L, Ma Y, Jang H, Le N, et al. Three-Dimensional Ultrashort Echo Time Imaging With Tricomponent Analysis for Human Cortical Bone. *Magn Reson Med* (2019) 82(1):348–55. doi: 10.1002/mrm.27718
28. Levey AS, Stevens LA, Schmid CH, Zhang YL, Castro AF3rd, Feldman HI, et al. A New Equation to Estimate Glomerular Filtration Rate. *Ann Intern Med* (2009) 150(9):604–12. doi: 10.7326/0003-4819-150-9-200905050-00006

29. Tingley D, Yamamoto T, Hirose K, Keele L, Imai K. Mediation: R Package for Causal Mediation Analysis. *J Stat Software* (2014) 59:1–38. doi: 10.18637/jss.v059.i05
30. Sundh D, Mellström D, Nilsson M, Karlsson M, Ohlsson C, Lorentzon M. Increased Cortical Porosity in Older Men With Fracture. *J Bone Miner Res* (2015) 30(9):1692–700. doi: 10.1002/jbmr.2509
31. Cooper DM, Kawalilak CE, Harrison K, Johnston BD, Johnston JD. Cortical Bone Porosity: What Is It, Why Is It Important, and How Can We Detect it? *Curr Osteoporos Rep* (2016) 14(5):187–98. doi: 10.1007/s11914-016-0319-y
32. Metzger CE, Swallow EA, Allen MR. Elevations in Cortical Porosity Occur Prior to Significant Rise in Serum Parathyroid Hormone in Young Female Mice With Adenine-Induced CKD. *Calcif Tissue Int* (2020) 106(4):392–400. doi: 10.1007/s00223-019-00642-w
33. Nickolas TL, Cremers S, Zhang A, Thomas V, Stein E, Cohen A, et al. Discriminants of Prevalent Fractures in Chronic Kidney Disease. *J Am Soc Nephrol* (2011) 22(8):1560–72. doi: 10.1681/ASN.2010121275
34. Allen MR, Swallow EA, Metzger CE. Kidney Disease and Bone: Changing the Way We Look at Skeletal Health. *Curr Osteoporos Rep* (2020) 18(3):242–6. doi: 10.1007/s11914-020-00580-9
35. Sprague SM, Bellorin-Font E, Jorgetti V, Carvalho AB, Malluche HH, Ferreira A, et al. Diagnostic Accuracy of Bone Turnover Markers and Bone Histology in Patients With CKD Treated by Dialysis. *Am J Kidney Dis* (2016) 67(4):559–66. doi: 10.1053/j.ajkd.2015.06.023
36. Bellido T, Saini V, Pajevic PD. Effects of PTH on Osteocyte Function. *Bone* (2013) 54(2):250–7. doi: 10.1016/j.bone.2012.09.016
37. Metzger CE, Swallow EA, Stacy AJ, Allen MR. Strain-Specific Alterations in the Skeletal Response to Adenine-Induced Chronic Kidney Disease Are Associated With Differences in Parathyroid Hormone Levels. *Bone* (2021) 148:115963. doi: 10.1016/j.bone.2021.115963
38. Araujo MJ, Karohl C, Elias RM, Barreto FC, Barreto DV, Canziani ME, et al. The Pitfall of Treating Low Bone Turnover: Effects on Cortical Porosity. *Bone* (2016) 91:75–80. doi: 10.1016/j.bone.2016.07.009
39. Wheater G, Elshahaly M, Tuck SP, Datta HK, van Laar JM. The Clinical Utility of Bone Marker Measurements in Osteoporosis. *J Transl Med* (2013) 11:201. doi: 10.1186/1479-5876-11-201
40. Sharma AK, Masterson R, Holt SG, Toussaint ND. Emerging Role of High-Resolution Imaging in the Detection of Renal Osteodystrophy. *Nephrol (Carlton)* (2016) 21(10):801–11. doi: 10.1111/nep.12790
41. Duan Y, De Luca V, Seeman E. Parathyroid Hormone Deficiency and Excess: Similar Effects on Trabecular Bone But Differing Effects on Cortical Bone. *J Clin Endocrinol Metab* (1999) 84(2):718–22. doi: 10.1210/jcem.84.2.5498
42. Catarina C, Magalhães J, Neto R, Pereira L, Branco P, Adragão T, et al. Cortical Bone Analysis in a Predialysis Population: A Comparison With a Dialysis Population. *J Bone Miner Metab* (2017) 35(5):513–21. doi: 10.1007/s00774-016-0781-8

Conflict of Interest: The authors declare that the research was conducted in the absence of any commercial or financial relationships that could be construed as a potential conflict of interest.

frontiers in Endocrinology

ORIGINAL RESEARCH
published: 23 November 2021
doi: 10.3389/fendo.2021.771997

Prediction of Treatment Response According to ASAS-EULAR Management Recommendations in 1 Year for Hip Involvement in Axial Spondyloarthritis Based on MRI and Clinical Indicators

Zhuoyao Xie[1], Zixiao Lu[1], Hao Chen[2], Qiang Ye[1], Chang Guo[1], Kai Zheng[1], Xin Li[1], Qiuxia Xie[1], Shaoyong Hu[1], Quan Zhou[1] and Yinghua Zhao[1]**

[1] Department of Radiology, The Third Affiliated Hospital of Southern Medical University (Academy of Orthopedics, Guangdong Province), Guangzhou, China, [2] Department of Computer Science and Engineering, The Hong Kong University of Science and Technology, Hong Kong, Hong Kong SAR, China

Background: To predict the treatment response for axial spondyloarthritis (axSpA) with hip involvement in 1 year based on MRI and clinical indicators.

Methods: A total of 77 axSpA patients with hip involvement (60 males; median age, 25 years; interquartile, 22–31 years old) were treated with a drug recommended by the Assessment of SpondyloArthritis international Society and the European League Against Rheumatism (ASAS-EULAR) management. They were prospectively enrolled according to Assessment in SpondyloArthritis international Society (ASAS) criteria. Clinical indicators, including age, gender, disease duration, erythrocyte sedimentation rate (ESR) and C-reactive protein (CRP), were collected at baseline and in 3 months to 1-year follow-up. Treatment response was evaluated according to ASAS response criteria. MRI indicators consisting of bone marrow edema (BME) in acetabulum and femoral head, hip effusion, fat deposition, thickened synovium, bone erosion, bone proliferation, muscle involvement, enthesitis and bony ankylosis were assessed at baseline. Spearman's correlation analysis was utilized for indicator selection. The selected clinical and MRI indicators were integrated with previous clinical knowledge to develop multivariable logistic regression models. Receiver operator characteristic curve and area under the curve (AUC) were used to assess the performance of the constructed models.

Results: The model combining MR indicators comprising hip effusion, BME in acetabulum and femoral head and clinical indicators consisting of disease duration, ESR and CRP yielded AUC values of 0.811 and 0.753 for the training and validation cohorts, respectively.

OPEN ACCESS

Edited by:
Yajun Ma,
University of California, San Diego, United States

Reviewed by:
Clément Prati,
Centre Hospitalier Universitaire de Besançon, France
Alecio Lombardi,
University of California, San Diego, United States

***Correspondence:**
Quan Zhou
zhouquan3777@smu.edu.cn
Yinghua Zhao
zhaoyh@smu.edu.cn

Specialty section:
This article was submitted to Bone Research, a section of the journal Frontiers in Endocrinology

Received: 07 September 2021
Accepted: 14 October 2021
Published: 23 November 2021

Citation:
Xie Z, Lu Z, Chen H, Ye Q, Guo C, Zheng K, Li X, Xie Q, Hu S, Zhou Q and Zhao Y (2021) Prediction of Treatment Response According to ASAS-EULAR Management Recommendations in 1 Year for Hip Involvement in Axial Spondyloarthritis Based on MRI and Clinical Indicators. Front. Endocrinol. 12:771997. doi: 10.3389/fendo.2021.771997

Conclusion: The model combining MRI and clinical indicators could predict treatment response for axSpA with hip involvement in 1 year.

Keywords: magnetic resonance imaging, axial spondyloarthritis, hip involvement, treatment response, predictive model

INTRODUCTION

Axial spondyloarthritis (axSpA) is a chronic autoimmune and autoinflammatory disease characterized by low back pain and morning back stiffness with the prevalence of 0.24% in Europe and 0.17% in Asia (1, 2). The severity of axial disease and poor long-term outcome are strongly correlated with hip involvement, which commonly accounts for 18% to 25% in axSpA patients (3). Generally, inflammation with bone marrow edema (BME), synovitis, bone erosions and osteophytes can affect hip joints, which would lead to ankylosis progression and functional impairment (3, 4).

The 2016 update of the Assessment of SpondyloArthritis international Society and the European League Against Rheumatism (ASAS-EULAR) firstly recommends non-pharmacological management and drug treatment for axSpA. Regarding drug treatment, nonsteroidal anti-inflammatory drugs (NSAIDs) and biological disease-modifying antirheumatic drugs (bDMARDs) are recommended for axSpA, whereas conventional synthetic disease-modifying antirheumatic drugs (csDMARDs) may be considered for axSpA patients with peripheral joints involvement (5, 6). However, not all axSpA patients with hip involvement are suitable for the recommendation because adverse events, including infections, gastrointestinal disorders and injection site reactions, might occur in some patients receiving drug treatment (2, 6). In particular, drug resistance in patients with systemic autoimmune disorders is still a challenge in treatment (7). Discontinuation or switching from drug therapy might lead to significantly worse clinical outcomes, including poor disease control and increased disease flares (8). Hence, predicting response to treatment and switching treatment plans before drug treatment help patients avoid adverse events and drug resistance.

Currently, hip involvement can be defined by different imaging techniques in axSpA patients, such as X-ray/computed tomography (CT) and magnetic resonance image (MRI) (4). Conventional radiography/CT can find structure damage and plays an essential role in the diagnosis and classification of axSpA, but it could not be used to detect early disease and predict treatment response (4). Comparatively, MRI could detect active inflammatory changes in early-stage axSpA, such as BME, synovitis, joint effusion and enthesitis (9). The Hip Inflammation MRI Scoring System (HIMRISS) is a feasible and reliable tool for evaluating BME and hip effusion (10). Some semi-quantitative MRI parameters of hip involvement proposed by radiologists have been used to evaluate disease progression and predict treatment response in axSpA (11, 12). Nonetheless, single MRI indicator could not predict treatment response in the individual axSpA patient with hip involvement. Berlin MRI spine score combined with symptom duration and C-reactive protein (CRP) could be used to predict response to drug treatment in axSpA (11, 12). However, an effective method for predicting therapy response for the hip involvement in axSpA to support physicians in clinical practice is still lacking.

We hypothesize that MRI indicators combined with clinical indicators might be associated with response to treatment for hip involvement in axSpA. Our study aimed to determine the potential predictive factors based on MRI and clinical indicators for treatment response in axSpA patients with hip involvement and build a robust model to predict whether the patient would benefit from pharmacological treatment in 1 year.

MATERIALS AND METHODS

Patients

According to the Assessment in SpondyloArthritis international Society (ASAS) (13), all consecutive axSpA patients with hip involvement treated with drugs at baseline were enrolled from January 2016 to June 2020 in our institution. An overview of the patient recruitment process is shown in **Figure 1**. Pharmacological treatment for patients were csDMARDs consisting of sulfasalazine and methotrexate (MTX) and bDMARDs, such as tumour necrosis factor inhibitor (TNFi) recommended by the ASAS-EULAR management (5). MR examination was performed within 2 weeks before or after treatment starting. Clinical indicators in axSpA patients at baseline and after 3 months to 1-year follow-up were obtained to evaluate treatment response. Hip involvement in our study was defined as abnormal MR findings in hip joint, such as bone marrow edema, effusion, fat deposition, thickened synovium, enthesitis, bone erosion, muscle involvement, bone proliferation and ankylosis. The patients were excluded in the following cases: (i) without more than two treatment response evaluation; (ii) lesions were located in other joints, such as shoulder, knee and ankle joints; (iii) hip involvement was accompanied with osteoarthritis, rheumatoid arthritis and other types of arthritis; (iv) poor or missing images for evaluation. Using 10-fold cross-validation, all patients were randomly divided into training and validation sets with a ratio of 9:1 according to treatment response.

Clinical Indicator and Treatment Response

Clinical indicators included age, gender, disease duration, smoking status, history of drug treatment, presence of extra articular manifestations, human leukocyte antigen (HLA) B27, erythrocyte sedimentation rate (ESR), CRP, spinal pain, patient

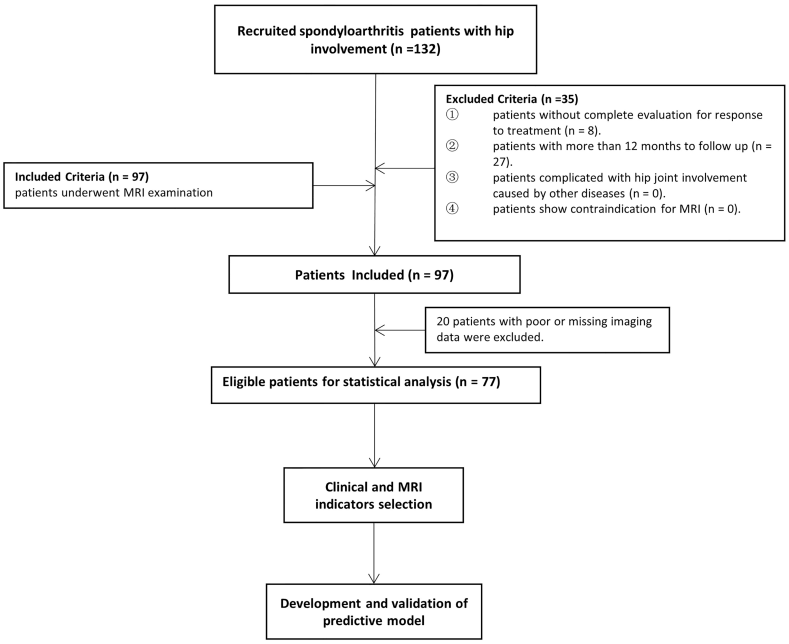

FIGURE 1 | Flow chart of patients enrolled in the study.

global assessment, Bath Ankylosing Spondylitis Disease Activity Index (BASDAI) and Bath Ankylosing Spondylitis Functional Index (BASFI). BASDAI and BASFI were described in **Appendix E1**, which were used to assess disease activity and function in axSpA, respectively (14, 15). Treatment response was assessed according to ASAS20, ASAS40, ASAS5/6 and ASAS partial remission improvement criteria (**Appendix E2**) (13).

MRI Protocol

Clinical 3.0T system (Achieva 3.0T, Philips Healthcare, Best, Netherlands) was used to scan axSpA patients at baseline. Three axial MR sequences of the bilateral hip joints were conducted for the supine position. The sequence parameters are described in **Appendix E3**.

Definition and Assessment of MRI Indicators

The MRI indicators at hip joint were determined in axSpA patients with hip involvement, consisting of seven categorical, two semi-quantitative and one quantitative indicators. The methods for assessment of categorical MRI indicators, including fat deposition, thickened synovium, enthesitis, bone erosion, muscle involvement, bone proliferation and ankylosis are detailed in **Appendix E4**, and these indicators were recorded as present (1) or absent (0). The method to assess the semi-quantitative indicator BME at hip joint is described in **Appendix E5**. The quantitative indicator for hip joint, namely, hip effusion, is specified in **Appendix E6**. **Figure 2** demonstrates the scoring system for BME and hip effusion on axial MRI in hip joint. Inter-observer agreement for MR indicators in 30 patients was respectively assessed by two radiologists with 2 and 10 years of experience in musculoskeletal imaging (ZY.X and Q.Y). Both radiologists were blinded to the clinical indicators at baseline and the response to treatment within 1 year. Inter-observer agreement for MR indicators in 30 patients was independently evaluated twice by one radiologist (ZY.X). Controversial MRI assessments between the two radiologists were reviewed by a radiology expert (YH.Z, who has 30 years of experience in musculoskeletal imaging) to make an arbitration for further analysis. The remaining cases were independently evaluated by the radiologist (ZY.X) with 2 years of experience.

Statistical Analysis

All data were analysed using Statistical Product and Service Solutions (SPSS) (version 22.0; IBM, Armonk, NY). Continuous variables of clinical data and MRI indicators were described as mean ± standard deviation or median (interquartile range [IQR]), and categorical variables were presented as binary numbers and n (%), as appropriate. The Cohen's kappa coefficients and intraclass correlation coefficients (ICCs) were utilized to evaluate intra- and inter-observer agreement of categorical variables and continuous variables for MRI indicators, respectively. The Cohen's kappa coefficients were descripted as follows: <0.20 (Poor), 0.21–0.40 (Fair), 0.41–0.60 (Moderate), 0.61- 0.80 (Good) and 0.81–1.00 (Perfect), respectively. Values less than 0.5, between 0.5 and 0.75 and greater than 0.75 indicated poor, moderate and good agreement for ICCs, respectively. The differences between the responders and non-responders were compared using the Mann-Whitney U test and Chi-square test with continuity correction,

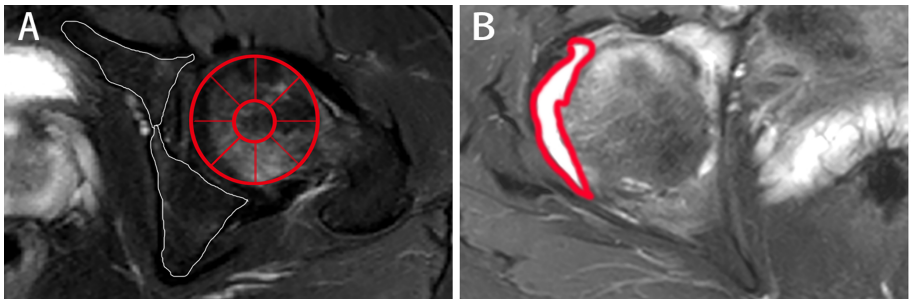

FIGURE 2 | The scoring system on axial MRI in axSpA patients with hip involvement. **(A)** BME assessment in the two regions of left acetabulum delineated by white line and the nine regions of left femoral head segmented by red line is shown on SPAIR imaging, respectively. **(B)** Effusion assessment in the right hip is outlined by the thick red line on SPAIR imaging. AxSpA, Axial spondyloarthritis; BME, Bone marrow edema; SPAIR, Spectral attenuated inversion recovery.

as appropriate. A two-tailed P value of less than 0.05 was regarded as statistically significant. MATLAB version 2018a was used to perform further analysis. To improve the performance of predictive models, we first normalized all the clinical and MRI indicator to a range of [-1,1] by subtracting the mean value of each indicator and dividing it by the standard deviation. Spearman's correlation analysis was used to select indicators for further analysis. The multivariable logistic regression model was developed to find the best predictive linear combination of these indicators for predicting treatment response, thereby maximizing the conditional probability of the treatment response corresponding to the input data. All the models were trained and evaluated on the whole data set by using 10-fold cross-validation. Receiver operator characteristic (ROC) curve and area under the curve (AUC) were utilized to evaluate the models' performance. The details regarding indicator selection and further developments and validation of the predictive model are described in **Appendixes E7** and **E8**, respectively.

TABLE 1 | Patient characteristics.

Clinical characteristics	Patients (n = 77)
Age (y)	25 (22-31)
Gender	
Male	60 (77.9%)
Female	17 (22.1%)
Disease duration (mon)	24 (11-60)
Smoking status	
Smoker	60 (1.3%)
Non-Smoker	72 (93.5%)
Extra-articular manifestation	
With	4 (5.2%)
Without	69 (89.6%)
History of drug treatments	
With	57 (74.0%)
Without	16 (20.8%)
HLA B27	
(+)	56 (72.7%)
(-)	15 (19.5%)
ESR (mm/h)	14 (6-32)
CRP (mg/L)	8 (3-21.5)

Continuous variables inconsistent with a normal distribution were presented as median (interquartile range). Categorical variables were presented as the number (percentage). HLA B27, human leukocyte antigen B27; ESR, erythrocyte sedimentation; CRP, C-reactive protein; BME, bone marrow edema.

RESULTS

Patient Characteristics

A total of 132 patients were consecutively recruited from our institution in the study. A total of 55 patients were excluded because follow-up lasted for more than 12 months (n = 27), as well as insufficient images (n = 20) and incomplete clinical indicators to evaluate treatment response (n = 8). Seventy-seven patients (60 males and 17 females; median age, 25 years old; IQR, 22–31 years old) were ultimately enrolled for further analysis. The patient characteristics were summarized in **Table 1**. There were 4 (5.2%) patients without record of smoking status, history of drug treatment and extra articular manifestations and 6 (7.8%) patients without record of HLA B27 examination. 18 (23.4%) patients were treated with biologicals and 55 (71.2%) patients were not before our study, according to the ASAS-EULAR management before our study. All 77 patients obtained ASAS20 and ASAS40 results, whereas one patient lacked ASAS5/6 and ASAS partial remission results. The response rates evaluated according to ASAS20, ASAS40, ASAS5/6 and ASAS partial remission were 44.2%, 26.0%, 26.3% and 21.1%, respectively.

Clinical and MRI Indicators for Treatment Response Prediction

Figure 3 displays various MRI findings in axSpA patients with hip involvement. Regarding MRI indicators in the 77 patients, hip effusion area, BME score in acetabulum and femoral head were 142 (94–210) mm^2, 0 (0-5) and 0 (0–4), respectively. Forty-one (53.2%) patients presented fat a and 16 (20.8%) patients revealed thickened synovium. Bone proliferation appeared in 8 (10.4%) patients. Five (6.5%) patients displayed bone erosion. Five (6.5%) patients showed muscle involvement. In addition, enthesitis and bony ankylosis were not found. ICCs for the eight

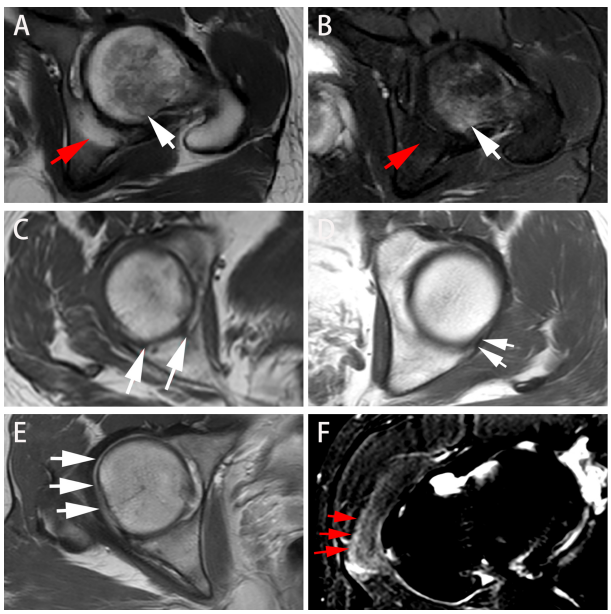

FIGURE 3 | Different presentations on axial MRI in axSpA patients with hip involvement. **(A, B)** A 27-year-old male demonstrated BME (white arrow) in left femoral head and fat deposition (red arrow) in left acetabulum on T1WI and SPAIR imaging, respectively. **(C, D)** A 25-year-old male manifested erosion (arrows) in right acetabulum and bone proliferation (arrows) in left acetabulum, respectively. **(E)** A 16-year-old male revealed thickened synovium with slightly high signal strip in right hip on contrast-enhanced T1WI (arrows). **(F)** A 31-year-old male showed gluteus medius edema (arrows) in right hip on SPAIR imaging. AxSpA: Axial spondyloarthritis; BME: Bone marrow edema; T1WI: T1-weighted imaging; SPAIR: Spectral attenuated inversion recovery.

MRI indicators are tabulated in **Table 2**, and good observer agreements (ranged from 0.768 to 0.969) in hip joint evaluation were showed. Clinical and MRI indicators in responders and non-responders are summarized in **Table 3**. Four clinical and MRI indicators compromising disease duration (P = 0.038), ESR (P = 0.011), BME in acetabulum (P = 0.028) and hip effusion (P = 0.012) showed significant differences between responders and non-responders according to ASAS20. ESR (P = 0.044) and hip effusion (P = 0.019) were significantly different between responders and non-responders evaluated by ASAS40 criteria.

Indicator Selection and Development of Predictive Model

Two steps were used for indicator selection. First, the four clinical and MRI indicators demonstrating significant differences in ASAS20 response evaluation were further analysed by Spearman's rank correlation test, the results of which are tabulated in **Table 4**. Second, MRI indicators together with the clinical indicators were selected in accordance to the significant correlation with ASAS20 to build the logistic regression model for predicting treatment response. We constructed a primary model comprising disease duration, ESR, CRP and BME in the acetabulum. Disease duration, CRP, ESR and BME were reported as predictors of treatment response (12, 16). Referring to prior clinical knowledge, we considered that disease duration, ESR, CRP, hip effusion and BME in acetabulum and femoral head could be used to develop a predictive model.

Performance of Predictive Model of Treatment Response

ROC analysis for the performance of predictive model is displayed in **Figure 4**. The model combining disease duration, ESR, CRP and BME in acetabulum yielded an AUC of 0.735 for the training set and an AUC of 0.664 for the validation set. The model integrating disease duration, ESR, CRP, hip effusion and BME in acetabulum and femoral head demonstrated AUC values of 0.811 and 0.753 for the training and validation sets, respectively.

DISCUSSION

In this prospective study, we developed and validated a model to predict curative effect before drug treatment in axSpA patients with hip involvement in 1 year. The model consisting of MRI (BME and hip effusion) and clinical indicators (disease duration, ESR and CRP) demonstrated optimal performance in predicting treatment response.

Our study firstly demonstrated that hip effusion (r = 0.288, P < 0.05) was the MR indicator with the highest number of correlations with responses to drug treatment in axSpA patients with hip involvement. No research has previously been

TABLE 2 | Intra and inter-observer agreement for MRI assessments of two radiologists.

Parameters	Intra-observeragreement	95% CI	Inter-observeragreement	95% CI
BME in acetabulum	0.892	0.757-1.000	0.839	0.682-0.996
BME in femoral head	0.899	0.772-1.000	0.848	0.699-0.997
Hip effusion (mm^2)	0.950	0.889-0.941	0.950	0.890-0.942
Fat deposition	0.867	0.691-1.000	0.800	0.590-1.000
Bone erosion	0.783	0.373-1.000	0.783	0.373-1.000
Bone proliferation	0.839	0.531-1.000	0.839	0.531-1.000
Thickened synovium	0.793	0.523-1.000	0.889	0.680-1.000
Muscle involvement	0.870	0.621-1.000	0.870	0.621-1.000

Calculation of Cohen's kappa was performed for categorical variables. Intraclass correlation coefficients were applied for continuous variables; CI, confidence interval; BME, bone marrow edema.

TABLE 3 | Comparison of clinical and MRI indicators of treatment responders and non-responders.

Parameters	ASAS20		*P*	ASAS40		*P*	ASAS5/6		*P*	ASAS partial remission		*P*
	Responder	Non-responder		Responder	Non-responder		Responder	Non-responder		Responder	Non-responder	
Clinical indicators												
Age (y)	25.5 (21.75-30.25)	25 (22-31)	0.939	25 (21-33.25)	25 (22-30.5)	0.825	26 (21.5-34.5)	24.5 (22-30.75)	0.457	25 (20.75-34)	25 (22-30)	0.853
Gender			0.779			0.497			0.521			0.957
Male	27 (79.4%)	33 (76.7%)		14 (70.0%)	46 (80.7%)		14 (70.0%)	45 (80.4%)		13 (81.3%)	46 (76.7%)	
Female	7 (20.6%)	10 (23.3%)		6 (30.0%)	11 (19.3%)		6 (30.0%)	11 (19.6%)		3 (18.8%)	16 (23.3%)	
Disease duration (mon)	24 (6-42)	35 (12-72)	0.038	24 (6-54)	27 (12-67.5)	0.213	24 (8.25-87)	25 (10.5-57)	0.714	24 (4-54)	25 (12-60)	0.561
Smoking status			1.000			1.000			1.000			1.000
Smoker	0 (0%)	1 (2.3%)		0 (0%)	1 (1.8%)		0 (0%)	1 (1.8%)		0 (0%)	1 (1.7%)	
Non-Smoker	32 (94.1%)	40 (93.0%)		20 (100%)	52 (91.2%)		20 (100%)	51 (91.1%)		15 (93.8%)	56 (93.3%)	
Extra-articular manifestation			1.000			0.641			1.000			1.000
With	2 (5.9%)	2 (4.7%)		2 (10.0%)	2 (3.5%)		1 (5.0%)	3 (5.4%)		1 (6.3%)	3 (5.0%)	
Without	30 (88.2%)	39 (90.7%)		18 (90.0%)	51 (89.5%)		19 (95.0%)	49 (87.5%)		14 (87.5%)	54 (90.0%)	
History of drug treatments			0.257			0.479			1.000			0.907
With	23 (67.6%)	34 (79.1%)		14 (70.0%)	43 (75.4%)		4 (20.0 %)	40 (71.4%)		11 (68.8%)	45 (75.0%)	
Without	9 (26.5%)	7 (16.3%)		6 (30.0%)	10 (17.5%)		16 (80.0%)	12 (21.4%)		4 (25.0%)	12 (20.0%)	
HLA B27			0.395			0.750			0.779			1.000
(+)	23 (67.6%)	33 (76.7%)		14 (70.0%)	42 (73.7%)		14 (70.0%)	41 (73.2%)		12 (75.0%)	43 (71.7%)	
(-)	8 (23.5%)	7 (16.3%)		5 (25.0%)	10 (17.5%)		5 (25.0%)	10 (17.9%)		3 (18.8%)	12 (20.0%)	
ESR (mm/h)	19 (10-46.25)	11 (3-27)	0.011	17.5 (11.5-48.75)	12 (3.5-29.5)	0.044	17.5 (10-47)	13.5 (4.25-29.5)	0.182	12.5 (6.25-19.75)	15 (4.25-36)	0.628
CRP (mg/L)	11.5 (5.5-20.25)	5 (0.5-26)	0.122	12.5 (4.5-20.75)	6 (0.5-22.5)	0.195	9.5 (4.5-20.75)	6 (0.63-21.75)	0.331	6.5 (3.25-16.5)	8.5 (0.5-24.5)	0.773
MRI indicators												
BME in acetabulum	2 (0-8)	2 (0-8)	0.028	4.5 (0-9.25)	0 (0-2.5)	0.056	0 (0-5.75)	0 (0-5)	0.979	0 (0-4.75)	0 (0-5)	0.578
BME in femoral head	0 (0-4)	0 (0-4)	0.602	0 (0-3.75)	0 (0-4)	0.810	0 (0-3.75)	0 (0-4)	0.823	0 (0-2)	0 (0-8.5)	0.287
Hip effusion (mm^2)	168.5 (99.5-256)	128 (85-166)	0.012	181.5 (105.25-302)	137 (86-179)	0.019	181.5 (105.25-266)	137 (90.75-181.5)	0.066	133.5 (95.25-207.25)	149 (87.75-211)	0.736
Fat deposition	19 (55.9%)	22 (51.2%)	0.680	9 (45.0%)	32 (56.1%)	0.390	13 (65.0%)	28 (50.0%)	0.248	8 (50.0%)	33 (55.0%)	0.721
Bone erosion	2 (5.9%)	3 (7.0%)	1.000	0 (0%)	5 (8.8 %)	0.400	0 (0%)	5 (8.9%)	0.391	0 (0%)	5 (8.3%)	0.531
Bone proliferation	3 (8.8%)	5 (11.6%)	0.981	1 (5.0%)	7 (12.3 %)	0.623	1 (5.0%)	7 (12.5%)	0.607	1 (6.3%)	7 (11.7%)	0.866
Thickened synovium	7 (20.6%)	9 (20.9%)	0.971	5 (25.0%)	11 (19.3%)	0.826	4 (20%)	12 (21.4%)	1.000	3 (18.8%)	13 (21.7%)	1.000
Muscle involvement	2 (5.9 %)	3 (7.0%)	1.000	0 (0%)	5 (8.8%)	0.400	0 (0%)	5 (8.9%)	0.391	1 (6.3%)	4 (6.7%)	1.000

Continuous variables inconsistent with a normal distribution were presented as median (interquartile range). Categorical variables were presented as the number (percentage). The differences in continuous variables were compared using the Mann-Whitney U test. The differences in categorical variables were compared using the Chi-square test with continuity correction as appropriate. HLA B27, human leukocyte antigen B27; ESR, erythrocyte sedimentation; CRP, C-reactive protein; BME, bone marrow edema.

conducted on the association between hip effusion and treatment response for axSpA. Gaffney et al.'s study validated that joint effusion could be used to predict pain response in patients with knee osteoarthritis (OA) treated with intra-articular steroid injections (IASI) at 1 and 6 weeks, respectively (17). Similarly, another study on knee OA stated that joint effusion was associated with the increased benefit of IASI treatment (18). Some researchers found that joint effusion-synovitis could not offer sufficient insight into clinical responses of patients with hip OA who were treated after 8 weeks and of RA patients treated after 2 years (19, 20). Although these studies involved various diseases and different joints, and the patients were treated with different drugs, the joint effusion was still an essential predictor of treatment response. The explicit association between hip effusion and the improvement in axSpA patients with hip involvement after drug treatment needs to be confirmed by others studies.

BME in acetabulum could be a predictor of good treatment response within 1 year. Additionally, BME in femoral head helped improve the performance of the predictive model, which indicated that it was a potential factor for response prediction. Similarly, Rudwaleit et al.'s finding indicated that BME evaluated by Berlin MRI spine score in axial joints contributed to the prediction of treatment response in axSpA patients (11, 12). A small sample size study concentrated on short-term predictive outcome of BME for radiographic progression from 6 to 12 months in rheumatoid arthritis (RA) (21). Hetland et al. identified BME as a predictor of progression at long-term follow-up in RA (20, 22). The predictive

TABLE 4 | Results of indicators significantly correlated with treatment response.

Parameters	ASAS20		ASAS40		ASAS5/6		ASAS partial remission	
	r	*P*	*r*	*P*	*r*	*P*	*r*	*P*
Disease duration (mon)	-0.238	0.037	-0.143	0.215	0.042	0.717	-0.056	0.631
ESR (mm/h)	0.293	0.010	0.231	0.043	0.154	0.184	-0.067	0.565
BME in acetabulum	0.251	0.027	0.220	0.055	-0.003	0.979	-0.064	0.581
Hip effusion (mm^2)	0.288	0.011	0.269	0.018	0.213	0.065	-0.039	0.738

ESR, erythrocyte sedimentation rate; BME, Bone marrow edema. "r", Spearman correlation coefficient.

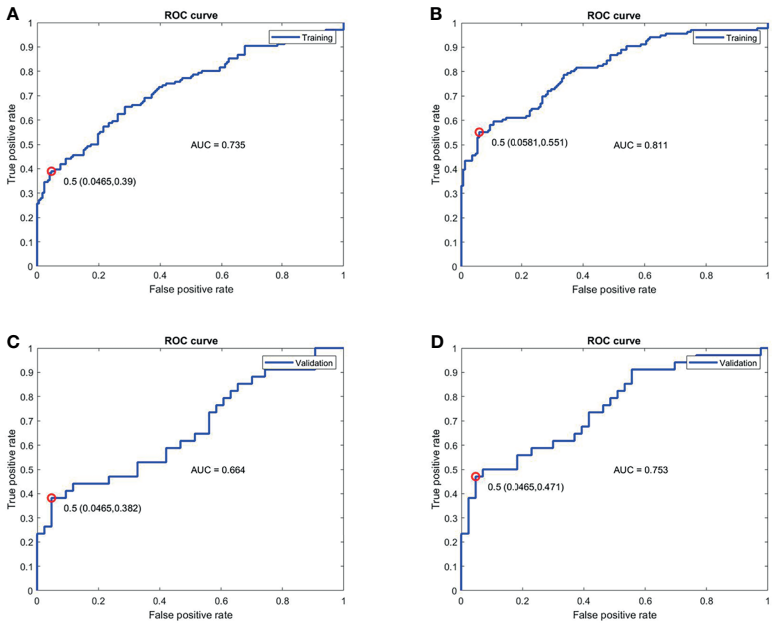

FIGURE 4 | ROC analysis for the performance of the two models for treatment response prediction on the training and validation cohorts. **(A, C)** The model combining disease duration, ESR, hip effusion and BME in acetabulum showed AUC values of 0.735 and 0.664 for training and validation cohorts, respectively. **(B, D)** The model integrated disease duration, CRP, ESR, hip effusion and BME in the acetabulum and femoral head obtained better predictive ability with AUC values of 0.811 and 0.753 in the training and validation cohorts, respectively. ROC, Receiver operator characteristic; ESR, erythrocyte sedimentation rate; CRP, C-reactive protein; BME, Bone marrow edema; AUC, Area under the curve.

value of BME was not reported in the same rheumatic disease or in the follow-up interval in these studies, making direct comparisons with our study results difficult. Nevertheless, BME could still provide sufficient predictive value for patients before drug treatment. Notably, widespread active inflammation in the joint was manifested as BME on MRI in axSpA, OA and RA (23, 24); it was considered as an additional predictive value for treatment response in our study. Local inflammation in the involved joint (BME) could be visualized and assessed on MRI, whereas the inflammatory markers (CRP and ESR) could reflect the global inflammation disease, thereby implying that these predictors were complementary components. A previous study supported our results that a combination of BME and CRP demonstrated more powerful predictive capacity than a single parameter (12).

Fat deposition and bone erosion showed poor predictive value for treatment response in 1 year. However, Koo et al. demonstrated that fat deposition in the sacroiliac joint indicated a chronic stage of SpA, and the quantitative biomarker fat fraction was related to a worse outcome (25). No research has concentrated on the association between bone erosion and treatment response in SpA patients. However, similar to our results, research on RA patients indicated that bone erosion on MRI at baseline was not an independent predictor for radiographic progression in patients with early RA after 2 years (20). The follow-up time was relatively short in our study; thus, we were aware that long-term outcomes and life status after pharmacological treatment might be different from short-term results in SpA patients with hip involvement. More studies on long-term results are necessary, although they might be challenging. As thinner slices (2 or 3 mm) demonstrated high diagnostic accuracy and specificity for assessment of bone erosion on T1WI (26), 3 mm T1WI was applied to obtain a reliable and accurate assessment of bone erosion and to help identify the predictive value for treatment response in our study.

Higher ESR level and shorter disease duration predicted better treatment response. Despite that CRP showed no significance for prediction, it was reasonably added into the predictive model because of its advantage in response prediction (27), and the model performance was practically improved. These results were consistent with those of Lubrano et al., in which high ESR and CRP levels and low disease duration at baseline were confirmed to be significantly associated with improvement of BASFI (16), one of the four domains in the ASAS20 response criteria (13). Therefore, ESR and CRP levels could predict a better response to drug treatment in axSpA (28). Deodhar et al. confirmed our result that short disease duration was an important predictor for pharmacological response (29). ESR and CRP were important inflammatory markers but were limited because of their lack of sensitivity or specificity. Moreover, they might be affected by either non-infectious conditions or inflammation (30). Nonetheless, a combination of ESR and CRP with MRI indicators could improve the accuracy of the predictive model, which was currently used to help predict drug treatment response and guide patients' treatment in clinical practice (27).

To our knowledge, this is the first time that MRI indicators were specifically considered in the construction of a predictive model for treatment response in axSpA patients with hip involvement. More evidence suggested that axSpA progression detected on MRI was related to treatment response (31). Inflammatory MRI findings on hip joint were an objective measurement whose association with inflammation on histopathology had been validated; they could serve as a reliable indicator (27). Some axSpA patients might benefit from MR examination before drug treatment; it could help prevent adverse events including infections and gastrointestinal disorder (2, 6), drug resistance (7), increased disease flares due to discontinuation of or switch from drug therapy (8) and the risk of undergoing total hip arthroplasty, i.e. heterotopic ossification and revision surgery (5, 32). We developed a predictive model consisting of six selected MRI and clinical indicators and showed that the model could successfully identify which patient can potentially benefit from a drug treatment with AUC values of 0.811 and 0.753 in training and validation cohorts, respectively. Thus, the constructed model could help rheumatologists discriminate responders and non-responders before treatment to increase the safety and effectiveness of drug therapy.

Several limitations should be acknowledged in our study. First, the sample size was relatively small in this single-centre study, which might lead to selection bias and influence the accuracy of our predictive model. Second, we used a scoring system similar to the HIMRISS and evaluated the hip joint on the axial plane instead of the coronal plane on MRI. Therefore, the reliability of our evaluation for hip joint and its correlation with the previous scoring system should be further tested. Third, many MRI indicators except for hip effusion were not quantitatively assessed, and assessment would be restricted by subjectivity and variability. Finally, the short-term effect (≤ 1 year) of treatment response was investigated in the study. As axSpA is a chronic condition, and continuous medication is regularly taken by patients (5), long-term outcomes of drug therapy need to be explored.

In conclusion, short disease duration, high ESR levels, hip effusion and BME in acetabulum predicted better treatment response within 1 year. The combination of MRI indicators, including hip effusion, BME in acetabulum and femoral head, and clinical indicators consisting of disease duration, ESR and CRP provided sufficient insights into response prediction. Prediction results would serve as promising guides in clinical decision-making for axSpA patients with hip involvement.

DATA AVAILABILITY STATEMENT

The raw data supporting the conclusions of this article will be made available by the authors, without undue reservation.

ETHICS STATEMENT

The studies involving human participants were reviewed and approved by the institutional review board of the Third Affiliated Hospital of Southern Medical University (IRB number 201501003). Written informed consent from the participants' legal guardian/next of kin was not required to participate in this study in accordance with the national legislation and the institutional requirements.

AUTHOR CONTRIBUTIONS

ZX: Conceptualization, methodology, validation, investigation, data curation, software, and writing – original draft. ZL: Methodology, software, validation, formal analysis, and writing – review and editing. HC: Validation. QY: Visualization. CG: Data curation and investigation. KZ Data curation. XL: Investigation. QX: Data curation. SH: Data curation. QZ: Resource. YZ: Conceptualization, methodology, visualization, validation, writing – review and editing. All authors contributed to the article and approved the submitted version.

FUNDING

This study is supported by the National Natural Science Foundation of China (Grant No. 81871510).

SUPPLEMENTARY MATERIAL

The Supplementary Material for this article can be found online at: https://www.frontiersin.org/articles/10.3389/fendo.2021.771997/full#supplementary-material

REFERENCES

1. Sieper J, Braun J, Dougados M, Baeten D. Axial Spondyloarthritis. *Nat Rev Dis Primers* (2015) 1:15013. doi: 10.1038/nrdp.2015.13
2. Taurog JD, Chhabra A, Colbert RA. Ankylosing Spondylitis and Axial Spondyloarthritis. *N Engl J Med* (2016) 374(26):2563–74. doi: 10.1056/NEJMra1406182
3. Wink F, Arends S, Maas F, Bootsma H, Griep EN, Bruyn GAW, et al. High Prevalence of Hip Involvement and Decrease in Inflammatory Ultrasound Lesions During Tumour Necrosis Factor-α Blocking Therapy in Ankylosing Spondylitis. *Rheumatology (Ox Engl)* (2019) 58(6):1040–6. doi: 10.1093/rheumatology/key382
4. Vander Cruyssen B, Vastesaeger N, Collantes-Estévez E. Hip Disease in Ankylosing Spondylitis. *Curr Opin Rheumatol* (2013) 25(4):448–54. doi: 10.1097/BOR.0b013e3283620e04
5. van der Heijde D, Ramiro S, Landewé R, Baraliakos X, Van den Bosch F, Sepriano A, et al. Update of the ASAS-EULAR Management Recommendations for Axial Spondyloarthritis. *Ann Rheum Dis* (2017) 76(6):978–91. doi: 10.1136/annrheumdis-2016-210770
6. Navarro-Sarabia F, Fernández-Sueiro JL, Torre-Alonso JC, Gratacos J, Queiro R, Gonzalez C, et al. High-Dose Etanercept in Ankylosing Spondylitis: Results of a 12-Week Randomized, Double Blind, Controlled Multicentre Study (LOADET Study). *Rheumatology (Ox Engl)* (2011) 50(10):1828–37. doi: 10.1093/rheumatology/ker083
7. Picchianti-Diamanti A, Rosado MM, Scarsella M, Laganà B, D'Amelio R. P-Glycoprotein and Drug Resistance in Systemic Autoimmune Diseases. *Int J Mol Sci* (2014) 15(3):4965–76. doi: 10.3390/ijms15034965
8. Wolf D, Skup M, Yang H, Fang AP, Kageleiry A, Chao J, et al. Clinical Outcomes Associated With Switching or Discontinuation From Anti-TNF Inhibitors for Nonmedical Reasons. *Clin Ther* (2017) 39(4):849–62.e6. doi: 10.1016/j.clinthera.2017.03.005
9. Althoff CE, Sieper J, Song I-H, Haibel H, Weiß A, Diekhoff T, et al. Active Inflammation and Structural Change in Early Active Axial Spondyloarthritis as Detected by Whole-Body MRI. *Ann Rheum Dis* (2013) 72(6):967–73. doi: 10.1136/annrheumdis-2012-201545
10. Maksymowych WP, Cibere J, Loeuille D, Weber U, Zubler V, Roemer FW, et al. Preliminary Validation of 2 Magnetic Resonance Image Scoring Systems for Osteoarthritis of the Hip According to the OMERACT Filter. *J Rheumatol* (2014) 41(2):370–8. doi: 10.3899/jrheum.131083
11. van der Heijde D, Landewé R, Hermann K-G, Rudwaleit M, Østergaard M, Oostveen A, et al. Is There a Preferred Method for Scoring Activity of the Spine by Magnetic Resonance Imaging in Ankylosing Spondylitis? *J Rheumatol* (2007) 34(4):871–3.
12. Rudwaleit M, Schwarzlose S, Hilgert ES, Listing J, Braun J, Sieper J. MRI in Predicting a Major Clinical Response to Anti-Tumour Necrosis Factor Treatment in Ankylosing Spondylitis. *Ann Rheum Dis* (2008) 67(9):1276–81. doi: 10.1136/ard.2007.073098
13. Sieper J, Rudwaleit M, Baraliakos X, Brandt J, Braun J, Burgos-Vargas R, et al. The Assessment of SpondyloArthritis International Society (ASAS) Handbook: A Guide to Assess Spondyloarthritis. *Ann Rheum Dis* (2009) 68 Suppl 2:ii1–44. doi: 10.1136/ard.2008.104018
14. Garrett S, Jenkinson T, Kennedy LG, Whitelock H, Gaisford P, Calin A. A New Approach to Defining Disease Status in Ankylosing Spondylitis: The Bath Ankylosing Spondylitis Disease Activity Index. *J Rheumatol* (1994) 21(12):2286–91.
15. Calin A, Jones SD, Garrett SL, Kennedy LG. Bath Ankylosing Spondylitis Functional Index. *Br J Rheumatol* (1995) 34(8):793–4. doi: 10.1093/rheumatology/34.8.793
16. Lubrano E, Perrotta FM, Manara M, D'Angelo S, Ramonda R, Punzi L, et al. Improvement of Function and Its Determinants in a Group of Axial Spondyloarthritis Patients Treated With TNF Inhibitors: A Real-Life Study. *Rheumatol Ther* (2020) 7(2):301–10. doi: 10.1007/s40744-020-00197-5
17. Gaffney K, Ledingham J, Perry JD. Intra-Articular Triamcinolone Hexacetonide in Knee Osteoarthritis: Factors Influencing the Clinical Response. *Ann Rheum Dis* (1995) 54(5):379–81. doi: 10.1136/ard.54.5.379
18. Arden NK, Reading IC, Jordan KM, Thomas L, Platten H, Hassan A, et al. A Randomised Controlled Trial of Tidal Irrigation vs Corticosteroid Injection in Knee Osteoarthritis: The KIVIS Study. *Osteoarthritis Cartilage* (2008) 16 (6):733–9. doi: 10.1016/j.joca.2007.10.011
19. Steer KJD, Bostick GP, Woodhouse LJ, Nguyen TT, Schankath A, Lambert RGW, et al. Can Effusion-Synovitis Measured on Ultrasound or MRI Predict Response to Intra-Articular Steroid Injection in Hip Osteoarthritis? *Skeletal Radiol* (2019) 48(2):227–37. doi: 10.1007/s00256-018-3010-9
20. Hetland ML, Ejbjerg B, Hørslev-Petersen K, Jacobsen S, Vestergaard A, Jurik AG, et al. MRI Bone Oedema Is the Strongest Predictor of Subsequent Radiographic Progression in Early Rheumatoid Arthritis. Results From a 2-Year Randomised Controlled Trial (CIMESTRA). *Ann Rheum Dis* (2009) 68 (3):384–90. doi: 10.1136/ard.2008.088245
21. Tamai M, Arima K, Nakashima Y, Kita J, Umeda M, Fukui S, et al. Baseline MRI Bone Erosion Predicts the Subsequent Radiographic Progression in Early Rheumatoid Arthritis Patients Who Achieved Sustained Good Clinical Response. *Mod Rheumatol* (2017) 27(6):961–6. doi: 10.1080/14397595.2017.1294280
22. Hetland ML, Østergaard M, Stengaard-Pedersen K, Junker P, Ejbjerg B, Jacobsen S, et al. Anti-Cyclic Citrullinated Peptide Antibodies, 28-Joint Disease Activity Score, and Magnetic Resonance Imaging Bone Oedema at Baseline Predict 11 Years' Functional and Radiographic Outcome in Early Rheumatoid Arthritis. *Scand J Rheumatol* (2019) 48(1):1–8. doi: 10.1080/03009742.2018.1466362
23. Manara M, Varenna M. A Clinical Overview of Bone Marrow Edema. *Reumatismo* (2014) 66(2):184–96. doi: 10.4081/reumatismo.2014.790
24. Narváez JA, Narváez J, de Albert M, De Lama E, Serrallonga M, Nolla JM. Bone Marrow Edema in the Cervical Spine of Symptomatic Rheumatoid Arthritis Patients. *Semin Arthritis Rheumatol* (2009) 38(4):281–8. doi: 10.1016/j.semarthrit.2008.01.005
25. Koo BS, Song Y, Shin JH, Lee S, Kim T-H. Evaluation of Disease Chronicity by Bone Marrow Fat Fraction Using Sacroiliac Joint Magnetic Resonance Imaging in Patients With Spondyloarthritis: A Retrospective Study. *Int J Rheum Dis* (2019) 22(4):734–41. doi: 10.1111/1756-185X.13485
26. Chen M, Herregods N, Jaremko JL, Carron P, Elewaut D, den Bosch FV, et al. Diagnostic Performance for Erosion Detection in Sacroiliac Joints on MR T1-Weighted Images: Comparison Between Different Slice Thicknesses. *Eur J Radiol* (2020) 133:109352. doi: 10.1016/j.ejrad.2020.109352
27. Maksymowych WP. Biomarkers for Diagnosis of Axial Spondyloarthritis, Disease Activity, Prognosis, and Prediction of Response to Therapy. *Front Immunol* (2019) 10:305. doi: 10.3389/fimmu.2019.00305
28. Arends S, Brouwer E, van der Veer E, Groen H, Leijsma MK, Houtman PM, et al. Baseline Predictors of Response and Discontinuation of Tumor Necrosis Factor-Alpha Blocking Therapy in Ankylosing Spondylitis: A Prospective Longitudinal Observational Cohort Study. *Arthritis Res Ther* (2011) 13(3): R94. doi: 10.1186/ar3369
29. Deodhar A, Yu D. Switching Tumor Necrosis Factor Inhibitors in the Treatment of Axial Spondyloarthritis. *Semin Arthritis Rheumatol* (2017) 47 (3):343–50. doi: 10.1016/j.semarthrit.2017.04.005
30. Bray C, Bell LN, Liang H, Haykal R, Kaiksow F, Mazza JJ, et al. Erythrocyte Sedimentation Rate and C-Reactive Protein Measurements and Their Relevance in Clinical Medicine. *WMJ* (2016) 115(6):317–21.
31. van der Heijde D. Radiographic Progression in Rheumatoid Arthritis: Does It Reflect Outcome? Does It Reflect Treatment? *Ann Rheum Dis* (2001) 60 Suppl 3:iii47–50. doi: 10.1136/ard.60.90003.iii47
32. Joshi AB, Markovic L, Hardinge K, Murphy JCM. Total Hip Arthroplasty in Ankylosing Spondylitis: An Analysis of 181 Hips. *J Arthroplasty* (2002) 17 (4):427–33. doi: 10.1054/arth.2002.32170

Conflict of Interest: The authors declare that the research was conducted in the absence of any commercial or financial relationships that could be construed as a potential conflict of interest.

frontiers in Endocrinology

ORIGINAL RESEARCH
published: 22 December 2021
doi: 10.3389/fendo.2021.785604

Evaluation of Bone Marrow Texture and Trabecular Changes With Quantitative DCE-MRI and QCT in Alloxan-Induced Diabetic Rabbit Models

Pianpian Chen[1], Yunfei Zha[1], Li Wang[1], Liang Li[1], Lei Hu[1], Dong Xing[1], Baiyu Liu[1], Liu Yang[1], Qi Yang[1], Changsheng Liu[1], Huan Liu[2] and Weiyin Liu[3]*

[1] Department Radiology, Renmin Hospital of Wuhan University, Wuhan, China, [2] Precision Healthcare Institute, GE Healthcare, Shanghai, China, [3] MR Research, GE Healthcare, Shanghai, China

OPEN ACCESS

Edited by:
Shaolin Li,
The Fifth Affiliated Hospital of Sun Yat-sen University, China

Reviewed by:
Quan Zhou,
Third Affiliated Hospital of Southern Medical University (Academy of Orthopedics Guangdong Province), China
Peisen Zhang,
Guangzhou First People's Hospital, China

***Correspondence:**
Yunfei Zha
zhayunfei999@126.com

Specialty section:
This article was submitted to Bone Research, a section of the journal Frontiers in Endocrinology

Received: 29 September 2021
Accepted: 26 November 2021
Published: 22 December 2021

Citation:
Chen P, Zha Y, Wang L, Li L, Hu L, Xing D, Liu B, Yang L, Yang Q, Liu C, Liu H and Liu W (2021) Evaluation of Bone Marrow Texture and Trabecular Changes With Quantitative DCE-MRI and QCT in Alloxan-Induced Diabetic Rabbit Models. Front. Endocrinol. 12:785604. doi: 10.3389/fendo.2021.785604

Purpose: To investigate whether the microvascular permeability of lumbar marrow and bone trabecular changes in early-stage diabetic rabbits can be quantitatively evaluated using dynamic contrast-enhanced magnetic resonance imaging (DCE-MRI), quantitative computed tomography, and texture-analyzed permeability parameter K^{trans} map of DCE-MRI.

Materials and Methods: This prospective study included 24 rabbits that were randomly assigned to diabetic (n = 14) and control (n = 10) groups. All rabbits underwent sagittal MRI of the lumbar region at 0, 4, 8, 12, and 16 weeks after alloxan injection. Pearson correlation coefficient was performed to determine the correlation between permeability parameter and bone mineral density (BMD). Repeated-measures ANOVA was used to analyze the changes in lumbar BMD over time in each group and the texture parameters of diabetic rabbit lumbar marrow at different time points. Mann–Whitney U rank sum test was used to compare the differences of each index between the two groups and calculate the area under the curve (AUC).

Results: BMD was correlated with K^{trans}, K_{ep}, and V_e but not with V_p. At weeks 0–16, the BMD of the rabbits in the diabetic and normal groups was not statistically significant, but the change in BMD showed an overall downward trend. For texture analysis, entropy, energy, and Uniformized positive pixel (UPP) parameters extracted from the K^{trans} map showed significant differences from week 0 to 16 between the two groups. The identification ability at 8–12 weeks was higher than that at 12–16 weeks, and the AUCs were 0.734, 0.766, and 0.734, respectively ($P < 0.05$ for all).

Conclusions: The changes in BMD measured using quantitative computed tomography occurred later than those measured using bone trabecular morphometry. Texture analysis parameters based on DCE-MRI quantitative parameter Ktrans map are feasible to identify early changes in lumbar marrow structure in diabetic rabbits.

Keywords: Diabetes MILES Study, lumbar marrow, DCE-MRI, texture analysis, quantitative CT

INTRODUCTION

The global prevalence of type 1 diabetes mellitus has been increasing by 2%–5% annually, leading to elevated occurrence of diabetes-related pathologies, such as bone disorders (1), cartilage alterations, and bone loss (2, 3). The main complications of diabetes, osteopenia, and bone microstructural changes increase the possibilities of fractures and friability and decrease bone strength (4). A meta-analysis of 16 studies reported no difference in lumbar spine bone marrow density (BMD) between adults with type I diabetes (T1D) and healthy subjects, controlling for age and gender effect (5). The associations of glycemic control and diabetes duration with BMD reported in many studies have been contradictory, but microvascular complications (retinopathy, neuropathy, and nephropathy) have been found in low-BMD patients with T1D (6–8). The pathophysiological mechanism of diabetic bone diseases remains unclear, but little evidence indicates that diabetic bone disease might be a chronic microvascular complication (9). In addition, the relatively modest BMD reduction in patients with T1D does not fully account for increased fracture risk.

Due to the high transport rate of MRI contrast agents such as paramagnetic Gd(III) –chelate (10), quantitative dynamic contrast-enhanced magnetic resonance imaging (DCE-MRI) based on a pharmacokinetic model can reflect the alterations of bone marrow permeability in early diabetes stage (11). Radiomics has been used to predict treatment outcomes and time-dependent reactions based on so-called quantitative texture features (i.e., the distribution patterns of pixelwise signal intensities of given images). Zhang et al. (12) reported here that an Fe_3O_4 nanoparticle-based glutathione (GSH)-responsive MRI probe correlate between the interlocked MRI signals and local GSH concentration was established and further applied for mapping the heterogeneous distribution of GSH within an intracranial tumor *in vivo*, which will offer a practical route for quantitatively mapping tumor-specific biomarkers *in vivo*. Application of texture analysis on medical images, such as MRI, CT, and plain radiographic images, has demonstrated great potential in disease diagnosis (13) and lesion detection and characterization (14) and even in monitoring disease progression and longitudinal evaluation of emerging therapies (15). However, no radiomic report on diabetic permeability maps, which are likely to detect early diabetes-induced abnormal bone alterations, is available. Therefore, investigating the potential role of texture analysis based on permeability maps and determining texture analysis results may provide more information on the relationship between lumbar bone marrow heterogeneity and permeability occurrence.

Current studies have indicated that quantitative computed tomography (QCT) can more sensitively detect the changes in cancellous bone microstructure caused by changes in bone turnover (16). Since QCT can measure bone mineral content per unit volume of cortical bone and cancellous bone (13), it has unique advantages in evaluating diabetic lumbar vertebra disease and could act as a reference of true volumetric BMD to reflect the spinal structure stability. Determining the feasibility of measuring bone density using QCT combined with texture analysis on MR permeability map is important to investigate the complex relationship between diabetic bone marrow microvascular disease and bone density, bone structure, bone transformation, and fracture risk assessment.

The aim of this study was to evaluate the correlation between bone marrow microvascular permeability parameters, BMD, and quantitative trabecular bone morphometric parameters with DCE-MR and QCT in alloxan-induced rabbit diabetic model. We also investigated whether texture analysis based on the permeability parameter map could evaluate the microstructural changes in lumbar trabeculae in early-stage diabetic rabbits.

MATERIALS AND METHODS

Animals and Diabetic Rabbit Model

This experiment was reviewed and approved by the ethics committee of our university. Twenty-four healthy adult male Japanese white rabbits (fasting weight, 2.8–3.1 kg; average fasting weight, 3.0 ± 0.1 kg) were provided by our Animal Experimental Center. All rabbits were kept for 1 week. They were fasted for 12 h before being modeled and allowed to eat and drink water within 48 h afterward. The fasting blood glucose level was confirmed to be <6.0 mmol/l with an average of 5.5 ± 0.3 mmol/l. The rabbits were randomly divided into diabetes (n = 14) and control (n = 10) groups. For the diabetic group, alloxan monohydrate (100 mg/kg of body weight; Sigma-Aldrich Chemical, St. Louis, MO, USA) was dissolved in sterile normal saline to achieve a 5% concentration and was immediately administered intravenously *via* the marginal ear vein over a 2-min period by using a 25-gauge butterfly catheter. The diabetic state was achieved 48 h later and was verified by quantitative determination of blood glucose levels. The control rabbits were injected with 100 ml/kg physiological saline. After 48 h, the peripheral blood glucose concentration was measured with a blood glucose meter (Sannuo blood glucose meter). When a single measurement showed a peripheral blood glucose level ≥14 mmol/l or two measurements showed a peripheral blood glucose level ≥11 mmol/l, the rabbits were identified as being successfully

modelled (17). Blood glucose levels were monitored in all rabbits in both groups weekly by using the Optium Xceed glucometer (Abbott, Bedford, MA, USA) for the subsequent 4 weeks and tended to stabilize after 4 weeks. Subsequently, the blood glucose level was measured every 4 weeks before the MRI and CT examinations.

Routine MRI and DCE-MRI Examination

All MRI scans were conducted with a 3.0 T MRI scanner (Discovery MR750; GE Healthcare) at 48 h as baseline and at the fourth, eighth, 12th, and 16th week after the successful modeling. These rabbits were anesthetized with an intravenous injection of 3% sodium pentobarbital solution (1.3 ml/kg) through the ear margin. After successful anesthesia, all rabbits were fixed in the supine position into an eight-channel phased-array knee coil. The sagittal fast spin echo T_1-weighted imaging (FSE-T_1WI) (TR = 300 ms, TE = Min Full, slice thickness = 3 mm without gap, 12 slices were acquired, FOV = 160 mm × 160 mm, in-plane matrix = 320 × 288), FSE-T_2WI (TR = 2,500 ms, TE = 120 ms, slice thickness = 3 mm without gap, 12 slices were acquired, FOV = 160 mm × 160 mm, matrix = 320 × 2 88), and DCE-MRI based on liver acquisition volume acceleration sequence (before contrast injection: flip angles of 9° and 12° before contrast injection and of 10° after contrast injection, TR = 3.5 ms, TE = 1.6 ms, slice thickness = 3 mm, 12 slices, FOV = 200 mm × 160 mm, matrix = 192 × 192) of lumbar vertebrae were scanned. Before contrast injection, two liver acquisition volume acceleration sequence scans were used to obtain T_1 mapping. The acquisition time was 8 s for a single three-dimensional (3D) volume, and 35 continuous temporal phases were acquired. A dosage of Omniscan (Gadodiamide, GE Healthcare, Ireland) of 0.2 mmol/kg was injected at a flow rate of 1.0 ml/s. After two dynamic phases were scanned as baseline, the contrast agent was injected into the rabbit ear vein by using a US MeoRao double-tube high-pressure syringe, followed by 5-ml physiological saline.

QCT Examination

After anesthesia, the rabbits were placed in the supine position and the lower limbs were straightened. A solid phantom (V.4.0) was placed under the waist, and the lumbar vertebrae of the rabbits were scanned with GE Bright Speed 16-slice spiral CT. The scanning line was parallel to the upper and lower edges of the experimental rabbit lumbar vertebral body. The scanning parameters were as follows: tube voltage = 120 kV, tube current = 250 mAs, bed height = 179 cm, screw pitch = 0.531, SFOV = large body, matrix = 512 × 512, slice thickness = 1 mm, standard algorithm reconstruction.

Data Measurement and Analysis

DCE parameters were measured using a quantitative DCE-MRI software package (Omni-Kinetics; GE Healthcare). First, 3D non-rigid registration was performed on all acquired 3D images to reduce respiratory motion artifacts. Subsequently, the liver acquisition volume acceleration images with 9° and 12° of flip angles were introduced for T_1 mapping calculation. The motion-corrected dynamic images were then used for DCE analysis. During the calculation, the contrast time–concentration curve in the abdominal aorta was selected as the arterial input function of the lumbar spine, and the extended Tofts linear model was used for DCE model fitting. To avoid the intervertebral disc, vertebral venous plexus, and bone island, one region of interest (ROI) was manually outlined at each slice, and all were merged into a 3D volume of interest. Since the image structure of enhanced scan is not as clear as that of sagittal FSE-T_1WI and FSE-T_2WI, we used sagittal FSE-T_1WI and FSE-T_2WI for comparison during postprocessing to draw the ROI (**Figure 1**). The permeability parameters, including the volume transfer constant (K^{trans}) between the blood plasma and the extracellular extravascular space, extracellular extravascular volume fraction (V_e), rate constant ($K_{ep} = K^{trans}/V_e$) between the plasma and the extracellular extravascular space volume, and contrast agent plasma volume (V_p), were calculated automatically. The postprocessing images of DCE-MRI are shown in **Figure 2**. High K^{trans} value indicates high permeability and perfusion volume. K_{ep} shows the flow between the leakage space and the plasma. In addition, different contrast agents have different K^{trans} and V_e.

The QCT images were uploaded to the Mindways Pro postprocessing software, and the BMD of the rabbit lumbar 4–7 vertebrae was computed. ROIs were drawn as shown in **Figure 3**.

Texture Feature Extraction

All images were transferred in digital imaging and communications in medicine format. K^{trans} map was measured using a quantitative DCE-MRI software package (Omni-Kinetics; GE Healthcare). Sixty-eight texture features including histogram parameters, morphological parameters, gray-level co-occurrence matrix (GLCM) parameters, and gray-level run length matrix parameters in the 3D ROI of K^{trans} map were extracted for the three repeated measurements. The average of each parameter was also used as the final result.

Sample Selection and Histologic Analysis

After MRI and CT examinations were completed at the 16th week, all rabbits were killed by air embolization. The seventh lumbar vertebral body was fixed with a universal tissue fixative (4% paraformaldehyde buffer solution, neutral pH). After decalcification and paraffin embedding, the largest cross-section of the lumbar vertebral body was selected and made in the thick section of 4 μm. Subsequently, hematoxylin and eosin (H&E) staining and CD34 immunohistochemical staining were performed. Four independent regions with the same area were selected for observation and filming under an optical microscope (OLYMPUS BX51). H&E-stained images were analyzed using Image-Pro Plus 6 (Media Cybernetics, Inc., MD, USA) software to measure structural parameters of the trabecular bone in the sections, including trabecular bone number (Tb.N) and trabecular bone area (Tb.Ar) (**Figure 4**).

Statistical Analysis

Statistical analyses were performed with SPSS 25.0. Pearson correlation coefficient was used to investigate the correlation

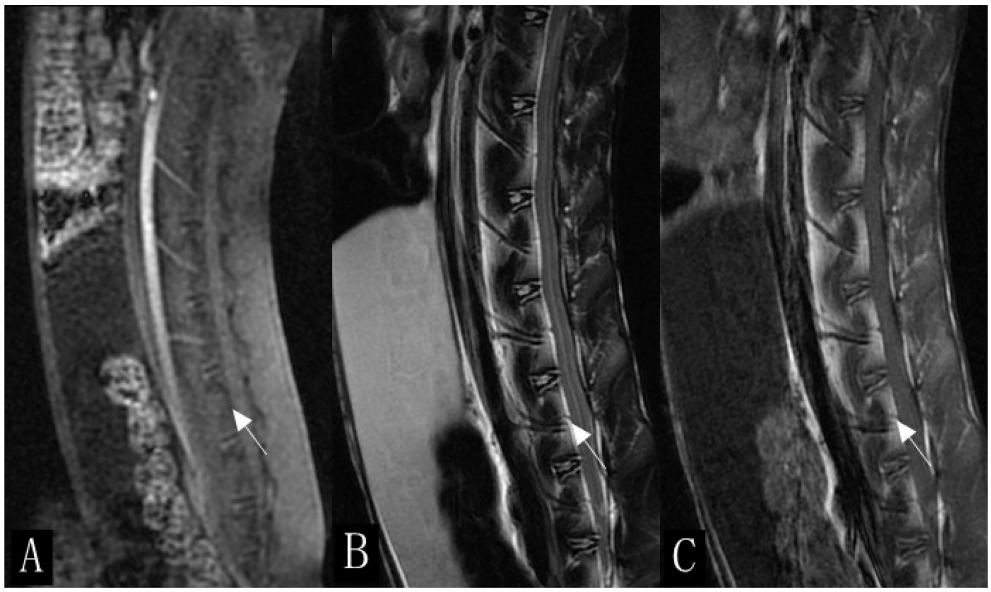

FIGURE 1 | Sagittal scan of lumbar spine in rabbits (white arrow). **(A)** Enhanced scan image. **(B)** T2-weighted imaging (T_2WI). **(C)** T_1WI.

between permeability parameters and BMD. Repeated-measures ANOVA was used to analyze the changes in lumbar BMD trend over time in each group and the lumbar marrow texture parameters of diabetic rabbits at different time points. The two-sample t-test or the Mann–Whitney U test was performed to compare the differences of all variables between the diabetic and control groups. Receiver operating characteristic curves were drawn for the parameters with statistical significance. Two-sample t-tests were used to compare the differences in lumbar bone trabecular morphometric parameters between the two groups. Two-sided $P < 0.05$ was considered statistically significant.

RESULTS

In the disease progression, four diabetic rabbits died due to bad health conditions, and two normal rabbits died due to poor

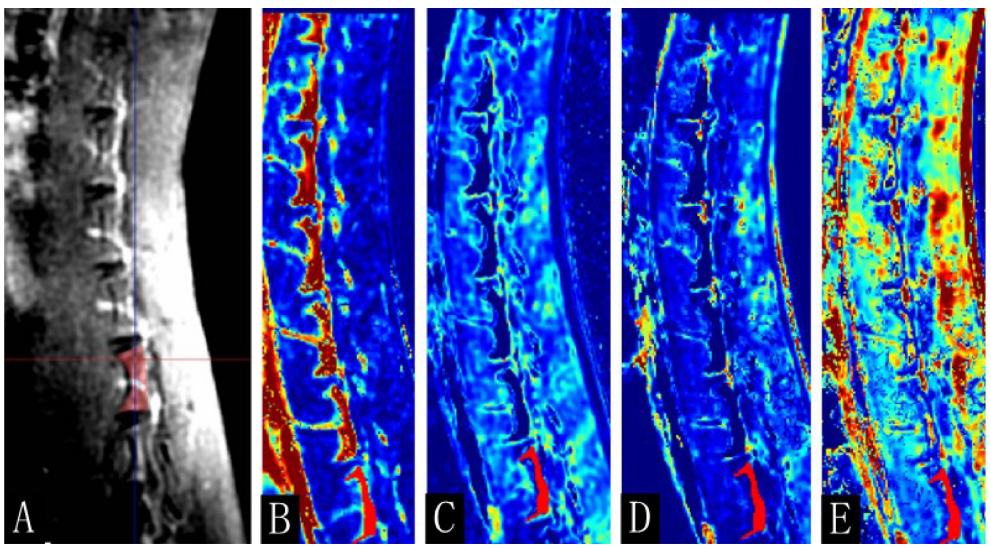

FIGURE 2 | The postprocessing images of dynamic contrast-enhanced magnetic resonance imaging (DCE-MRI). **(A)** Enhanced T_1-weighted imaging (T_1WI) map, **(B)** K^{trans}, **(C)** K_{ep}, **(D)** V_e, and **(E)** V_p map of the 16th-week normal rabbits. The lumbar vertebra region of interest was manually drawn (red area).

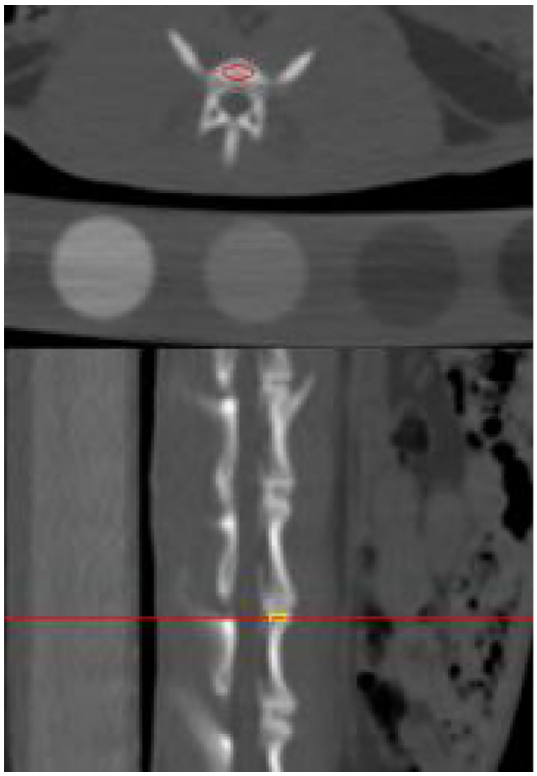

FIGURE 3 | Illustration of the outlined region of interest on postprocessed quantitative computed tomography.

anesthesia. Thus, 10 rabbits in the diabetic group and eight rabbits in the control group were finally included in the analysis.

At weeks 0–16, the BMD of the rabbits in the diabetic and normal groups was not statistically significant (P = 0.796, P = 0.75, P = 0.789, P = 0.083, P = 0.055) (**Table 1**). However, when the BMD data of the rabbits in the diabetic group were compared from 0 to 16 weeks, the change in BMD showed an overall downward trend (**Figure 5**).

For texture analysis, of the 68 parameters extracted from the K^{trans} map, only entropy, energy, and UPP parameters showed significant differences from week 0 to 16 between the two groups (all P < 0.05) (**Table 2**). Thus, we excluded the remaining 65

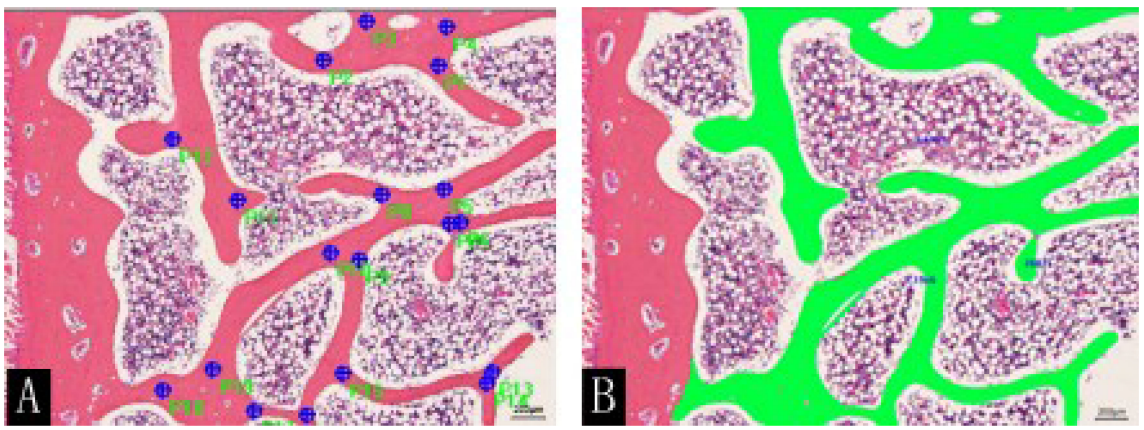

FIGURE 4 | H&E staining (×50) of rabbit lumbar vertebrae in the control group at the 16th week. **(A)** Marks (blue dots) and **(B)** sketches (green color) of the trabecular bone were performed using the Image-Pro Plus software.

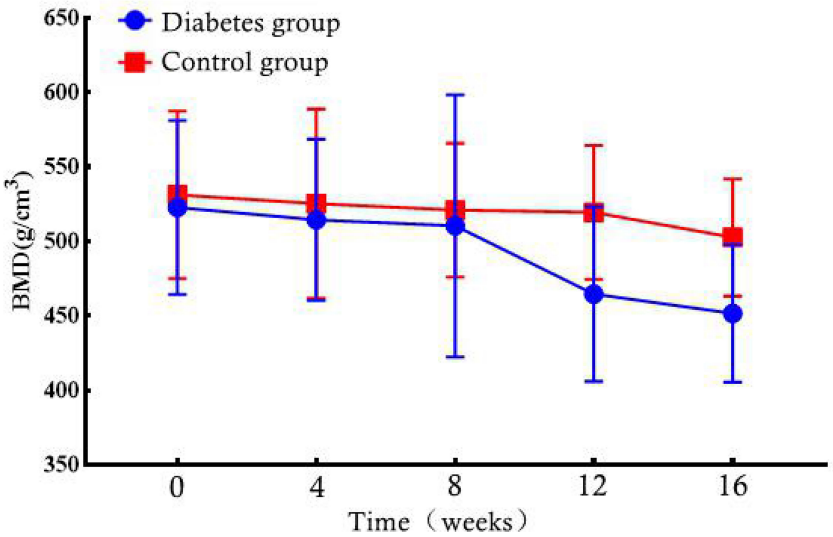

FIGURE 5 | Bone marrow density (BMD) changes in the diabetic and control rabbit lumbar vertebrae over time.

parameters, and only the three parameters selected were analyzed using the receiver operating characteristic curves. In the diabetic group, the identification ability at 8–12 weeks was higher than that at 12–16 weeks, and the areas under the curve (AUCs) were 0.734, 0.766, and 0.734, respectively (**Tables 3**, **4; Figures 6**, **7**).

Pearson correlation coefficient showed that BMD was correlated with K^{trans}, K_{ep}, and V_e (r = 0.134, 0.299, and -0.252; P ≤ 0.001) but not correlated with V_p (r = -0.038, P = 0.373) (**Table 5**).

At the time of sacrifice (after 16 weeks), the H&E staining results of the lumbar vertebrae in the diabetic group showed that the decreased number of trabecular bone and smaller area was observed with the naked eye and statistically different from that of the control group (t = 12.472; t = 4.961; P < 0.001) (**Figure 8**, **Table 6**). The immunohistochemistry of bone marrow CD34 showed that the number of cells in the bone marrow increased significantly and more widespread, indicating increased heterogeneity of images (**Figures 9**).

DISCUSSION

This study used both DCE-MRI and QCT as well as texture analysis to evaluate the changes in bone marrow microcirculation and BMD in the alloxan-induced diabetic rabbit model. The results showed that DCE-MRI permeability parameters of the lumbar spinal marrow were correlated with BMD. No statistically significant changes were found in BMD in the diabetic group during the disease progression. However, the trabecular bone histometry parameters were statistically different between the baseline and the 16th week and between groups except for baseline. The histogram and GLCM of K^{trans} map showed viability of identifying early microstructural changes in diabetic bone marrows.

Oikawa et al. (18) initially showed that the femoral and tibial bone marrow microvascular diseases in T1D rats occur; osteopenia, bone marrow fat cell accumulation, increment of microvascular permeability, and reduction of blood flow volume, arteriole, capillary network, and bone marrow sinusoids were observed. Hu et al (11) found significantly increased microvascular permeability and fat content, decreased microvessel density of bone marrow, and destroyed microenvironment of bone marrow osteoblasts in diabetic rabbit lumbar vertebra after 12 weeks. Our data showed that the microvascular permeability of diabetic rabbit bone marrow decreased during the experiment. A clear correlation was noted between changes in bone marrow microvascular permeability and BMD at early-stage diabetes. Diabetic bone metabolism disorders mainly include osteopenia and

TABLE 1 | Group differences of BMD values in the lumbar vertebrae.

Time	Diabetes group	Control group	*T*	P
0 week	522.81 ± 58.44	531.25 ± 56.29	0.265	0.796
4 weeks	514.45 ± 54.22	525.28 ± 63.48	0.327	0.75
8 weeks	510.39 ± 88.04	520.95 ± 44.87	0.266	0.789
12 weeks	464.63 ± 58.73	519.53 ± 44.97	1.909	0.083
16 weeks	451.69 ± 46.17	502.63 ± 39.35	2.151	0.055

Data are expressed as mean ± standard deviation.
BMD, bone marrow density.

TABLE 2 | Group comparison of K^{trans}-derived texture parameters at the same time points.

Indicators		Control group			Diabetic group			Z	P-value
		Median	P25	P75	Median	P25	P75		
T0									
	K^{trans}-Energy	0.500	0.330	1.000	0.330	0.200	1.000	-3.195	0.001
	K^{trans}-Entropy	0.000	0.000	0.000	0.000	0.000	1.000	-3.605	<0.001
	K^{trans}-UPP	0.500	0.330	1.000	0.330	0.200	1.000	-3.195	0.001
T1									
	K^{trans}-Energy	1.000	0.500	1.000	0.500	0.250	1.000	-3.646	<0.001
	K^{trans}-Entropy	0.000	0.000	0.000	0.000	0.000	0.000	-2.322	0.020
	K^{trans}-UPP	1.000	0.500	1.000	0.500	0.250	1.000	-3.646	<0.001
T2									
	K^{trans}-Energy	0.500	0.290	1.000	1.000	0.500	1.000	-2.195	0.028
	K^{trans}-Entropy	0.000	0.000	0.000	0.000	0.000	0.000	-2.938	0.003
	K^{trans}-UPP	0.500	0.290	1.000	1.000	0.500	1.000	-2.195	0.028
T3									
	K^{trans}-Energy	1.000	1.000	1.000	0.500	0.250	1.000	-2.957	0.003
	K^{trans}-Entropy	0.000	0.000	0.000	0.000	0.000	0.000	-5.474	0.000
	K^{trans}-UPP	1.000	1.000	1.000	0.500	0.250	1.000	-2.957	0.003
T4									
	K^{trans}-Energy	1.000	1.000	1.000	1.000	0.330	1.000	-2.448	0.014
	K^{trans}-Entropy	0.000	0.000	0.000	0.000	0.000	0.000	-3.350	0.001
	K^{trans}-UPP	1.000	1.000	1.000	1.000	0.330	1.000	-2.448	0.014

Represented that the difference between the normal group and the control group at the same time point was statistically significant (P < 0.05).

osteoporosis. Diabetes with bone marrow microvascular disease can aggravate bone metabolic disorders, and diabetes with a primary osteoporosis disease can exacerbate the condition of osteoporosis in patients (9). Bone marrow microangiopathy is an important indicator of risk, prevention, and treatment for bone diseases. Starting a long-term prospective research before the progression of microvascular disease and performing large-scale epidemiological studies are necessary to better understand the relationship between bone marrow microangiopathy and BMD changes and fracture risks.

The pathophysiological mechanisms of early diabetic bone marrow microangiopathy in either type 1 or 2 diabetes (T2D) have not been elucidated (9, 18). The QCT results in our study showed that the BMD of the lumbar vertebra in the diabetic group had a downward trend without significant differences to that of the control group, in accordance with the results obtained by Register et al. (19). At present, no T1D-related QCT studies have been performed, and only type II diabetes-related QCT studies are used as a reference for comparison at the 16th week. The H&E staining results showed that the number of trabecular bone and trabecular bone area was significantly smaller in the diabetic group than that in the control group. No correlation was found between BMD and trabecular bone parameters. We speculated that identification of changes in lumbar vertebra BMD by using QCT only partially reflected the histological changes in trabecular morphometry. Since QCT in T1D is rarely applied and a study has shown that the high-resolution peripheral QCT parameters are not different between type 1 and 2 diabetes patients in the adjusted analyses except for an increased stiffness at the tibia in T2D patients (20), it is only possible to explain our QCT results based on previous T2D research. The microfinite element analysis showed that bone strength in T2D patients is associated with increased cortical porosity in the distal radius compared with that in healthy

TABLE 3 | Area under the ROC curve shows the diagnostic ability of lumbar bone marrow texture differentiation by comparing the texture parameters at week 12 when taking week 8 as baseline.

Area under the curve					
Test result variable(s)	Area	Std. error[a]	Asymptotic sig.[b]	Asymptotic 95% confidence interval	
				Lower bound	Upper bound
K^{trans}-Energy	0.734	0.136	0.115	0.469	1.000
K^{trans}-Entropy	0.766	0.128	0.074	0.516	1.000
K^{trans}-UPP	0.734	0.136	0.115	0.469	1.000

Test result variable(s): K^{trans}-Entropy has at least one tie between the positive actual state group and the negative actual state group. Statistics may be biased.

[a]*Under the nonparametric assumption.*

[b]*Null hypothesis: true area = 0.5.*

ROC, receiver operating characteristic.

TABLE 4 | Area under the ROC curve shows the diagnostic ability of the texture parameters at week 16 compared with week 12 at baseline.

Area under the curve					
Test result variable(s)	**Area**	**Std. error[a]**	**Asymptotic Sig.[b]**	**Asymptotic 95% confidence interval**	
				Lower bound	**Upper bound**
K^{trans}-Energy	0.508	0.153	0.958	0.208	0.808
K^{trans}-Entropy	0.594	0.148	0.529	0.304	0.884
K^{trans}-UPP	0.508	0.153	0.958	0.208	0.808

Test result variable(s): K^{trans}-Energy, K^{trans}-Entropy, and K^{trans}-UPP have at least one tie between the positive actual state group and the negative actual state group. Statistics may be biased.

[a]*Under the nonparametric assumption.*

[b]*Null hypothesis: true area = 0.5.*

ROC, receiver operating characteristic; UPP, uniformized positive pixel.

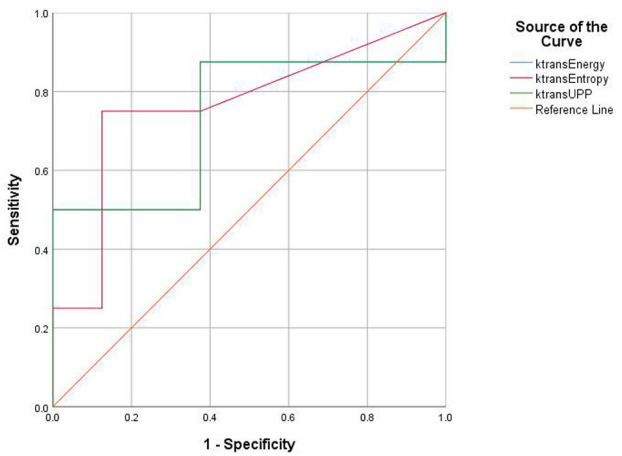

FIGURE 6 | Receiver operating characteristic (ROC) curves demonstrate the diagnostic ability in the differentiation of lumbar bone marrow texture between groups at the 12th week.

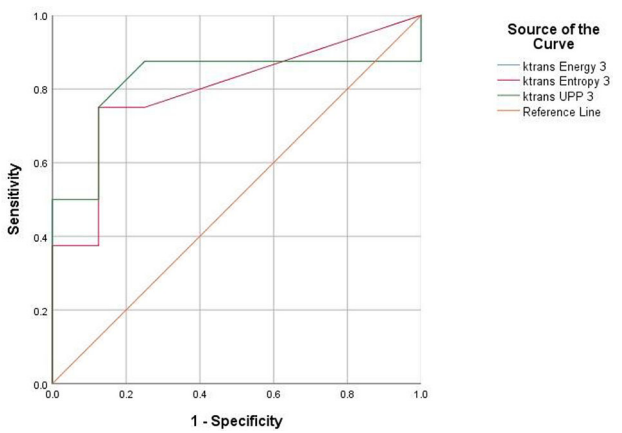

FIGURE 7 | Receiver operating characteristic (ROC) curves demonstrate the diagnostic ability in the differentiation of lumbar bone marrow texture between groups at the eighth week.

controls (21, 22). In addition, cortical osteoporosis and trabecular heterogeneity are more pronounced in T2D patients with fractures compared with T2D patients without fractures (23). Higher cortical and periosteal cortical voids in T2D patients with fractures compared with those without fractures suggest that cortical subchambers may be more sensitive to the T2D-induced toxicity and reflect the extent of microvascular disease lesions (24). In our study, the delineated ROI on QCT images without including the cortical area when measuring BMD may explain the insignificantly declined BMD. Future research should focus on evaluating the structural determinants (microstructure, material properties) of bone fragility to assess the accuracy and reproducibility of QCT for measuring lumbar BMD in diabetic rabbit models.

In our study, some texture parameters based on the K^{trans} map showed differences between the diabetic and control groups. "Entropy," "UPP," and "energy" at eighth, 12th, and 16th week were significantly different between the two groups. Moreover, the diagnostic efficiency of texture parameters at 8–16 weeks was higher than that at 12–16 weeks. The AUC of entropy was the largest among all texture parameters, indicating that entropy is more effective in identifying early microstructural changes in diabetic bone marrow.

Entropy has been used for computer-aided evaluation of bone regeneration process and structural complexity (e.g., the formation of mature trabecular bone) (25). Mookiah et al. (26) showed that some GLCM texture parameters (energy, entropy, uniformity) acquired from routine-enhanced multidetector CT and analyzed with a single vector machine could be applied to screen opportunistic osteoporosis. Higher GLCM entropy in the diabetic group than that in the control group indicated that the texture distribution was more complicated.

TABLE 5 | Pearson correlation coefficients of BMMP parameters and BMD.

Correlation with BMD	**r**	**P**
K^{trans}	0.134	0.001
K_{ep}	0.299	<0.001
V_e	-0.252	<0.001
V_p	-0.038	0.373

BMMP, bone marrow microvascular permeability; BMD, bone marrow density.

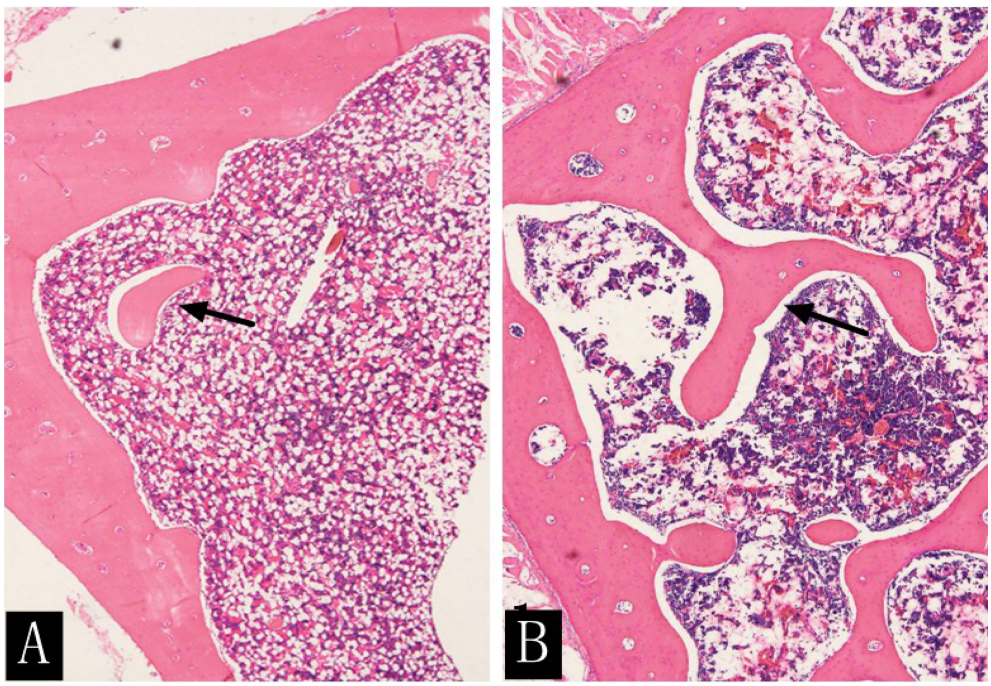

FIGURE 8 | H&E staining (×400) of rabbit lumbar vertebrae in the diabetic group **(A)** and the control group **(B)** at the 16th week. The rabbit lumbar trabecular bone was more densely distributed and had a larger area in the control group than in the diabetic group (arrow).

TABLE 6 | Comparison of the number of trabecular bone and trabecular bone area in the diabetic and control groups at the 16th week.

16th week	Diabetes group	Control group	*Z*	P
Tb.N	6.00 (4.00–11.00)	21.50 (17.50–26.00)	3.863	<0.001
Tb.Ar	574,017.64 (279,256.13–847,322.88)	1,825,414.82 (1,307,484.69–2,063,523.82)	3.627	<0.001

Data are expressed as mean (range).
Tb.N, trabecular bone number; Tb.Ar, trabecular bone area.

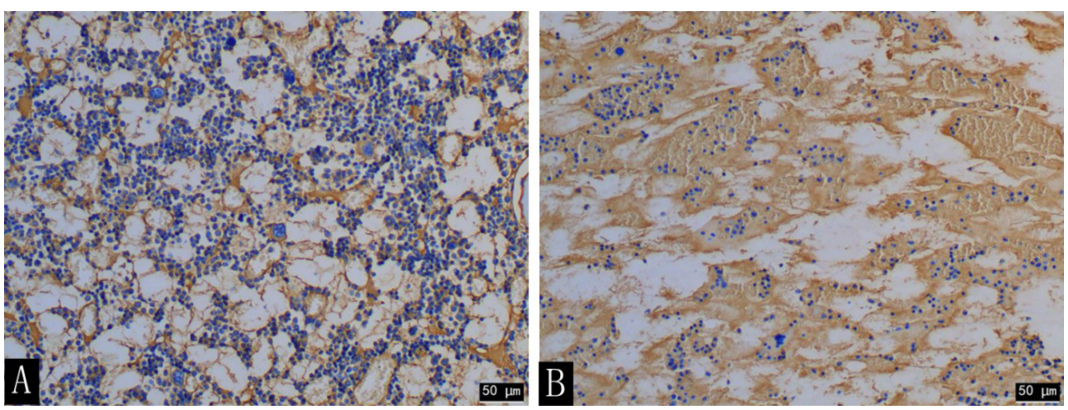

FIGURE 9 | CD34 immunohistochemical staining (×200) of the rabbit lumbar bone marrow in the diabetic group **(A)** and the control group **(B)** at the 16th week. The number of cells in the lumbar bone marrow was significantly increased in the diabetic group compared with that in the control group.

The microscope-scale results of texture analysis and histopathology were different, but a certain relationship existed between them. MacKay et al. (15) reported that texture features of the high-spatial resolution coronal T_1-weighted MRI images (e.g., histogram variance) acquired from 10 patients with knee arthritis aged 57–84 years are significantly correlated with the histological parameters of the subchondral bone tissue of the tibial plateau during total knee arthroplasty. In our study, CD34 immunohistochemical pathology showed that the number of bone marrow cells was higher, and the distribution range was wider in the lumbar vertebra of the diabetic group than that of the control group, leading to elevated regional variation and tissue complexity. This was reflected by increased entropy. In addition, lower BMD in the diabetic rabbits than in the control group could result in the distinct distribution of contrast agents in the bone marrow, which was also the possible reason for the increased entropy of K^{trans} map in this study.

In addition, we also found that the "energy" value in the texture parameters had a higher ability to identify the changes in bone microstructure in the diabetic group. Shu et al. (27) showed that the statistical parameter "energy" extracted from the gray intensity distribution is able to distinguish the femoral cortical bone development in two different diet groups.

This study has several limitations. First, the experimental objects were T1D-like rabbits. The incidence of T1D increased with age. The highest incidence occurs in the 10–14-year-old population (1). The New Zealand white rabbits used in the study were 8–9 weeks old, equivalent to 10 human years. The experiment lasted 16 weeks, and the age of the rabbits was about that of an 18-year-old human at the end of the experiment. Our experimental results only indicated no correlation between the changes in bone marrow microvascular permeability and BMD at the early stage of diabetes; thus, variation of more complete time series between the two factors remains to be further studied. Second, this experiment failed to observe the results of the trabecular bone specimens in the entire process. Further improvement in the subsequent research is warranted. Finally, our experimental sample size was small, and the AUCs of the texture parameters with statistically significant differences between the diabetic and control groups were between 0.5 and 0.8, indicating that the diagnostic efficiency is moderate. Detailed information on the changes in texture characteristics of microvascular disease should be further verified by large sample experiments and radiomic methods.

In summary, no correlation was found between the changes in microvascular permeability parameters of lumbar spine bone marrow and bone density and trabecular morphometric parameters at the early stage of diabetes model induced by alloxan. The bone marrow BMD changes measured using QCT occurred later than those measured using trabecular morphometrics. The texture analysis based on the DCE-MRI K^{trans} map could identify bone marrow microstructure changes at the early stage of diabetes.

DATA AVAILABILITY STATEMENT

The raw data supporting the conclusions of this article will be made available by the authors without undue reservation.

ETHICS STATEMENT

The animal study was reviewed and approved by the ethics committee of Wuhan University.

AUTHOR CONTRIBUTIONS

YZ and PC incubated and designed the experiments. PC, BL, QY, and LY conducted the research. PC, HL, and WL analyzed and interpreted the data. PC drafted this article. YZ made a critical review of the intellectual content of the article. LW, LL, LH, DX, and CL provided administrative, technical, or material support. All authors contributed to the article and approved the submitted version.

FUNDING

This study was funded by the National Natural Science Foundation of China (nos. 81871332).

REFERENCES

1. Maahs DM, West NA, Lawrence JM, Mayer-Davis EJ. Epidemiology of Type 1 Diabetes. *Endocrinol Metab Clinics North America* (2010) 39(3):481–97. doi: 10.1016/j.ecl.2010.05.011
2. Coe LM, Jing Z, Mccabe LR. Both Spontaneous Ins2+/- and Streptozotocin-Induced Type I Diabetes Cause Bone Loss in Young Mice. *J Cell Physiol* (2013) 228(4):689–95. doi: 10.1002/jcp.24177
3. Motyl KJ, McCabe LR. Leptin Treatment Prevents Type I Diabetic Marrow Adiposity But Not Bone Loss in Mice. *J Cell Physiol* (2009) 218(2):376–84. doi: 10.1002/jcp.21608
4. Li X-J, Zhu Z, Han S-L, Zhang Z-L. Bergapten Exerts Inhibitory Effects on Diabetes-Related Osteoporosis *via* the Regulation of the PI3K/AKT, JNK/MAPK and NF-κb Signaling Pathways in Osteoprotegerin Knockout Mice. *Int J Mol Med* (2016) 38(6):1661–72. doi: 10.3892/ijmm.2016.2794
5. Green A, Brutti G, Patterson CC, Dahlquist G, Stephenson C. Variation and Trends in Incidence of Childhood Diabetes in Europe. *Lancet* (2000) 355 (9207):873–6. doi: 10.1016/S0140-6736(99)07125-1
6. Eisenbarth GS. Type I Diabetes Mellitus. A Chronic Autoimmune Disease. *N Engl J Med* (1986) 314(21):1360–8. doi: 10.1056/NEJM198605223142106
7. Group TDP. Incidence and Trends of Childhood Type?1 Diabetes Worldwide 1990–1999. *Diabetic Med* (2006) 23(8):857–66. doi: 10.1111/j.1464-5491.2006.01925.x
8. Hermann R, Knip M, Veijola R, Simell O, Laine AP, Akerblom HK, et al. Temporal Changes in the Frequencies of HLA Genotypes in Patients With Type 1 Diabetes–Indication of an Increased Environmental Pressure? *Diabetologia* (2003) 46(3):420–5. doi: 10.1007/s00125-003-1045-4
9. Shanbhogue VV, Hansen S, Frost M, Brixen K, Hermann AP. Bone Disease in Diabetes: Another Manifestation of Microvascular Disease? *Lancet Diabetes Endocrinol* (2017) 5(10):827–38. doi: 10.1016/S2213-8587(17)30134-1

10. Zhang P, Wang Z, Wang Y, Wang Y, Liu C, Cao K, et al. An MRI Contrast Agent Based on a Zwitterionic Metal-Chelating Polymer for Hepatorenal Angiography and Tumor Imaging. *J Mater Chem B* (2020) 8(31):6956–63. doi: 10.1039/d0tb00893a
11. Lei Z, Yun F, Wang L, Li L, Xing D, Gong W, et al. Quantitative Evaluation of Vertebral Microvascular Permeability and Fat Fraction in Alloxan-Induced Diabetic Rabbits. *Radiology* (2018) 287(1):128–36. doi: 10.1148/radiol.2017170760
12. Zhang P, Zeng J, Li Y, Yang C, Meng J, Hou Y, et al. Quantitative Mapping of Glutathione Within Intracranial Tumors Through Interlocked MRI Signals of a Responsive Nanoprobe. *Angew Chem Int Ed Engl* (2021) 60(15):8130–8. doi: 10.1002/anie.202014348
13. Zaia A. Fractal Lacunarity of Trabecular Bone and Magnetic Resonance Imaging: New Perspectives for Osteoporotic Fracture Risk Assessment. *World J Orthop* (2015) 6(2):221–35. doi: 10.5312/wjo.v6.i2.221
14. Lisson CS, Lisson CG, Flosdorf K, Mayer-Steinacker R, Schultheiss M, von Baer A, et al. Diagnostic Value of MRI-Based 3D Texture Analysis for Tissue Characterisation and Discrimination of Low-Grade Chondrosarcoma From Enchondroma: A Pilot Study. *Eur Radiol* (2018) 28(2):468–77. doi: 10.1007/s00330-017-5014-6
15. MacKay JW, Murray PJ, Kasmai B, Johnson G, Donell ST, Toms AP. Subchondral Bone in Osteoarthritis: Association Between MRI Texture Analysis and Histomorphometry. *Osteoarthr Cartilage* (2017) 25(5):700–7. doi: 10.1016/j.joca.2016.12.011
16. Cataldo SD, Ficarra E. Mining Textural Knowledge in Biological Images: Applications, Methods and Trends. *Comput Struct Biotechnol J* (2017) 15 (C):56–67. doi: 10.1016/j.csbj.2016.11.002
17. Liu T, Zhao H, Li J, Korantzopoulos P, Li G. Rosiglitazone Attenuates Atrial Structural Remodeling and Atrial Fibrillation Promotion in Alloxan-Induced Diabetic Rabbits. *Cardiovasc Ther* (2014) 32(4):178–83. doi: 10.1111/1755-5922.12079
18. Oikawa A, Siragusa M, Quaini F, Mangialardi G, Katare RG, Caporali A, et al. Diabetes Mellitus Induces Bone Marrow Microangiopathy. *Arterioscler Thromb Vasc Biol* (2010) 30(3):498–508. doi: 10.1161/ATVBAHA.109.200154
19. Register TC, Lenchik L, Hsu FC, Lohman KK, Freedman BI, Bowden DW, et al. Type 2 Diabetes is Not Independently Associated With Spinal Trabecular Volumetric Bone Mineral Density Measured by QCT in the Diabetes Heart Study. *Bone* (2006) 39(3):628–33. doi: 10.1016/j.bone.2006.03.003
20. Starup-Linde J, Lykkeboe S, Gregersen S, Hauge EM, Langdahl BL, Handberg A, et al. Bone Structure and Predictors of Fracture in Type 1 and Type 2 Diabetes. *J Clin Endocrinol Metab* (2016) 101(3):928–36. doi: 10.1210/jc.2015-3882
21. Burghardt AJ, Kazakia GJ, Sode M, de Papp AE, Link TM, Majumdar S. A Longitudinal HR-pQCT Study of Alendronate Treatment in Postmenopausal Women With Low Bone Density: Relations Among Density, Cortical and Trabecular Microarchitecture, Biomechanics, and Bone Turnover. *J Bone Miner Res* (2010) 25(12):2558–71. doi: 10.1002/jbmr.157
22. Nilsson AG, Sundh D, Johansson L, Nilsson M, Mellstrom D, Rudang R, et al. Type 2 Diabetes Mellitus Is Associated With Better Bone Microarchitecture But Lower Bone Material Strength and Poorer Physical Function in Elderly Women: A Population-Based Study. *J Bone Miner Res* (2017) 32(5):1062–71. doi: 10.1002/jbmr.3057
23. Tao B, Liu JM, Zhao HY, Sun LH, Wang WQ, Li XY, et al. Differences Between Measurements of Bone Mineral Densities by Quantitative Ultrasound and Dual-Energy X-Ray Absorptiometry in Type 2 Diabetic Postmenopausal Women. *J Clin Endocrinol Metab* (2008) 93(5):1670–5. doi: 10.1210/jc.2007-1760
24. Heilmeier U, Cheng K, Pasco C, Parrish R, Nirody J, Patsch JM, et al. Cortical Bone Laminar Analysis Reveals Increased Midcortical and Periosteal Porosity in Type 2 Diabetic Postmenopausal Women With History of Fragility Fractures Compared to Fracture-Free Diabetics. *Osteoporos Int* (2016) 27 (9):2791–802. doi: 10.1007/s00198-016-3614-7
25. Kolacinski M, Kozakiewicz M, Materka A. Textural Entropy as a Potential Feature for Quantitative Assessment of Jaw Bone Healing Process. *Arch Med Sci* (2015) 11(1):78–84. doi: 10.5114/aoms.2013.33557
26. Mookiah M, Rohrmeier A, Dieckmeyer M, Mei K, Kopp FK, Noel PB, et al. Feasibility of Opportunistic Osteoporosis Screening in Routine Contrast-Enhanced Multi Detector Computed Tomography (MDCT) Using Texture Analysis. *Osteoporos Int* (2018) 29(4):825–35. doi: 10.1007/s00198-017-4342-3
27. Tu S-J, Wang S-P, Cheng F-C, Chen Y-J. Extraction of Gray-Scale Intensity Distributions From Micro Computed Tomography Imaging for Femoral Cortical Bone Differentiation Between Low-Magnesium and Normal Diets in a Laboratory Mouse Model. *Sci Rep-Uk* (2019) 9(1):8135. doi: 10.1038/s41598-019-44610-8

Conflict of Interest: The authors declare that the research was conducted in the absence of any commercial or financial relationships that could be construed as a potential conflict of interest.

Publisher's Note: All claims expressed in this article are solely those of the authors and do not necessarily represent those of their affiliated organizations, or those of the publisher, the editors and the reviewers. Any product that may be evaluated in this article, or claim that may be made by its manufacturer, is not guaranteed or endorsed by the publisher.

frontiers in Endocrinology

ORIGINAL RESEARCH
published: 07 January 2022
doi: 10.3389/fendo.2021.800398

High-Contrast Lumbar Spinal Bone Imaging Using a 3D Slab-Selective UTE Sequence

Amir Masoud Afsahi[1†], Alecio F. Lombardi[1,2†], Zhao Wei[1], Michael Carl[3], Jiyo Athertya[1], Koichi Masuda[4], Mark Wallace[5], Roland R. Lee[1,2] and Ya-Jun Ma[1]*

[1] Department of Radiology, University of California San Diego, San Diego, CA, United States, [2] Research Service, Veterans Affairs San Diego Healthcare System, San Diego, CA, United States, [3] GE Healthcare, San Diego, CA, United States, [4] Department of Orthopedic Surgery, University of California San Diego, San Diego, CA, United States, [5] Department of Anesthesiology, University of California San Diego, San Diego, CA, United States

Ultra-short echo time (UTE) MRI with post-processing is a promising technique in bone imaging that produces a similar contrast to computed tomography (CT). Here, we propose a 3D slab-selective ultrashort echo time (UTE) sequence together with image post-processing to image bone structures in the lumbar spine. We also explore the intermodality agreement between the UTE and CT images. The lumbar spines of two healthy volunteers were imaged with 3D UTE using five different resolutions to determine the best imaging protocol. Then, four patients with low back pain were imaged with both the 3D UTE sequence and CT to investigate agreement between the imaging methods. Two other patients with low back pain were then imaged with the 3D UTE sequence and clinical conventional T_1-weighted and T_2-weighted fast spin-echo (FSE) MRI sequences for qualitative comparison. The 3D UTE sequence together with post-processing showed high contrast images of bone and high intermodality agreement with CT images. In conclusion, post-processed slab-selective UTE imaging is a feasible approach for highlighting bone structures in the lumbar spine and demonstrates significant anatomical correlation with CT images.

Keywords: UTE MRI, bone imaging, lumbar spine, slab selective, CT-like contrast, ZTE MRI

OPEN ACCESS

Edited by:
Bing Wu,
GE Healthcare, China

Reviewed by:
Yan Xiong,
Huazhong University of Science and Technology, China
Yong-Can Huang,
Peking University Shenzhen Hospital, China

***Correspondence:**
Ya-Jun Ma
yam013@ucsd.edu

[†]These authors have contributed equally to this work

Specialty section:
This article was submitted to Bone Research, a section of the journal Frontiers in Endocrinology

Received: *23 October 2021*
Accepted: *13 December 2021*
Published: *07 January 2022*

Citation:
Afsahi AM, Lombardi AF, Wei Z, Carl M, Athertya J, Masuda K, Wallace M, Lee RR and Ma Y-J (2022) High-Contrast Lumbar Spinal Bone Imaging Using a 3D Slab-Selective UTE Sequence. Front. Endocrinol. 12:800398. doi: 10.3389/fendo.2021.800398

INTRODUCTION

Spinal disorders are a major medical, social, and economic issue due to their high prevalence and increasing incidence, especially among the elderly (1). Computed tomography (CT) offers both high-resolution and high-contrast imaging of bone, but due to the modality's involvement of ionizing radiation exposure, it is not recommended for children or patients who require frequent examinations. Most recently, zero echo time (ZTE) combined with data post-processing (2) has been applied for high contrast bone imaging of the head (3), shoulder (4), cervical spine (5), and hip (6). ZTE imaging uses a non-selective radiofrequency (RF) pulse (i.e., a short rectangular pulse) for signal excitation in which all body parts are excited simultaneously. In addition, ZTE uses the

Abbreviations: UTE, Ultrashort Echo Time; ZTE, Zero Echo Time; CT, Computed Tomography; FSE, Fast Spin-Echo; PD, Proton Density; TE, Echo Time; RF, Radiofrequency; FOV, Field-of-View.

shortest echo time achievable in the MR system and some coils require a relatively long ring-down time after excitation (between 10 and 200 μs) (7, 8). Data acquired during this ring-down period may lead to spatial signal inhomogeneity.

Ultrashort echo time (UTE) is an MR technique that also enables sufficiently fast data acquisition to detect signals from bone (9, 10). UTE applies slab-selectivity using a half, soft RF pulse for signal excitation during a slice-selective gradient that reduces artifacts related to respiratory motion. That way, UTE can selectively excite the spine without simultaneous excitation of the adjacent organs. In addition, echo time is more easily adjusted in the UTE sequence minimizing artifacts induced by the coil ring-down. Moreover, UTE MRI allows for visualization of structures in the spine that are not directly seen with conventional MRI due to their rapid signal decay, including pars interarticularis, longitudinal ligaments, annulus fibrosus, and the cartilaginous endplate (11, 12). For example, it has been shown that the diagnostic confidence for spondylolysis in cadaveric spines is higher when using UTE MRI than either conventional gradient-echo or short tau inversion recovery (STIR) sequences (13). Another potential application—and advantage—of UTE sequences over conventional MRI may be the quantitative assessment of enthesis in patients with inflammatory arthropathies (14, 15).

In this study, we investigated the performance of a 3D slab-selective UTE sequence together with signal post-processing to image bone structures in the lumbar spine in comparison with CT. We hypothesized that the post-processed slab-selective UTE images could show bone structures in the lumbar spine with high resolution and a high intermodality agreement with CT.

METHODS

MR Acquisition and *In Vivo* Study

Informed consent was obtained from all subjects following the guidelines of the local Institutional Review Board. All sequences were implemented on a 3T GE MR750 scanner (GE Healthcare Technologies, Milwaukee, WI) and a standard spine coil was used for signal reception. **Figure 1** shows the features of the 3D slab-selective UTE sequence. The UTE sequence enables slab selection by using a slice-selective short, half pulse (Shinnar-Le Roux (SLR) design, duration = 628 μs, and bandwidth = 15 kHz) with a variable-rate selective excitation (VERSE) design for excitation (16). After excitation, the spatial-encoding gradient is turned on and simultaneous data acquisition begins. As a result, the UTE data close to the k-space center are acquired on the gradient ramp.

All UTE scans were performed in the coronal plane to exclude soft tissues in the abdomen (i.e., the major structures involved in respiratory motion artifacts). A 5-second calibration scan was performed to correct the coil sensitivity inhomogeneity. To optimize the UTE sequence parameters and determine the best resolution and contrast, five scans with different isotropic resolutions (i.e., 0.9, 1.0, 1.2, 1.6, and 2 mm^3) were performed on the two abovementioned healthy volunteers (detailed sequence parameters in **Table 1**). Two experienced radiologists (A.F.L. and E.Y.C.) reviewed the images of different resolutions and determined which UTE imaging protocol performed best qualitatively. The final UTE protocol (i.e., with a resolution of 1.2 mm^3), (see the *Results* section) was then tested by scanning five healthy volunteers (28 to 48 years old, three males, two females). Oversampling in UTE imaging is beneficial for improving signal-to-noise ratio (SNR) and for reducing aliasing artifacts. Therefore, we oversampled the UTE acquisitions to improve the image quality for a scan that ran about 9 min. We also performed UTE MRI with and without RF pulse slab-selectivity (with the same sequence parameters) in the lumbar spine of a 40-year-old male healthy volunteer to compare performance in bone imaging.

Next, four patients (46 to 75 years old, all males) with low back pain were recruited and underwent UTE imaging for comparison against their most recent CT images.

Finally, two other patients (42 years old and 35 years old, both males) with low back pain were recruited and underwent both UTE imaging and conventional MR sequences [T_1-weighted fast spin-echo (T_{1w}-FSE) and T_2-weighted FSE (T_2w-FSE)] for comparison.

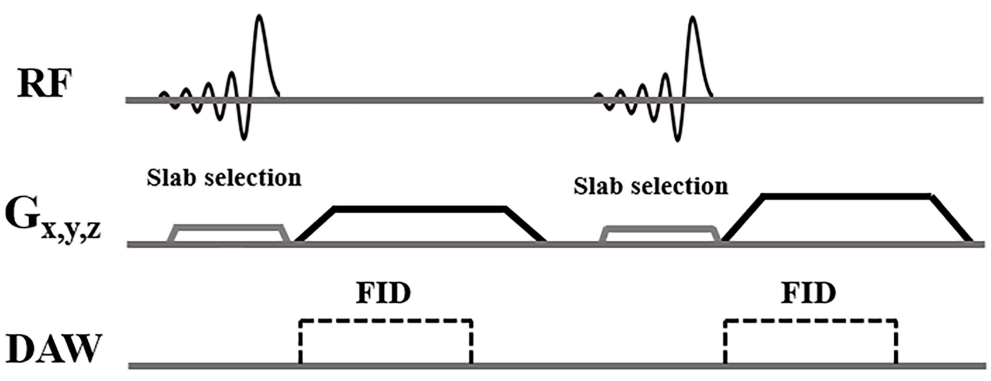

FIGURE 1 | 3D slab-selective UTE sequences. The 3D UTE sequence enables slab selection by using a half, soft pulse for excitation together with a slice-selective gradient. After excitation, the spatial encoding gradient is turned on and simultaneous data acquisition begins.

TABLE 1 | UTE sequence parameters for different resolutions.

Seq / Scan	FOV (cm^3)	Resolution (mm^3)	TR/TE (ms)	FA	BW (kHz)	Oversampling Factor	Average	Scan Time (min)
#1	32x32x7.2	0.9x0.9x0.9	2.4/0.028	1°	125	1	2	9.6
#2	32x32x8.0	1.0x1.0x1.0	2.2/0.028	1°	125	1.1	2	9.3
#3	32x32x9.6	1.2x1.2x1.2	2.0/0.028	1°	125	1.5	2	9
#4	32x32x9.6	1.6x1.6x1.6	1.7/0.028	1°	125	2.2	2	6.5
#5	32x32x12	2.0x2.0x2.0	1.6/0.028	1°	125	2.2	2	4.8

FOV, field-of-view; TR, repetition time; TE, echo time; FA, flip angle; BW, bandwidth.

Bone Imaging Post-Processing

The standardized post-processing procedure available in the workstation of the GE scanner was automatically completed for the acquired UTE images to render images with a "CT-like" contrast between bone and soft tissue (3, 17). The procedure includes an N4ITK bias correction algorithm (18), which was first applied to correct for intensity irregularities in the acquired UTE images due to the transmit coil profile inhomogeneity. Then, the contrasts of these bias-corrected images were logarithmically transformed and inverted. The process required approximately 1 to 3 minutes.

Comparison Between Non-Selective and Slab-Selective UTE Acquisitions

UTE imaging of the lumbar spine with non-selective and slab-selective RF pulses were performed in a healthy volunteer to compare focus measure and image blurring. A quantitative measure of focus was performed by placing a Laplacian filter on the image to detect edges, then performing a calculation of the variance of the filtered image (19). Convolution of a 3x3 Laplacian kernel was applied to the UTE images to detect tissue edges, with a higher variance measurement implying greater image sharpness/less blurring. OpenCV python library was used to perform the image convolution and focus measurement (20).

Automatic Image Registration for Intermodality Agreement Evaluation

To demonstrate the morphological similarities of images between our proposed UTE sequence and CT, a 3D volumetric registration framework using the Insight Toolkit (ITK) (21) was implemented in the four patients submitted to both UTE and CT images. First, the 3D volumetric images were pre-processed to highlight the targeting bone and minimize soft tissue contrast. Then, we performed rigid registration with a centered transform initializer which provides the initial center of rotation and translation. This step aligns each respective geometric center of the two volumes. The rigid registration used the mutual information as the similarity metric with gradient descent optimization. The number of iterations was 100 with a learning rate of 1.0. The sampling strategy was set to random, and the interpolator type set to linear.

Statistical Analysis

In addition to the quantitative image registration framework, one fellowship-trained musculoskeletal radiologist reviewed the images of the four patients submitted to both UTE and CT images, for intermodality agreement comparison. Measurements of vertebral body height and anteroposterior length using reconstructed sagittal CT and UTE MR images were performed in 20 vertebral bodies. A mid-sagittal plane was chosen for the measurements as it showed all the vertebral bodies simultaneously, in contrast with the coronal plane in which the lumbar lordosis prevented the simultaneous visualization of all vertebral bodies. The Shapiro-Wilk test was performed to test for normality of data distribution and a nonparametric statistics test was used to compare mean values between both image methods. Bias and limit-of-agreement (LoA) values (1.96 x standard deviation of difference) were calculated using the Bland and Altman method (22) and analyses were performed using R v.4.0.2 (R Core Team, 2014) and RStudio v.1.3.1073 (RStudio Core Team, 2020) (23, 24). P <.05 was considered as statistically significant.

RESULTS

Figure 2 shows the five 3D UTE scans with different resolutions from the same healthy volunteer. The SNR was lower when the resolution was higher, but when the resolution was too low, the bone structures were not well-demonstrated. The resolution with a voxel size of 1.2 mm^3 showed a good balance between image SNR and resolution of bone structures, as qualitatively verified by two radiologists.

As seen in **Supplementary Figure 1**, the slab-selective UTE acquisition shows the boundaries of bone more clearly than the non-slab-selective acquisition. The focus measure of the slab-selective UTE image shows a value about 2.5x higher value than that of the non-slab-selective image in the lumbar vertebral bone region, demonstrating that the slab-selective UTE acquisition produces better bone sharpness than the non-slab-selective acquisition due to its greater capability to alleviate the interference of respiratory motion artifacts. On the other hand, no apparent motion artifacts were observed in the non-slab-selective UTE images. This is because the non-Cartesian acquisition is inherently less sensitive to motion artifacts than a Cartesian acquisition and the artifacts are shown as image blurriness as can be seen in **Supplementary Figure 1**. Moreover, because of the motion average effect, the oversampling strategy also helps reduce the artifacts included by the periodical respiratory motion. For registration, all the images were pre-processed with modified contrast and reduced resolution in

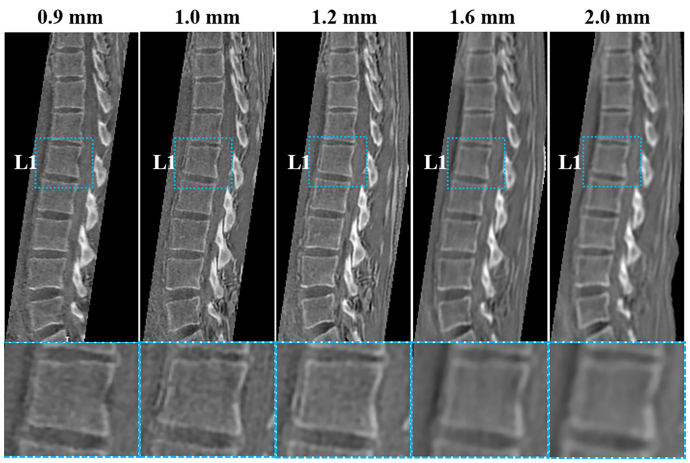

FIGURE 2 | UTE images with five different resolutions (0.9, 1.0, 1.2, 1.6, and 2 mm^3) of a healthy volunteer (29-year-old female). The corresponding UTE zoomed-in images of L1 (blue boxes in second row) are shown for better comparison. The resolution with a voxel size of 1.2 mm^3 shows a good balance between image SNR and bone structure visualization.

order to facilitate a faster and better registration between the UTE and CT images and, as a result, the image quality in **Supplementary Figure 1** was not only lower than that of the images shown in the remaining figures but also inadequate for diagnosis.

The high intermodality agreement was also confirmed using the rigid registration framework. A representative example showing the correlation between specific points in one normal and one fractured vertebral body on both imaging methods is shown in **Supplementary Figure 2**. Using vertebral body height and anteroposterior vertebral body length as comparison measures among the four patients with back pain, we found high intermodality agreement. The summary of the vertebral body height and anteroposterior vertebral body length measurements can be found in **Table 2**. Similar values with no statistical differences were found in these measurements for the CT and UTE images ($P > .05$). **Figure 3** shows the corresponding Bland-Altman plots. The LoAs in our data include more than 95% of differences between the two measurement methods ($P < .01$), reinforcing the similarities that exist between them.

TABLE 2 | Summary of the mean vertebral bodies' height and length of patients measured on CT and UTE MRI.

		VB Height (mm)		VB Length (mm)		Wilcoxon
		CT	UTE	CT	UTE	
Patient 1	L1	2.83	2.79	3.88	3.82	p >.05
	L2	2.85	2.83	4.14	4.11	
	L3	1.71	1.69	4.57	4.51	
	L4	2.78	2.75	3.83	3.84	
	L5	2.8	2.76	3.5	3.38	
Patient 2	L1	2.67	2.68	3	3.1	p >.05
	L2	2.65	2.74	3.11	3.17	
	L3	2.73	2.78	3.1	3.14	
	L4	2.88	2.9	2.93	2.99	
	L5	2.84	2.83	2.9	3.00	
Patient 3	L1	2.37	2.36	3.29	3.28	p >.05
	L2	2.49	2.52	3.2	3.28	
	L3	2.44	2.52	3.2	3.26	
	L4	2.62	2.63	3.14	3.2	
	L5	2.6	2.59	3.27	3.18	
Patient 4	L1	2.49	2.42	3.06	3.06	p >.05
	L2	2.51	2.52	3.2	3.15	
	L3	2.58	2.66	3.27	3.22	
	L4	14.6	15.3	3.85	3.89	
	L5	23.8	24.2	34.8	33.6	

VB, Vertebral body; Wilcoxon, Wilcoxon rank sum test.

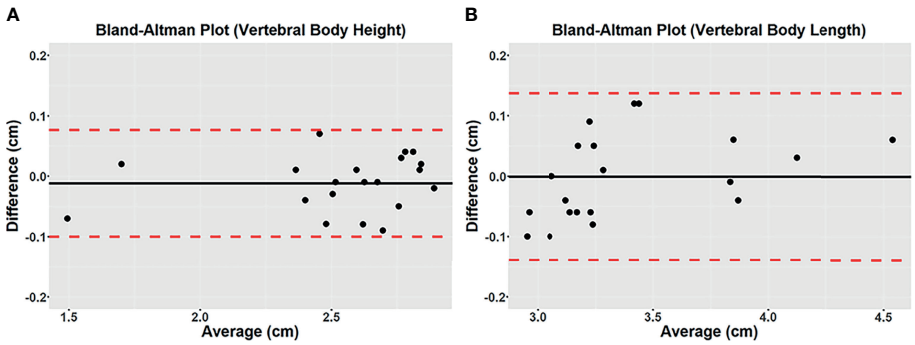

FIGURE 3 | Bland-Altman plots of differences between 3D CT and 3D UTE MRI for vertebral body height **(A)** and vertebral body length **(B)** measured on the mid-sagittal plane from the *in vivo* study. A solid line represents the mean of all differences (bias), while a dashed line indicates the 95% interval confidence of agreement. All measurements were within the 95% confidence interval limits.

Figure 4 shows one example of both modalities being applied to the lumbar spine of a patient with low back pain. The boundaries of the vertebral bodies have similar contrast and resolution, and the bone fractures can be visualized on both CT and UTE MRI in all three planes.

Figure 5 shows a comparison between CT and UTE MRI from a 55-year-old patient with low back pain. The MR images were acquired four months after the CT images. On the MRI, the fracture in L1 shows reduced vertebral body height and superior endplate fragmentation compared to the previous CT.

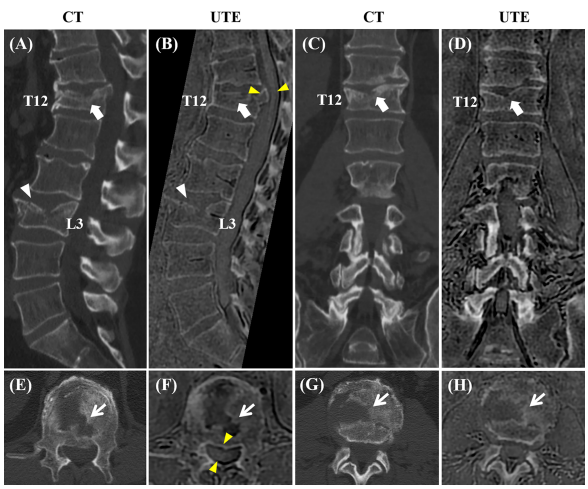

FIGURE 4 | Correlation between CT and the 3D slab-selective UTE MRI sequence in a 72-year-old male with low back pain (T11-L5). Compression fractures are seen in T12 and L3 on the CT image (arrow and arrowhead in **(A)**, respectively), showing excellent anatomic correlation with the 3D slab-selective UTE sequence (arrow and arrowhead in **(B)**, respectively). Coronal **(C, D)** and axial **(E–H)** images also showed excellent anatomic correlation of the fractures between the CT scan and the 3D slab-selective UTE sequence (arrows in **(E–H)**. Note the retropulsion of a bone fragment in T12 narrowing the spinal canal as well as its proximity to the spinal cord which can be seen on the UTE sequence (yellow arrowheads in **(B, F)**.

In this case, MRI allowed for the evaluation of bone marrow edema using the T_2-weighted sequence and suggested acute or subacute fracture, information not available when using only CT images.

Figure 6 shows a comparison between CT and 3D UTE in another patient with low back pain. Facet joint osteoarthritis, characterized by joint space narrowing and subchondral bone sclerosis, as well as subchondral bone cysts can be seen in both methods with good morphological correlation.

Schmorl's nodes (**Figure 7**) showed more conspicuity on UTE MRI, compared to conventional MRI sequences. In addition, chronic pars interarticularis fractures that may sometimes be hard to diagnose using T_1-weighted or T_2-weighted sequences were easily characterized on the 3D UTE sequence as seen in **Supplementary Figure 3**.

DISCUSSION

In this study we showed that a 3D slab-selective UTE sequence together with post-processing is feasible for bone imaging of the lumbar spine, displaying both high contrast and excellent anatomical correlation with CT images. This supports the argument for the potential implementation of the 3D UTE sequence into the clinical workflow.

The UTE sequence uses a soft RF pulse for signal excitation, offering the possibility of slab selectivity as a way to limit the 3D FOV and potentially reduce its sensitivity to respiratory motion artifacts (25). This is especially advantageous in the clinical evaluation of the dorsal and lumbar spine. Additionally, more efficient k-space trajectories such as spirals (26), twisted (27), or cones (28) are possible in UTE imaging because the UTE sequence readout gradient is applied after the RF pulse, ultimately facilitating reduction of SNR issues and scan time. These prolonged readout gradients together with the inherent ramp sampling in UTE sequence add more T_2* contrast between bone and soft tissues and facilitate further highlighting of the bone in post-processed images.

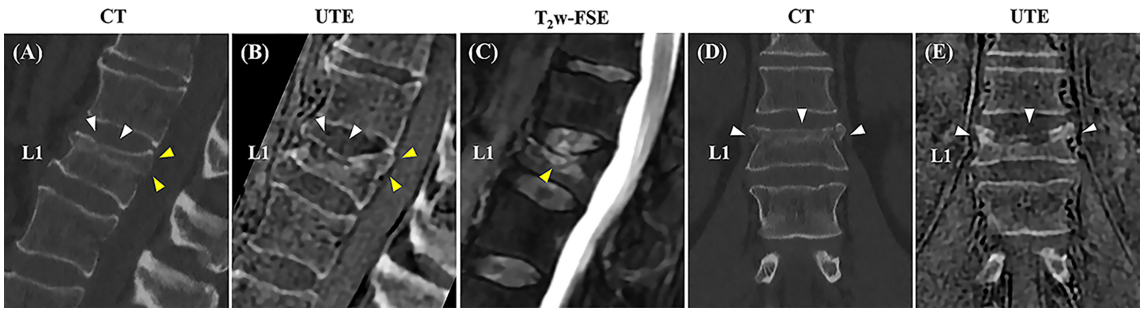

FIGURE 5 | Correlation between sagittal and coronal CT images and the 3D slab-selective UTE MRI sequence obtained three months apart in a 55-year-old male with low back pain. A compression fracture is seen in L1 on both the CT images (white arrowheads in **A**, **D**) and clinical MR image **(C)** associated with retropulsion of the posterior vertebral body cortex (yellow arrowheads in **A**). The 3D slab-selective UTE sequence shows the progression of the fracture with further loss of vertebral body height and fragmentation of the upper endplate (white arrowheads in **B**, **E**) in comparison to CT images. Note also the retropulsion of the posterior vertebral body cortex (yellow arrowheads in **B**).

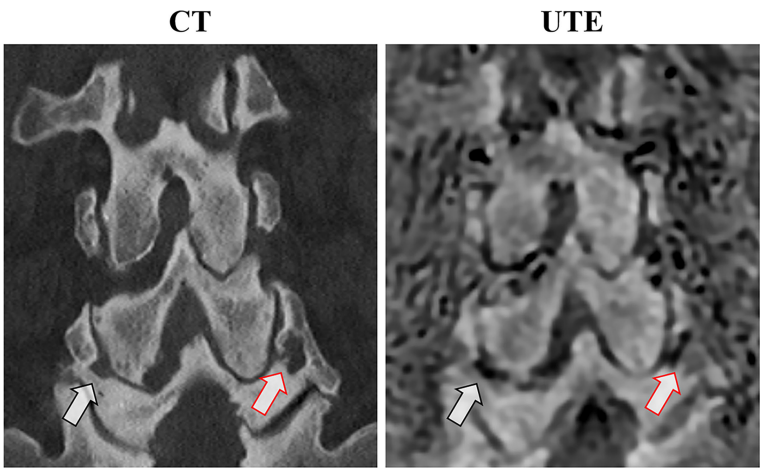

FIGURE 6 | Anatomical correlation between coronal CT and the 3D slab-selective UTE MRI sequence in a 75-year-old male with low back pain. Note the bilateral facet joint osteoarthritis with subchondral irregularities and cysts (arrows).

The post-processed UTE images showed bone structures with high resolution and high SNR. The vertebral body contours were well-defined, especially in the anterior portion of the spine which is in contact with abdominal organs and, therefore, more subject to respiratory motion artifacts (see **Figures 4** and **5**). There was high agreement between the UTE and CT images, showing excellent anatomical correlation between both methods as demonstrated by the image registration framework and the Bland-Altman analysis. Therefore, the UTE-based bone imaging may be useful for longitudinal studies or studies involving children given that UTE poses no threat of ionizing radiation exposure for the patient. Furthermore, lesions such as the Schmorl's nodes and other compressive fractures were also clearly seen on the UTE images, with clinical MRI used as the reference standard.

The UTE image shows some differences with the corresponding CT images as can be seen in **Figure 7**. This is probably because the slice thickness and patient positioning (non-rigid motion) were different between UTE and CT scans. It is technically challenging to get a perfect registration for non-rigid motion, especially for the small structures. A more advanced registration technique will be used to improve the co-registration in our future study (29).

There are more complicated structures in the UTE images than in the corresponding CT images. This is because UTE MRI can detect signals from all kinds of soft tissues with high signal intensities. The soft tissue boundaries may also be highlighted due to the fast T_2* decay (induced by the susceptibility differences between tissues) in these regions. Moreover, the fatty tissue may create more contrast due to the chemical shift artifacts in non-

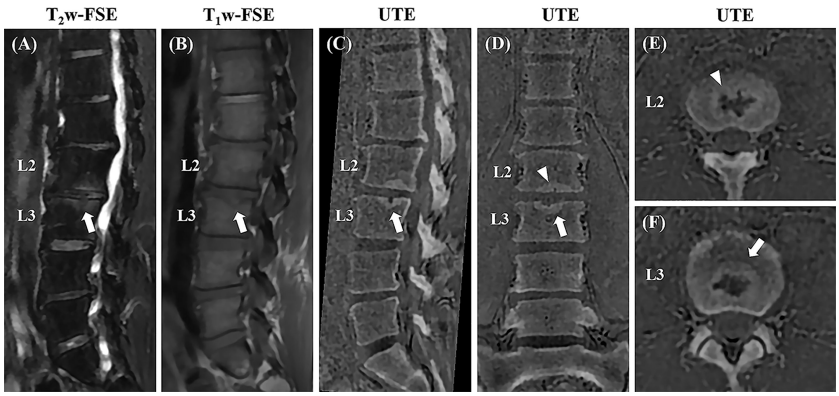

FIGURE 7 | Sagittal T_2w-FS and T_1w-FSE images **(A, B)** and sagittal **(C)**, coronal **(D)**, and axial **(E, F)** 3D slab-selective UTE images from a 42-year-old male patient with low back pain (T12-L5). Note the Schmorl's node in the superior endplate of L3 (arrows in **(A, B)** which demonstrates excellent anatomic correlation with the 3D slab-selective UTE sequence on the sagittal **(C)**, coronal **(D)**, and axial **(E, F)** images (arrows). Another Schmorl's node can be seen in the inferior endplate of L2 [arrowheads in **(D, E)**].

Cartesian UTE acquisition. ZTE imaging may be preferable in terms of reducing this off resonance-induced contrast since it has a shorter effective echo time than UTE. This will be investigated in a future UTE and ZTE comparison study.

Degenerative alterations and compressive fractures can be easily detected by clinical MRI. We propose that the UTE MRI technique be used as a complementary modality to improve MRI-only cortical and trabecular bone assessment, circumventing CT's unnecessary ionizing radiation exposure. This is particularly appealing in the cases of young patients or patients who would need to undergo repeated examinations. However, in some anatomical regions, it may be difficult to determine whether there is indeed a fracture present on clinical MRI, such as was the case with our patient who had a pars interarticularis fracture. Other spinal diseases such as spinal tumors and infections will be investigated in our future studies. It is well recognized that the clinical MRI ability to differentiate acute or subacute from chronic vertebral body fractures (e.g., the patient represented in **Figure 5**) is a clear advantage over CT, especially when no previous exams are available for comparison and, as a result, UTE combined with clinical MRI may provide much more useful information for diagnosis than CT alone in clinical practice.

UTE MRI has been very useful to image the cartilaginous endplate (CEP). We have recently developed a new inversion recovery-prepared and fat-saturated UTE (IR-FS-UTE) sequence to highlight the CEP signal (30). However, in this study, a proton density-weighted UTE sequence (flip angle = 1°) was used for bone imaging. Even though the CEP has a short T_2/T_2^*, its proton density is much higher than that of bone. Thus, the signal intensity of CEP is actually similar to that of other long T_2 soft tissues and, as a result, we don't expect that CEP signal would affect vertebral bone imaging. In addition, we would suggest using a highly T_1-weighted UTE sequence (e.g., an increased excitation flip angle (e.g., 15°) in the UTE sequence) to image CEP as the CEP has a much shorter T_1 than the nucleus pulposus (30).

This study has several limitations. First, a small number of subjects were used in this technical feasibility study. More patients will be recruited for a more comprehensive comparison of UTE MRI with CT and clinical MRI in a future study. Second, the 3D slab-selective UTE MRI can be reconstructed in three orthogonal planes; however, it is not yet feasible to complete 3D rendering at this stage. Technical developments to further improve the bone contrast for 3D rendering are under development and will be demonstrated in future studies. Third, CT is better at showing certain bone structures than UTE, such as fractured bones with soft tissue contamination. In such a case, the bone contrast in the UTE image is low due to the partial volume effect. UTE imaging with a higher resolution may solve this problem, but the scan time would significantly increase. Advanced fast imaging techniques, such as compressed sensing (31) and deep learning (32), could potentially be used to generate high resolution UTE images without compromising scan time.

CONCLUSION

In conclusion, the proposed 3D slab-selective UTE sequence together with image post-processing is capable of imaging spinal bone with high resolution with high intermodality agreement with CT and is promising as a clinical technique in spinal bone imaging.

DATA AVAILABILITY STATEMENT

The original contributions presented in the study are included in the article/**Supplementary Material**. Further inquiries can be directed to the corresponding author.

ETHICS STATEMENT

The studies involving human participants were reviewed and approved by IRB University of California San Diego. The patients/participants provided their written informed consent to participate in this study.

AUTHOR CONTRIBUTIONS

Y-JM contributed to conception and design of the study. AA, AL, ZW, MC, and JA organized the database. AL and JA performed the statistical analysis. AA, AL, and Y-JM wrote the first draft of the manuscript. JA, KM, MW, and RL wrote sections of the manuscript. All authors contributed to manuscript revision, read, and approved the submitted version.

FUNDING

The authors acknowledge grant support from NIH (R21AR075851). The authors declare that this study received funding from GE Healthcare and that this funder was not involved in the study design, collection, analysis, interpretation of data, the writing of this article or the decision to submit it for publication.

SUPPLEMENTARY MATERIAL

The Supplementary Material for this article can be found online at: https://www.frontiersin.org/articles/10.3389/fendo.2021.800398/full#supplementary-material

Supplementary Figure 1 | Coronal **(A–D)** and sagittal **(E–H)** UTE images with slab-selective and non-slab-selective RF pulses for signal excitation. Greater bone sharpness was observed in the slab-selective UTE images **(A, E)** than the corresponding non-slab-selective images **(B, F)**. The corresponding focus measure for the Laplacian filtered slab-selective UTE images **(C, G)** shows about 2.5x higher value than that of the non-slab-selective images **(D, H)**.

Supplementary Figure 2 | Volumetric automatic rigid registration between CT and 3D UTE MRI on a normal vertebral body **(A, C)** and a fractured vertebral body **(B, D)**. A centered initialization was followed by rigid registration. The red crosses represent corresponding points automatically detected by the registration algorithm. The yellow dashed lines (fracture) and orange dashed circles (vessel) have been drawn to highlight regions for visual comparison.

Supplementary Figure 3 | Sagittal T_2w-FS and T_1w-FSE images **(A, B)** and sagittal **(C)**, axial **(D)**, and coronal **(E)** 3D slab-selective UTE images from a 35-year-old male patient with low back pain (T12-L5). A spondylolysis of the pars interarticularis of L5 with anterior spondylolisthesis of L5 is better distinguished on the 3D slab-selective UTE MR sequence [arrows in **(A–C)**]. An axial oblique reconstructed image of the UTE MR sequence shows the bilateral fractures of the pars interarticularis in detail [arrows in **(D)**]. The coronal reconstructed image of the 3D slab-selective UTE MR sequence shows the corresponding expected location of the fractures [arrowheads in **(E)**] as well as a Schmorl's node in the superior endplate of S1 [arrow in **(E)**].

REFERENCES

1. Fehlings MG, Tetreault L, Nater A, Choma T, Harrop J, Mroz T, et al. The Aging of the Global Population: The Changing Epidemiology of Disease and Spinal Disorders. *Neurosurgery* (2015) 77(suppl_1):S1–5. doi: 10.1227/NEU.0000000000000953
2. Delso G, Wiesinger F, Sacolick LI, Kaushik SS, Shanbhag DD, Hüllner M, et al. Clinical Evaluation of Zero-Echo-Time MR Imaging for the Segmentation of the Skull. *J Nucl Med* (2015) 56(3):417–22. doi: 10.2967/jnumed.114.149997
3. Wiesinger F, Sacolick LI, Menini A, Kaushik SS, Ahn S, Veit-Haibach P, et al. Zero TE MR Bone Imaging in the Head. *Magnetic Reson Med* (2016) 75 (1):107–14. doi: 10.1002/mrm.25545
4. de Mello RAF, Ma YJ, Ashir A, Jerban S, Hoenecke H, Carl M, et al. Three-Dimensional Zero Echo Time Magnetic Resonance Imaging Versus 3-Dimensional Computed Tomography for Glenoid Bone Assessment. *Arthroscopy* (2020) 36(9):2391–400. doi: 10.1016/j.arthro.2020.05.042
5. Argentieri EC, Koff MF, Breighner RE, Endo Y, Shah PH, Sneag DB. Diagnostic Accuracy of Zero-Echo Time MRI for the Evaluation of Cervical Neural Foraminal Stenosis. *Spine (Phila Pa 1976)* (2018) 43 (13):928–33. doi: 10.1097/BRS.0000000000002462
6. Breighner RE, Bogner EA, Lee SC, Koff MF, Potter HG. Evaluation of Osseous Morphology of the Hip Using Zero Echo Time Magnetic Resonance Imaging. *Am J Sports Med* (2019) 47(14):3460–8. doi: 10.1177/0363546519878170
7. Fabich HT, Benning M, Sederman AJ, Holland DJ. Ultrashort Echo Time (UTE) Imaging Using Gradient Pre-Equalization and Compressed Sensing. *J Magn Reson* (2014) 245:116–24. doi: 10.1016/j.jmr.2014.06.015
8. Larson PE, Gurney PT, Nayak K, Gold GE, Pauly JM, Nishimura DG, et al. Designing Long-T2 Suppression Pulses for Ultra-Short Echo Time (UTE) Imaging. *Magn Reson Med* (2006) 56(1):94–103. doi: 10.1002/mrm.20926
9. Robson MD, Gatehouse PD, Bydder M, Bydder GM. Magnetic Resonance: An Introduction to Ultrashort TE (UTE) Imaging. *J Comput Assisted Tomogr* (2003) 27(6):825–46. doi: 10.1097/00004728-200311000-00001
10. Du J, Carl M, Bydder M, Takahashi A, Chung CB, Bydder GM. Qualitative and Quantitative Ultrashort Echo Time (UTE) Imaging of Cortical Bone. *J Magn Reson* (2010) 207(2):304–11. doi: 10.1016/j.jmr.2010.09.013
11. Chang EY, Du J, Chung CB. UTE Imaging in the Musculoskeletal System. *J Magn Reson Imaging* (2015) 41(4):870–83. doi: 10.1002/jmri.24713
12. Bae WC, Statum S, Zhang Z, Yamaguchi T, Wolfson T, Gamst AC, et al. Morphology of the Cartilaginous Endplates in Human Intervertebral Disks With Ultrashort Echo Time MR Imaging. *Radiol* (2013) 266(2):564–74. doi: 10.1148/radiol.12121181
13. Finkenstaedt T, Siriwanarangsun P, Achar S, Carl M, Finkenstaedt S, Abeydeera N, et al. Ultrashort Time-To-Echo Magnetic Resonance Imaging at 3 T for the Detection of Spondylolysis in Cadaveric Spines: Comparison With Ct. *Invest Radiol* (2019) 54(1):32–8. doi: 10.1097/RLI.0000000000000506
14. Chen B, Zhao Y, Cheng X, Ma Y, Chang EY, Kavanaugh A, et al. Three-Dimensional Ultrashort Echo Time Cones (3D UTE-Cones) Magnetic Resonance Imaging of Entheses and Tendons. *Magn Reson Imaging* (2018) 49:4–9. doi: 10.1016/j.mri.2017.12.034
15. Chen B, Cheng X, Dorthe EW, Zhao Y, D'Lima D, Bydder GM, et al. Evaluation of Normal Cadaveric Achilles Tendon and Enthesis With Ultrashort Echo Time (UTE) Magnetic Resonance Imaging and Indentation Testing. *NMR Biomed* (2019) 32(1):e4034. doi: 10.1002/nbm.4034
16. Hargreaves BA, Cunningham CH, Nishimura DG, Conolly SM. Variable-Rate Selective Excitation for Rapid MRI Sequences. *Magn Reson Med* (2004) 52 (3):590–7. doi: 10.1002/mrm.20168
17. Breighner RE, Endo Y, Konin GP, Gulotta LV, Koff MF, Potter HG. Technical Developments: Zero Echo Time Imaging of the Shoulder: Enhanced Osseous Detail by Using MR Imaging. *Radiol* (2018) 286(3):960–6. doi: 10.1148/radiol.2017170906
18. Tustison NJ, Avants BB, Cook PA, Zheng Y, Egan A, Yushkevich PA, et al. N4ITK: Improved N3 Bias Correction. *IEEE Trans Med imaging* (2010) 29 (6):1310–20. doi: 10.1109/TMI.2010.2046908
19. Pertuz S, Puig D, Garcia MA. Analysis of Focus Measure Operators for Shape-From-Focus. *Pattern Recognit* (2013) 46(5):1415–32. doi: 10.1016/j.patcog.2012.11.011
20. Bradski GTOLDDxsJoST. The OpenCV Library. *J Software Tools* (2000) 120:122–5.

21. McCormick M, Liu X, Ibanez L, Jomier J, Marion C. ITK: Enabling Reproducible Research and Open Science. *Front Neuroinf* (2014) 8(13). doi: 10.3389/fninf.2014.00013
22. Bland JM, Altman D. Statistical Methods for Assessing Agreement Between Two Methods of Clinical Measurement. *Lancet* (1986) 327(8476):307–10. doi: 10.1016/S0140-6736(86)90837-8
23. R Core Team. *R: A Language and Environment for Statistical Computing. R Foundation for Statistical*. Vienna, Austria: Computing (2014). Available at: http://wwwR-projectorg/.
24. RStudio Team. *RStudio: Integrated Development for R*. Boston, MA: RStudio, PBC (2020). Available at: http://wwwrstudiocom/.
25. Pauly J. *Slice-Selective Excitation for Very Short T_2 Species* Vol. 28. Amsterdam, Nederland: SMRM 1989 (1989).
26. Du J, Bydder M, Takahashi AM, Chung CB. Two-Dimensional Ultrashort Echo Time Imaging Using a Spiral Trajectory. *Magn Reson Imaging* (2008) 26 (3):304–12. doi: 10.1016/j.mri.2007.08.005
27. Boada FE, Gillen JS, Shen GX, Chang SY, Thulborn KR. Fast Three Dimensional Sodium Imaging. *Magn Reson Med* (1997) 37(5):706–15. doi: 10.1002/mrm.1910370512
28. Gurney PT, Hargreaves BA, Nishimura DG. Design and Analysis of a Practical 3D Cones Trajectory. *Magn Reson Med* (2006) 55(3):575–82. doi: 10.1002/mrm.20796
29. Klein S, Staring M, Murphy K, Viergever MA, Pluim JP. Elastix: A Toolbox for Intensity-Based Medical Image Registration. *IEEE Trans Med Imaging* (2009) 29(1):196–205. doi: 10.1109/TMI.2009.2035616
30. Lombardi AF, Wei Z, Wong J, Carl M, Lee RR, Wallace M, et al. High Contrast Cartilaginous Endplate Imaging Using a 3D Adiabatic Inversion-Recovery-Prepared Fat-Saturated Ultrashort Echo Time (3D IR-FS-UTE) Sequence. *NMR Biomed* (2021) 34(10):e4579. doi: 10.1002/nbm.4579
31. Lustig M, Donoho D, Pauly JM. Sparse MRI: The Application of Compressed Sensing for Rapid MR Imaging. *Magn Reson Med: Off J Int Soc Magn Reson Med* (2007) 58(6):1182–95. doi: 10.1002/mrm.21391
32. Zhu B, Liu JZ, Cauley SF, Rosen BR, Rosen MS. Image Reconstruction by Domain-Transform Manifold Learning. *Nat* (2018) 555(7697):487–92. doi: 10.1038/nature25988

Conflict of Interest: MC was employed by the company GE Healthcare.

The remaining authors declare that the research was conducted in the absence of any commercial or financial relationships that could be construed as a potential conflict of interest.

Publisher's Note: All claims expressed in this article are solely those of the authors and do not necessarily represent those of their affiliated organizations, or those of the publisher, the editors and the reviewers. Any product that may be evaluated in this article, or claim that may be made by its manufacturer, is not guaranteed or endorsed by the publisher.

frontiers in Endocrinology

ORIGINAL RESEARCH
published: 16 February 2022
doi: 10.3389/fendo.2022.801930

Assessment of Osteoporosis in Lumbar Spine: *In Vivo* Quantitative MR Imaging of Collagen Bound Water in Trabecular Bone

Jin Liu[1†], Jian-Wei Liao[1†], Wei Li[1], Xiao-Jun Chen[1], Jia-Xin Feng[1], Lin Yao[1], Pan-Hui Huang[1], Zhi-Hai Su[2], Hai Lu[2], Yu-Ting Liao[3], Shao-Lin Li[1‡] and Ya-Jun Ma[4‡]*

[1] Department of Radiology, The Fifth Affiliated Hospital of Sun Yat-Sen University, Zhuhai, China, [2] Department of Spinal Surgery, The Fifth Affiliated Hospital of Sun Yat-Sen University, Zhuhai, China, [3] MR Research, GE Healthcare, Guangzhou, China, [4] Department of Radiology, University of California San Diego, La Jolla, CA, United States

Aim: Bone collagen matrix makes a crucial contribution to the mechanical properties of bone by imparting tensile strength and elasticity. The collagen content of bone is accessible *via* quantification of collagen bound water (CBW) indirectly. We prospectively study the performance of the CBW proton density (CBWPD) measured by a 3D short repetition time adiabatic inversion recovery prepared ultrashort echo time (STAIR-UTE) magnetic resonance imaging (MRI) sequence in the diagnosis of osteoporosis in human lumbar spine.

Methods: A total of 189 participants with a mean age of 56 (ranged from 50 to 86) years old were underwent MRI, quantitative computed tomography (QCT), and dual-energy X-ray absorptiometry (DXA) in lumbar spine. Major fracture risk was also evaluated for all participants using Fracture Risk Assessment Tool (FRAX). Lumbar CBWPD, bone marrow fat fraction (BMFF), bone mineral density (BMD) and T score values were calculated in three vertebrae (L2–L4) for each subject. Both the CBWPD and BMFF were correlated with BMD, T score, and FRAX score for comparison. The abilities of the CBWPD and BMFF to discriminate between three different cohorts, which included normal subjects, patients with osteopenia, and patients with osteoporosis, were also evaluated and compared using receiver operator characteristic (ROC) analysis.

Results: The CBWPD showed strong correlation with standard BMD (R^2 = 0.75, P < 0.001) and T score (R^2 = 0.59, P < 0.001), as well as a moderate correlation with FRAX score (R^2 = 0.48, P < 0.001). High area under the curve (AUC) values (≥ 0.84 using QCT as reference; ≥ 0.76 using DXA as reference) obtained from ROC analysis demonstrated that the CBWPD was capable of well differentiating between the three different subject cohorts. Moreover, the CBWPD had better correlations with BMD, T score, and FRAX score than BMFF, and also performed better in cohort discrimination.

OPEN ACCESS

Edited by:
Bing Wu,
GE Healthcare, China

Reviewed by:
Liheng Ma,
The First Affiliated Hospital of Guangdong Pharmaceutical University, China
Yunfei Zha,
Renmin Hospital of Wuhan University, China

***Correspondence:**
Shao-Lin Li
lishaolin1963@126.com

[†]These authors have contributed equally to this work and share first authorship

[‡]These authors have contributed equally to this work and share last authorship

Specialty section:
This article was submitted to Bone Research, a section of the journal Frontiers in Endocrinology

Received: *26 October 2021*
Accepted: *21 January 2022*
Published: *16 February 2022*

Citation:
Liu J, Liao J-W, Li W, Chen X-J, Feng J-X, Yao L, Huang P-H, Su Z-H, Lu H, Liao Y-T, Li S-L and Ma Y-J (2022) Assessment of Osteoporosis in Lumbar Spine: In Vivo Quantitative MR Imaging of Collagen Bound Water in Trabecular Bone. Front. Endocrinol. 13:801930. doi: 10.3389/fendo.2022.801930

Conclusion: The STAIR-UTE-measured CBWPD is a promising biomarker in the assessment of bone quality and fracture risk.

Keywords: osteoporosis, ultrashort echo time, collagen bound water proton density, bone mineral density, bone marrow fat fraction

INTRODUCTION

Osteoporosis (OP) has become a major public health burden as the population continues to age (1, 2). Each year, about 200 million people worldwide suffer from OP, with approximately 89 million fractures occurring on an annual basis (3). OP is characterized by a decrease in bone strength combined with an increased risk of fracture as a result of low bone mass and microarchitectural deterioration of bone tissue (4).

Bone mineral density (BMD) plays a major role in bone strength and its measurement of trabecular bone in the spine and/or hip using dual-energy x-ray absorptiometry (DXA) is the clinical standard for assessments of both OP and fracture risk (5–7). Quantitative computed tomography (QCT) utilizes 3D volumetric imaging and quantification to further improve the accuracy of these BMD measurements but with increased ionizing radiation.

The organic matrix, another important bone component, provides tensile strength and elasticity, also contributing significantly to the mechanical properties of bone (8). Because changes in the collagen density and integrity within the bone's organic matrix affect overall bone quality (9), quantitative evaluation of the collagen matrix is likely to provide valuable information on an individual's bone strength (10–12).

Unfortunately, both DXA and QCT are limited in their abilities to assess changes in the collagen matrix due to their low soft tissue contrast. Magnetic resonance imaging (MRI) is a superior method in that it offers high-contrast soft tissue imaging. However, collagen cannot be directly imaged by MRI due to its extremely short T_2 relaxation time (about 10 μs) (13–15). Alternatively, indirect evaluation of the collagen matrix can be performed by quantification of the water molecules which are tightly bound to the collagen matrix (i.e., collagen bound water (CBW)) and are highly correlated with the matrix collagen's density and integrity (16). Like collagen itself, the CBW also has a relatively short T_2 relaxation time—around 300 μs. While CBW is not accessible to clinical sequences with long echo times (TEs) (i.e., several to hundreds of milliseconds) such as gradient recalled echo (GRE) and fast spin echo (FSE) (17, 18), a specialized MRI technique known as the ultrashort echo time (UTE) sequence has been developed with a TE less than 100 μs to specifically target tissues with short T_2 relaxation times. This UTE MRI approach can be used to image and quantify the CBW (19).

In the last decade, UTE MRI imaging of CBW has been studied by several groups as a possible surrogate measure for the bone's collagen matrix (18, 20–23). It was found that the UTE measurements scale to an almost linear degree with collagen matrix density (22, 24, 25), and highly correlated with yield, peak stress, and elastic toughness (25, 26). However, most of the previous studies were focused on CBW measurement in cortical bone. CBW evaluation in trabecular bone has the potential to be even more valuable a measurement because not only do most osteoporotic fractures occur in trabecular bone, but trabecular bone is also highly responsive to metabolic stimuli (27–30). However, quantification of CBW in trabecular bone is more technically challenging than in cortical bone due to trabecular bone's much lower CBW content and higher concentration of tissue components with long T_2 relaxation times, such as marrow fat (31).

Most recently, a new 3D short repetition time adiabatic inversion recovery prepared UTE (3D STAIR-UTE) Cones sequence was developed which could volumetrically quantify CBW proton density (CBWPD) of trabecular bone *in vivo* for the first time (17). The STAIR-UTE sequence can generate high contrast imaging of CBW with sufficient suppression of all the long T_2 signals.

The purpose of our study was to investigate the STAIR-UTE-measured CBWPD in the classification of patients as normal, osteopenic and osteoporotic in the lumbar spine with golden standard QCT-measured BMD and DXA-measured T score as reference. The CBWPD was also correlated with fracture risk score which was characterized by Fracture Risk Assessment Tool (FRAX). Moreover, vertebral bone marrow fat fraction (BMFF)—another quantitative imaging biomarker that has been studied extensively in OP assessment—was also employed for comparison against CBWPD.

MATERIALS AND METHODS

Subject Recruitment

This study was conducted under Institutional Review Board approval; written informed consent was obtained from all participants. Between June 2020 and January 2021, 189 participants with a mean age of 56 (ranged from 50 to 86) years old were recruited to participate in this prospective study. MRI, QCT, and DXA examinations of the lumbar spine for each participant were performed in the same week. Subjects were excluded if they had known preexisting bone diseases (e.g., lumbar fracture, tumor, metastases, dysplasia, or metabolic disorders), a history of lumbar surgery, or a history of drug therapy targeted at BMD. We also excluded any subjects who had a history of osteoarthritis, inflammatory arthritis, cancer, Paget disease, endocrinologic or gastrointestinal disorder, glucocorticoid use, selective serotonin uptake inhibitor use, or anticonvulsant use.

QCT and DXA Examinations

QCT examinations of the lumbar region were performed on a 128-channel multi-detector CT scanner (uCT 760, United

Imaging Healthcare). All CT parameters were set in accordance with the "China Health Quantitative CT Big Data Project Research Program" (32) as follows: collimation: 0.625 mm, tube voltage: 120 kVp, tube current: automatic. All CT images were reconstructed to 512×512 matrices using iterative reconstruction algorithms available from the vendor's CT scanners. The reconstruction intervals were 1.0 mm. Our QCT post-processing can only quantify three vertebral bodies at a time, so the center three vertebral elements of the lumbar spine (i.e., L2-L4) were chosen for the quantification.

Standard DXA scan (Osteocore, Medilink 90kv and 2mA) was performed according to WHO guidelines (33) to acquire T score in the lumbar spine. Images of the lumbar spine were obtained in posterior-anterior projection.

MR Imaging

All 189 participants underwent spine MR imaging on a 3T clinical scanner (Pioneer, GE Healthcare Technologies, Milwaukee, WI) with a spine-array surface coil for signal reception. Clinical sagittal T_1-weighted FSE (repetition time (TR): 540 ms, TE: 8 ms, flip angle (FA): 80°, field-of-view (FOV): 32×32 cm^2, pixel size: 1.0×1.4 mm^2, number of slices: 13, slice thickness: 4 mm, scan time: 1 min) and T_2-weighted FSE (TR: 2291 ms, TE: 90 ms, FA: 90°, FOV: 32×32 cm^2, pixel size: 1.0×1.4 mm^2, number of slices: 13, slice thickness: 4 mm, scan time: 2 min) scans of the lumbar spine were included. A product sequence, IDEAL-IQ (Iterative decomposition of water and fat with echo asymmetry and least squares estimation) (34), was used to quantify BMFF (TR: 7.3 ms; TEs: 1.2, 2.1, 3.1, 4.1, 5.0, and 6.0 ms; FA: 4°; FOV: 32×32 cm^2; pixel size: 2.0×2.0 mm^2; number of slices: 12; slice thickness: 8 mm; and scan time: 16 sec).

The 3D STAIR-UTE Cones sequence was performed in the sagittal plane for the CBW imaging (17) (TR: 150 ms, TE: 0.032 ms, inversion time (TI): 64 ms, FA: 18°, number of spokes per-TR: 5, spoke interval: 5.5 ms, FOV: 30 cm×30 cm, pixel size: 2.1×2.1mm^2, number of slices: 16, slice thickness: 4.5 mm, oversampling factor: 2, scan time: 10 min). In order to acquire a spine coil sensitivity profile for correction of the STAIR-UTE imaging inhomogeneity, the 3D UTE Cones sequence was applied twice without STAIR preparation, using spine and body coils for signal reception, respectively (17) (TR: 6 ms, TE: 0.032 ms, FA: 2°, FOV: 30 cm×30 cm; pixel size, 2.1×2.1 mm^2, number of slices: 16, slice thickness: 4.5 mm, and scan time: 1 min. A rubber band with a T2* of 0.34 ms and a premeasured proton density of 18 mol/L was placed between the spine coil and participants during scanning to serve as a reference standard. The CBWPD of trabecular bone was calculated using Equation [9] in Ref (17).. Ten healthy volunteers were recruited to study the reproducibility of the STAIR-UTE Cones sequence. Each volunteer was scanned three times over three consecutive days.

Fracture Risk Characterization

The major fracture risk (i.e., 10-year probability of osteoporotic fracture) of each participant was characterized using FRAX (https://www.sheffield.ac.uk/FRAX) with 11 clinical variables taken into consideration (i.e., age, sex, weight, height, previous fracture, parental hip fracture, current smoking status, glucocorticoid use, rheumatoid arthritis, secondary OP, and alcohol use of three or more units per day).

Data Analysis

The CBWPD calculation was performed in MATLAB (The MathWorks, Natick, MA). Regions of interest (ROIs) were manually drawn in the trabecular bone region—avoiding the subchondral bone region—to measure BMD, CBWPD, and BMFF in L2–L4. Mean lumbar BMD, CBWPD, and BMFF values were computed by averaging them across these three vertebrae for each subject. ROIs were independently drawn by two radiologists with 10 (W.L.) and 8 (J.L.) years of respective experience to assess inter-observer agreement of ROIs. To assess intra-observer agreement of ROI drawing, this procedure was repeated by the radiologist with 10 years of experience two months after the initial ROI drawing.

For the DXA experiment, T score was used to assess osteoporosis since all the participants were over 50 years old according to WHO guidelines (35). The scanned subjects were grouped into three cohorts (normal, osteopenia, and OP). A BMD (measured by QCT) greater than 120 mg/cm^3 (equivalent to a DXA T score > -1.0 standard deviation (SD)) indicates normal, a BMD value between 80 mg/cm^3 and 120 mg/cm^3 (equivalent to a DXA T score < -1.0 SD and > -2.5 SD) indicates osteopenia, and a BMD less than 80 mg/cm^3 (equivalent to a DXA T score of < -2.5 SD) indicates OP.

Statistical Analysis

Statistical analysis was performed using Statistical Package for Social Sciences (SPSS) software (version 23.0). $P < 0.05$ was considered statistically significant. Linear regression and Bland–Altman analysis were performed to assess the reproducibility of the STAIR-UTE Cones sequence. Intra- and interclass correlation coefficients (ICC) were calculated to assess both the interobserver and intra-observer reproducibility of CBWPD and BMFF measurements. The differences in age, body mass index (BMI), BMD, T score, CBWPD, BMFF, and FRAX score among all three cohorts (normal, osteopenia, and OP) were determined using the Kruskal-Wallis test. The differences in sex among all three cohorts were determined using the Chi-square test. Linear regression was performed to correlate the CBWPD and BMFF with BMD and T score, respectively. Non-linear regression using an exponential function was performed to correlate the CBWPD and BMFF with FRAX score. To evaluate the performances of the CBWPD and BMFF in discriminating between the three cohorts, receiver operating characteristic (ROC) analysis was performed and the area under the curve (AUC) with 95% confidence interval (CI) was computed using Medcalc software (version 20.0.3). The DeLong test was used to compare the ROC curves (i.e., AUCs) between CBWPD and BMFF.

RESULTS

Data analysis was performed on 162 of the recruited 189 participants, with the 27 exclusions made due to bone disease (n = 17) and poor MR image quality caused by motion during the

scan (n = 10). Participant characteristics are described in **Table 1**. Age, BMD, T score, CBWPD, BMFF, and FRAX score all showed significant differences among the three cohorts, with QCT and DXA used as the respective reference standards.

Figure 1 shows representative BMD, T score, CBWPD, and BMFF maps of the lumbar spines of three subjects: one from each cohort (normal, osteopenia, and OP). Lower CBWPD, BMD, and T score, as well as higher BMFF, were found in more osteoporotic subjects.

Reproducibility

The results of linear regression and Bland–Altman analysis of the STAIR-UTE measured CBWPDs for the three repeated volunteer scans are shown in **Figure 2**. Strong correlations and high agreements of the CBWPD measurements were found between the first and the second scans with a $R^2 = 0.96$ ($P < 0.001$) and a mean bias of -0.02 mol/L (± 1.96 SD: range –0.30 to 0.27 mol/L) (**Figure 2A**) respectively, between the first and the third scans with a $R^2 = 0.90$ ($P < 0.001$) and a mean bias of -0.003 mol/L (± 1.96 SD: range –0.42 to 0.41 mol/L) (**Figure 2B**) respectively, and between the second and the third scans with a $R^2 = 0.91$ ($P < 0.001$) and a mean bias of 0.01 mol/L (± 1.96 SD: range –0.37 to 0.40 mol/L) (**Figure 2C**) respectively. These results demonstrate an excellent reproducibility for the STAIR-UTE Cones scans.

The interobserver ICCs for the CBWPD and BMFF measurements between the two radiologists were 0.93 and 0.92, respectively. The intra-observer ICCs for the CBWPD and BMFF quantification were 0.95 and 0.93, respectively. These high ICC values demonstrate excellent reproducibility for both interobserver and intra-observer measurements.

Correlations

The CBWPD showed a positive correlation with BMD ($R^2 = 0.75$, $P < 0.001$) (**Figure 3A**), a positive correlation with T score ($R^2 = 0.59$, $P < 0.001$) (**Figure 3B**), and a negative correlation with FRAX score ($R^2 = 0.48$, $P < 0.001$) (**Figure 3C**).

The BMFF showed a negative correlation with BMD ($R^2 = 0.45$, $P < 0.001$) (**Figure 3D**), a negative correlation with T score ($R^2 = 0.23$, $P < 0.001$) (**Figure 3E**), and a positive correlation with FRAX score ($R^2 = 0.20$, $P < 0.001$) (**Figure 3F**).

As demonstrated by these results, the CBWPD correlates better with BMD, T score, and FRAX score than the BMFF does.

ROC Analysis

Figures 4A–C show the ROC curves of $CBWPD^{QCT}$ and $BMFF^{QCT}$ (with QCT as reference standard) in differentiating normal subjects, patients with osteopenia, and patients with OP. **Table 2** summarizes all the criteria that were used to evaluate the diagnostic performance of $CBWPD^{QCT}$ and $BMFF^{QCT}$. The AUC values of $CBWPD^{QCT}$ and $BMFF^{QCT}$ were 0.84 and 0.70 ($P < 0.001$) for normal vs. osteopenia, 0.98 and 0.89 ($P < 0.001$) for normal vs. OP, and 0.90 and 0.79 ($P < 0.001$) for osteopenia vs. OP, respectively. The AUC values of $CBWPD^{QCT}$ were consistently higher than the corresponding AUC values of $BMFF^{QCT}$.

Figures 4D–F show the ROC curves of $CBWPD^{DXA}$ and $BMFF^{DXA}$ (with DXA as reference standard) in differentiating normal subjects, patients with osteopenia, and patients with OP. **Table 3** summarizes all the criteria that were used to evaluate the diagnostic performance of $CBWPD^{DXA}$ and $BMFF^{DXA}$. The AUC values of $CBWPD^{DXA}$ and $BMFF^{DXA}$ were 0.83 and 0.68 ($P < 0.001$) for normal vs. osteopenia, 0.93 and 0.82 ($P < 0.001$) for normal vs. OP, and 0.76 and 0.65 ($P = 0.005$) for osteopenia vs. OP, respectively. The AUC values of $CBWPD^{DXA}$ were consistently higher than the corresponding AUC values of $BMFF^{DXA}$.

As demonstrated by these results, the CBWPD shows high capability to classify patients as normal, osteopenic and

TABLE 1 | Characteristics of patients in three cohorts of normal subjects, patients with osteopenia, and patients with osteoporosis.

		QCT as reference standard				DXA as reference standard			
	All subjects (n=162)	**Normal (n = 86)**	**Osteopenia (n = 41)**	**Osteoporosis (n = 35)**	***P*Value**	**Normal (n = 88)**	**Osteopenia (n = 46)**	**Osteoporosis (n = 28)**	***P*Value**
Sex					0.198				0.148
male	65 (40%)	35 (41%)	20 (49%)	10 (29%)		36 (41%)	22 (48%)	7 (25%)	
female	97 (60%)	51 (59%)	21 (51%)	25 (71%)		52 (59%)	24 (52%)	21 (75%)	
Age (years)	58 (9)	53 (5)	60 (8)	68 (9)	<0.001	55 (6)	60 (9)	66 (10)	<0.001
BMI (kg/m^2)	23.4 (21.3-25.4)	23.4 (21.5-25.5)	23.8 (21.1-26.8)	22.9 (20.5-25.0)	0.517	23.7 (21.7-26.0)	23.9 (21.3-26.1)	21.68 (20.1-23.6)	0.004
BMD (mg/cm^3)	119.8 (83.6-154.7)	155.6 (132.5-175.7)	100.7 (90.0-111.1)	54.1 (43.9-67.9)	<0.001	148.9 (125.5-174.7)	99.8 (80.2-120.6)	60.9 (47.9-71.1)	<0.001
T score	0.5 (-2.1 to -0.6)	0.8 (-0.3 to 2.0)	-1.3 (-2.0 to -0.3)	-2.7 (-3.4 to -2.3)	<0.001	1.0 (0.0 to 2.0)	-1.7 (-2.1 to -1.3)	-3.1 (-3.5 to -2.6)	<0.001
CBWPD (mol/L)	2.5 (1.9-2.9)	2.9 (2.5-3.3)	2.3 (2.1-2.5)	1.6 (1.3-1.8)	<0.001	2.9 (2.4-3.2)	2.2 (1.8-2.4)	1.7 (1.4-1.9)	<0.001
BMFF (%)	54.2 (44.4-63.3)	48.0 (41.2-55.2)	55.8 (48.2-62.8)	67.5 (60.0-73.4)	<0.001	49.2 (42.0-56.5)	57.1 (46.7-67.9)	65.0 (58.1-72.7)	<0.001
FRAX score (%)	3.7 (1.5-4.7)	1.9 (1.2-2.0)	3.80 (1.9-5.0)	7.8 (4.6-9.5)	<0.001	1.7 (1.2-1.9)	3.9 (2.3-4.8)	9.3 (6.2-10.0)	<0.001

Data are presented as n (%), mean (SD), or median (IQR). All comparisons between the three cohorts were significant (P < 0.001) except for sex (P = 0.198, taking QCT as reference standard; P = 0.148, taking DXA as reference standard) and BMI (P = 0.517, taking QCT as reference standard; P = 0.004, taking DXA as reference standard).

BMI, body mass index; CBWPD, collagen bound water proton density; QCT, quantitative computed tomography; BMD, bone mineral density; DXA, dual-energy X-ray absorptiometry; BMFF, bone marrow fat fraction; FRAX, Fracture Risk Assessment Tool; IQR, interquartile range.

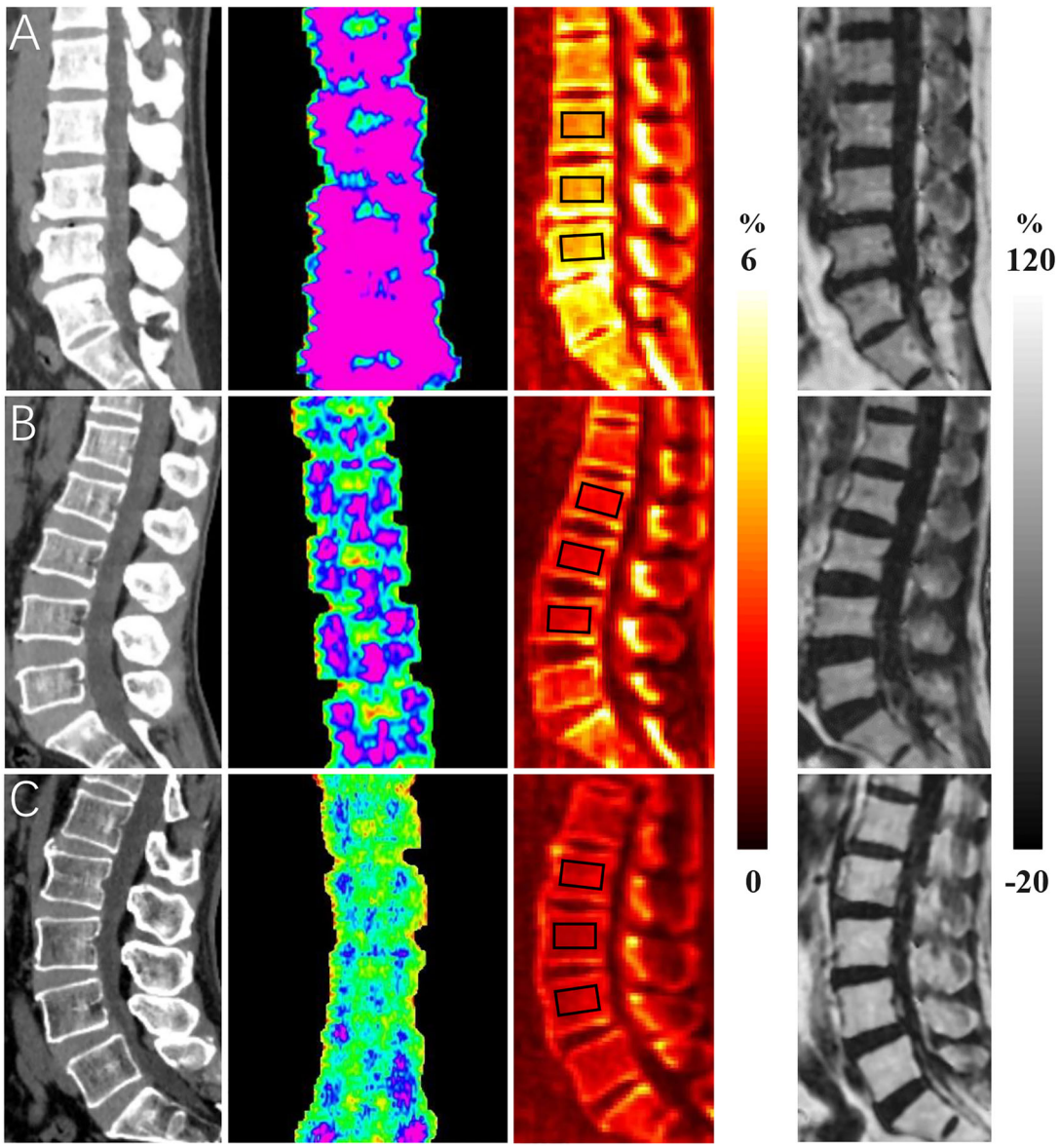

FIGURE 1 | Representative bone mineral density (BMD) (first column), T score (second column), collagen bound water proton density (CBWPD) (third column), and bone marrow fat fraction (BMFF) (fourth column) maps in the lumbar spine of three subjects with normal bone mass (first row **(A)**, 50-year-old male), osteopenia (second row **(B)**, 54-year-old female), and osteoporosis (last row **(C)**, 66-year-old male). ROIs inside of black squares were drawn for data analysis.

osteoporotic. It also performs better than the BMFF in discrimination of the three cohorts whether using QCT or DXA as the reference standard.

DISCUSSION

In this prospective study, we presented a noninvasive and nondestructive MRI technique to measure CBWPD in the human lumbar spine for assessment of trabecular bone quality using QCT and DXA as the reference standard. To the best of our knowledge, this is the first study of trabecular CBWPD in the diagnosis of OP *in vivo*. The CBWPD showed strong correlations with standard BMD ($R^2 = 0.75$) and T score ($R^2 = 0.59$), as well as a moderate correlation with FRAX score ($R^2 = 0.48$). High AUC values (≥ 0.84 using QCT as reference, ≥ 0.76 using DXA as reference) obtained from ROC analysis demonstrated that the CBWPD was capable of discriminating between the three subject cohorts which included normal subjects, patients with osteopenia, and patients with OP. Moreover, the CBWPD had stronger correlations with BMD, T score, and FRAX score than BMFF did, and also performed better in cohort discrimination. This study demonstrates that the STAIR-

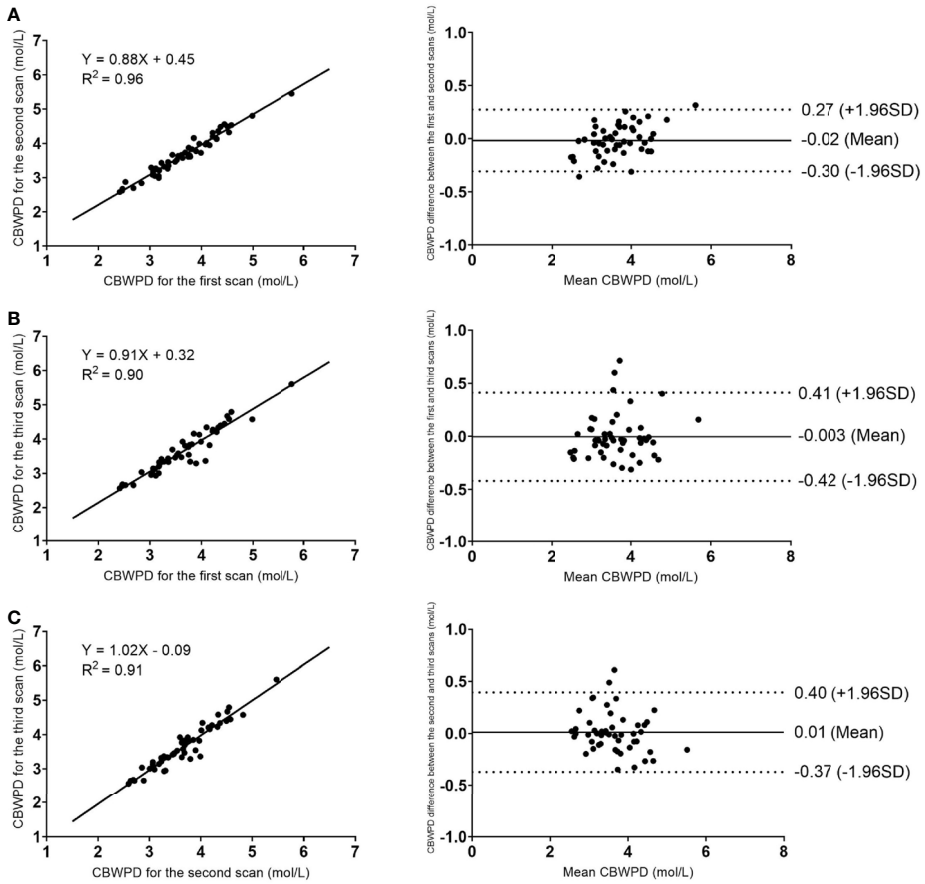

FIGURE 2 | Reproducibility results of the STAIR-UTE Cones scans: linear regression (left column) and Bland–Altman analysis (right column) plots of the STAIR-UTE measured CBWPDs between the first and the second scans **(A)**, between the first and the third scans **(B)**, and between the second and the third scans **(C)**. Dotted lines in the Bland–Altman difference plots (right column) demarcate 1.96 standard deviations of the mean difference.

UTE-measured CBWPD is a promising biomarker to be used in clinical practice for assessment of bone quality and fracture risk.

The STAIR-UTE sequence used in this study is able to efficiently suppress all the long T_2 components in trabecular bone, including marrow fat and free water, and selectively image CBW. As can be seen in Ref. 17, numerical simulation results showed that, when a sufficiently short TR was used, the STAIR-UTE sequence achieved efficient signal suppression for long T_2 tissues with a wide range of T_{1s}. When a minimal TR (i.e., TR = 150 ms, restricted by SAR limitation) was used in the STAIR-UTE sequence on a clinical 3T scanner, only short T_2 signals were detected in the *in vivo* vertebral bone with a T_2* of 0.31 ms, clearly demonstrating the technical feasibility of the STAIR-UTE sequence in sufficient suppression of all the long T_2 signals. At the long T_2 signal null point (TI_{null}), signal from the short T_2 component (i.e., the CBW) can be efficiently detected by the 3D UTE Cones sequence with a minimal TE of 32 μs. In addition, the relatively low STAIR-UTE resolution used in this study was able to increase the SNR of short T_2 imaging and thereby improve the accuracy of CBW quantification.

Approximately 40-50% of women and 13-22% of men are at risk of osteoporotic fracture after the age of 50, and major osteoporotic fractures result in substantial morbidity and mortality (2, 36). Early assessment of bone quality and fracture risk is crucial for effective intervention or treatment. The collagen matrix makes a crucial contribution to the mechanical properties of bone by imparting tensile strength and elasticity (37). However, changes in the organic matrix are inaccessible to DXA, QCT, and even clinical MRI due to the technical limitations of these imaging modalities (14, 15).

The STAIR-UTE MRI technique is capable of indirectly accessing properties in the collagen matrix by performing measurements of the CBWPD in trabecular bone (17). The CBW provides important information regarding the collagen density and hydration state of the organic matrix to which it is bound. In this way, CBW quantification could act as a possible surrogate for assessment of the collagen matrix.

It is known that mineral crystals are scattered in the gaps between continuous collagen fibers (38), suggesting that the quantity of collagen fibers may be related to the BMD. In our

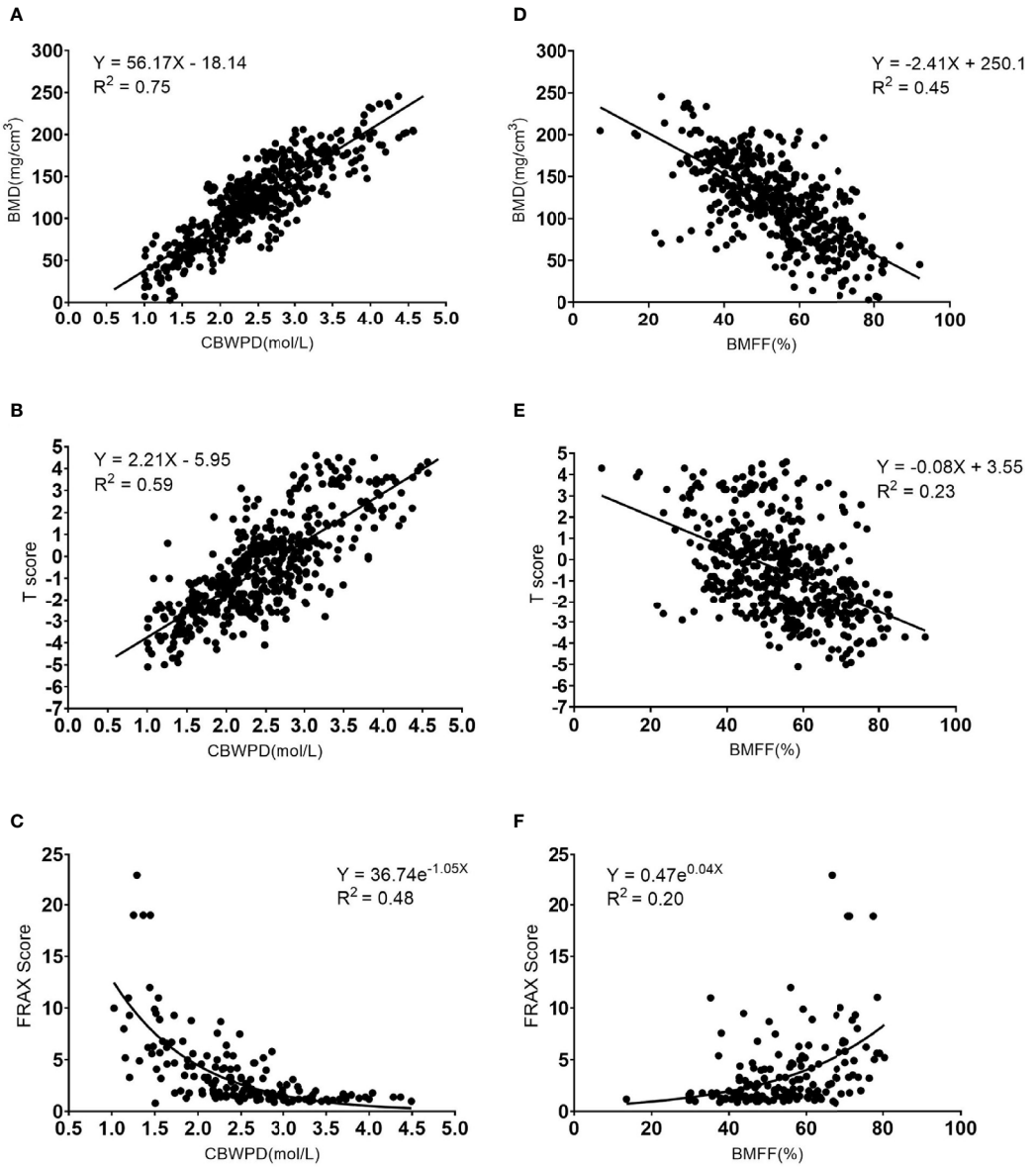

FIGURE 3 | Correlation curves and scatter plots for the measurements between **(A)** collagen bound water proton density (CBWPD) and bone mineral density (BMD), **(B)** CBWPD and T score, **(C)** CBWPD and Fracture Risk Assessment Tool (FRAX) score, **(D)** bone marrow fat fraction (BMFF) and BMD, **(E)** BMFF and T score, and **(F)** BMFF and FRAX score.

trabecular bone study, the strong positive correlation between CBWPD and BMD was in line with the findings in previous cortical bone studies as it demonstrated that both the bone mineral and organic matrix were decreased in OP (39–41).

A moderate correlation between the CBWPD and FRAX score demonstrated that the STAIR-UTE-measured CBWPD has the potential to be useful in assessing fracture risk or could even be combined into the FRAX score calculation for further improved risk assessment. Another advantage of the STAIR-UTE MRI technique is the absence of ionizing radiation which may make it a preferable technique for regular examinations (an important approach for early detection of bone loss) or longitudinal studies that monitor patient response to treatment.

Many studies have shown increased marrow fat during OP (42–47). In our study, it was clear that CBWPD was more sensitive to the changes in bone than BMFF, evidenced by the CBWPD's improved correlations with BMD, T score, and FRAX score over BMFF, as well as its superior performance in terms of cohort discrimination. CBWPD's increased sensitivity to bone changes is not surprising because BMFF does not reveal true bone loss: some patients with normal BMFF have been reported to have bone loss or abnormal bone mineralization (48).

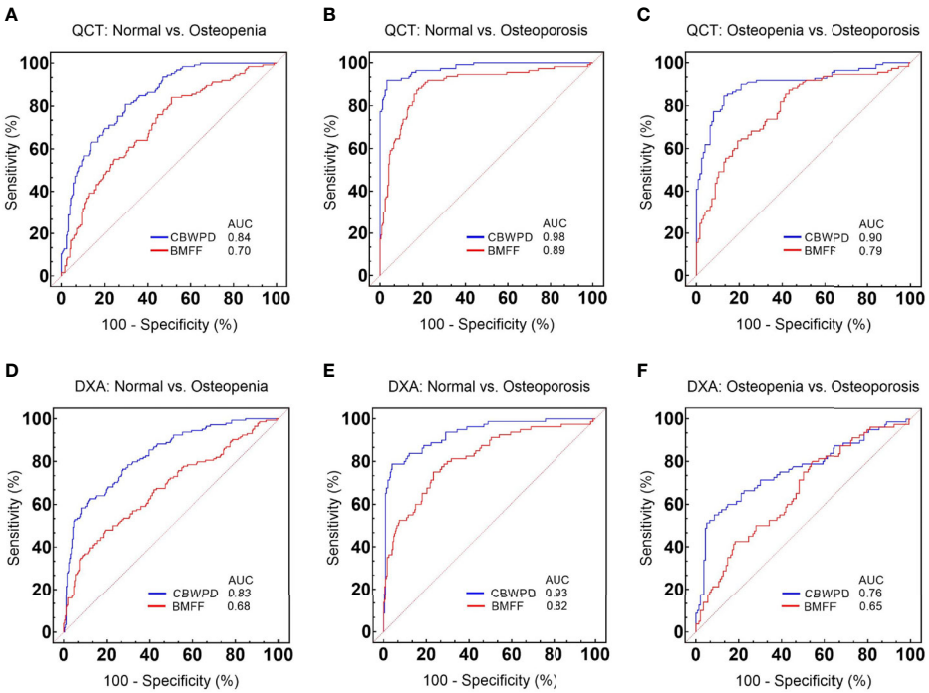

FIGURE 4 | Receiver operating characteristic (ROC) curves and corresponding area under the curve (AUC) values of collagen bound water proton density ($CBWPD^{QCT}$) and bone marrow fat fraction ($BMFF^{QCT}$) between **(A)** normal and osteoporosis, **(B)** normal and osteopenia, and **(C)** osteopenia and osteoporosis, with quantitative computed tomography (QCT) as reference standard. ROC curves and corresponding AUC values of $CBWPD^{DXA}$ and $BMFF^{DXA}$ between **(D)** normal and osteoporosis, **(E)** normal and osteopenia, and **(F)** osteopenia and osteoporosis, with dual-energy X-ray absorptiometry (DXA) as reference standard.

TABLE 2 | Performance of the $CBWPD^{QCT}$ and $BMFF^{QCT}$ in discrimination between three cohorts of normal subjects, patients with osteopenia, and patients with osteoporosis, with QCT as reference standard.

	$CBWPD^{QCT}$			$BMFF^{QCT}$		
	Normal vs. osteopenia	**Normal vs. osteoporosis**	**Osteopenia vs. osteoporosis**	**Normal vs. osteopenia**	**Normal vs. osteoporosis**	**Osteopenia vs. osteoporosis**
AUC (95%CI)	0.839 (0.799, 0.879)	0.978 (0.963, 0.992)	0.902 (0.861, 0.944)	0.704 (0.649, 0.759)	0.894 (0.854, 0.933)	0.786 (0.728, 0.845)
Sensitivity (95%CI)	0.705 (0.649, 0.762)	0.968 (0.946, 0.990)	0.872 (0.813, 0.931)	0.840 (0.776, 0.904)	0.882 (0.821, 0.942)	0.636 (0.546, 0.726)
Specificity (95%CI)	0.808 (0.739, 0.877)	0.918 (0.867, 0.969)	0.845 (0.778, 0.913)	0.490 (0.428, 0.552)	0.821 (0.773, 0.868)	0.808 (0.739, 0.877)
ACC (95%CI)	0.739 (0.738, 0.740)	0.953 (0.953, 0.953)	0.860 (0.859, 0.861)	0.606 (0.605, 0.608)	0.839 (0.839, 0.840)	0.728 (0.726, 0.729)
PPV (95%CI)	0.881 (0.836, 0.925)	0.964 (0.941, 0.987)	0.865 (0.805, 0.925)	0.451 (0.387, 0.515)	0.683 (0.607, 0.760)	0.745 (0.657, 0.833)
NPV (95%CI)	0.577 (0.504, 0.650)	0.927 (0.878, 0.976)	0.853 (0.787, 0.920)	0.860 (0.803, 0.917)	0.941 (0.909, 0.972)	0.716 (0.642, 0.791)

CBWPD, collagen bound water proton density; BMFF, bone marrow fat fraction; QCT, quantitative computed tomography; AUC, area under curve; ACC, Accuracy; PPV, Positive Predictive Value; NPV, Negative Predictive Value; CI, Confidence Interval.

There are several limitations in this study. First, the scan time of the CBWPD measurement protocol was relatively long (around 12 min in total) compared to clinical sequences. Advanced image reconstruction methods such as compressed sensing or deep learning could be incorporated to accelerate the scan with comparable image quality (49, 50) in the future. Second, we did not follow up on the fracture rate of these patients for 5-10 years, though such a long-term study will be completed in future work. The longitudinal study would be valuable in further validating the proposed technique and in

TABLE 3 | Performance of the $CBWPD^{DXA}$ and $BMFF^{DXA}$ in discrimination between three cohorts of normal subjects, patients with osteopenia, and patients with osteoporosis, with DXA as reference standard.

	$CBWPD^{DXA}$			$BMFF^{DXA}$		
	Normal vs. osteopenia	**Normal vs. osteoporosis**	**Osteopenia vs. osteoporosis**	**Normal vs. osteopenia**	**Normal vs. osteoporosis**	**Osteopenia vs. osteoporosis**
AUC (95%CI)	0.832 (0.792, 0.873)	0.930 (0.897, 0.963)	0.761 (0.690, 0.831)	0.676 (0.619, 0.732)	0.816 (0.760, 0.872)	0.655 (0.580, 0.729)
Sensitivity (95% CI)	0.882 (0.843, 0.921)	0.958 (0.934, 0.982)	0.917 (0.872, 0.962)	0.479 (0.398, 0.561)	0.750 (0.655, 0.845)	0.800 (0.712, 0.888)
Specificity (95% CI)	0.625 (0.546, 0.704)	0.788 (0.698, 0.877)	0.550 (0.441, 0.659)	0.809 (0.762, 0.857)	0.763 (0.712, 0.815)	0.458 (0.377, 0.540)
ACC (95%CI)	0.791 (0.790, 0.791)	0.918 (0.918, 0.919)	0.786 (0.784, 0.787)	0.692 (0.691, 0.693)	0.760 (0.759, 0.761)	0.580 (0.578, 0.582)
PPV (95%CI)	0.811 (0.765, 0.856)	0.937 (0.907, 0.966)	0.786 (0.724, 0.848)	0.580 (0.491, 0.669)	0.492 (0.403, 0.581)	0.451 (0.369, 0.533)
NPV (95%CI)	0.744 (0.666, 0.822)	0.851 (0.770, 0.932)	0.786 (0.678, 0.893)	0.739 (0.688, 0.790)	0.909 (0.871, 0.947)	0.805 (0.719, 0.891)

CBWPD, collagen bound water proton density; BMFF, bone marrow fat fraction; DXA, dual-energy X-ray absorptiometry; AUC, area under curve; ACC, Accuracy; PPV, Positive Predictive Value; NPV, Negative Predictive Value; CI, Confidence Interval.

providing information about collagen matrix changes that accompany aging.

In conclusion, the STAIR-UTE-measured CBWPD is a promising biomarker for evaluation of the bone changes in OP and of osteoporotic fracture risk.

DATA AVAILABILITY STATEMENT

The original contributions presented in the study are included in the article/supplementary material. Further inquiries can be directed to the corresponding author.

ETHICS STATEMENT

The studies involving human participants were reviewed and approved by ethical approval from the institutional review board of The Fifth Affiliated Hospital of Sun Yat-Sen University. The patients/participants provided their written informed consent to participate in this study.

AUTHOR CONTRIBUTIONS

JL, S-LL, and Y-JM conceived the study. WL, X-JC, J-XF, LY, P-HH, Z-HS, and HL collected the data. JL, Y-JM, and Y-TL analyzed the data. All the authors collaborated in interpretation of the results and drafting and revision of the report. All authors contributed to the article and approved the submitted version.

FUNDING

This work was supported by the National Natural Science Foundation of China (Grant Nos. 82172053).

REFERENCES

1. Khosla S, Hofbauer LC. Osteoporosis Treatment: Recent Developments and Ongoing Challenges. *Lancet Diabetes Endocrinol* (2017) 5(11):898–907. doi: 10.1016/S2213-8587(17)30188-2
2. Roux C, Briot K. The Crisis of Inadequate Treatment in Osteoporosis. *Lancet Rheumatol* (2020) 2(2):e110–9. doi: 10.1016/S2665-9913(19)30136-5
3. Pisani P, Renna MD, Conversano F, Casciaro E, Di Paola M, Quarta E, et al. Major Osteoporotic Fragility Fractures: Risk Factor Updates and Societal Impact. *World J Orthop* (2016) 7(3):171–81. doi: 10.5312/wjo.v7.i3.171
4. Hennemann A. Osteoporosis Prevention, Diagnosis, and Therapy. *Jama* (2001) 285(6):785–95. doi: 10.1001/jama.285.6.785
5. Bandirali M, Lanza E, Messina C, Sconfienza LM, Brambilla R, Maurizio R, et al. Dose Absorption in Lumbar and Femoral Dual Energy X-Ray Absorptiometry Examinations Using Three Different Scan Modalities: An Anthropomorphic Phantom Study. *J Clin Densitom* (2013) 16(3):279–82. doi: 10.1016/j.jocd.2013.02.005
6. Blake GM, Fogelman I. The Role of DXA Bone Density Scans in the Diagnosis and Treatment of Osteoporosis. *Postgrad Med J* (2007) 83(982):509–17. doi: 10.1136/pgmj.2007.057505
7. Wehrli FW, Saha PK, Gomberg BR, Song HK, Snyder PJ, Benito M, et al. Role of Magnetic Resonance for Assessing Structure and Function of Trabecular Bone. *Top Magn Reson Imaging* (2002) 13(5):335–55. doi: 10.1097/00002142-200210000-00005
8. Mehta SS, Oz OK, Antich PP. Bone Elasticity and Ultrasound Velocity Are Affected by Subtle Changes in the Organic Matrix. *J Bone Miner Res* (1998) 13(1):114–21. doi: 10.1359/jbmr.1998.13.1.114
9. Paschalis EP, Mendelsohn R, Boskey AL. Infrared Assessment of Bone Quality: A Review. *Clin Orthop Relat Res* (2011) 469(8):2170–8. doi: 10.1007/s11999-010-1751-4
10. Nyman JS, Gorochow LE, Adam Horch R, Uppuganti S, Zein-Sabatto A, Manhard MK, et al. Partial Removal of Pore and Loosely Bound Water by Low-Energy Drying Decreases Cortical Bone Toughness in Young and Old Donors. *J Mech Behav BioMed Mater* (2013) 22:136–45. doi: 10.1016/j.jmbbm.2012.08.013
11. Unal M, Yang S, Akkus O. Molecular Spectroscopic Identification of the Water Compartments in Bone. *Bone* (2014) 67:228–36. doi: 10.1016/j.bone.2014.07.021
12. Samuel J, Sinha D, Zhao JC, Wang X. Water Residing in Small Ultrastructural Spaces Plays a Critical Role in the Mechanical Behavior of Bone. *Bone* (2014) 59:199–206. doi: 10.1016/j.bone.2013.11.018
13. Ma YJ, Tadros A, Du J, Chang EY. Quantitative Two-Dimensional Ultrashort Echo Time Magnetization Transfer (2D UTE-MT) Imaging of Cortical Bone. *Magn Reson Med* (2018) 79(4):1941–9. doi: 10.1002/mrm.26846
14. Hodgson RJ, Evans R, Wright P, Grainger AJ, O'Connor PJ, Helliwell P, et al. Quantitative Magnetization Transfer Ultrashort Echo Time Imaging of the Achilles Tendon. *Magn Reson Med* (2011) 65(5):1372–6. doi: 10.1002/mrm.22715
15. Ma YJ, Chang EY, Bydder GM, Du J. Can Ultrashort-TE (UTE) MRI Sequences on a 3-T Clinical Scanner Detect Signal Directly From Collagen

Protons: Freeze-Dry and D2 O Exchange Studies of Cortical Bone and Achilles Tendon Specimens. *NMR BioMed* (2016) 29(7):912–7. doi: 10.1002/nbm.3547
16. Loegering IF, Denning SC, Johnson KM, Liu F, Lee KS, Thelen DG. Ultrashort Echo Time (UTE) Imaging Reveals a Shift in Bound Water That Is Sensitive to Sub-Clinical Tendinopathy in Older Adults. *Skeletal Radiol* (2021) 50(1):107–13. doi: 10.1007/s00256-020-03538-1
17. Ma YJ, Chen Y, Li L, Cai Z, Wei Z, Jerban S, et al. Trabecular Bone Imaging Using a 3D Adiabatic Inversion Recovery Prepared Ultrashort TE Cones Sequence at 3T. *Magn Reson Med* (2020) 83(5):1640–51. doi: 10.1002/mrm.28027
18. Du J, Diaz E, Carl M, Bae W, Chung CB, Bydder GM. Ultrashort Echo Time Imaging With Bicomponent Analysis. *Magn Reson Med* (2012) 67(3):645–9. doi: 10.1002/mrm.23047
19. Du J, Carl M, Bydder M, Takahashi A, Chung CB, Bydder GM. Qualitative and Quantitative Ultrashort Echo Time (UTE) Imaging of Cortical Bone. *J Magn Reson* (2010) 207(2):304–11. doi: 10.1016/j.jmr.2010.09.013
20. Diaz E, Chung CB, Bae WC, Statum S, Znamirowski R, Bydder GM, et al. Ultrashort Echo Time Spectroscopic Imaging (UTESI): An Efficient Method for Quantifying Bound and Free Water. *NMR BioMed* (2012) 25(1):161–8. doi: 10.1002/nbm.1728
21. Biswas R, Bae W, Diaz E, Masuda K, Chung CB, Bydder GM, et al. Ultrashort Echo Time (UTE) Imaging With Bi-Component Analysis: Bound and Free Water Evaluation of Bovine Cortical Bone Subject to Sequential Drying. *Bone* (2012) 50(3):749–55. doi: 10.1016/j.bone.2011.11.029
22. Horch RA, Gochberg DF, Nyman JS, Does MD. Clinically Compatible MRI Strategies for Discriminating Bound and Pore Water in Cortical Bone. *Magn Reson Med* (2012) 68(6):1774–84. doi: 10.1002/mrm.24186
23. Manhard MK, Horch RA, Harkins KD, Gochberg DF, Nyman JS, Does MD. Validation of Quantitative Bound- and Pore-Water Imaging in Cortical Bone. *Magn Reson Med* (2014) 71(6):2166–71. doi: 10.1002/mrm.24870
24. Horch RA, Nyman JS, Gochberg DF, Dortch RD, Does MD. Characterization of 1H NMR Signal in Human Cortical Bone for Magnetic Resonance Imaging. *Magn Reson Med* (2010) 64(3):680–7. doi: 10.1002/mrm.22459
25. Horch RA, Gochberg DF, Nyman JS, Does MD. Non-Invasive Predictors of Human Cortical Bone Mechanical Properties: T(2)-Discriminated H NMR Compared With High Resolution X-Ray. *PloS One* (2011) 6(1):e16359. doi: 10.1371/journal.pone.0016359
26. Nyman JS, Ni Q, Nicolella DP, Wang X. Measurements of Mobile and Bound Water by Nuclear Magnetic Resonance Correlate With Mechanical Properties of Bone. *Bone* (2008) 42(1):193–9. doi: 10.1016/j.bone.2007.09.049
27. Majumdar S. Magnetic Resonance Imaging of Trabecular Bone Structure. *Top Magn Reson Imaging* (2002) 13(5):323–34. doi: 10.1097/00002142-200210000-00004
28. Amstrup AK, Jakobsen NF, Moser E, Sikjaer T, Mosekilde L, Rejnmark L. Association Between Bone Indices Assessed by DXA, HR-pQCT and QCT Scans in Post-Menopausal Women. *J Bone Miner Metab* (2016) 34(6):638–45. doi: 10.1007/s00774-015-0708-9
29. Bergot C, Laval-Jeantet AM, Hutchinson K, Dautraix I, Caulin F, Genant HK. A Comparison of Spinal Quantitative Computed Tomography With Dual Energy X-Ray Absorptiometry in European Women With Vertebral and Nonvertebral Fractures. *Calcif Tissue Int* (2001) 68(2):74–82. doi: 10.1007/bf02678144
30. Wehrli FW, Song HK, Saha PK, Wright AC. Quantitative MRI for the Assessment of Bone Structure and Function. *NMR BioMed* (2006) 19 (7):731–64. doi: 10.1002/nbm.1066
31. Marcon M, Keller D, Wurnig MC, Eberhardt C, Weiger M, Eberli D, et al. Separation of Collagen-Bound and Porous Bone Water Transverse Relaxation in Mice: Proposal of a Multi-Step Approach. *NMR BioMed* (2016) 29(7):866–72. doi: 10.1002/nbm.3533
32. Wu Y, Guo Z, Fu X, Wu J, Gao J, Zeng Q, et al. The Study Protocol for the China Health Big Data (China Biobank) Project. *Quant Imaging Med Surg* (2019) 9(6):1095–102. doi: 10.21037/qims.2019.06.16
33. Kanis JA. Assessment of Fracture Risk and Its Application to Screening for Postmenopausal Osteoporosis: Synopsis of a WHO Report. WHO Study Group. *Osteoporos Int* (1994) 4(6):368–81. doi: 10.1007/bf01622200
34. Yu H, McKenzie CA, Shimakawa A, Vu AT, Brau AC, Beatty PJ, et al. Multiecho Reconstruction for Simultaneous Water-Fat Decomposition and T2* Estimation. *J Magn Reson Imaging* (2007) 26(4):1153–61. doi: 10.1002/jmri.21090
35. Engelke K, Adams JE, Armbrecht G, Augat P, Bogado CE, Bouxsein ML, et al. Clinical Use of Quantitative Computed Tomography and Peripheral Quantitative Computed Tomography in the Management of Osteoporosis in Adults: The 2007 ISCD Official Positions. *J Clin Densitom* (2008) 11 (1):123–62. doi: 10.1016/j.jocd.2007.12.010
36. Pickhardt PJ, Lee LJ, del Rio AM, Lauder T, Bruce RJ, Summers RM, et al. Simultaneous Screening for Osteoporosis at CT Colonography: Bone Mineral Density Assessment Using MDCT Attenuation Techniques Compared With the DXA Reference Standard. *J Bone Miner Res* (2011) 26(9):2194–203. doi: 10.1002/jbmr.428
37. Seifert AC, Li C, Rajapakse CS, Bashoor-Zadeh M, Bhagat YA, Wright AC, et al. Bone Mineral (31)P and Matrix-Bound Water Densities Measured by Solid-State (31)P and (1)H MRI. *NMR BioMed* (2014) 27(7):739–48. doi: 10.1002/nbm.3107
38. Ritchie RO, Buehler MJ, Hansma P. Plasticity and Toughness in Bone. *Phys Today* (2009) 62(6):41–7. doi: 10.1063/1.3156332
39. Jerban S, Lu X, Dorthe EW, Alenezi S, Ma Y, Kakos L, et al. Correlations of Cortical Bone Microstructural and Mechanical Properties With Water Proton Fractions Obtained From Ultrashort Echo Time (UTE) MRI Tricomponent T2* Model. *NMR BioMed* (2020) 33(3):e4233. doi: 10.1002/nbm.4233
40. Seifert AC, Li C, Wehrli SL, Wehrli FW. A Surrogate Measure of Cortical Bone Matrix Density by Long T2 -Suppressed MRI. *J Bone Miner Res* (2015) 30 (12):2229–38. doi: 10.1002/jbmr.2580
41. Ong HH, Wright AC, Wehrli FW. Deuterium Nuclear Magnetic Resonance Unambiguously Quantifies Pore and Collagen-Bound Water in Cortical Bone. *J Bone Miner Res* (2012) 27(12):2573–81. doi: 10.1002/jbmr.1709
42. He J, Fang H, Li X. Vertebral Bone Marrow Fat Content in Normal Adults With Varying Bone Densities at 3T Magnetic Resonance Imaging. *Acta Radiol* (2019) 60(4):509–15. doi: 10.1177/0284185118786073
43. Li CJ, Cheng P, Liang MK, Chen YS, Lu Q, Wang JY, et al. MicroRNA-188 Regulates Age-Related Switch Between Osteoblast and Adipocyte Differentiation. *J Clin Invest* (2015) 125(4):1509–22. doi: 10.1172/jci77716
44. Griffith JF, Yeung DK, Tsang PH, Choi KC, Kwok TC, Ahuja AT, et al. Compromised Bone Marrow Perfusion in Osteoporosis. *J Bone Miner Res* (2008) 23(7):1068–75. doi: 10.1359/jbmr.080233
45. Kim H, Taksali SE, Dufour S, Befroy D, Goodman TR, Petersen KF, et al. Comparative MR Study of Hepatic Fat Quantification Using Single-Voxel Proton Spectroscopy, Two-Point Dixon and Three-Point IDEAL. *Magn Reson Med* (2008) 59(3):521–7. doi: 10.1002/mrm.21561
46. Aoki T, Yamaguchi S, Kinoshita S, Hayashida Y, Korogi Y. Quantification of Bone Marrow Fat Content Using Iterative Decomposition of Water and Fat With Echo Asymmetry and Least-Squares Estimation (IDEAL): Reproducibility, Site Variation and Correlation With Age and Menopause. *Br J Radiol* (2016) 89(1065):20150538. doi: 10.1259/bjr.20150538
47. Kanis JA, Johnell O, Oden A, Johansson H, McCloskey E. FRAX and the Assessment of Fracture Probability in Men and Women From the UK. *Osteoporos Int* (2008) 19(4):385–97. doi: 10.1007/s00198-007-0543-5
48. Griffith JF, Yeung DK, Antonio GE, Lee FK, Hong AW, Wong SY, et al. Vertebral Bone Mineral Density, Marrow Perfusion, and Fat Content in Healthy Men and Men With Osteoporosis: Dynamic Contrast-Enhanced MR Imaging and MR Spectroscopy. *Radiology* (2005) 236(3):945–51. doi: 10.1148/radiol.2363041425
49. Lustig M, Donoho D, Pauly JM. Sparse MRI: The Application of Compressed Sensing for Rapid MR Imaging. *Magn Reson Med* (2007) 58(6):1182–95. doi: 10.1002/mrm.21391
50. Zhu B, Liu JZ, Cauley SF, Rosen BR, Rosen MS. Image Reconstruction by Domain-Transform Manifold Learning. *Nature* (2018) 555(7697):487–92. doi: 10.1038/nature25988

Conflict of Interest: Author Y-TL was employed by GE Healthcare.

The remaining authors declare that the research was conducted in the absence of any commercial or financial relationships that could be construed as a potential conflict of interest.

this article, or claim that may be made by its manufacturer, is not guaranteed or endorsed by the publisher.

frontiers in Endocrinology

ORIGINAL RESEARCH
published: 22 February 2022
doi: 10.3389/fendo.2022.844351

Simultaneous Quantitative Susceptibility Mapping of Articular Cartilage and Cortical Bone of Human Knee Joint Using Ultrashort Echo Time Sequences

*Ming Zhang[1], Zhihui Li[2], Hanqi Wang[2], Tongtong Chen[2], Yong Lu[2], Fuhua Yan[2], Yuyao Zhang[3] and Hongjiang Wei[1]**

[1] School of Biomedical Engineering, Shanghai Jiao Tong University, Shanghai, China, [2] Department of Radiology, Ruijin Hospital, School of Medicine, Shanghai Jiao Tong University, Shanghai, China, [3] School of Information and Science and Technology, ShanghaiTech University, Shanghai, China

OPEN ACCESS

Edited by:
Bing Wu,
GE Healthcare, China

Reviewed by:
Aixia Sun,
Michigan State University, United States
Lihui Wang,
Guizhou University, China

****Correspondence:***
Hongjiang Wei
hongjiang.wei@sjtu.edu.cn

Specialty section:
This article was submitted to Bone Research, a section of the journal Frontiers in Endocrinology

Received: *28 December 2021*
Accepted: *31 January 2022*
Published: *22 February 2022*

Citation:
Zhang M, Li Z, Wang H, Chen T, Lu Y, Yan F, Zhang Y and Wei H (2022) Simultaneous Quantitative Susceptibility Mapping of Articular Cartilage and Cortical Bone of Human Knee Joint Using Ultrashort Echo Time Sequences. Front. Endocrinol. 13:844351. doi: 10.3389/fendo.2022.844351

Background: It is of great clinical importance to assess the microstructure of the articular cartilage and cortical bone of the human knee joint. While quantitative susceptibility mapping (QSM) is a promising tool for investigating the knee joint, however, previous QSM studies using conventional gradient recalled echo sequences or ultrashort echo time (UTE) sequences only focused on mapping the magnetic susceptibility of the articular cartilage or cortical bone, respectively. Simultaneously mapping the underlying susceptibilities of the articular cartilage and cortical bone of human *in vivo* has not been explored and reported.

Method: Three-dimensional multi-echo radial UTE sequences with the shortest TE of 0.07 msec and computed tomography (CT) were performed on the bilateral knee joints of five healthy volunteers for this prospective study. UTE-QSM was reconstructed from the local field map after water-fat separation and background field removal. Spearman's correlation analysis was used to explore the relationship between the magnetic susceptibility and CT values in 158 representative regions of interest of cortical bone.

Result: The susceptibility properties of the articular cartilage and cortical bone were successfully quantified by UTE-QSM. The laminar structure of articular cartilage was characterized by the difference of susceptibility value in each layer. Susceptibility was mostly diamagnetic in cortical bone. A significant negative correlation ($r=-0.43$, $p<0.001$) between the susceptibility value and CT value in cortical bone was observed.

Conclusion: UTE-QSM enables simultaneous susceptibility mapping of the articular cartilage and cortical bone of human *in vivo*. Good association between susceptibility and CT values in cortical bone suggests the potential of UTE-QSM for bone mapping for further clinical application.

Keywords: quantitative susceptibility mapping, ultrashort echo time, articular cartilage, cortical bone, computed tomography

INTRODUCTION

Cartilage and bone, providing stiffness and strength, are two fundamental knee joint structures. Articular cartilage degradation is regarded as a typical feature involved in the development of osteoarthritis (OA) (1). Bone tissues consist of two types, cortical bone and cancellous bone. Cortical bone plays a key role in the mechanical competence of bone, which occupies approximately 80% of the total bone mass (2) and accounts for 80% of all sites where bone fractures occur (3, 4). Therefore, a useful tool to noninvasively investigate the microstructure of the articular cartilage and cortical bone is of great importance for clinical evaluation.

Computed tomography (CT) has been widely used in clinical practice for bone mapping. However, CT involves ionizing radiation and exhibits poor contrast for soft tissue structures, e.g., the cartilage. Magnetic resonance imaging (MRI) can overcome the disadvantages of the X-ray-based technique and offers superior image contrast in soft tissues. However, there are signal voids in regions (e.g., the cortical bone) (5) with rapid signal decay (0.1~1 msec) (6) on MRI images using conventional sequences with echo time (TE) of a few msec or longer. The MRI-based ultrashort echo time (UTE) sequences, which collect signals immediately after pulse excitation resulting in a very short TE (typically less than 0.1 msec), provide the feasibility for direct cortical bone imaging (7–9).

Quantitative susceptibility mapping (QSM) is a post-processing MRI technique that quantitatively estimates the underlying magnetic susceptibilities of tissues, typically using gradient recalled echo (GRE) sequences (10, 11). Since magnetic susceptibility is an intrinsic physical property of tissue, this unique contrast mechanism has made QSM a promising tool for tissue quantification and disease detection, such as for early brain development (12), brain aging (13, 14) and diseased brain (15, 16). Recently, researchers have applied QSM in the musculoskeletal system (17–20). However, studies using GRE sequences (GRE-QSM) failed in mapping the susceptibility of cortical bone due to signal void and low signal-to-noise ratio (SNR) at a typical TE longer than one msec. Therefore, the cortical bone regions were usually masked out for QSM processing due to unreliable susceptibility values measured from the local field map (17). Luckily, benefiting from the ability of the UTE sequence for detecting rapidly decayed signals, UTE-based QSM (UTE-QSM) could be capable of quantifying the susceptibility property of cortical bone. However, related studies mainly focused on imaging the cortical bone and didn't quantify soft tissue susceptibility. UTE-QSM has not been applied to explore the articular cartilage of human *in vivo* (21, 22). Simultaneous susceptibility mapping of the articular cartilage and cortical bone with a single MRI scan is still lacking and highly needed.

In this study, we aimed to simultaneously quantify the magnetic susceptibilities of the articular cartilage and cortical bone of the human knee joint using UTE-QSM. To explore the clinical potentials of UTE-QSM, the relationship between the susceptibility and CT values in cortical bone was also assessed.

MATERIALS AND METHODS

Subjects

This study was approved by the Human Ethics Committee of Shanghai Jiao Tong University. Five healthy young volunteers (4 males, mean age of 23.6 years old) were included in this study with both MRI and low dose CT examinations on bilateral knee joints. No history of knee injury from the participants was reported. All participants were informed of the experiment protocol and informed consent was provided from each subject. The time interval between MRI and CT examinations was within a month.

CT Examination

The low dose CT scan (volume CT dose: 6.74 mGy, dose length product: 132.8 mGy*cm) for each participant was performed using a clinical CT scanner (SOMATOM Definition AS, Siemens Healthcare, Erlangen, Germany). The scanning parameters were: X-ray tube voltage of 120 kV, tube current of 100 mA; slice thickness of 0.7 mm, 252 slices; matrix size of 512×512, spatial resolution of 0.85×0.85 mm^2.

MRI Examination

Each subject has their right and left knee joints scanned on a 3 Tesla MRI scanner (uMR 790, United Image Healthcare, Shanghai, China). For the three-dimensional UTE sequence, a non-selective hard pulse was used to excite the whole knee joint. The free induced decay (FID) signal (i.e., ultrashort TE signal) and gradient recalled echoes (i.e., normal TE signals) were collected in the center-out and center-in radial trajectories, respectively (23). Two continuous UTE sessions, each with one ultrashort TE and two normal TEs, were taken for imaging each limb of the participants without repositioning, resulting in 6 TEs in total. TEs of the first UTE scan, 0.07/2.24/3.55 msec; TEs of the second UTE scan, 0.1/2.8/4.6 msec. Other parameters for UTE were: axial view; repetition time, 10 msec; flip angle, 8°; field of view (FOV), 180×160×144 mm^3; image matrix, 208×184×160; spatial resolution, 0.9×0.9×0.9 mm^3; spoke number, 40960; scan time, 7 min 6 sec per scan.

UTE Processing

The UTE raw data from the MRI scanner was sent to a high-performance workstation for processing. The density function was calculated to compensate for the measured signals due to the nonuniform radial sampling pattern (24). Nonuniform fast Fourier transform was applied for gridding to interpolate the data from radial spokes into Cartesian grids (25). Each channel of the UTE image was combined to generate four-dimensional complex-valued data. Subsequently, image registration was performed on the magnitude images to reduce the possible error induced by slight inter-scan motion during two separate UTE scans. The FMRIB's Linear Image Registration Tool (26, 27) with 6 degrees of freedom and a maximum rotation angle of 10° was used for registration. The transformation matrices were

automatically saved and applied to the real and imaginary parts of UTE data to bring two separate UTE complex-valued images into an identical space.

UTE-QSM Reconstruction

The water-fat separation method was applied to UTE images to eliminate the chemical shift effect due to the presence of fat in the knee joint, which could further hamper the susceptibility quantification due to the inaccurate field map estimation (28). The B_0 field map was derived during this procedure using the graph cut-based water-fat separation algorithm (29) with the conventional six fat peaks model on a slice-by-slice basis.

A binary mask was generated by thresholding the sum-of-squares of the UTE magnitude image (15% of the maximum intensity) to exclude the background. The V-SHARP (variable-kernel sophisticated harmonic artifact reduction for phase data) algorithm (30) was used to recover the local field map from the total field map. The susceptibility map was quantitatively reconstructed using STAR-QSM (streaking artifact reduction for QSM) (31).

To compare with UTE-QSM, QSM from normal TEs (normal TE-QSM) was also calculated without the use of 2 ultrashort TEs following the same pipeline for QSM reconstruction.

The magnetic susceptibility value was not referenced to any areas in this study. The magnetic susceptibility value was reported in parts per million (ppm).

CT Processing

For the CT image, the left and right knee joints were separated by dividing the whole CT image into two parts for following usages. The CT value was reported in Hounsfield units (HU). The background signal of the CT image was set to zero.

Regions of Interest (ROIs) of Cortical Bone

The multi-modal registration between UTE and CT images was achieved using Advanced Normalization Tools (32) with the rigid plus affine transformation, plus symmetric image normalization manner. The sum-of-squares of the UTE magnitude image served as the reference.

The ROIs of cortical bone were extracted from the UTE magnitude images on 12~26 consecutive slices of each limb using threshold binarization since there was a relatively low signal intensity in cortical bone. The ROIs were placed both on UTE magnitude images and corresponding aligned CT images to visually check the isolation accuracy using the open-source ITK-SNAP software (33). A total of 158 ROIs were obtained. The mean magnetic susceptibility and CT values were calculated for each ROI. Detailed values could be found in the **Supplementary Materials**.

Statistical Analysis

Spearman's correlation coefficient (r) was used to investigate the relationship between the mean susceptibility value and CT value in cortical bone using data from 158 ROIs. The threshold of p-value for statistical significance was set as 0.05. The correlation analysis was conducted using MATLAB (version 2019b, MathWorks, Natick, MA) with the "*corr*" function.

RESULTS

Figure 1 illustrates the segmented ROIs of cortical bone overlaid on their corresponding UTE magnitude images and warped CT images. The ROIs could finely match the anatomical structures of cortical bone, both on UTE and CT images.

Figure 2 shows the representative slices of UTE-QSM in articular cartilage and cortical bone in the sagittal and axial views of two subjects. Gradual magnetic susceptibility change from diamagnetic to paramagnetic was visible from the deep layer (near the subchondral bone) to the superficial layer of the articular cartilage. There was a clear susceptibility difference between the deep layer of articular cartilage (light blue, less diamagnetic) and the subchondral bone (dark blue, more diamagnetic), although the deep layer of articular cartilage was relatively thin (1~2 pixels) on UTE-QSM. UTE-QSM was generally diamagnetic in cortical bone.

Figure 3 compares the reconstructed susceptibility maps from UTE-QSM and normal TE-QSM in cortical bone and articular cartilage. As could be seen, UTE-QSM exhibited an

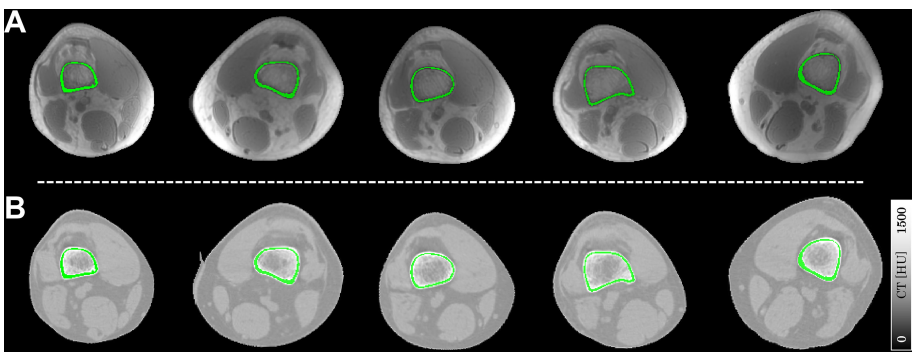

FIGURE 1 | Representative slices of ROIs of cortical bone (in green) overlaid on the UTE magnitude images **(A)** and registered CT images **(B)**. Each column represents a typical ROI from an individual subject in this study.

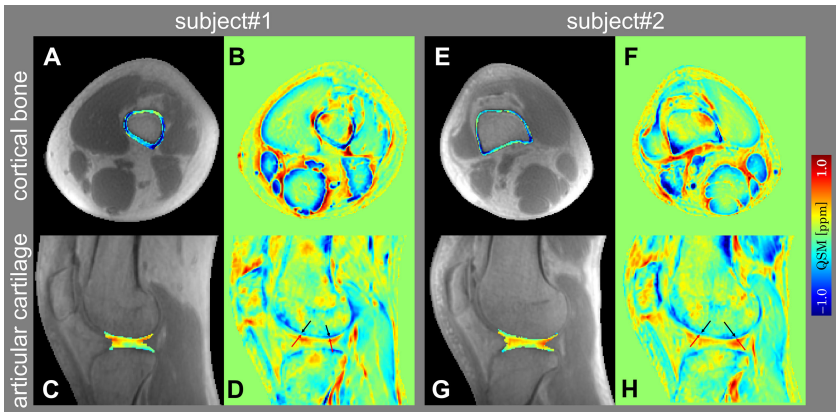

FIGURE 2 | Representative slices of UTE-QSM in cortical bone **(A, E)** and articular cartilage **(C, G)** overlaid on the UTE magnitude images in axial and sagittal views of two subjects. **(B, F)** and **(D, H)** are the color-coded magnetic susceptibility maps within the whole FOV corresponding to **(A, E)** and **(C, G)**. The black and red arrows in **(D, H)** point to the subchondral bone and deep layer of articular cartilage, respectively.

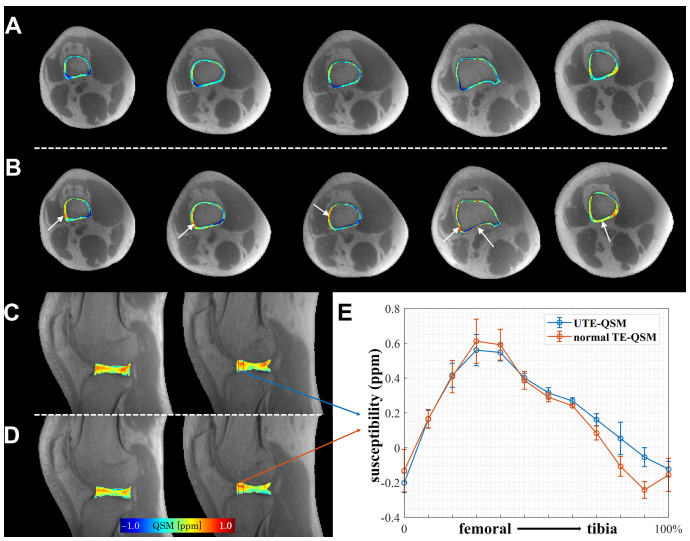

FIGURE 3 | Comparison of UTE-QSM and normal TE-QSM in cortical bone and articular cartilage. In cortical bone, UTE-QSM **(A)** was more homogenously diamagnetic than normal TE-QSM **(B)** (regions indicated by white arrows). In articular cartilage, the susceptibility contrasts between UTE-QSM **(C)** and normal TE-QSM **(D)** were similar. **(E)** shows the susceptibility profiles of UTE-QSM and normal TE-QSM from femoral to tibia cartilages in the selected red box (5×12 pixels) on one healthy volunteer. Data are presented as mean±standard deviation. Each column of cortical bone in **(A, B)** or articular cartilage in **(C, D)** represents a typical image slice from an individual subject in this study.

overall more homogeneous diamagnetic susceptibility in cortical bone. In contrast, certain regions exhibit paramagnetic susceptibilities in cortical bone on normal TE-QSM, resulting from inaccurate bone susceptibility quantification due to the uncertain phase measurement using relatively long TE. In articular cartilage, the susceptibility contrasts between UTE-QSM and normal TE-QSM were similar, based on the typical image slices and quantitative susceptibility profiles.

Figure 4 shows the result of correlation analysis of UTE-QSM versus CT values in cortical bone. A significant negative correlation ($r=-0.43$, $p<0.001$) between the mean susceptibility and CT values in cortical bone was observed.

DISCUSSION

In this study, we described the feasibility of UTE-QSM for simultaneous susceptibility mapping of the articular cartilage and cortical bone of the human knee joint *in vivo*. The laminar structure of articular cartilage was revealed on UTE-QSM,

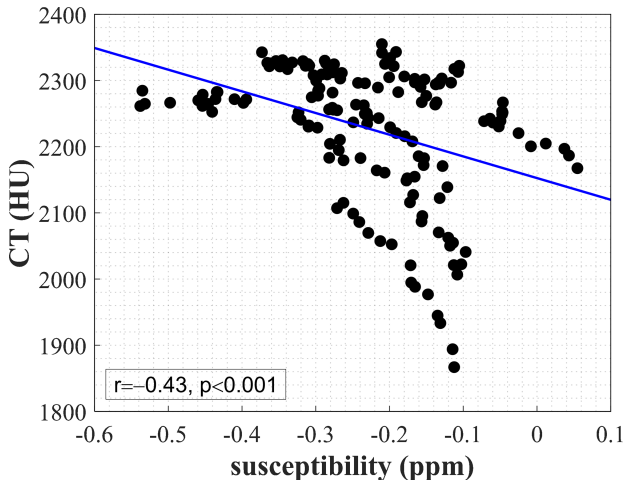

FIGURE 4 | A significant negative correlation (r=–0.43, p<0.001) between the mean susceptibility value and mean CT value in 158 ROIs of cortical bone from the bilateral knee joints of 5 subjects. The blue line was obtained from linear regression.

similar to conventional GRE-based QSM with long TE. Meanwhile, the susceptibility map in cortical bone could be accurately estimated from the collected phase data by UTE-QSM. The correlation study further demonstrated the potential of UTE-QSM to assess the cortical bone without radiation from CT.

We achieved simultaneous susceptibility mapping of the articular cartilage and cortical bone based on UTE-QSM. In previous studies using the GRE sequences, the bone regions were usually masked out to eliminate the unreliable phase measurement with low SNR. With the help of the UTE sequence, it was possible to use a larger FOV to include the whole knee joint into QSM reconstruction. The necessity of UTE sequence for cortical bone susceptibility mapping was evaluated from the comparison between UTE-QSM and normal TE-QSM. In previous studies, a high in-plane resolution with relatively thick slice thickness was often adopted (17, 21). The spatial resolution of UTE was set as 0.9 mm isotropic in this research because the cortical bone and articular cartilage were usually viewed in two different planes, the axial and the sagittal. Therefore, an isotropic spatial resolution was more preferred for simultaneous visualization.

The articular cartilage contains complex organizations. Generally, the articular cartilage can be divided into three layers, the deep, middle and superficial layers, with parallel, random and perpendicular collagen fiber orientations with respect to the subchondral bone (34). The varied collagen fiber arrangement in each layer was considered as the main susceptibility source on QSM images (17, 35). Wei et al. demonstrated the ability of GRE-QSM to reflect the collagen fiber organization in each layer of articular cartilage since the susceptibility of collagen fiber was orientation-dependent (17). A quantitative study demonstrated that the variation of magnetic susceptibility was associated with the stage of OA (36). Recent work further validated the feasibility of GRE-QSM for detecting the early microstructural change in degenerated cartilage by performing GRE-QSM on marathon runners after repetitive running (37). However, the susceptibility property using UTE-QSM in articular cartilage was not fully explored (38). We demonstrated that UTE-QSM also exhibited similar susceptibility differences at different depths of articular cartilage compared with GRE-QSM. This was mainly because that the susceptibility was expected to be TE-independent with adequate phase accumulation and SNR. However, slight differences were observed since there were intermediate steps for QSM reconstruction and possible errors could exist during these procedures due to imperfect mathematical or physical modeling (39). In this study, the deep layer of articular cartilage was relatively thinner on UTE-QSM compared with previous GRE-QSM studies, due to the limited image resolution.

In cortical bone, calcium is the primary biological source of magnetic susceptibility (40). Therefore, the susceptibility of cortical bone should be mostly diamagnetic, which was in agreement with our UTE-QSM result. The potential clinical application of UTE-QSM has been shown in several papers. For example, UTE-QSM was used for detecting hemosiderin deposition in patients with hemophilic arthropathy (22). The susceptibility was presented as high intensity in affected regions with high iron concentrations. Jerban et al. found a significant correlation between the UTE-QSM value and bone mineral density (BMD) measured by micro-CT on human cortical bone specimens, indicating that UTE-QSM could serve as an effective approach for BMD assessment (21). Although UTE-QSM could be a more general tool for knee joint mapping than GRE-QSM, more studies were still needed to fully explore the clinical value of UTE-QSM in the skeletal system, including but not limited to the knee joint (41, 42).

We found a significant correlation between the mean susceptibility and CT values in cortical bone. UTE-QSM may be considered as a potential substitution in imaging the cortical bone. There were a few studies that have attempted to explore the relationship between QSM and CT values. Dimov et al. found that UTE-QSM negatively correlated with CT value in diamagnetic susceptibility regions, such as in the trabecular and cortical areas on a porcine specimen (38). Oshima et al. conducted comprehensive experiments for assessing the general association between susceptibility and CT values with both phantom and human studies using GRE-QSM (43). The phantom experiment demonstrated that the CT value and susceptibility value positively and negatively correlated with $CaCO_3$ concentration, respectively (43). These studies above could support our result of the negative correlation between magnetic susceptibility and CT values in cortical bone.

This work has several limitations. First, the sample size was relatively small, which could lead to statistical bias in correlation analysis. Second, this study only conducted experiments on young and healthy subjects, making the study cohort fairly homogeneous in age and healthy conditions. The feasibility of UTE-QSM on patients with OA or osteoporosis should be

further involved to explore the potential applications of UTE-QSM for clinical purposes. Third, a higher isotropic image resolution could be better for visualizing the cortical bone and articular cartilage. Fourth, although the registration performances between two continuous UTE scans and between CT and UTE images were both visually checked and were reasonable, future studies should use quantitative metrics to evaluate the registration accuracy.

In conclusion, we demonstrated the feasibility of UTE-QSM for simultaneous susceptibility mapping of cortical bone and articular cartilage *in vivo*. UTE-QSM may serve as a valuable imaging tool for investigating the knee joint.

DATA AVAILABILITY STATEMENT

The original contributions presented in the study are included in the article/**Supplementary Material**. Further inquiries can be directed to the corresponding author.

ETHICS STATEMENT

The studies involving human participants were reviewed and approved by the Human Ethics Committee of Shanghai Jiao Tong University. The patients/participants provided their written informed consent to participate in this study.

AUTHOR CONTRIBUTIONS

MZ: methodology, data acquisition, data analysis, interpretation of findings, and manuscript drafting. ZL, HQW, and TC: methodology and data acquisition. YL, FY, and YZ: conceptualization, methodology, supervision, and manuscript editing. HJW: conceptualization, methodology, supervision, interpretation of findings, funding acquisition, and manuscript editing. All authors contributed to the article and approved the submitted version.

FUNDING

This study was supported by the National Natural Science Foundation of China (91949120).

ACKNOWLEDGMENTS

We would like to thank all the volunteers in this study.

SUPPLEMENTARY MATERIAL

The Supplementary Material for this article can be found online at: https://www.frontiersin.org/articles/10.3389/fendo.2022.844351/full#supplementary-material

REFERENCES

1. Goldring MB. Articular Cartilage Degradation in Osteoarthritis. *HSS J* (2012) 8(1):7–9. doi: 10.1007/s11420-011-9250-z
2. Jee W. Integrated Bone Tissue Physiology: Anatomy and Physiology. In: Cowin SC, editor. *Bone Mechanics Handbook*. Boca Raton: CRC Press (2001). p. 1–68.
3. Harrison KD, Hiebert BD, Panahifar A, Andronowski JM, Ashique AM, King GA, et al. Cortical Bone Porosity in Rabbit Models of Osteoporosis. *J Bone Mineral Res* (2020) 35(11):2211–28. doi: 10.1002/jbmr.4124
4. Zebaze R, Seeman E. Cortical Bone: A Challenging Geography. *J Bone Mineral Res* (2015) 30(1):24–9. doi: 10.1002/jbmr.2419
5. Reichert IL, Robson MD, Gatehouse PD, He T, Chappell KE, Holmes J, et al. Magnetic Resonance Imaging of Cortical Bone With Ultrashort TE Pulse Sequences. *Magnetic Resonance Imaging* (2005) 23(5):611–8. doi: 10.1016/j.mri.2005.02.017
6. Bydder G. The Agfa Mayneord Lecture: MRI of Short and Ultrashort T 2 and T 2* Components of Tissues, Fluids and Materials Using Clinical Systems. *Br J Radiol* (2011) 84(1008):1067–82. doi: 10.1259/bjr/74368403
7. Du J, Bydder GM. Qualitative and Quantitative Ultrashort-TE MRI of Cortical Bone. *NMR Biomedicine* (2013) 26(5):489–506. doi: 10.1002/nbm.2906
8. Ma YJ, Jerban S, Jang H, Chang D, Chang EY, Du J. Quantitative Ultrashort Echo Time (UTE) Magnetic Resonance Imaging of Bone: An Update. *Front Endocrinol* (2020) 11:567417. doi: 10.3389/fendo.2020.567417
9. Talebi M, Abbasi-Rad S, Malekzadeh M, Shahgholi M, Ardakani AA, Foudeh K, et al. Cortical Bone Mechanical Assessment *via* Free Water Relaxometry at 3 T. *J Magn Reson Imaging* (2021) 54(6):1744–51. doi: 10.1002/jmri.27765
10. Liu C, Li W, Tong KA, Yeom KW, Kuzminski S. Susceptibility-Weighted Imaging and Quantitative Susceptibility Mapping in the Brain. *J Magn Reson Imaging* (2015) 42(1):23–41. doi: 10.1002/jmri.24768
11. Wang Y, Liu T. Quantitative Susceptibility Mapping (QSM): Decoding MRI Data for a Tissue Magnetic Biomarker. *Magn Reson Med* (2015) 73(1):82–101. doi: 10.1002/mrm.25358
12. Zhang Y, Shi J, Wei H, Han V, Zhu W-Z, Liu C. Neonate and Infant Brain Development From Birth to 2 Years Assessed Using MRI-Based Quantitative Susceptibility Mapping. *NeuroImage* (2019) 185:349–60. doi: 10.1016/j.neuroimage.2018.10.031
13. Treit S, Naji N, Seres P, Rickard J, Stolz E, Wilman AH, et al. R2* and Quantitative Susceptibility Mapping in Deep Gray Matter of 498 Healthy Controls From 5 to 90 Years. *Hum Brain Mapp* (2021) 42(14):4597–610. doi: 10.1002/hbm.25569
14. Zhang Y, Wei H, Cronin MJ, He N, Yan F, Liu C. Longitudinal Atlas for Normative Human Brain Development and Aging Over the Lifespan Using Quantitative Susceptibility Mapping. *NeuroImage* (2018) 171:176–89. doi: 10.1016/j.neuroimage.2018.01.008
15. Zivadinov R, Tavazzi E, Bergsland N, Hagemeier J, Lin F, Dwyer MG, et al. Brain Iron at Quantitative MRI Is Associated With Disability in Multiple Sclerosis. *Radiology* (2018) 289(2):487–96. doi: 10.1148/radiol.2018180136
16. Acosta-Cabronero J, Cardenas-Blanco A, Betts MJ, Butryn M, Valdes-Herrera JP, Galazky I, et al. The Whole-Brain Pattern of Magnetic Susceptibility Perturbations in Parkinson's Disease. *Brain* (2017) 140(1):118–31. doi: 10.1093/brain/aww278
17. Wei H, Dibb R, Decker K, Wang N, Zhang Y, Zong X, et al. Investigating Magnetic Susceptibility of Human Knee Joint at 7 Tesla. *Magn Reson Med* (2017) 78(5):1933–43. doi: 10.1002/mrm.26596
18. Wang L, Nissi MJ, Toth F, Johnson CP, Garwood M, Carlson CS, et al. Quantitative Susceptibility Mapping Detects Abnormalities in Cartilage Canals in a Goat Model of Preclinical Osteochondritis Dissecans. *Magn Reson Med* (2017) 77(3):1276–83. doi: 10.1002/mrm.26214
19. Nykanen O, Rieppo L, Toyras J, Kolehmainen V, Saarakkala S, Shmueli K, et al. Quantitative Susceptibility Mapping of Articular Cartilage: *Ex Vivo* Findings at Multiple Orientations and Following Different Degradation Treatments. *Magn Reson Med* (2018) 80(6):2702–16. doi: 10.1002/mrm.27216
20. Nykänen O, Sarin JK, Ketola JH, Leskinen H, te Moller NCR, Tiitu V, et al. T2* and Quantitative Susceptibility Mapping in an Equine Model of Post-Traumatic Osteoarthritis: Assessment of Mechanical and Structural

Properties of Articular Cartilage. *Osteoarthr Cartil* (2019) 27(10):1481–90. doi: 10.1016/j.joca.2019.06.009
21. Jerban S, Lu X, Jang H, Ma Y, Namiranian B, Le N, et al. Significant Correlations Between Human Cortical Bone Mineral Density and Quantitative Susceptibility Mapping (QSM) Obtained With 3D Cones Ultrashort Echo Time Magnetic Resonance Imaging (UTE-MRI). *Magn Reson Imaging* (2019) 62:104–10. doi: 10.1016/j.mri.2019.06.016
22. Jang H, von Drygalski A, Wong J, Zhou JY, Aguero P, Lu X, et al. Ultrashort Echo Time Quantitative Susceptibility Mapping (UTE-QSM) for Detection of Hemosiderin Deposition in Hemophilic Arthropathy: A Feasibility Study. *Magn Reson Med* (2020) 84(6):3246–55. doi: 10.1002/mrm.28388
23. Yang S, Zhang Y, Shen J, Dai Y, Ling Y, Lu H, et al. Clinical Potential of UTE-MRI for Assessing COVID-19: Patient- and Lesion-Based Comparative Analysis. *J Magnetic Reson Imaging* (2020) 52(2):397–406. doi: 10.1002/jmri.27208
24. Rasche V, Proksa R, Sinkus R, Bornert P, Eggers H. Resampling of Data Between Arbitrary Grids Using Convolution Interpolation. *IEEE Trans Med Imaging* (1999) 18(5):385–92. doi: 10.1109/42.774166
25. Fessler JA. On NUFFT-Based Gridding for Non-Cartesian MRI. *J Magnetic Resonance* (2007) 188(2):191–5. doi: 10.1016/j.jmr.2007.06.012
26. Jenkinson M, Smith S. A Global Optimisation Method for Robust Affine Registration of Brain Images. *Med Image Anal* (2001) 5(2):143–56. doi: 10.1016/S1361-8415(01)00036-6
27. Jenkinson M, Bannister P, Brady M, Smith S. Improved Optimization for the Robust and Accurate Linear Registration and Motion Correction of Brain Images. *Neuroimage* (2002) 17(2):825–41. doi: 10.1016/s1053-8119(02)91132-8
28. Diefenbach MN, Meineke J, Ruschke S, Baum T, Gersing A, Karampinos DC. On the Sensitivity of Quantitative Susceptibility Mapping for Measuring Trabecular Bone Density. *Magn Reson Med* (2019) 81(3):1739–54. doi: 10.1002/mrm.27531
29. Hernando D, Kellman P, Haldar JP, Liang Z-P. Robust Water/Fat Separation in the Presence of Large Field Inhomogeneities Using a Graph Cut Algorithm. *Magn Reson Med* (2010) 63(1):79–90. doi: 10.1002/mrm.22177
30. Wu B, Li W, Guidon A, Liu C. Whole Brain Susceptibility Mapping Using Compressed Sensing. *Magn Reson Med* (2012) 67(1):137–47. doi: 10.1002/mrm.23000
31. Wei H, Dibb R, Zhou Y, Sun Y, Xu J, Wang N, et al. Streaking Artifact Reduction for Quantitative Susceptibility Mapping of Sources With Large Dynamic Range. *NMR BioMed* (2015) 28(10):1294–303. doi: 10.1002/nbm.3383
32. Avants BB, Epstein CL, Grossman M, Gee JC. Symmetric Diffeomorphic Image Registration With Cross-Correlation: Evaluating Automated Labeling of Elderly and Neurodegenerative Brain. *Med Image Anal* (2008) 12(1):26–41. doi: 10.1016/j.media.2007.06.004
33. Yushkevich PA, Piven J, Hazlett HC, Smith RG, Ho S, Gee JC, et al. User-Guided 3D Active Contour Segmentation of Anatomical Structures: Significantly Improved Efficiency and Reliability. *NeuroImage* (2006) 31 (3):1116–28. doi: 10.1016/j.neuroimage.2006.01.015
34. Hunziker EB, Quinn TM, Häuselmann HJ. Quantitative Structural Organization of Normal Adult Human Articular Cartilage. *Osteoarthritis Cartilage* (2002) 10(7):564–72. doi: 10.1053/joca.2002.0814
35. Wei H, Gibbs E, Zhao P, Wang N, Cofer GP, Zhang Y, et al. Susceptibility Tensor Imaging and Tractography of Collagen Fibrils in the Articular Cartilage. *Magn Reson Med* (2017) 78(5):1683–90. doi: 10.1002/mrm.26882
36. Wei H, Lin H, Qin L, Cao S, Zhang Y, He N, et al. Quantitative Susceptibility Mapping of Articular Cartilage in Patients With Osteoarthritis at 3T. *J Magn Reson Imaging* (2019) 49(6):1665–75. doi: 10.1002/jmri.26535
37. Zhang M, Li Y, Feng R, Wang Z, Wang W, Zheng N, et al. Change in Susceptibility Values in Knee Cartilage After Marathon Running Measured Using Quantitative Susceptibility Mapping. *J Magn Reson Imaging* (2021) 54 (5):1585–93. doi: 10.1002/jmri.27745
38. Dimov AV, Liu Z, Spincemaille P, Prince MR, Du J, Wang Y. Bone Quantitative Susceptibility Mapping Using a Chemical Species-Specific R2* Signal Model With Ultrashort and Conventional Echo Data. *Magn Reson Med* (2018) 79(1):121–8. doi: 10.1002/mrm.26648
39. Cronin MJ, Wang N, Decker KS, Wei H, Zhu WZ, Liu C. Exploring the Origins of Echo-Time-Dependent Quantitative Susceptibility Mapping (QSM) Measurements in Healthy Tissue and Cerebral Microbleeds. *Neuroimage* (2017) 149:98–113. doi: 10.1016/j.neuroimage.2017.01.053
40. Hwang SN, Wehrli FW. The Calculation of the Susceptibility-Induced Magnetic Field From 3D NMR Images With Applications to Trabecular Bone. *J Magn Reson Ser B* (1995) 109(2):126–45. doi: 10.1006/jmrb.1995.0002
41. Guo Y, Chen Y, Zhang X, Mei Y, Yi P, Wang Y, et al. Magnetic Susceptibility and Fat Content in the Lumbar Spine of Postmenopausal Women With Varying Bone Mineral Density. *J Magn Reson Imaging* (2019) 49(4):1020–8. doi: 10.1002/jmri.26279
42. Chen Y, Guo Y, Zhang X, Mei Y, Feng Y, Zhang X. Bone Susceptibility Mapping With MRI Is an Alternative and Reliable Biomarker of Osteoporosis in Postmenopausal Women. *Eur Radiol* (2018) 28(12):5027–34. doi: 10.1007/s00330-018-5419-x
43. Oshima S, Fushimi Y, Okada T, Takakura K, Liu C, Yokota Y, et al. Brain MRI With Quantitative Susceptibility Mapping: Relationship to CT Attenuation Values. *Radiology* (2020) 294(3):600–9. doi: 10.1148/radiol.2019182934

Conflict of Interest: The authors declare that the research was conducted in the absence of any commercial or financial relationships that could be construed as a potential conflict of interest.

Publisher's Note: All claims expressed in this article are solely those of the authors and do not necessarily represent those of their affiliated organizations, or those of the publisher, the editors and the reviewers. Any product that may be evaluated in this article, or claim that may be made by its manufacturer, is not guaranteed or endorsed by the publisher.

frontiers | Frontiers in Endocrinology

ORIGINAL RESEARCH
published: 10 May 2022
doi: 10.3389/fendo.2022.876784

Tractography of Porcine Meniscus Microstructure Using High-Resolution Diffusion Magnetic Resonance Imaging

*Jikai Shen[1,2], Qi Zhao[3], Yi Qi[4], Gary Cofer[4], G. Allan Johnson[1,4] and Nian Wang[4,5,6]**

[1] Department of Biomedical Engineering, Duke University, Durham, NC, United States, [2] School of Life Sciences, Westlake University, Hangzhou, China, [3] Physical Education Institute, Jimei University, Xiamen, China, [4] Department of Radiology, Duke University School of Medicine, Durham, NC, United States, [5] Department of Radiology and Imaging Sciences, Indiana University School of Medicine, Indianapolis, IN, United States, [6] Stark Neurosciences Research Institute, Indiana University, Indianapolis, IN, United States

OPEN ACCESS

Edited by:
Yajun Ma,
University of California, San Diego, United States

Reviewed by:
Zhao Wei,
Institute of Electrical Engineering (CAS), China
Lidi Wan,
Tongji University, China

***Correspondence:**
Nian Wang
nianwang@iu.edu

Specialty section:
This article was submitted to Bone Research, a section of the journal Frontiers in Endocrinology

Received: 15 February 2022
Accepted: 04 April 2022
Published: 10 May 2022

Citation:
Shen J, Zhao Q, Qi Y, Cofer G, Johnson GA and Wang N (2022) Tractography of Porcine Meniscus Microstructure Using High-Resolution Diffusion Magnetic Resonance Imaging. Front. Endocrinol. 13:876784. doi: 10.3389/fendo.2022.876784

To noninvasively evaluate the three-dimensional collagen fiber architecture of porcine meniscus using diffusion MRI, meniscal specimens were scanned using a 3D diffusion-weighted spin-echo pulse sequence at 7.0 T. The collagen fiber alignment was revealed in each voxel and the complex 3D collagen network was visualized for the entire meniscus using tractography. The proposed automatic segmentation methods divided the whole meniscus to different zones (Red-Red, Red-White, and White-White) and different parts (anterior, body, and posterior). The diffusion tensor imaging (DTI) metrics were quantified based on the segmentation results. The heatmap was generated to investigate the connections among different regions of meniscus. Strong zonal-dependent diffusion properties were demonstrated by DTI metrics. The fractional anisotropy (FA) value increased from 0.13 (White-White zone) to 0.26 (Red-Red zone) and the radial diffusivity (RD) value changed from 1.0×10^{-3} mm^2/s (White-White zone) to 0.7×10^{-3} mm^2/s (Red-Red zone). Coexistence of both radial and circumferential collagen fibers in the meniscus was evident by diffusion tractography. Weak connections were found between White-White zone and Red-Red zone in each part of the meniscus. The anterior part and posterior part were less connected, while the body part showed high connections to both anterior part and posterior part. The tractography based on diffusion MRI may provide a complementary method to study the integrity of meniscus and nondestructively visualize the 3D collagen fiber architecture.

Keywords: DTI, knee, tractography, meniscus, connectivity, segmentation

Abbreviations: DTI, diffusion tensor imaging; FA, fractional anisotropy; MD, mean diffusivity; AD, axial diffusivity; RD, radial diffusivity; GAG, glycosaminoglycan; DSI, Diffusion spectrum imaging; UTE, ultra-short echo; R-R, Red-Red; R-W, Red-White; W-W, White-White.

INTRODUCTION

Magnetic resonance imaging (MRI) is the modality of choice for diagnosing meniscal tears with both high sensitivity and specificity (1, 2). Conventional morphological MRI relies on the assessment of surface integrity and sub-surface signal intensity as indicators of tissue defects, which is qualitative and has limitations to detect the meniscal composition changes before surface breakdown or small tears (3). Relaxation time-based quantitative MRI such as T1 and T2 mappings have been widely used to investigate the compositional tissue features beyond morphology and structure (4, 5).

Diffusion MRI (dMRI) has been extensively used to reveal the microstructure of different tissues due to its sensitivity to the microscopic cellular organization (6). Diffusion based tractography has been performed to identify anatomic connections in mouse brains (7). The derived structural connectivity maps provide insight into the network of interconnected brain regions and ultimately lead to improved diagnosis of various brain disorders (8). Recently, dMRI and tractography in musculoskeletal system has attracted more and more attention to investigate the tissue microstructure, local collagen fiber alignment, and the 3D collagen network (9–11). To the best of our knowledge, noninvasively probing the 3D collagen fiber architecture and connections among different parts of the porcine meniscus have not been reported yet, probably due to a few reasons. First, the tractography is challenging in menisci due to the low fractional anisotropy (FA) and short T2 (4). Second, the spatial resolution is often limited for meniscus MRI due to its thin-layer anatomical structure. Third, the structural connectivity analysis relies on segmenting the meniscus to different sub-regions (12). However, structural connection by diffusion tensor imaging (DTI) reveals not only the local tissue properties but also the 3D fiber network through the whole tissue area.

Besides tractography, the scalar metrics from DTI model are known to be related to the tissue microstructure (8, 13, 14). For instance, the FA and mean diffusivity (MD) are found to be sensitive to the collagen architecture and glycosaminoglycan (GAG) content in different zones of cartilage (15). Exploring the FA and MD variations at different zones of meniscus may help to better understand the microstructure of meniscus, which requires to segment the tissue manually or automatically. Cooper's classification is one of the most commonly used meniscal classification systems based on the blood supply (16). According to the classification, menisci can be divided into Red-Red zone (outer third of the meniscus), Red-White zone (middle third of the meniscus), and White-White zone (inner third of the meniscus) (17).

Menisci often show low signal intensity on MR images due to the short T2 relaxation time and conventional MRI cannot adequately distinguish red zone and white zone because of little contrast difference between these zones (18). It is possible to visualize enhancement selectively in the red zone of the meniscus using ultrashort echo time (UTE) pulse sequence, but dividing the meniscus to white and red zones is still challenging (19). Conventionally, the meniscus can be manually segmented to different zones, but it is an expertise-intensive and time-consuming process (20). Numerous subjective interpretations for separating adjacent structures with similar image contrasts result in low repeatability and less efficiency. Therefore, automation of the segmentation process is highly desirable.

In this study, we first acquired 3D diffusion-weighed spin-echo pulse sequence to probe the microstructure of porcine meniscus. We then developed a segmentation method with rotational and radial directions to divide the meniscus into different sub-regions. The automatic segmentation method was further validated in the human knee MRI images obtained from the Osteoarthritis Initiative (OAI) database. The water diffusion properties derived from DTI have been quantified at different zones of meniscus. Diffusion tractography was performed through whole meniscus to visualize the 3D collagen fiber network. Combining tractography and automatic segmentation, we were able to observe the structural connections among different areas of the meniscus.

MATERIALS AND METHODS

Specimen Preparation

Five normal porcine menisci were harvested shortly after the sacrifice of mature porcine knee joints obtained from a local abattoir. The specimens were then immersed in a phosphate buffered solution (PBS) solution of 0.5% gadoteridol (Prohance® Bracco Diagnostics Inc., Princeton, NJ) to shorten the T1 relaxation time to about 110 ms and to reduce the scan time (21).

Microscopic MRI (μMRI) Protocols

The specimens were scanned on a 7.0 T small animal MRI system (Magnex Scientific, Yarnton, Oxford, UK) equipped with 650 mT/m Resonance Research gradient coils (Resonance Research Inc., MA, USA). RF transmission and reception were achieved using a homemade solenoid coil ($10 \times 5 \times 5$ cm^3) (7). A modified 3D Stejskal-Tanner diffusion-weighted spin-echo pulse sequence to support k-space under sampling was performed for diffusion MRI scans (22). The imaging parameters were: TR = 100 ms, Matrix size = $512 \times 256 \times 256$, FOV = $64 \times 32 \times 32$ mm^3, TE = 13.0 ms, 125 μm isotropic spatial resolution, b value = 1000 s/mm^2 with 81 diffusion gradient encoding directions and 8 non-diffusion-weighted (b0) measurements. The gradient separation time was 5.5 ms and the diffusion gradient duration time was 4.5 ms for all scans. Acceleration factor (AF) of 8.0 was used for a sparsity approach, which has been described in detail previously (22). The scan time was 20.1 hours. The maximum gradient amplitude was about 60 G/cm. The diffusion gradient orientations (distributed over half sphere) were optimized to ensure the uniformity of encoding directions on the shell. The representative diffusion-weighted images (DWIs) and the signal intensity variations at different gradient orientations were shown in **Supplementary Figure 1**. The temperature was monitored throughout all the scans and the fluctuation was less than 1°C.

T2-weighed images were extracted from the non-diffusion-weighted (b0) images for segmentation purpose only.

3D multi-echo gradient echo (MGRE) scans were acquired at the spatial resolution of 250 μm with matrix size = 96 × 60 × 40 and 24 echoes (TE = 1.80/1.43/34.69 ms); FOV = 48 mm × 30 mm × 20 mm, flip angle = 30°, bandwidth (BW) = 125 kHz, and TR = 100 ms. The scan time was about 16 minutes. The T2*-weighted image derived from MGRE scans were used for segmentation purpose only.

Human Knee MRI

To validate the robustness of the automatic segmentation method, the human knee MRI images were obtained from the OAI database, which is available for public access (https://nda.nih.gov/oai/). A sagittal 3D WE DESS (water excitation double-echo steady-state) MR dataset of the knee featuring a high spatial resolution (0.37 x 0.37 mm^2 in plane, 0.7 mm slice thickness) was selected. The meniscus mask was manually drawn in ITK-SNAP software.

Manual Segmentation

Manual segmentation is common for meniscus analysis. However, due to the irregular shape of the meniscus, the accuracy of manual segmentation has not been investigated in detail. The porcine meniscus was manually segmented using ITK-SNAP software based on DWI. The meniscus was divided slice by slice into three zones in the Cartesian acquisition coordinate frame according to Cooper's classification: Red-Red (R-R) zone, Red-White (R-W) zone, White-White (W-W) zone (**Supplementary Figure 1**).

Automatic Segmentation

Radial Segmentation

The meniscus was divided into three zones according to Cooper's classification: Red-Red (R-R) zone, Red-White (R-W) zone, White-White (W-W) zone. First, a binary mask (**Figure 1B**) was generated based on the DWI image (**Figure 1A**). The whole meniscus mask was rotated clockwise (0° - 90°) and anticlockwise (-90° - 0°) with the step size of 0.5° with respect to the central plane (**Figure 1C**). A 2D cross-section image by the central plane was generated by each rotation. Each 2D image was then trisected to R-R, R-W, and W-W zones evenly based on the length in the radial direction (red dash lines in **Figure 1C** and **Supplementary Figure 2E**). Last, all the 2D segmented images were reassembled into the final 3D zonal segmentation. The automatic segmentation was implemented in Matlab (MathWorks, Natick, MA). Compared to automatic segmentation, the R-W and R-R zones were partially covered by W-W zone using manual segmentation (**Supplementary Figure 2**).

Rotational Segmentation

The whole meniscus could also be divided into 3 parts: anterior part, body part, and posterior part. To achieve this, the similar rotations were performed clockwise and anticlockwise for a certain degree to distinguish the three different parts (**Figure 1D**). Then the anterior, body, and posterior parts were segmented based on the rotation angle (60° in the current study). Note that no specific rotation degree can be defined as the ground truth, this angle was set to be adjustable for the Rotational Segmentation method (**Supplementary Figure 3**). In addition, we combined the Radial Segmentation and Rotational Segmentation methods to further divide meniscus to 9 regions, where each zone (R-R, R-W, or W-W) contained anterior, body, and posterior parts (**Figure 1E**).

Diffusion Metrics of Meniscus

All the DWIs were registered to the baseline images (b0). The DTI model was used to capture the primary diffusion direction of the collagen fiber. The scalar indices including FA, MD, axial diffusivity (AD), and radial diffusivity (RD) were calculated for both manual and automatic segmentation. Deterministic fiber

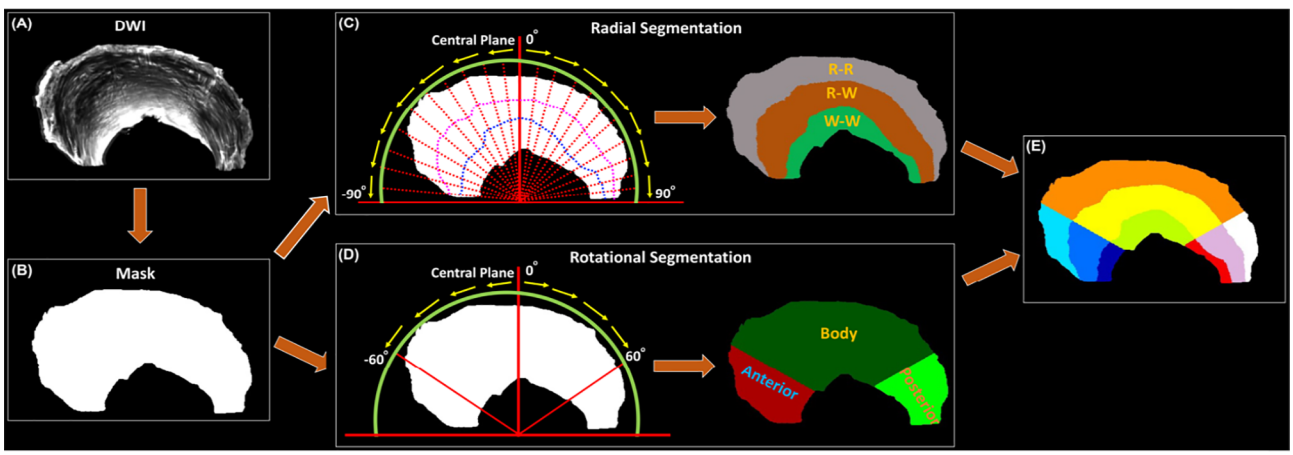

FIGURE 1 | The automatic segmentation process used in this study, from the acquired DWI **(A)** to the 9 different areas of meniscus **(E)**. Both Radial Segmentation **(C)** and Rotational Segmentation **(D)** were derived from the binary mask **(B)**. These two methods were further combined to divide the whole meniscus to 9 regions **(E)**. R-R, Red-Red zone; R-W, Red-White zone; W-W, White-White zone.

tracking was performed for the whole meniscus as well as the ROIs at three different zones (manually drawn in ITK-SNAP software). The propagation process was repeated until the tracking trajectory exceeded the turning angle greater than 45°. The connection strength map among different zones and parts was generated after whole meniscus tractography. All fiber tracking operations were performed using Diffusion Spectrum Imaging (DSI) studio toolbox (https://dsi-studio.labsolver.org/) (23).

Statistics

The volume and DTI metrics from 5 menisci were reported with their mean value and standard deviation. Direct comparison of volume and DTI metrics among different zones (R-R, R-W, and W-W) were performed using one-way ANOVA analysis in MATLAB, where *p*-value below 0.05 stands for a significant difference of DTI metrics among different zones.

RESULTS

Figure 2 showed the mean volumes and quantitative DTI metrics (FA, MD, AD, and RD) in three different zones. The heterogeneous appearance of the meniscus at different zones was evident in FA image (2A). The volume (2B) gradually increased from W-W zone (10.4%) to R-R zone (53.1%). Similar to the volume, the FA values (2C) gradually increased from W-W zone (0.13) to R-R zone (0.26) with a 100% increase. In contrast, MD, AD, and RD values (2D-2F) gradually decreased from W-W zone to R-R zone. For instance, the RD values changed from 1.0×10^{-3} mm^2/s (W-W zone) to 0.7×10^{-3} mm^2/s (R-R zone), which decreased 30%. Significant differences ($p < 0.01$) of volume and all the DTI metrics had been found among three different zones. The values of volumes and DTI metrics were summarized in **Table 1**.

Figure 3 showed the color-FA and the fiber orientation images of meniscus in different regions. The collagen fiber exhibited orthotropic directions between the anterior part (ROI 1, green color) and the body part (ROI 3, red color), between the posterior part (ROI 4, green color) and the body part. The fiber directions were found to gradually change from anterior part to the body part (ROI 2). These fiber directions were also evident from the individual tracts (**Figure 4**), where the seeding regions (**Figure 4A**) are from R-R zone (red area), R-W zone (green area), and W-W zone (white area), respectively. The circumferential collagen fibers were found in all three zones.

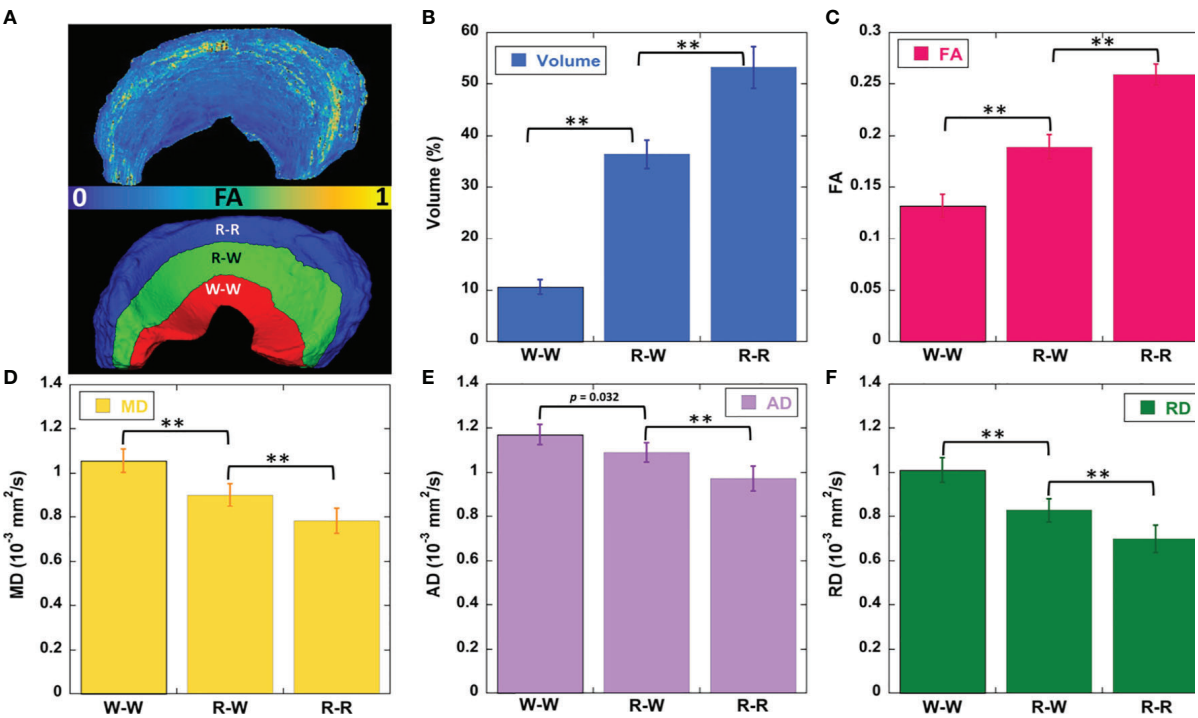

FIGURE 2 | The FA and segmentation 3D rendering images **(A)**, volume **(B)**, DTI metrics of FA **(C)**, mean diffusivity **(D)**, axial diffusivity **(E)**, and radial diffusivity **(F)** values at different zones. FA value gradually decreases from R-R to W-W zone **(C)**. The diffusivity metrics exhibit the opposite trends **(D–F)**. ** stands for *p*-value <0.001. R-R, Red-Red zone; R-W, Red-White zone; W-W, White-White zone.

TABLE 1 | The volumes and DTI metrics at different zones of meniscus.

Zones	Volume (%)	FA	MD (10^{-3} mm^2/s)	AD (10^{-3} mm^2/s)	RD (10^{-3} mm^2/s)
W-W	10.40 ± 1.41	0.13 ± 0.01	1.06 ± 0.09	1.17 ± 0.06	1.00 ± 0.06
R-W	36.50 ± 2.80	0.19 ± 0.02	0.90 ± 0.07	1.09 ± 0.06	0.83 ± 0.05
W-W	53.10 ± 4.08	0.26 ± 0.02	0.78 ± 0.06	0.97 ± 0.07	0.70 ± 0.05

In order to explore the entire meniscus 3D collagen fiber network, the tractography were performed in the whole meniscus area (**Figures 5A**, **C**, front and back view). The tractography showed similar collagen fiber architectures as **Figure 4**: the circumferential collagen fibers through anterior part to posterior part. However, the whole meniscus tracts revealed the coexistence of both radial and circumferential collagen fibers, especially in ROIs of 1 and 3 (front view), 5 and 6 (back view). The consistent tractography and fiber orientation results were demonstrated in all five menisci (**Supplementary Figure 4**).

Figure 6 exhibited the automatic segmentation (6A), the diffusion tractography (6B), and the connection heatmap of meniscus (6E). Several distinct characteristics can be identified from the tractography images and heatmap. First, the anterior part showed low connections to the posterior part (red box in 6C), while the body part showed high connections to both anterior part and posterior part (white box in 6C). Second, in the same part (anterior, body, or posterior), the R-W zone exhibited high connections to the adjacent parts (green box and yellow box).

In order to explore the robustness of the automatic segmentation method, the Radial Segmentation was also applied to T2- and T2*-weighted images (**Supplementary Figure 5**). We further extended our methods for human knee meniscus segmentation (**Supplementary Figure 6**). Both Radial Segmentation and Rotational Segmentation (**Supplementary Figures 6B, C**) methods showed visually comparable results to porcine meniscal segmentations.

DISCUSSION

MRI has emerged as an invaluable component of pathogenesis research in meniscal tear. Quantitative MRI (qMRI) has been applied to study the correlation between the parametric mapping and the severity of tissue degradation (4, 5). Most of the qMRI used to access the biochemical status of the menisci are based on relaxation times, such as T2, T2*, T1rho, and T1, which are challenging to estimate the local collagen fiber alignment directly (24, 25). In order to investigate the comprehensive collagenous fibril texture of meniscus, other imaging modalities such as polarized light imaging (PLM), reflectance confocal microscopy, and scanning electron microscopy (SEM) have been used in previous studies (26–29). While it is well appreciated that complex fiber structures (circumferential and radial) exist within the meniscus using these technologies, they are often limited in a small region and presented as two-dimensional (2D) images. Recently, DTI has been used to

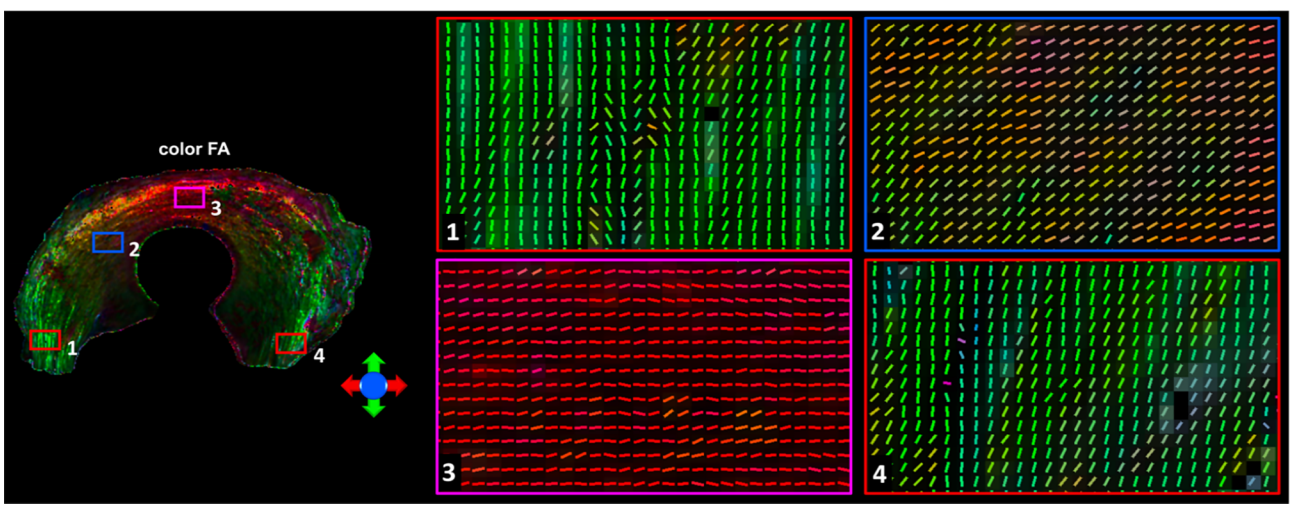

FIGURE 3 | The color-FA and the fiber orientation images of meniscus at different regions. Red for horizontal fiber, green for vertical, blue for inside-out. The collagen fiber orientations were shown at 4 different regions.

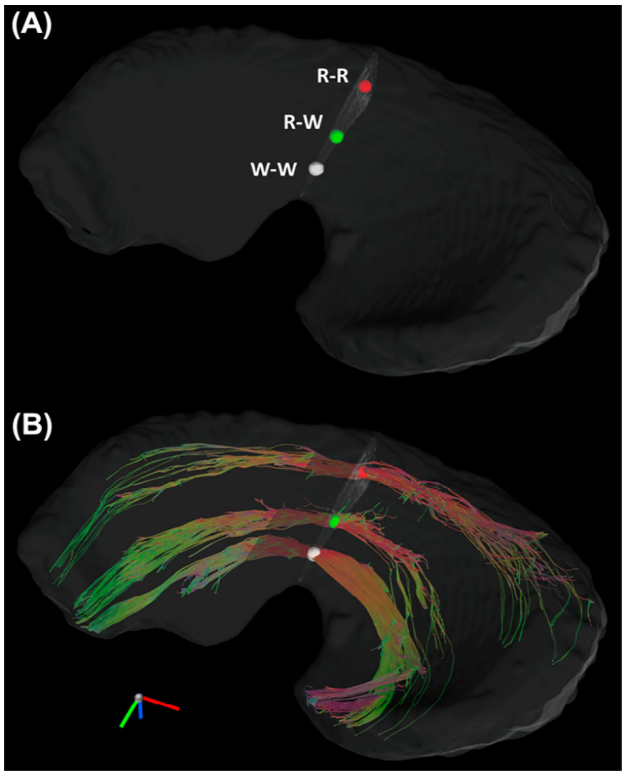

FIGURE 4 | The Tracts **(B)** from three seeding regions **(A)**: red area in R-R zone, white area in R-W zone, and white area from W-W zone. R-R, Red-Red zone; R-W, Red-White zone; W-W, White-White zone.

study the tissue microstructure and quantify the local collagen fiber direction in knee joint (21, 30–32). The local fiber orientation from DTI model affords an alternative to probe the complex collagen fiber directions of the whole meniscus.

Tractography, as a promising technology to visualize the complex 3D fiber network, has been recently applied to individual connective tissues in knee joint, such as cartilage, anterior cruciate ligament (ACL), and tendon (9, 10, 33, 34). However, the application of tractography to probe the meniscal microstructure is rare, probably due to the low signal-to-noise ratio (SNR) and short T2* values (35–37). To overcome this issue, the menisci were images in a preclinical 7T system with powerful gradients to increase the SNR by minimizing the TE value to 13.0 ms. With the proposed automatic segmentation methods, the connection heatmap has been generated to quantify the connections among different zones (R-R, R-W, and W-W) and different parts (anterior, body, and posterior). Compared to the exisiting qMRI methods focusing on the local change of the tissue properties, the alteration of the connections in meniscus may provide a complementary method to study the integrity of meniscus and meniscal tears in future studies.

It has been reported that FA is sensitive to collagen architecture and MD is sensitive to GAG content in cartilage (31). Cartilage has been found to show depth-dependent response to the degradation, especially in the superficial zone at early osteoarthritis (OA) (18). The variations of DTI metrics at different parts and zones may be related to the meniscal microstructure and composition changes after degradation. Several automatic and semi-automatic segmentation methods have been developed to segment the cartilage, bone, and meniscus in knee joint (38, 39). Although these methods

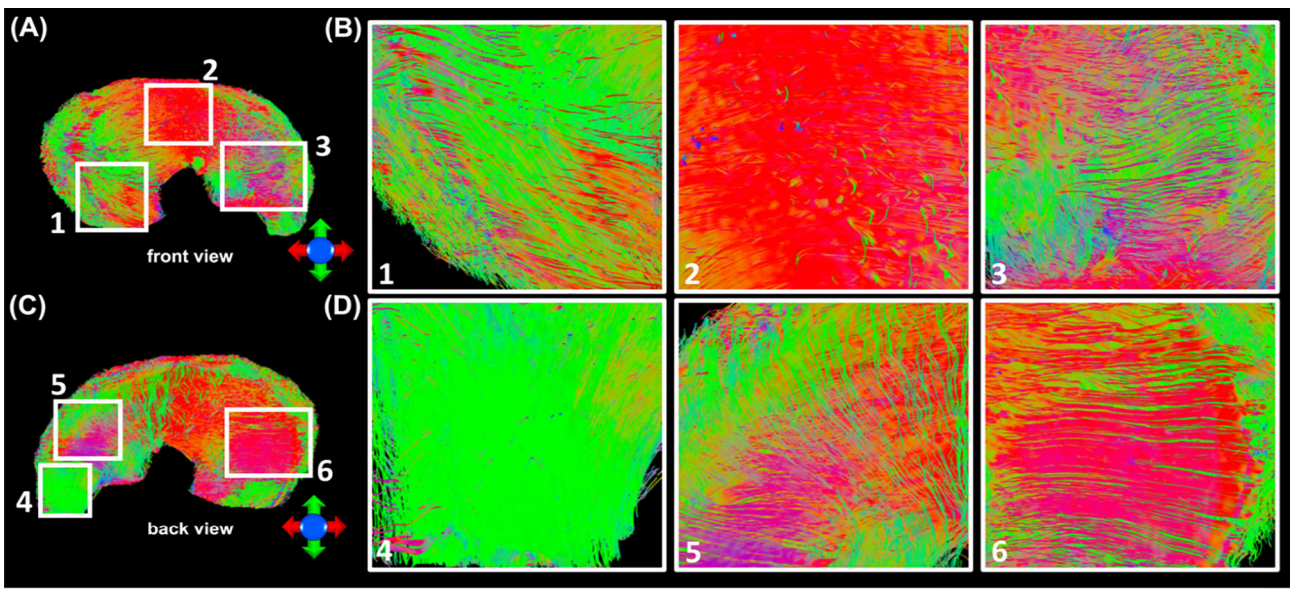

FIGURE 5 | The entire meniscus 3D collagen fiber network **(A, C)** resolved by tractography. The coexistence of both radial and circumferential collagen fibers was found from ROIs 1 and 3 (front view, **B**), and ROIs 5 and 6 (back view, **D**).

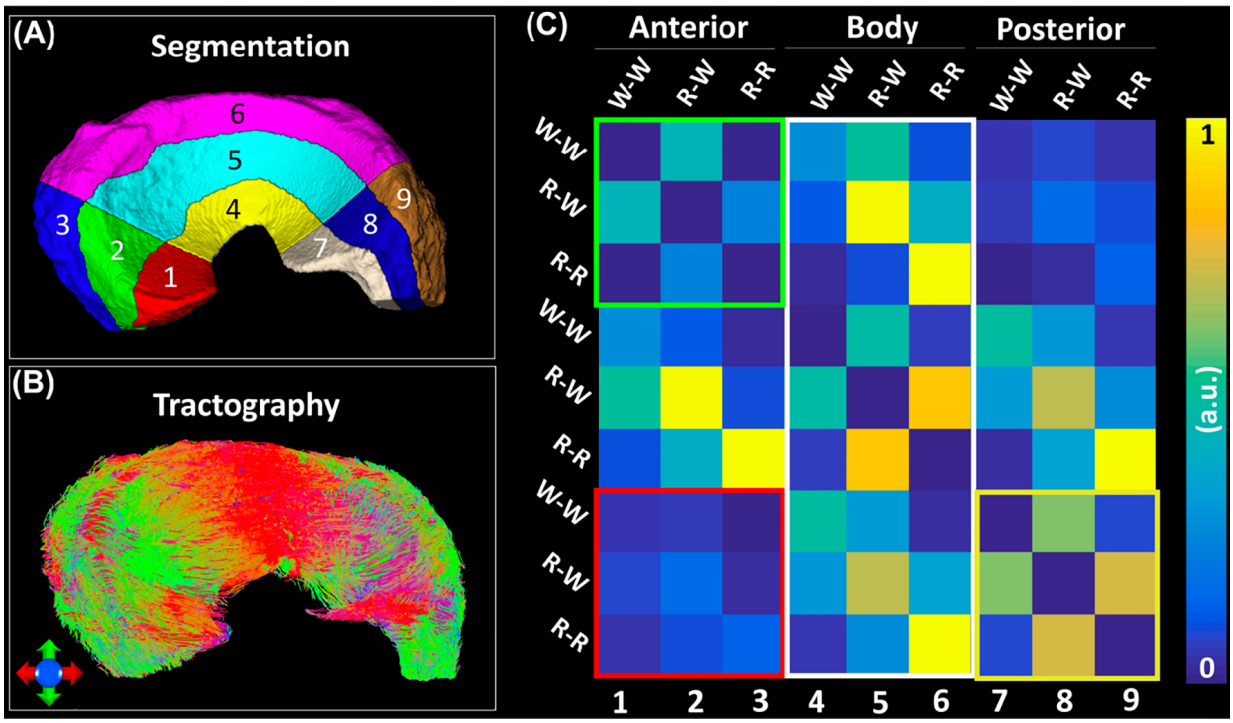

FIGURE 6 | The structural connection heatmap of meniscus **(C)** obtained by the automatic parcellation **(A)** and tractography **(B)**.

provide excellent segmentation accuracy to distinguish meniscus to other soft tissues, automatically dividing the meniscus to different zones and parts is still limited. Unlike the articular cartilage, which can be divided into three zones according to the collagen fiber directions, both red zone and white zone show similar fiber directions in meniscus (40). The lack of apparent image contrasts between red zone and white zone makes the segmentation more challenging.

In this study, we adapted Cooper's classification for the segmentation. The segmentation allows us to investigate the diffusion properties of menisci at different zones or parts. It also helps us to obtain the heatmap to show the structural connections among different regions. The proposed segmentation, even is not a gold standard, does afford a convenient way for quantitative analysis of meniscus diffusion properties. The proposed segmentation method requires a simple binary mask of the meniscus, which is relatively easy to obtain from MRI scans, such as T2-weighted image, T2*-weighted image, and DWI (41). The automatic segmentation method may not be limited to MRI and can be applied to different imaging modalities as long as the binary mask is available. Furthermore, the method also shows robust results for human meniscus segmentation, which suggests that our method holds the potential to segment meniscus to different sub-regions for human studies (42).

There are a few limitations in our study. First, the sample size is small due to the extremely long scan time, the consistent collagen fiber alignment and tractography were demonstrated in all five specimens. Second, the dMRI was acquired with a preclinical setting that may not relevant to the clinical study. To the best of our knowledge, it's still challenging to achieve high quality meniscus dMRI and tractography for *in vivo* human studies. Advanced acquisition technologies, stronger gradients, higher magnetic field, and novel reconstruction methods shed the light to bridge the gap (43). Third, although the collagen fiber architecture revealed by dMRI is consistent with other imaging modalities in previous studies, complete validation of MRI findings using other imaging modalities is warranted in future studies. Last, this Cooper's classification is originally defined for human meniscus, our method may be improved for animal meniscal studies when further shape information about different species is known.

In conclusion, the porcine meniscus microstructure was investigated using a 3D diffusion-weighed spin-echo pulse sequence. Strong zonal-dependent diffusion properties were demonstrated by DTI metrics (FA, MD, AD, and RD). The complex 3D collagen fiber architecture of the entire meniscus was visualized by diffusion tractography. Combining tractography and automatic segmentation method, we were able to observe the structural connections among different

areas of the meniscus. It may offer a novel method to evaluate the local meniscus tears and address the alteration of connections among different regions of the meniscus.

DATA AVAILABILITY STATEMENT

The raw data supporting the conclusions of this article will be made available by the authors, without undue reservation.

ETHICS STATEMENT

The animal study was reviewed and approved by institutional animal care and use committee (IACUC).

AUTHOR CONTRIBUTIONS

JS: Methodology, Formal analysis, Writing-review and editing. QZ: Editing, Formal analysis, Validation. YQ: Specimen preparation, Methodology, Writing-review and editing. GC: MRI acquisition, Writing-review and editing. GJ: Conceptualization, Investigation, Writing-review and editing, Supervision, Funding acquisition. NW: Conceptualization, Methodology, MRI acquisition, Formal analysis, Investigation, Writing -original draft, Funding acquisition, Writing-review and editing. All authors contributed to the article and approved the submitted version.

FUNDING

This work was supported by the NIH/NIBIB National Biomedical Technology Resource Center P41 EB015897 (to GJ), Charles E. Putman MD Vision Award of the Department of Radiology, Duke University School of Medicine (to NW and Charles E. SPritzer), and Strategic Research Initiative (SRI) IUH and Indiana University School of Medicine (to NW).

ACKNOWLEDGMENTS

The authors thank Abigail Holt, Dr. Amy L. McNulty, and Dr. Louise E. DeFrate for providing porcine menisci and insightful discussions, Tatiana Johnson for editorial comments on the manuscript and James Cook and Lucy Upchurch for significant technical support.

SUPPLEMENTARY MATERIAL

The Supplementary Material for this article can be found online at: https://www.frontiersin.org/articles/10.3389/fendo.2022.876784/full#supplementary-material

REFERENCES

1. Terzidis IP, Christodoulou A, Ploumis A, Givissis P, Natsis K, Koimtzis M. Meniscal Tear Characteristics in Young Athletes With a Stable Knee - Arthroscopic Evaluation. *Am J Sport Med* (2006) 34(7):1170–5. doi: 10.1177/0363546506287939
2. Nguyen JC, De Smet AA, Graf BK, Rosas HG. MR Imaging-Based Diagnosis and Classification of Meniscal Tears. *Radiographics* (2014) 34(4):981–99. doi: 10.1148/rg.344125202
3. Nebelung S, Tingart M, Pufe T, Kuhl C, Jahr H, Truhn D. *Ex Vivo* Quantitative Multiparametric MRI Mapping of Human Meniscus Degeneration. *Skeletal Radiol* (2016) 45(12):1649–60. doi: 10.1007/s00256-016-2480-x
4. Rauscher I, Stahl R, Cheng J, Li XJ, Huber MB, Luke A, et al. Meniscal Measurements of T1(rho) and T2 at MR Imaging in Healthy Subjects and Patients With Osteoarthritis. *Radiology* (2008) 249(2):591–600. doi: 10.1148/radiol.2492071870
5. Chu CR, Williams AA, West RV, Qian Y, Fu FH, Do BH, et al. Quantitative Magnetic Resonance Imaging UTE-T2* Mapping of Cartilage and Meniscus Healing After Anatomic Anterior Cruciate Ligament Reconstruction. *Am J Sports Med* (2014) 42(8):1847–56. doi: 10.1177/0363546514532227
6. Tuch DS, Reese TG, Wiegell MR, Wedeen VJ. Diffusion MRI of Complex Neural Architecture. *Neuron* (2003) 40(5):885–95. doi: 10.1016/S0896-6273(03)00758-X
7. Wang N, Zhang JY, Cofer G, Qi Y, Anderson RJ, White LE, et al. Neurite Orientation Dispersion and Density Imaging of Mouse Brain Microstructure. *Brain Struct Funct* (2019) 224(5):1797–813. doi: 10.1007/s00429-019-01877-x
8. Rovaris M, Gass A, Bammer R, Hickman SJ, Ciccarelli O, Miller DH, et al. Diffusion MRI in Multiple Sclerosis. *Neurology* (2005) 65(10):1526–32. doi: 10.1212/01.wnl.0000184471.83948.e0
9. Van Dyck P, Froeling M, De Smet E, Pullens P, Torfs M, Verdonk P, et al. Diffusion Tensor Imaging of the Anterior Cruciate Ligament Graft. *J Magn Reson Imag* (2017) 46(5):1423–32. doi: 10.1002/jmri.25666
10. Wengler K, Tank D, Fukuda T, Paci JM, Huang M, Schweitzer ME, et al. Diffusion Tensor Imaging of Human Achilles Tendon by Stimulated Echo Readout-Segmented EPI (Ste-RS-EPI). *Magn Reson Med* (2018) 80(6):2464–74. doi: 10.1002/mrm.27220
11. Bedoya MA, Delgado J, Berman JI, Chauvin NA, Zurakowski D, Ramirez-Grueso R, et al. Diffusion-Tensor Imaging of the Physes: A Possible Biomarker for Skeletal Growth-Experience With 151 Children. *Radiology* (2017) 284(1):210–8. doi: 10.1148/radiol.2017160681
12. Saygili A, Albayrak S. An Efficient and Fast Computer-Aided Method for Fully Automated Diagnosis of Meniscal Tears From Magnetic Resonance Images. *Artif Intell Med* (2019) 97:118–30. doi: 10.1016/j.artmed.2018.11.008
13. Filidoro L, Dietrich O, Weber J, Rauch E, Oerther T, Wick M, et al. High-Resolution Diffusion Tensor Imaging of Human Patellar Cartilage: Feasibility and Preliminary Findings. *Magn Reson Med* (2005) 53(5):993–8. doi: 10.1002/mrm.20469
14. Meder R, de Visser SK, Bowden JC, Bostrom T, Pope JM. Diffusion Tensor Imaging of Articular Cartilage as a Measure of Tissue Microstructure. *Osteoarthritis Cartilage* (2006) 14(9):875–81. doi: 10.1016/j.joca.2006.03.002
15. Ukai T, Sato M, Yamashita T, Imai Y, Mitani G, Takagaki T, et al. Diffusion Tensor Imaging Can Detect the Early Stages of Cartilage Damage: A Comparison Study. *BMC Musculoskel Dis* (2015) 16:35. doi: 10.1186/s12891-015-0499-0
16. Cooper DE, Arnoczky SP, Warren RF. Meniscal Repair. *Clin Sports Med* (1991) 10(3)529–48. doi: 10.1016/S0278-5919(20)30608-6
17. Rao AJ EB, Cvetanovich GL, Yanke AB, Bach BRJr., Cole BJ. The Meniscus-Deficient Knee: Biomechanics, Evaluation, and Treatment Options.

Orthopaedic J Sports Med (2015) 3(10):2325967115611386. doi: 10.1177/2325967115611386
18. Eijgenraam SM, Bovendeert FAT, Verschueren J, van Tiel J, Bastiaansen-Jenniskens YM, Wesdorp MA, et al. T-2 Mapping of the Meniscus Is a Biomarker for Early Osteoarthritis. *Eur Radiol* (2019) 29(10):5664–72. doi: 10.1007/s00330-019-06091-1
19. Hauger O, Frank LR, Boutin RD, Lektrakul N, Chung CB, Haghighi P, et al. Characterization of the "Red Zone" of Knee Meniscus: MR Imaging and Histologic Correlation. *Radiology* (2000) 217(1):193–200. doi: 10.1148/radiology.217.1.r00se36193
20. Hunter DJ, Guermazi A, Lo GH, Grainger AJ, Conaghan PG, Boudreau RM, et al. Evolution of Semi-Quantitative Whole Joint Assessment of Knee OA: MOAKS (MRI Osteoarthritis Knee Score) (Vol 19, Pg 990, 2011). *Osteoarthr Cartilage* (2011) 19(9):1168. doi: 10.1016/j.joca.2011.08.001
21. Wang N, Mirando AJ, Cofer G, Qi Y, Hilton MJ, Johnson GA. Diffusion Tractography of the Rat Knee at Microscopic Resolution. *Magnetic Resonance Med* (2019) 81(6):3775–86. doi: 10.1002/mrm.27652
22. Wang N, Mirando AJ, Cofer G, Qi Y, Hilton MJ, Johnson GA. Characterization Complex Collagen Fiber Architecture in Knee Joint Using High-Resolution Diffusion Imaging. *Magnetic Resonance Med* (2020) 84 (2):908–19. doi: 10.1002/mrm.28181
23. Yeh FC, Wedeen VJ, Tseng WYI. Generalized Q-Sampling Imaging. *IEEE T Med Imag* (2010) 29(9):1626–35. doi: 10.1109/Tmi.2010.2045126
24. Eijgenraam SM, Chaudhari AS, Reijman M, Bierma-Zeinstra SMA, Hargreaves BA, Runhaar J, et al. Time-Saving Opportunities in Knee Osteoarthritis: T-2 Mapping and Structural Imaging of the Knee Using a Single 5-Min MRI Scan. *Eur Radiol* (2020) 30(4):2231–40. doi: 10.1007/s00330-019-06542-9
25. Kajabi AW, Casula V, Nissi MJ, Peuna A, Podlipska J, Lammentausta E, et al. Assessment of Meniscus With Adiabatic T-1 Rho and T-2 Rho Relaxation Time in Asymptomatic Subjects and Patients With Mild Osteoarthritis: A Feasibility Study. *Osteoarthr Cartilage* (2018) 26(4):580–7. doi: 10.1016/j.joca.2017.12.006
26. Bansal S, Peloquin JM, Keah NM, O'Reilly OC, Elliott DM, Mauck RL, et al. Structure, Function, and Defect Tolerance With Maturation of the Radial Tie Fiber Network in the Knee Meniscus. *J Orthopaedic Res* (2020) 38(12):2709–20. doi: 10.1002/jor.24697
27. Petersen W, Tillmann B. Collagenous Fibril Texture of the Human Knee Joint Menisci. *Anat Embryol (Berl)* (1998) 197(4):317–24. doi: 10.1007/s004290050141
28. Li Q, Qu FN, Han B, Wang C, Li H, Mauck RL, et al. Micromechanical Anisotropy and Heterogeneity of the Meniscus Extracellular Matrix. *Acta Biomater* (2017) 54:356–66. doi: 10.1016/j.actbio.2017.02.043
29. Pinsard M, Laverty S, Richard H, Dubuc J, Schanne-Klein MC, Legare F. Maturation of the Meniscal Collagen Structure Revealed by Polarization-Resolved and Directional Second Harmonic Generation Microscopy. *Sci Rep* (2019) 9:18448. doi: 10.1038/s41598-019-54942-0
30. Duarte A, Ruiz A, Ferizi U, Bencardino J, Abramson SB, Samuels J, et al. Diffusion Tensor Imaging of Articular Cartilage Using a Navigated Radial Imaging Spin-Echo Diffusion (RAISED) Sequence. *Eur Radiol* (2019) 29 (5):2598–607. doi: 10.1007/s00330-018-5780-9
31. Raya JG. Techniques and Applications of *In Vivo* Diffusion Imaging of Articular Cartilage. *J Magn Reson Imag* (2015) 41(6):1487–504. doi: 10.1002/jmri.24767
32. Raya JG, Melkus G, Adam-Neumair S, Dietrich O, Mutzel E, Reiser MF, et al. Diffusion-Tensor Imaging of Human Articular Cartilage Specimens With Early Signs of Cartilage Damage. *Radiology* (2013) 266(3):831–41. doi: 10.1148/radiol.12120954
33. Mukherjee P, Berman JI, Chung SW, Hess CP, Henry RG. Diffusion Tensor MR Imaging and Fiber Tractography: Theoretic Underpinnings. *Am J Neuroradiol* (2008) 29(4):632–41. doi: 10.3174/ajnr.A1051
34. Barrera CA, Bedoya MA, Delgado J, Berman JI, Chauvin NA, Edgar JC, et al. Correlation Between Diffusion Tensor Imaging Parameters of the Distal Femoral Physis and Adjacent Metaphysis, and Subsequent Adolescent Growth. *Pediatr Radiol* (2019) 49(9):1192–200. doi: 10.1007/s00247-019-04443-z
35. Koff MF, Shah P, Pownder S, Romero B, Williams R, Gilbert S, et al. Correlation of Meniscal T2*with Multiphoton Microscopy, and Change of Articular Cartilage T2 in an Ovine Model of Meniscal Repair. *Osteoarthr Cartilage* (2013) 21(8):1083–91. doi: 10.1016/j.joca.2013.04.020
36. Chang EY, Du J, Chung CB. UTE Imaging in the Musculoskeletal System. *J Magnetic Resonance Imag* (2015) 41(4):870–83. doi: 10.1002/jmri.24713
37. Brinkhof S, te Moller N, Froeling M, Brommer H, van Weeren R, Ito K, et al. T2*mapping in an Equine Articular Groove Model: Visualizing Changes in Collagen Orientation. *J Orthopaedic Res* (2020) 38(11):2383–9. doi: 10.1002/jor.24764
38. Liu F, Zhou ZY, Jang H, Samsonov A, Zhao GY, Kijowski R. Deep Convolutional Neural Network and 3D Deformable Approach for Tissue Segmentation in Musculoskeletal Magnetic Resonance Imaging. *Magnetic Resonance Med* (2018) 79(4):2379–91. doi: 10.1002/mrm.26841
39. Tack A, Mukhopadhyay A, Zachow S. Knee Menisci Segmentation Using Convolutional Neural Networks: Data From the Osteoarthritis Initiative. *Osteoarthr Cartilage* (2018) 26(5):680–8. doi: 10.1016/j.joca.2018.02.907
40. Wang N, Badar F, Xia Y. MRI Properties of a Unique Hypo-Intense Layer in Degraded Articular Cartilage. *Phys Med Biol* (2015) 60(22):8709–21. doi: 10.1088/0031-9155/60/22/8709
41. Peterfy CG, Schneider E, Nevitt M. The Osteoarthritis Initiative: Report on the Design Rationale for the Magnetic Resonance Imaging Protocol for the Knee. *Osteoarthr Cartilage* (2008) 16(12):1433–41. doi: 10.1016/j.joca.2008.06.016
42. Eckstein F, Wirth W, Nevitt MC. Recent Advances in Osteoarthritis Imaging-the Osteoarthritis Initiative. *Nat Rev Rheumatol* (2012) 8(10):622–30. doi: 10.1038/nrrheum.2012.113
43. Roebroeck A, Miller KL, Aggarwal M. *Ex Vivo* Diffusion MRI of the Human Brain: Technical Challenges and Recent Advances. *Nmr Biomed* (2019) 32(4): e3941. doi: 10.1002/nbm.3941

Conflict of Interest: The authors declare that the research was conducted in the absence of any commercial or financial relationships that could be construed as a potential conflict of interest.

frontiers | Frontiers in Endocrinology

ORIGINAL RESEARCH
published: 13 May 2022
doi: 10.3389/fendo.2022.891088

Associations of Lumber Disc Degeneration With Paraspinal Muscles Myosteatosis in Discogenic Low Back Pain

Yilong Huang[1†], Ling Wang[2†], Baofa Luo[1], Kaiwen Yang[1], Xiaomin Zeng[1], Jiaxin Chen[1], Zhenguang Zhang[1], Yanlin Li[3], Xiaoguang Cheng[2] and Bo He[1]*

[1] Department of Medical Imaging, The First Affiliated Hospital of Kunming Medical University, Kunming, China, [2] Department of Radiology, Beijing Jishuitan Hospital, Beijing, China, [3] Department of Sports Medicine, The First Affiliated Hospital of Kunming Medical University, Kunming, China

Accompanied with intervertebral disc (IVD) degeneration, increasing fat infiltration of paraspinal muscles may be related to discogenic low back pain (DLBP), but their relationship is still unclear and the classical animal models are not completely applicable. The purpose of this study was to assess the paraspinal muscle fat infiltration in patients with DLBP by quantitative MRI, and to develop a novel DLBP rat model to explore the potential relationship between DLBP paraspinal muscle fat infiltration and TNF-α levels. We measured the proton density fat fraction (PDFF) of the multifidus and erector spinae muscles of 70 DLBP patients and 36 healthy volunteers by using quantitative MRI IDEAL-IQ. In addition, we developed a DLBP experimental rat model by puncturing the L4/5 and L5/6 IVDs under the guidance of X-ray fluoroscopy. Then various behavioral experiments, MRI and pathological examination of IVDs were used to evaluate the performance of the DLBP animal model. The gait analysis, hot plate test, acetone test, grasping test and tail suspension test were used to evaluate the pain and muscle dysfunction in rats. Through quantitative MRI and histological examination, the degeneration of IVDs and fat infiltration in the muscles were observed *in vivo* and ex vivo. Enzyme linked immunosorbent assay detects the level of TNF-α in rat IVDs and paraspinal muscles. In the human study, compared with healthy volunteers, the PDFF of multifidus and erector muscles of DLBP patients increased significantly at L4/5 and L5/S1 levels ($p<0.05$). In the rat experiment, compared with control group and sham group, DLBP group had reduced gait score, shortened response time to cold and heat stimuli, prolonged bending time, and shortened struggling time. Rat lumbar MRI T2WI showed that the signal intensity of L4/5 and L5/6 IVDs were progressively decreased. Histological examination revealed that IVDs had increased collagen fibers, reduced nucleus pulposus, thickened annulus fibrosus, and distorted shape. The PDFF of multifidus muscle at L4/5 and L5/6 level in the DLBP group were more than that in other groups ($p<0.05$), and HE staining and oil red O staining of paraspinal muscles showed that the muscle bundle space of the DLBP group muscles increased, and the muscle tissues Increased lipid

OPEN ACCESS

Edited by:
Bing Wu,
GE Healthcare, China

Reviewed by:
Weiqiang Dou,
GE Healthcare, China
Weiyin Vivian Liu,
GE Healthcare, China

***Correspondence:**
Bo He
hebo_ydyy@qq.com

[†]These authors have contributed equally to this work

Specialty section:
This article was submitted to Bone Research, a section of the journal Frontiers in Endocrinology

Received: *07 March 2022*
Accepted: *13 April 2022*
Published: *13 May 2022*

Citation:
Huang Y, Wang L, Luo B, Yang K, Zeng X, Chen J, Zhang Z, Li Y, Cheng X and He B (2022) Associations of Lumber Disc Degeneration With Paraspinal Muscles Myosteatosis in Discogenic Low Back Pain. Front. Endocrinol. 13:891088. doi: 10.3389/fendo.2022.891088

droplets. Finally, the expression of TNF-α in IVDs and paraspinal muscles in the DLBP group were significantly higher than that in the control group ($p<0.05$). It is reliable and feasible to establish a DLBP rat model by puncturing the lumbar IVDs under the guidance of X-ray fluoroscopy. The degeneration of lumbar IVDs with DLBP leads to the occurrence of fat infiltration of paraspinal muscles, which is related to the expression of TNF-α.

Keywords: discogenic low back pain, quantitative MRI, paraspinal muscles, fatty infiltration, lumbar intervertebral disk degeneration, inflammation

INTRODUCTION

Low back pain (LBP) is one of the most important challenges to global public health which leads to great economic burdens on society (1, 2). Discogenic low back pain (DLBP) is the most common type of chronic LBP, accounting for 39% of patients with chronic LBP (3). Intervertebral disc (IVD) degeneration is considered to be the leading cause of DLBP especially related to inflammation (4), but treatment is mainly limited to partial symptom relief (5). Paraspinal muscles (multifidus, erector spinae, and psoas major) are crucial to the stability and function of the lumbar spine (6). Muscle atrophy and fat replacement are considered to be the features of DLBP paraspinal muscle remodeling, and fat infiltration may worsen DLBP (7). Given the meaningful role of paraspinal muscles on the lumbar spine, fat infiltration may worsen DLBP. Therefore, it's crucial to assess the interaction between the fat infiltration in the paraspinal muscles and DLBP.

Previous studies have reported decreased computed tomography attenuation (8, 9) and increased T2-weighted imaging (T2WI) signal (10) in the paraspinal muscles of LBP patients due to fat infiltration. In recent years, the advanced chemical shift-encoded MRI (CSE-MRI) has been proposed for non-invasive quantitative assessment of fat in various parts of the human body (11, 12). The proton density fat fraction (PDFF) estimated by using CSE MRI is highly repeatable and accurate in the quantitative assessment of muscle fat composition (13). The iterative decomposition of water and fat with echo asymmetry and least-squares estimation (IDEAL-IQ) is one of CSE-MRI techniques. IDEAL-IQ is considered to be comparable to MR spectroscopy (the gold standard method *in vivo*) for quantification of muscle fat infiltration (14, 15). Further, IDEAL-IQ or other CSE-MRI imagings have significant advantages over magnetic resonance spectroscopy, such as rapid and volumetric data acquisition with visualization of anatomical structures. Therefore, PDFF may help to clarify and quantify the fat infiltration in the paraspinal muscles of DLBP.

In clinical studies, the muscle fat infiltration of patients is affected by many factors, such as age, gender, BMI, exercise etc (16). The direct causal relationship between IVD degeneration and paraspinal muscle fatty infiltration is unclear. Therefore, the study of animal experiments with single variable control is very necessary. In animal experiments, previous studies have proposed several *in-vivo* animal DLBP models (17–20), but none of them seem to be suitable for this study. Current *in-vivo* models can be categorized into natural models and artificial models. The natural model was age-related long-term IVDs degradation, just like humans. However, such models take a long time to implement and have the shortcoming of individual symptom variation and high cost. The artificial model aims to destroy the IVDs, leading to common clinical manifestations of DLBP similar to humans in animals. This method has been widely adopted for its simplicity and high efficiency. Several studies have demonstrated the possibility of surgically incising the abdomen or back and accurately destroying the IVDs to obtain effective DLBP animal models (18–21). But these DLBP animal models also destroy the muscles, nerves and bone structures around the spine. In contrast to the previous animal models, the animal IVDs are punctured under the guidance of X-ray fluoroscopy, which can accurately destroy the IVDs and ensure that other important structures of the lumbar spine are not damaged and integrity, especially the paraspinal muscles. This approach avoids paraspinal muscles being disturbed by surgery whenever possible, which is beneficial to further investigate the relationship between DLBP and paraspinal muscles. Besides, this animal model is more efficient, economical and may more closely resembled the process of natural IVDs degeneration.

In previous studies, inflammatory factors are an important player in IVD degeneration, especially TNF-α, and chronic low-level TNF-α may be an important factor in promoting the white adipogenesis of skeletal muscle (22–24). In summary, we propose the hypothesis that in DLBP patients and new animal models, the IVDs degeneration leads to fat infiltration of the paraspinal muscles, which is associated with inflammation.

In this study, firstly, we aim to clear the phenomenon of paraspinal muscle fat infiltration in DLBP patients by accurate quantitative MRI (IDEAL-IQ technology). Then, after establishing and evaluating a new DLBP animal model, we further revealed the direct causal relationship between DLBP and paraspinal muscle fatty infiltration, and explored the potential relationship between fatty infiltration and inflammatory response.

MATERIALS AND METHODS

Participants

Seventy patients with DLBP and thirty-six healthy volunteers were recruited in this study from January 2019 to May 2021 (53 males, 53 females; mean age: 44.50 years; age range: 21-74 years). Informed consent forms were signed by each participant, and ethical committee approval was obtained. The inclusion criteria were as follows: the untreated patient has symptoms of LBP for more than 3 months; Healthy volunteers have no symptoms of

LBP; BMI ranged from 18.7 to 23.4 kg/m^2. The exclusion criteria were visceral LBP (such as urinary tract stones); lumbar disc herniation, spinal stenosis, spinal trauma, fracture, tumor, infection, deformity, spondylolisthesis, surgery and other musculoskeletal diseases; pregnancy; and contraindications for MRI.

Animals

Male Sprague–Dawley (SD) rats (200–250 g) were used as experimental animals. The rats were raised under specific pathogen-free conditions and kept the ambient temperature (24-26°C) and humidity (30-50%) constant. Sterilized food and water were provided to all rats. All animal experiments were approved by the Institutional Animal Care and Use Committee of Kunming Medical University (approval number: Kmmu2021038).

DLBP Rat Model

We randomly divided sixty SD rats into three groups: control group, sham group and DLBP group (n = 20, each group). The rats in the DLBP group were anesthetized with an intraperitoneal injection of sodium pentobarbital (40 mg/kg). The rat was placed in the right decubitus position. Under the guidance of X-ray fluoroscopy, a Hamilton syringe (27G) was slowly inserted into the L4/5 and L5/6 IVDs from the posterior of the back. The puncture point was located between the transverse process and superior articular process, and the angle between the needle and horizontal plane was 45°. Anteroposterior and lateral X-ray examination of lumbar spine was used to confirmed that the needle was located in the central area of IVD (**Figures 1A–D**). The nucleus pulposus was destroyed through the needle, and sterile PBS (2.5 μL) was injected. The fluoroscopy conditions were tube voltage 52 kV and tube current 0.6 mAs. The sham group only punctured the paraspinal muscles at the L4/5 and L5/6 levels but did not puncture the IVDs. To exclude the interference caused by the puncture of paraspinal muscle, the sham group was set up. No operation in the control group. After the operation, the rats were placed under a warm lamp, put back into home cages, and recovered from anesthesia.

Behavioral Tests

Gait Analysis

At 1 day, 1 week, 2 weeks, 1 month, 3 months, and 6 months after surgery, behavioral tests were performed (gait analysis, hot plate test, acetone test, grasping test and tail suspension test) to evaluate the pain and dysfunction of the low back in the rats (**Figure 1E**).

First, the three groups of rats were scored for gait disorder (25). The rat was placed on the experiment table and its walking performance was observed. Scoring was based on the following criteria: 3 = severe dyskinesia and unable to walk; 2 = moderate dyskinesia, able to walk, but obvious limp; 1 = mild limp; 0 = normal physical activity.

Hot Plate Test

Hot plate test was used to evaluate the pain threshold to thermal stimuli (26). Rats were allowed to walk on the hot plate (55.0 ± 0.5°C) for up to 20 s. The time between the placement of the rats on the hot plate and licking the paws or jumping was recorded as the response time. Hot plate test was performed two times per rat with an intervening interval of 10 minutes.

Acetone Test

Cold hypersensitivity was assessed *via* the acetone test as previously described (27).

The acetone (50 μL) in the syringe was gently touched to the plantar skin of the left and right hind paw of the rat. Within 1 minute, the time from skin contact with acetone to paw flinching and biting was recorded. The average time on the left and right paw was taken as the response time.

Grasping Test

Grasping test was used to evaluate myodynamia (28). Briefly, the limbs grasped the upside-down iron net until it was unable to hold on within 20s. The time of grasping on the iron net reflects the muscle strength of the rat. Grasping test was measured twice and the mean value was calculated.

Tail Suspension Test

Tail suspension test (TST) was performed to evaluate muscle function in a specially manufactured tail suspension box (29). The rat was suspended 50 cm above the bottom of box by fixing its tail tip (1 cm) with adhesive tape. The time the rats struggled and bent over within 5 minutes was recorded respectively.

MR Data Acquisition

All MRI experiments were performed using a 3.0T MR system (Discovery 750w, GE Healthcare, USA). A 32-channel phased array spine coil was used for DLBP patients and healthy volunteers. To reduce motion artifacts, an abdominal bandage was used to compress the abdomen and a wedge-shaped foam pad was placed under the lower limbs of participants in a standard supine position. MRI scanning for participants included sagittal T1-weighted imaging (T1WI), T2WI of lumbar spine and axial T2WI, IDEAL-IQ of paraspinal muscles. A dedicated animal coil with an inner diameter 70 mm (CG-MUC49-H300-AG, Chenguang Medical Technologies, China) was applied for rats. After being anesthetized by an intraperitoneal injection of pentobarbital sodium (45 mg/kg), the rat was placed in a standard prone position. The towel maintains the rat's body temperature. Animal MRI included sagittal T2WI and IDEAL-IQ. The MRI protocols of participants and rats are summarized in **Table 1**.

Image Analyses

All raw MR images were transferred to a commercially available workstation (Advantage Windows 4.6, GE Medical Systems, USA). Proton density fat fraction (PDFF) was automatically postprocessed with a vendor-provided algorithm after MRI scanning. PDFF values of the bilateral paraspinal muscles were obtained on a region of interest (ROI) basis at the central level of human L4/5 and L5/S1(**Figure 2A**), and rat L4/5 and L5/6. The edges of ROI were closed to the epimysiums of multifidus and erector spinae, excluding the subcutaneous fat and fat under profundal fascia. The two radiologists manually delineated the

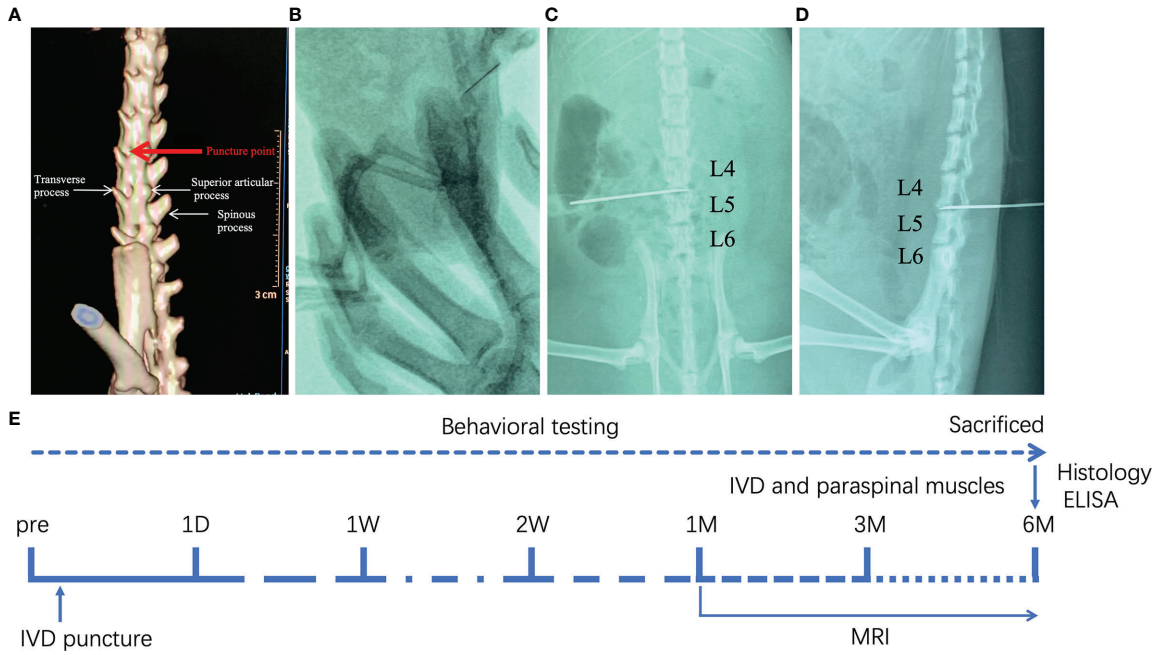

FIGURE 1 | Establishment of DLBP rat model guided by X-ray fluoroscopy. **(A)** The location of the needle puncture; **(B)** X-ray fluoroscopy; **(C, D)** X-ray lumbar spine positive and lateral positioning needle position in the IVD of L4/5 and L5/6; **(E)** the experimental schedule.

TABLE 1 | MRI scan parameters.

Images		TE (ms)	TR (ms)	ST (mm)	SL (mm)	FOV (mm^2)	NEX
Participants							
Spine	Sagittal T1WI	8.3	361	4	4	320×180	2
	Sagittal T2WI	142	2500	4	4	320×180	2
Muscles	Axial T2WI	110.5	4024	3	4	20×20	3
	IDEAL-IQ	1.2/3.2/5.2/ 7.2/9.2/11.2	7.8	4	0	24×24	2
Rat							
Spine	Sagittal T2WI	100	3190	1.2	0	10×10	4
Muscles	IDEAL-IQ	Min Full	14.4	2.0	0	15×15	2

T2WI, T2-weighted imaging; TR, time of repetition; TE, echo time; ST, slice thickness; SL, slice increment; FOV, field of view; NEX, number of excitation.

shape of the bilateral multifidus and erector spinae. The relative signal intensity of rat IVD = T2 signal intensity $_{L4/5 \text{ or } L5/6}$/T2 signal intensity $_{L3/4}$. The average of the two measurements was calculated and used for later analysis. ICC Coefficients showed a high reliability of estimates between two radiologists (ICC = 0.939, 95%CI: 0.852-0.975, p<0.001).

Histopathological Analysis

Rats in the three groups were sacrificed after the last MRI acquisition. After perfusion, the lumbar spine and paraspinal muscles at levels L4/5 and L5/6 were post-fixed in 4% paraformaldehyde. After immersion in decalcification solution for two days, the vertebral tissues were dehydrated. The decalcified lumbar spine and muscles were infiltrated and embedded with paraffin to form paraffin blocks. Then, the IVD and muscles were sliced into 5-mm-thick sections. Slices from the frontal plane were treated with xylene to remove paraffin, rehydrated in a gradient alcohol bath, and rinsed three times with PBS. The sections were respectively stained with HE and safranin O/fast green staining. Part of the separated paraspinal muscles were frozen with liquid nitrogen, and 10-micron frozen sections were obtained at -20°C. The sections were used for oil red O staining later (30). Histological images were obtained by a digital microscope.

Evaluation of TNF-α Levels

The protein levels of the cytokine TNF-α of IVDs and paraspinal muscles were measured in the rats by enzyme linked immunosorbent assay (ELISA). The IVDs and paraspinal muscles samples of rats were collected and weighed. The tissues were ground using a mortar and pestle, and homogenated in the PBS solution. High-speed hypothermal centrifugation (12000 rpm, 4°C) was performed for 10 min and the supernatant was obtained. The TNF-α protein levels were detected using an ELISA

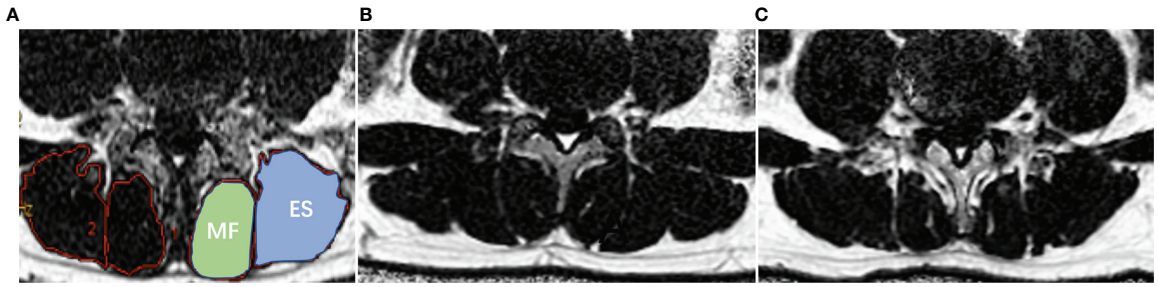

FIGURE 2 | Demonstration of paraspinal muscle segmentation and MRI PDFF of lumbar paraspinal muscle in patients with DLBP. **(A)** Processed PDFF maps of paraspinal muscles; manual segmentation of paraspinal muscles. MF: multifidus, and ES: erector spinae. **(B)** Healthy Volunteer, male, 32 years old, $PDFF_{left\ MF}$ = 7.3%, $PDFF_{right\ MF}$ = 7.8%, $PDFF_{left\ ES}$ = 8.5%, $PDFF_{right\ ES}$ = 8.7%. **(C)** Patient with DLBP, male, 28 years old, DLBP for 6 years, $PDFF_{left\ MF}$ = 18.4%, $PDFF_{right\ MF}$ =19.7%, $PDFF_{left\ ES}$ =12.0%, $PDFF_{right\ ES}$ = 13.9%.

test as previously described (31). Briefly, the cytokine TNF-α protein levels were quantified using a commercially available rat-specific ELISA kit (Rat TNF-α, ml002859, Meilian, Shanghai, China) according to the manufacturer's instructions. The samples were read at 450 nm using a spectrophotometer (SpectraMax, MD, USA).

Statistical Analysis

SPSS 22.0 was performed for the statistical analysis. Normality was tested with the Shapiro–Wilk normality test. Mean ± SD was used to express data. Comparisons between patients with DLBP and healthy volunteers were determined using the independent-sample *t*-test. One-way analysis of variance (ANOVA) was employed for the comparisons among multiple rat groups, and Tukey's multiple comparisons test was utilized for the *post hoc* test after ANOVA. A *p*-value <0.05 was reported statistically significant.

RESULT

Comparison of PDFF in the Paraspinal Muscle Between Healthy Volunteers and Patients With DLBP

Table 2 shows the baseline clinical characteristics of the participants. The PDFF of the multifidus and erector spinae of different levels of DLBP were significantly higher than those of healthy volunteers in the multifidus and erector spinae at L4/5 and L5/S1 level, and the differences were statistically significant (P<0.05, **Table 2**). The PDFF of paraspinal muscles were elevated in 1.79 times in patients with DLBP as compared to control (15.05 ± 4.50% *vs.* 8.43 ± 3.56%). **Figures 2B, C** shows the PDFF maps of the paraspinal muscles of healthy volunteers and DLBP patients. Patients with DLBP have increased fat infiltration of paraspinal muscles.

Analysis of Pain and Dysfunction Behavior in the DLBP Rats

After puncturing the lumbar IVD under X-ray guidance, the rats' gait, pain threshold to thermal and cold stimuli, grip strength and lumbar muscle function were observed. First, the gait score of the DLBP group was higher than that of the sham group and normal control group from the 2 weeks to the 6 months, and the difference was statistically significant (mean 0.78 ± 0.54 *vs.* 0.06 ± 0.23 *vs.* 0.00 ± 0.00, P <0.05, **Figure 3A**).

On the 1 week after the operation, compared with the normal group and the sham group, the DLBP group rats had increased sensitivity to heat and cold stimulation, and shorter tolerance latency in the hot plate test and the acetone test (P <0.05, **Figures 3B, C**). Compared with the normal group, the tolerance latency of the hot plate test in the DLBP group was

TABLE 2 | Comparison of Baseline Clinical Characteristics and PDFF of Paraspinal Muscle between Healthy Volunteers and DLBP Patients.

Characteristics	Healthy volunteers (n=36)	DLBP (n=70)	*p*
Male/Female	18/18	35/35	1.000
Age (year)	47.57 ± 15.78	41.67 ± 14.01	0.182
BMI (kg/m^2)	21.97 ± 1.60	22.57 ± 1.59	0.063
PDFF of MF (%)			
L4-5	7.49 ± 2.1	13.88 ± 4.70	<0.001*
L5-S1	8.03 ± 3.78	14.51 ± 4.24	<0.001*
PDFF of ES (%)			
L4-5	7.97 ± 2.8	14.57 ± 3.36	<0.001*
L5-S1	10.21 ± 4.63	17.17 ± 5.05	<0.001*

DLBP, Discogenic low back pain; PDFF, proton density fat fraction; MF, multifidus; ES, erector spinae. All values were expressed as mean ± standard deviation. Significant p-values are marked with "".*

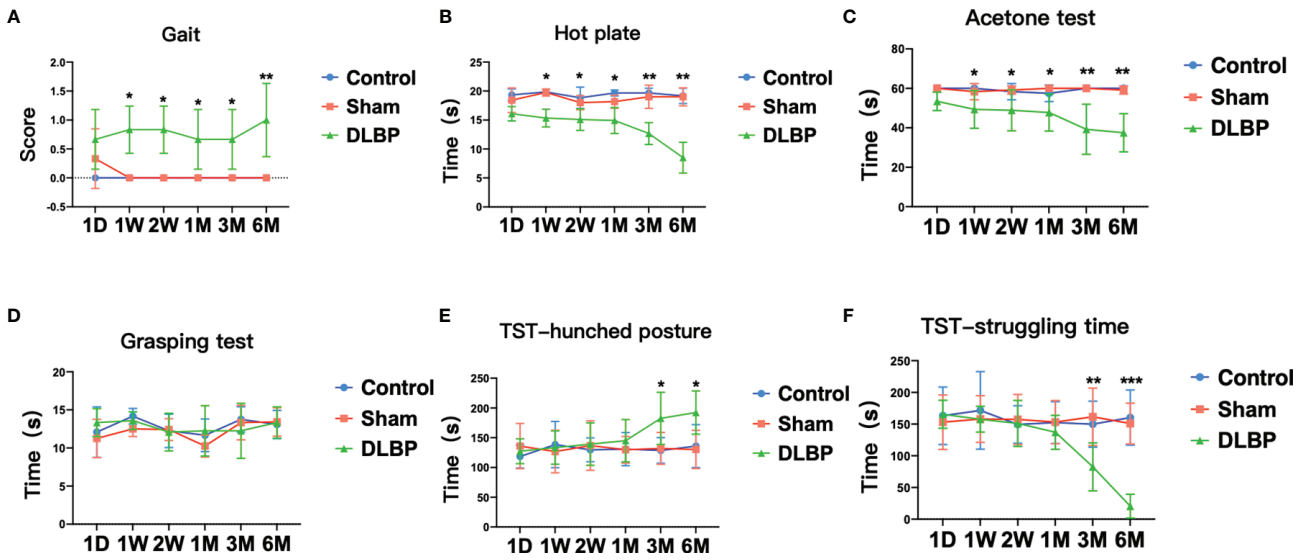

FIGURE 3 | Pain and dysfunction behavior in rats after intervertebral disc puncture. **(A)** Gait analysis; **(B)** Hot plate test, which assess thermal sensitivity; **(C)** Acetone test, which assess cold allodynia. **(D)** Grasping test; **(E, F)** TST, Tail suspension test, hunched posture **(E)** and struggling time **(F)**. Compared with control group, $^{*}p < 0.05$, $^{**}p < 0.01$, $^{***}p < 0.001$.

shortened by 4.50s, 3.70s, 4.70s, 7.00s and 10.67s from 1W to 6M, respectively. The tolerance latency of the acetone test in the DLBP group was shortened by 10.67s, 9.42s, 9.75s, 20.75s and 22.50s from 1W to 6M, respectively. However, the difference in grip strength among the three groups was not statistically significant (P>0.05, **Figure 3D**). In addition, the rats in the DLBP group had longer bending time and shorter struggling time than the normal group and sham group in the TST in the 3M and 6M (P<0.05, **Figures 3E, F**). There was no significant difference in the behavioral test between the normal group and sham group (P>0.05, **Figure 3**).

Quantitative MRI Changes in the IVD and Muscles Tissue

1 month, 3 months and 6 months after lumbar IVDs puncture in rats, the relative signal intensity of DLBP were significantly lower than those in the normal group at the L4/5 and L5/6 (1M: 0.59 ± 0.23 *vs.*1.08 ± 0.20; 3M: 0.50 ± 0.21 *vs.* 1.13 ± 0.13;6M: 0.45 ± 0.21 *vs.*1.02 ± 0.18;P <0.05, **Figure 4**). The relative T2 signal intensity of the DLBP group in 3 months and 6 months was less than 1 month, but the difference was not statistically significant (P > 0.05, **Figure 4D**). At the levels of L4/5 and L5/6, the multifidus PDFF values of the DLBP group were more than those of the normal group and sham group in the 6 months, and the difference was statistically significant (P <0.05, **Figures 5**, **6**).

Histologic and Structural Changes in IVD and Muscles Tissue and Increased TNF-α Expression

HE and Safranin Fast Green staining of IVDs showed that the histological morphology of the annulus fibrosus and nucleus pulposus in the DLBP group was changed. Compared with the control group and sham group, the collagen fibers of IVDs in the DLBP group were increased and twisted; the collagen in the cartilage was increased; the fibrous annulus was thickened, and the shape was distorted. The nucleus pulposus of the IVDs was replaced by hyperplastic cartilage cells (**Figure 7**). The HE and oil red O staining of the paraspinal muscles showed that the muscle bundle space of muscles in the DLBP group increased, and the lipid droplets in the muscle tissue increased (**Figure 8**). In addition, the expression of TNF-α in the IVDs and paraspinal muscles of the DLBP group were significantly higher than that of the control group and sham group (P <0.05, **Figure 9**). Compared with control and sham groups, TNF-α in multifidus was significantly increased in the DLBP group (DLBP *vs.* control *vs.* sham:19.52 ± 3.50 *vs.* 12.32 ± 6.65 *vs.* 12.71 ± 2.1, P <0.05). In the erector spinae, TNF-α of DLBP group were slightly increased, but no statistically significant differences were detected among three groups (DLBP *vs.* control *vs.* sham:15.33 ± 3.34 *vs.* 11.45 ± 5.96 *vs.* 13.47 ± 2.58, P >0.05).

DISCUSSION

In this study, we confirmed the increase in fat infiltration of the paraspinal muscles in clinical DLBP patients, which can be accurately quantified by MRI IDEAL-IQ. The IVDs were punctured under the guidance of X-ray fluoroscopy to establish a DLBP rat model. The animal model developed clinical symptoms, MRI findings and pathological changes consistent with human DLBP, which provides an experimental basis for studying DLBP IVDs and paraspinal muscles *in vivo*. In addition, we also found that the IVDs degeneration is directly

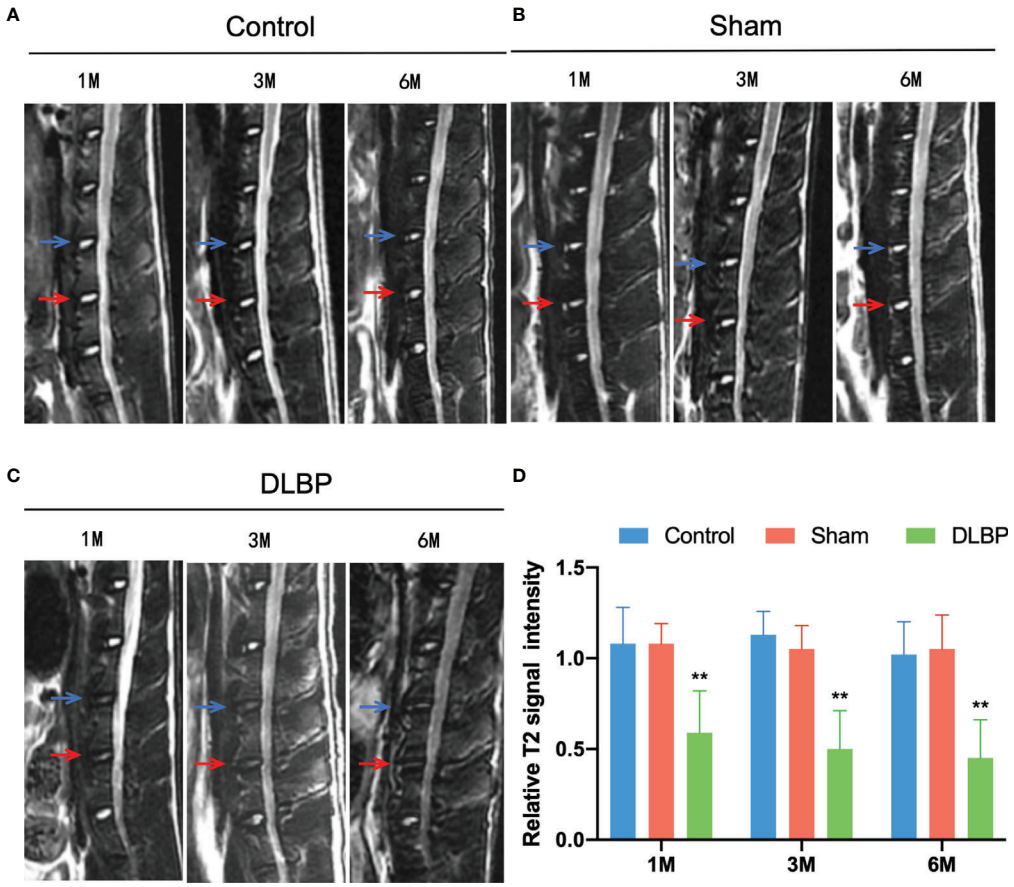

FIGURE 4 | MRI T2WI of lumbar spine of rat models from 1 month and 6 months. **(A)** Control group, L4/5 IVD (blue) and L5/6 IVD (red); **(B)** Sham group; **(C)** DLBP group; **(D)** Bar chart of relative signal intensity of IVD among three groups. Compared with control group, $^{**}p < 0.01$.

related to the fat infiltration of the paraspinal muscles in rats and may be related to inflammation.

Several previous studies have shown that the fat infiltration of paraspinal muscles may be increased in chronic LBP (10, 32), but there has been controversy (33, 34). This is related to the semi-quantitative subjective method used to assess fat infiltration in previous studies. In this study, we attempted to apply more accurate quantitative MRI to determine whether the paraspinal muscles of DLBP patients have fatty infiltration. our cross-sectional clinical study showed a significant increase in PDFF of the multifidus and erector spinae muscles at the L4/5 and L5/6 levels in patients with DLBP. This may imply that fat infiltration of paraspinal muscles may be a strategy for the treatment of DLBP.

Based on the previously reported animal model of DLBP (19, 21, 35–37), we minimally puncture and inject PBS into the lumber IVDs under the guidance of X-ray fluoroscopy to establish a DLBP rat model suitable for observing muscle changes. In humans, L4/5 and L5/S1 are predilection sites of lumbar disc disease (38, 39). To gain a better DLBP animal model, the L4/5 and L5/6 discs were punctured in rat. So, the level of the punctured discs (L4/5 and L5/6) are preferentially observed in this study. Through animal behavior experiments, we observed that the rats in the DLBP group had obvious low back pain and muscle dysfunction. *In vivo*, rat lumbar spine MRI T2WI imaging showed that the relative signal intensity of L4/5 and L5/6 IVDs decreased progressively from 1 to 3 months after the puncture, which was consistent with the T2WI findings of patients with IVDs degeneration (40, 41). Ex vivo, the typical pathological changes of IVDs degeneration have been observed in the HE staining and Safranin Fast Green staining of rat IVDs, including shrinkage of nucleus pulposus, an increase of collagen fibers, and distortion and thickening of annulus fibrosus. These histological changes are similar to Suh's DLBP model (21), but no obvious bone hyperplasia has been observed. This effective animal model is closer to the natural development of DLBP, because only the intervertebral disc is precisely damaged.

In experimental animals, we controlled degeneration of the lumbar IVDs as a single variable and then observe the dynamic development of the fat infiltration of the paraspinal muscle. After the rat's IVDs were punctured, paraspinal muscles fat content was measured by quantitative MRI *in vivo*. We found that the PDFF of the multifidus muscle of DLBP rats was significantly increased compared to the control group, which is consistent

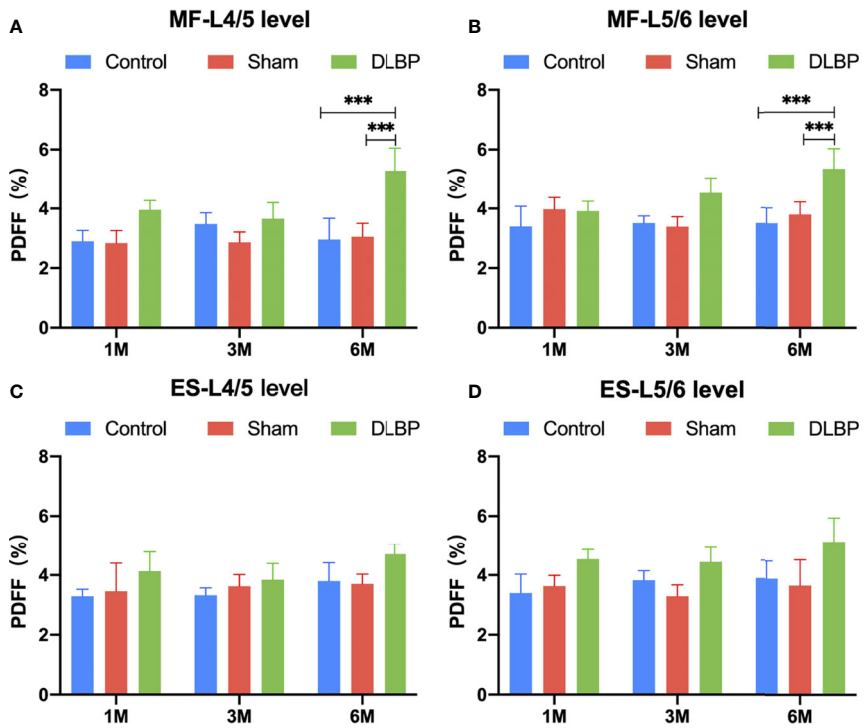

FIGURE 5 | PDFF in paraspinal muscles at L4/5 and L5/6 levels from 1 month to 6 months. **(A)** PDFF of multifidus at L4/5 level; **(B)** PDFF of multifidus at L5/6 level; **(C)** PDFF of erector spinae at L4/5 level; **(D)** PDFF of erector spinae at L5/6 level. MF, multifidus; ES, erector spinae. Compared with control group and sham group, ***$p < 0.001$.

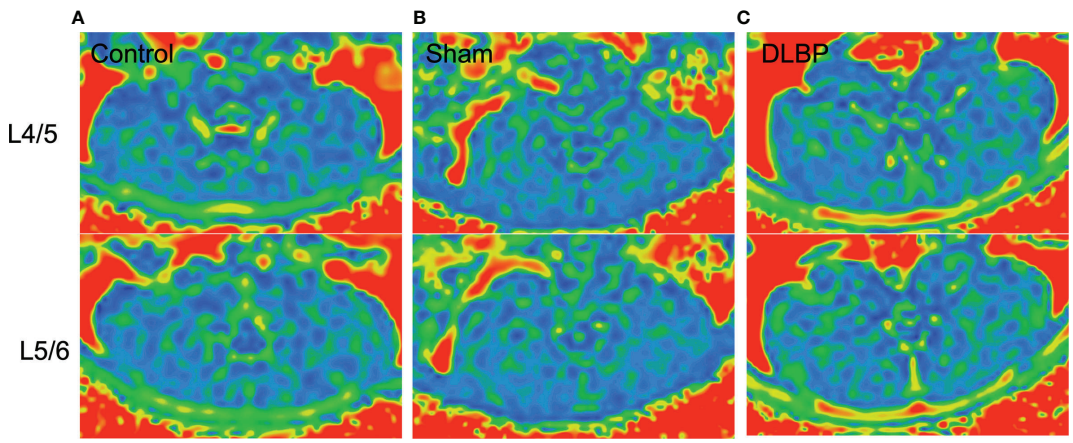

FIGURE 6 | Representative MRI PDFF images of paraspinal muscles in DLBP rats. **(A)** Control group; **(B)** Sham group; **(C)** DLBP group.

with the results of humans. Six months after puncture, we observed the widening of the muscle bundle interval and intramuscular lipids in the HE staining and Oil Red O staining of the muscle.

However, the overall muscle PDFF is lower in DLBP rats than that of clinical patients, and the increase in erector spinae muscle is not significant. This may be related to the course of the disease duration and the more developed paraspinal muscles in rats (42). But this may also imply that the multifidus muscle is a more vulnerable muscle in the paraspinal muscles of DLBP. Our study found the causal relationship between IVD degeneration and paraspinal muscle fat in DLBP rats.

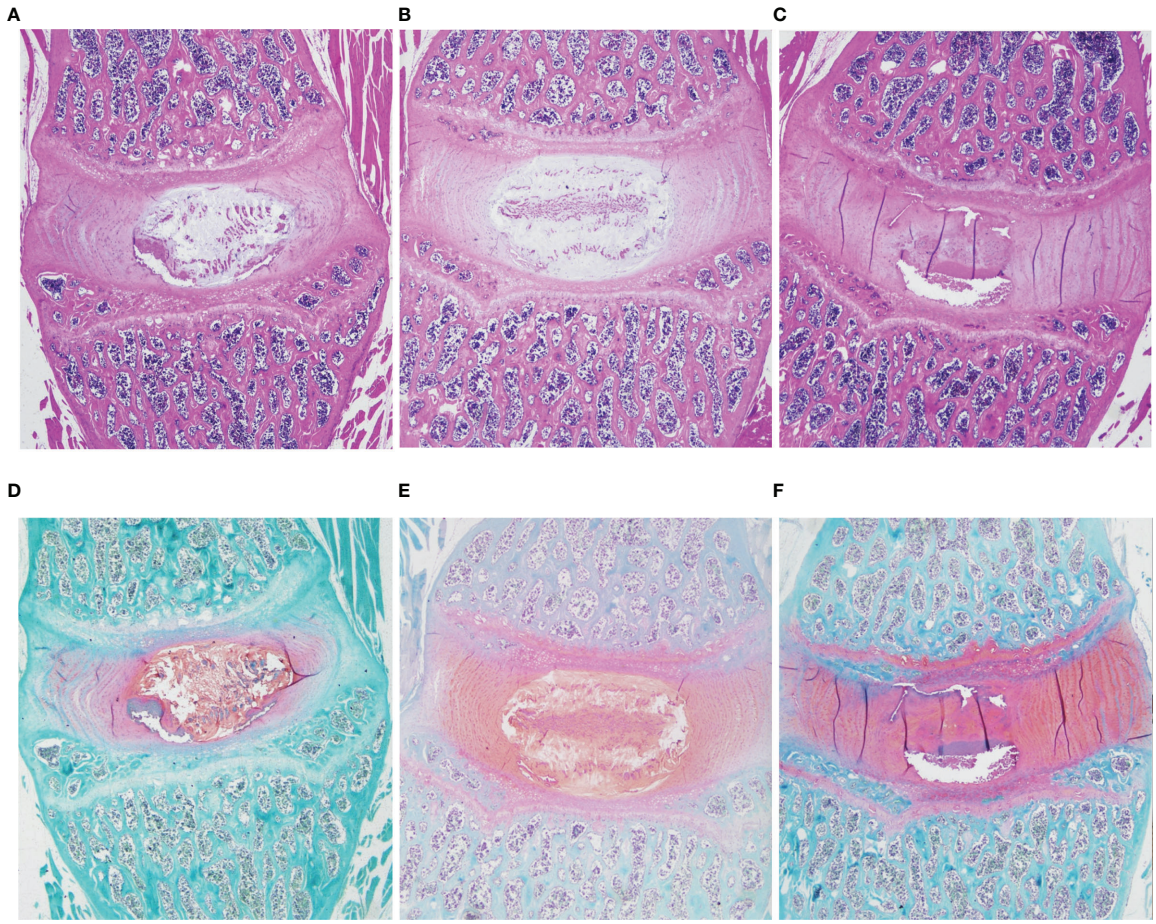

FIGURE 7 | Representative histopathological images of IVD with HE and safranin O/fast green staining at 6 months in the control, sham and DLBP groups. **(A–C)** HE, ×20; **(D–F)** Safranin O/fast green staining, ×20. HE, hematoxylin and eosin.

How the fat infiltration of paraspinal muscles occurs after IVD degeneration in the DLBP is unknown and complicated. Previous studies have reported the inflammatory response in degenerated IVDs, especially TNF-α (4, 43). In this study, the expression of TNF-α was simultaneously detected in the IVDs and paraspinal muscles of the DLBP rats. Recently, Zhu et al. found that inflammatory cells were increased in the paraspinal muscles in LBP by biopsy (44). Studies have revealed the regulatory relationship between inflammatory cells and muscle fat infiltration in diabetes (45, 46). But the interaction between inflammation in the IVD and inflammation in the muscle is still unclear. In an obesity mice model fed a high-fat diet, TNF-α may impair mitochondrial biogenesis and function in different tissues of obese rodents, suggesting that fat accumulation in skeletal muscle may be caused by movement dysfunction and inflammation (23). Meanwhile, impairment in white adipose tissue function, due to the abnormal fat accumulation, is characterized by increased production of specific pro-inflammatory proteins such as adipokines by white adipose tissue and of cytokines such as TNF by immune cells of the stromal compartment (24). In this study, inflammatory response may also contribute to the fat infiltration of paraspinal muscles in DLBP. Therefore, in this study, paraspinal muscles fat infiltration and inflammatory response may influence and promote each other in DLBP patients.

Our study has several limitations. First, due to the pelvis obscuring the L6/S1 intervertebral disc, we only punctured the L4-6 rat intervertebral disc. PBS was injected after puncturing the IVDs in this study. It may be more effective to inject some other drugs, such as nerve growth factor. Other chemicals may prove to be more effective in the future. We measured the total fat content of the paraspinal muscles in DLBP patients and rats, which will be valuable to further explore the fat distribution in the paraspinal muscles and clearly quantify the lipid levels inside and outside the muscle cells. Moreover, the regulatory relationship between inflammation and fat infiltration after IVDs degeneration is not yet clear, but we are actively conducting this research. Movement disorder after IVD puncture in rats is a potential influencing factor of fat infiltration of paraspinal muscles. Open-field test may be helpful in detecting the amount of exercise in rats. Finally, although the rat is the classic choice for the pain animal model, the physiology of humans and rats remains very

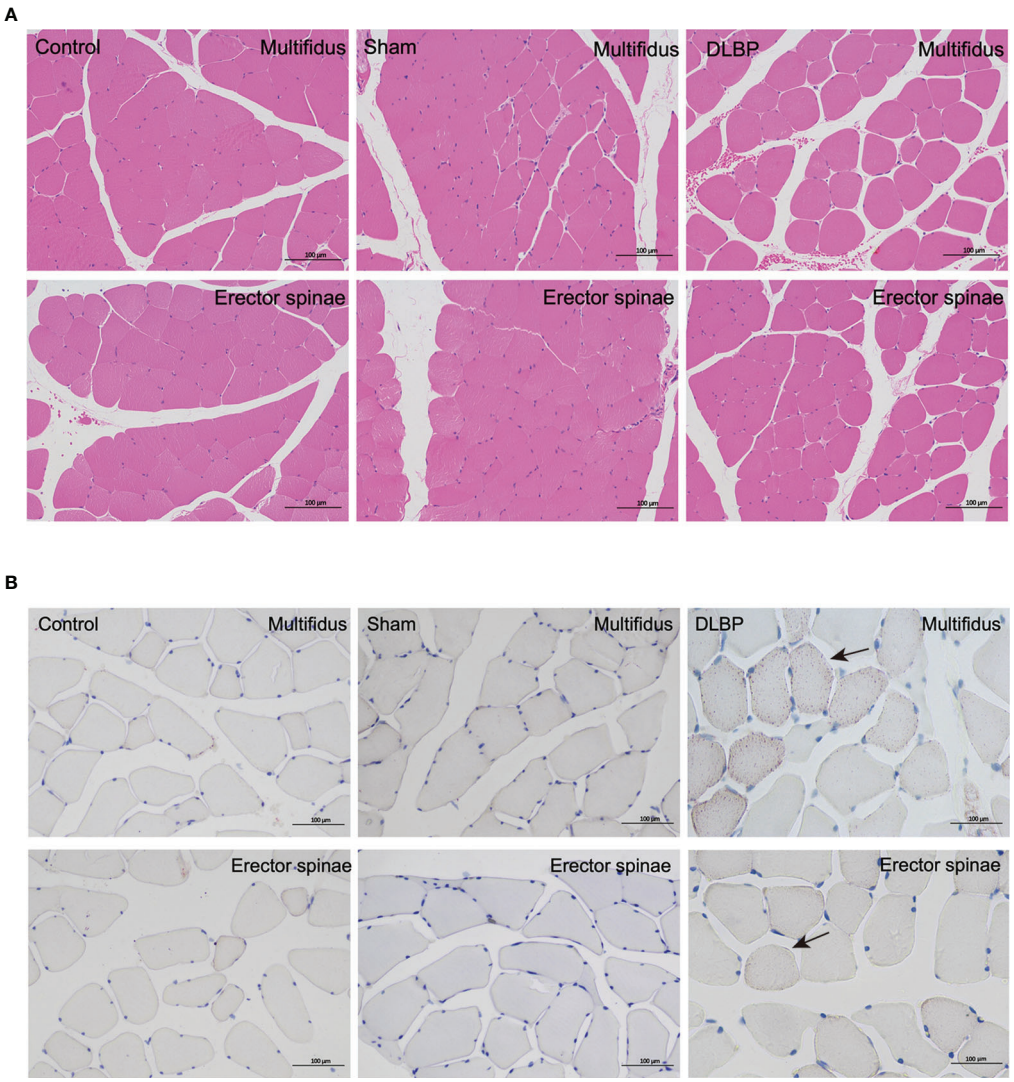

FIGURE 8 | Representative histopathological images of muscles with HE and Oil Red staining at 6 months in the control, sham and DLBP groups. **(A)** HE, ×200; **(B)** Oil Red staining, ×200. lipid droplets (black arrow). HE, hematoxylin and eosin.

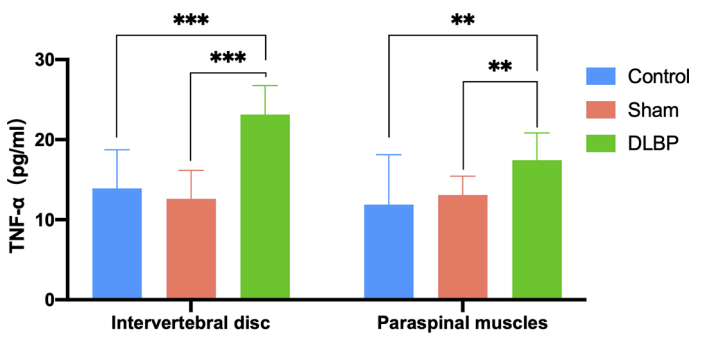

FIGURE 9 | TNF-α levels in the IVD and paraspinal muscles at 6 months. Compared with control group and sham group, $^{**}p < 0.01$, $^{***}p < 0.001$.

different. We look forward to animal experiments closer to human species or high-quality clinical cohort studies to verify the role of inflammation in the fat infiltration of paraspinal muscles after intervertebral disc degeneration.

In conclusion, we confirmed that the paraspinal muscles have fat infiltration in the DLBP patients and rats, and that there is a causal relationship between fat infiltration and IVDs degeneration. In addition, we have developed and verified a novel rat model of DLBP. We believe that this model is more suitable for future studies of DLBP muscle-related pathological mechanisms and screening of treatment strategies. After IVDs degeneration, the paraspinal muscle fat infiltration and inflammation are closely related. The paraspinal muscle fat infiltration is the detection point of the therapeutic effect of DLBP and reducing the inflammation of the paraspinal muscle is a potential strategy for DLBP treatment.

DATA AVAILABILITY STATEMENT

The original contributions presented in the study are included in the article/supplementary material. Further inquiries can be directed to the corresponding author.

ETHICS STATEMENT

The studies involving human participants were reviewed and approved by The Ethical Committee of Kunming Medical University. The patients/participants provided their written informed consent to participate in this study. The animal study was reviewed and approved by The Ethical Committee of Kunming Medical University. Written informed consent was obtained from the individual(s) for the publication of any potentially identifiable images or data included in this article.

AUTHOR CONTRIBUTIONS

BH: designed the study and conceived the report. YH and LW: wrote the draft of the manuscript and revised it critically. BL, KY, and YL: established the rat model and behavioral experiment. YH, XZ, and JC: human and animal MRI scan. YH, BL, KY, and ZZ: performed the histological experiment, including HE staining, Oil Red O staining and Safranin Fast Green Staining. YH, LW, XC and BH: data measurement, analysis and statistics. YH and LW: created the figures and tables. All authors contributed to the article and approved the submitted version.

FUNDING

This work is supported by the Applied Basic Research Project of Yunnan Province- Kunming Medical University Joint Fund (202001AY070001-038, 202001AY070001-200), Yunnan Provincial Bone and Joint Disease Clinical Medicine Center Project (ZX2019-03-04), and Beijing Hospitals Authority Youth Programme (QMS20200402).

REFERENCES

1. Buchbinder R, van Tulder M, Öberg B, Costa LM, Woolf A, Schoene M, et al. Low Back Pain: A Call for Action. *Lancet* (2018) 391(10137):2384–8. doi: 10.1016/s0140-6736(18)30488-4
2. Hartvigsen J, Hancock MJ, Kongsted A, Louw Q, Ferreira ML, Genevay S, et al. What Low Back Pain Is and Why We Need to Pay Attention. *Lancet* (2018) 391(10137):2356–67. doi: 10.1016/s0140-6736(18)30480-x
3. Zhang YG, Guo TM, Guo X, Wu SX. Clinical Diagnosis for Discogenic Low Back Pain. *Int J Biol Sci* (2009) 5(7):647–58. doi: 10.7150/ijbs.5.647
4. Lyu FJ, Cui H, Pan H, Mc Cheung K, Cao X, Iatridis JC, et al. Painful Intervertebral Disc Degeneration and Inflammation: From Laboratory Evidence to Clinical Interventions. *Bone Res* (2021) 9(1):7. doi: 10.1038/s41413-020-00125-x
5. Cherkin D, Balderson B, Wellman R, Hsu C, Sherman KJ, Evers SC, et al. Effect of Low Back Pain Risk-Stratification Strategy on Patient Outcomes and Care Processes: The MATCH Randomized Trial in Primary Care. *J Gen Intern Med* (2018) 33(8):1324–36. doi: 10.1007/s11606-018-4468-9
6. Hodges PW, Danneels L. Changes in Structure and Function of the Back Muscles in Low Back Pain: Different Time Points, Observations, and Mechanisms. *J Orthop Sports Phys Ther* (2019) 49(6):464–76. doi: 10.2519/jospt.2019.8827
7. Kjaer P, Bendix T, Sorensen JS, Korsholm L, Leboeuf-Yde C. Are MRI-Defined Fat Infiltrations in the Multifidus Muscles Associated With Low Back Pain? *BMC Med* (2007) 5:2. doi: 10.1186/1741-7015-5-2
8. Danneels LA, Vanderstraeten GG, Cambier DC, Witvrouw EE, De Cuyper HJ. CT Imaging of Trunk Muscles in Chronic Low Back Pain Patients and Healthy Control Subjects. *Eur Spine J* (2000) 9(4):266–72. doi: 10.1007/s005860000190
9. Kamaz M, Kireşi D, Oğuz H, Emlik D, Levendoğlu F. CT Measurement of Trunk Muscle Areas in Patients With Chronic Low Back Pain. *Diagn Interv Radiol* (2007) 13(3):144–8.
10. Wan Q, Lin C, Li X, Zeng W, Ma C. MRI Assessment of Paraspinal Muscles in Patients With Acute and Chronic Unilateral Low Back Pain. *Br J Radiol* (2015) 88(1053):20140546. doi: 10.1259/bjr.20140546
11. Sollmann N, Dieckmeyer M, Schlaeger S, Rohrmeier A, Syvaeri J, Diefenbach MN, et al. Associations Between Lumbar Vertebral Bone Marrow and Paraspinal Muscle Fat Compositions-An Investigation by Chemical Shift Encoding-Based Water-Fat MRI. *Front Endocrinol (Lausanne)* (2018) 9:563. doi: 10.3389/fendo.2018.00563
12. Jiang H, Chen HC, Lafata KJ, Bashir MR. Week 4 Liver Fat Reduction on MRI as an Early Predictor of Treatment Response in Participants With Nonalcoholic Steatohepatitis. *Radiology* (2021) 300(2):361–8. doi: 10.1148/radiol.2021204325
13. Grimm A, Meyer H, Nickel MD, Nittka M, Raithel E, Chaudry O, et al. Repeatability of Dixon Magnetic Resonance Imaging and Magnetic Resonance Spectroscopy for Quantitative Muscle Fat Assessments in the Thigh. *J Cachexia Sarcopenia Muscle* (2018) 9(6):1093–100. doi: 10.1002/jcsm.12343
14. Agten CA, Rosskopf AB, Gerber C, Pfirrmann CW. Quantification of Early Fatty Infiltration of the Rotator Cuff Muscles: Comparison of Multi-Echo Dixon With Single-Voxel MR Spectroscopy. *Eur Radiol* (2016) 26(10):3719–27. doi: 10.1007/s00330-015-4144-y
15. Mengiardi B, Schmid MR, Boos N, Pfirrmann CW, Brunner F, Elfering A, et al. Fat Content of Lumbar Paraspinal Muscles in Patients With Chronic Low Back Pain and in Asymptomatic Volunteers: Quantification With MR Spectroscopy. *Radiology* (2006) 240(3):786–92. doi: 10.1148/radiol.2403050820
16. Seyedhoseinpoor T, Taghipour M, Dadgoo M, Sanjari MA, Takamjani IE, Kazemnejad A, et al. Alteration of Lumbar Muscle Morphology and

Composition in Relation to Low Back Pain: A Systematic Review and Meta-Analysis. *Spine J* (2022) 22(4):660–76. doi: 10.1016/j.spinee.2021.10.018
17. Shi C, Qiu S, Riester SM, Das V, Zhu B, Wallace AA, et al. Animal Models for Studying the Etiology and Treatment of Low Back Pain. *J Orthop Res* (2018) 36(5):1305–12. doi: 10.1002/jor.23741
18. Kim JS, Kroin JS, Li X, An HS, Buvanendran A, Yan D, et al. The Rat Intervertebral Disk Degeneration Pain Model: Relationships Between Biological and Structural Alterations and Pain. *Arthritis Res Ther* (2011) 13 (5):R165. doi: 10.1186/ar3485
19. Lee M, Kim BJ, Lim EJ, Back SK, Lee JH, Yu SW, et al. Complete Freund's Adjuvant-Induced Intervertebral Discitis as an Animal Model for Discogenic Low Back Pain. *Anesth Analg* (2009) 109(4):1287–96. doi: 10.1213/ane.0b013e3181b31f39
20. Li Z, Liu H, Yang H, Wang J, Wang H, Zhang K, et al. Both Expression of Cytokines and Posterior Annulus Fibrosus Rupture Are Essential for Pain Behavior Changes Induced by Degenerative Intervertebral Disc: An Experimental Study in Rats. *J Orthop Res* (2014) 32(2):262–72. doi: 10.1002/jor.22494
21. Suh HR, Cho HY, Han HC. Development of a Novel Model of Intervertebral Disc Degeneration by the Intradiscal Application of Monosodium Iodoacetate (MIA) in Rat. *Spine J* (2021) 22(1):183–92. doi: 10.1016/j.spinee.2021.06.008
22. Wang Y, Che M, Xin J, Zheng Z, Li J, Zhang S. The Role of IL-1β and TNF-α in Intervertebral Disc Degeneration. *BioMed Pharmacother* (2020) 131:110660. doi: 10.1016/j.biopha.2020.110660
23. Valerio A, Cardile A, Cozzi V, Bracale R, Tedesco L, Pisconti A, et al. TNF-Alpha Downregulates eNOS Expression and Mitochondrial Biogenesis in Fat and Muscle of Obese Rodents. *J Clin Invest* (2006) 116(10):2791–8. doi: 10.1172/jci28570
24. Francisco V, Pino J, González-Gay M, Lago F, Karppinen J, Tervonen O, et al. A New Immunometabolic Perspective of Intervertebral Disc Degeneration. *Nat Rev Rheumatol* (2022) 18(1):47–60. doi: 10.1038/s41584-021-00713-z
25. Chatani K, Kawakami M, Weinstein JN, Meller ST, Gebhart GF. Characterization of Thermal Hyperalgesia, C-Fos Expression, and Alterations in Neuropeptides After Mechanical Irritation of the Dorsal Root Ganglion. *Spine (Phila Pa 1976)* (1995) 20(3):277–89; discussion 90. doi: 10.1097/00007632-199502000-00004
26. Wang G, Long C, Liu W, Xu C, Zhang M, Li Q, et al. Novel Sodium Channel Inhibitor From Leeches. *Front Pharmacol* (2018) 9:186. doi: 10.3389/fphar.2018.00186
27. Miyano K, Shiraishi S, Minami K, Sudo Y, Suzuki M, Yokoyama T, et al. Carboplatin Enhances the Activity of Human Transient Receptor Potential Ankyrin 1 Through the Cyclic AMP-Protein Kinase A-A-Kinase Anchoring Protein (AKAP) Pathways. *Int J Mol Sci* (2019) 20(13):3271. doi: 10.3390/ijms20133271
28. Dai C, Liu Y, Dong Z. Tanshinone I Alleviates Motor and Cognitive Impairments *via* Suppressing Oxidative Stress in the Neonatal Rats After Hypoxic-Ischemic Brain Damage. *Mol Brain* (2017) 10(1):52. doi: 10.1186/s13041-017-0332-9
29. Steru L, Chermat R, Thierry B, Simon P. The Tail Suspension Test: A New Method for Screening Antidepressants in Mice. *Psychopharmacol (Berl)* (1985) 85(3):367–70. doi: 10.1007/bf00428203
30. Mehlem A, Hagberg CE, Muhl L, Eriksson U, Falkevall A. Imaging of Neutral Lipids by Oil Red O for Analyzing the Metabolic Status in Health and Disease. *Nat Protoc* (2013) 8(6):1149–54. doi: 10.1038/nprot.2013.055
31. Liu K, Wei J, Li G, Liu R, Zhao D, Zhang Y, et al. Fexofenadine Protects Against Intervertebral Disc Degeneration Through TNF Signaling. *Front Cell Dev Biol* (2021) 9:687024. doi: 10.3389/fcell.2021.687024
32. Faur C, Patrascu JM, Haragus H, Anglitoiu B. Correlation Between Multifidus Fatty Atrophy and Lumbar Disc Degeneration in Low Back Pain. *BMC Musculoskelet Disord* (2019) 20(1):414. doi: 10.1186/s12891-019-2786-7
33. Ranger TA, Cicuttini FM, Jensen TS, Peiris WL, Hussain SM, Fairley J, et al. Are the Size and Composition of the Paraspinal Muscles Associated With Low Back Pain? A Systematic Review. *Spine J* (2017) 17(11):1729–48. doi: 10.1016/j.spinee.2017.07.002
34. Fortin M, Macedo LG. Multifidus and Paraspinal Muscle Group Cross-Sectional Areas of Patients With Low Back Pain and Control Patients: A Systematic Review With a Focus on Blinding. *Phys Ther* (2013) 93(7):873–88. doi: 10.2522/ptj.20120457
35. Lai A, Moon A, Purmessur D, Skovrlj B, Winkelstein BA, Cho SK, et al. Assessment of Functional and Behavioral Changes Sensitive to Painful Disc Degeneration. *J Orthop Res* (2015) 33(5):755–64. doi: 10.1002/jor.22833
36. Millecamps M, Tajerian M, Naso L, Sage HE, Stone LS. Lumbar Intervertebral Disc Degeneration Associated With Axial and Radiating Low Back Pain in Ageing SPARC-Null Mice. *Pain* (2012) 153(6):1167–79. doi: 10.1016/j.pain.2012.01.027
37. Millecamps M, Tajerian M, Sage EH, Stone LS. Behavioral Signs of Chronic Back Pain in the SPARC-Null Mouse. *Spine (Phila Pa 1976)* (2011) 36(2):95–102. doi: 10.1097/BRS.0b013e3181cd9d75
38. Porchet F, Wietlisbach V, Burnand B, Daeppen K, Villemure JG, Vader JP. Relationship Between Severity of Lumbar Disc Disease and Disability Scores in Sciatica Patients. *Neurosurgery* (2002) 50(6):1253–9; discussion 9-60. doi: 10.1097/00006123-200206000-00014
39. Lee SK, Jung JY, Kang YR, Jung JH, Yang JJ. Fat Quantification of Multifidus Muscle Using T2-Weighted Dixon: Which Measurement Methods are Best Suited for Revealing the Relationship Between Fat Infiltration and Herniated Nucleus Pulposus. *Skeletal Radiol* (2020) 49(2):263–71. doi: 10.1007/s00256-019-03270-5
40. Cao Y, Guo QW, Wan YD. Significant Association Between the T2 Values of Vertebral Cartilage Endplates and Pfirrmann Grading. *Orthop Surg* (2020) 12 (4):1164–72. doi: 10.1111/os.12727
41. Liang X, Xie R, Hou B, Li Y, Xiong Y, Yin C, et al. Feasibility Study for Evaluating Lumbar Intervertebral Disc Degeneration Using Histogram Analysis of T2* Values. *Eur Spine J* (2020) 29(10):2600–8. doi: 10.1007/s00586-020-06476-7
42. Inomata K, Tsuji K, Onuma H, Hoshino T, Udo M, Akiyama M, et al. Time Course Analyses of Structural Changes in the Infrapatellar Fat Pad and Synovial Membrane During Inflammation-Induced Persistent Pain Development in Rat Knee Joint. *BMC Musculoskelet Disord* (2019) 20(1):8. doi: 10.1186/s12891-018-2391-1
43. Ruiz-Fernández C, Francisco V, Pino J, Mera A, González-Gay MA, Gómez R, et al. Molecular Relationships Among Obesity, Inflammation and Intervertebral Disc Degeneration: Are Adipokines the Common Link? *Int J Mol Sci* (2019) 20(8):2030. doi: 10.3390/ijms20082030
44. Zhu DC, Lin JH, Xu JJ, Guo Q, Wang YH, Jiang C, et al. An Assessment of Morphological and Pathological Changes in Paravertebral Muscle Degeneration Using Imaging and Histological Analysis: A Cross-Sectional Study. *BMC Musculoskelet Disord* (2021) 22(1):854. doi: 10.1186/s12891-021-04734-3
45. Wu H, Ballantyne CM. Skeletal Muscle Inflammation and Insulin Resistance in Obesity. *J Clin Invest* (2017) 127(1):43–54. doi: 10.1172/jci88880
46. Shimobayashi M, Albert V, Woelnerhanssen B, Frei IC, Weissenberger D, Meyer-Gerspach AC, et al. Insulin Resistance Causes Inflammation in Adipose Tissue. *J Clin Invest* (2018) 128(4):1538–50. doi: 10.1172/jci96139

Conflict of Interest: The authors declare that the research was conducted in the absence of any commercial or financial relationships that could be construed as a potential conflict of interest.

frontiers | Frontiers in Endocrinology

ORIGINAL RESEARCH
published: 06 June 2022
doi: 10.3389/fendo.2022.890371

Automatic Grading of Disc Herniation, Central Canal Stenosis and Nerve Roots Compression in Lumbar Magnetic Resonance Image Diagnosis

Zhi-Hai Su[1†], Jin Liu[2†], Min-Sheng Yang[1], Zi-Yang Chen[1], Ke You[1], Jun Shen[1], Cheng-Jie Huang[1], Qing-Hao Zhao[3], En-Qing Liu[3], Lei Zhao[4], Qian-Jin Feng[4], Shu-Mao Pang[4], Shao-Lin Li[2‡] and Hai Lu[1*‡]*

[1] Department of Spinal Surgery, The Fifth Affiliated Hospital of Sun Yat-Sen University, Zhuhai, China, [2] Department of Radiology, The Fifth Affiliated Hospital of Sun Yat-Sen University, Zhuhai, China, [3] Department of Spinal Surgery, The Third Affiliated Hospital of Southern Medical University, Guangzhou, China, [4] School of Biomedical Engineering, Guangdong Provincial Key Laboratory of Medical Image Processing, Southern Medical University, Guangzhou, China

OPEN ACCESS

Edited by:
Bing Wu,
GE Healthcare (China), China

Reviewed by:
Lizhi Xie,
GE Healthcare (China), China
Jiulou Zhang,
Nanjing Medical University, China

***Correspondence:**
Hai Lu
lvhai@mail.sysu.edu.cn
Shao-Lin Li
lishlin5@mail.sysu.edu.cn

[†]These authors have contributed equally to this work and share first authorship

[‡]These authors have contributed equally to this work and share last authorship

Specialty section:
This article was submitted to Bone Research, a section of the journal Frontiers in Endocrinology

Received: *05 March 2022*
Accepted: *27 April 2022*
Published: *06 June 2022*

Citation:
Su Z-H, Liu J, Yang M-S, Chen Z-Y, You K, Shen J, Huang C-J, Zhao Q-H, Liu E-Q, Zhao L, Feng Q-J, Pang S-M, Li S-L and Lu H (2022) Automatic Grading of Disc Herniation, Central Canal Stenosis and Nerve Roots Compression in Lumbar Magnetic Resonance Image Diagnosis. Front. Endocrinol. 13:890371. doi: 10.3389/fendo.2022.890371

Aim: Accurate severity grading of lumbar spine disease by magnetic resonance images (MRIs) plays an important role in selecting appropriate treatment for the disease. However, interpreting these complex MRIs is a repetitive and time-consuming workload for clinicians, especially radiologists. Here, we aim to develop a multi-task classification model based on artificial intelligence for automated grading of lumbar disc herniation (LDH), lumbar central canal stenosis (LCCS) and lumbar nerve roots compression (LNRC) at lumbar axial MRIs.

Methods: Total 15254 lumbar axial T2W MRIs as the internal dataset obtained from the Fifth Affiliated Hospital of Sun Yat-sen University from January 2015 to May 2019 and 1273 axial T2W MRIs as the external test dataset obtained from the Third Affiliated Hospital of Southern Medical University from June 2016 to December 2017 were analyzed in this retrospective study. Two clinicians annotated and graded all MRIs using the three international classification systems. In agreement, these results served as the reference standard; In disagreement, outcomes were adjudicated by an expert surgeon to establish the reference standard. The internal dataset was randomly split into an internal training set (70%), validation set (15%) and test set (15%). The multi-task classification model based on ResNet-50 consists of a backbone network for feature extraction and three fully-connected (FC) networks for classification and performs the classification tasks of LDH, LCCS, and LNRC at lumbar MRIs. Precision, accuracy, sensitivity, specificity, F1 scores, confusion matrices, receiver-operating characteristics and interrater agreement (Gwet k) were utilized to assess the model's performance on the internal test dataset and external test datasets.

Results: A total of 1115 patients, including 1015 patients from the internal dataset and 100 patients from the external test dataset [mean age, 49 years ± 15 (standard deviation); 543 women], were evaluated in this study. The overall accuracies of grading for LDH, LCCS and LNRC were 84.17% (74.16%), 86.99% (79.65%) and 81.21% (74.16%)

respectively on the internal (external) test dataset. Internal and external testing of three spinal diseases showed substantial to the almost perfect agreement (k, 0.67 - 0.85) for the multi-task classification model.

Conclusion: The multi-task classification model has achieved promising performance in the automated grading of LDH, LCCS and LNRC at lumbar axial T2W MRIs.

Keywords: magnetic resonance imaging, diagnosis, deep learning, artificial intelligence, low back pain

INTRODUCTION

Low back pain (LBP) is the leading worldwide cause of years lost to disability, and its medical burden is growing alongside the increasing and aging population (1, 2). Lumbar disc herniation (LDH), lumbar central canal stenosis (LCCS) and lumbar nerve roots compression (LNRC) are the most common causes of LBP (1, 3), which are the leading reasons for individuals seeking medical care. Lumbar magnetic resonance (MR) imaging is a crucial tool to explain complicated causes of LBP and decide whether to treat it conservatively or surgically (4–6).

MR imaging is preferred in diagnosing LBP and can accurately grade LDH (7, 8), LCCS (9) and LNRC (10, 11). Each grading of these three diseases plays an essential role in determining appropriate treatment options. However, interpreting these complex MR images (MRIs) is a repetitive and time-consuming workload for radiologists (12). The artificial intelligence-based on deep-learning (DL) algorithm has great potential benefits in medical imaging diagnostics since it can provide semi-automated reports under the supervision of clinicians (13). It may improve the accuracy, consistency, objectivity and efficiency of disease degree assessment, further supporting clinical decision-making. Mathematically, disease diagnosis is a classification problem.

Recently, researchers have proposed some single-task classification models based on the DL algorithm for lumbar disease diagnosis from lumbar spine MRIs (14–16). These models based on the DL algorithm show that they can address this classification problem well with the advantage of automatically learning representative features from MRIs. However, one or more causes of low back pain may coexist on the same axial MRI image. The single-task classification model has the limitation of insufficient information utilization, resulting in missed or delayed diagnosis, which may be limited in clinical application. A multi-task classification model has become one of the current research hotspots to address this challenge. By identifying correlations between multiple training tasks, it carries on joint learning to these tasks, thereby improving the generalization ability of the model. A multi-task classification model for evaluating the severity of numerous lumbar diseases at MRIs would be desirable and help clinicians make a thorough diagnosis.

To the best of our knowledge, few multi-task classification models have been currently developed to classify multiple lumbar diseases at MRIs (17, 18). This study aimed to develop a multi-task classification model that can provide clinicians with a precise and comprehensive diagnostic way for automated grading of LDH, LCCS and LNRC at lumbar axial MRIs. After the model was trained, its accuracy performance was assessed on an internal test dataset and an external test dataset, compared with clinicians.

METHODS

The institutional review board of our institution approved this retrospective study with a waiver of informed consent.

Datasets Preparation

Our study analyzed 15254 axial T2W MRIs as the internal data set collected for 1015 patients who received lumbar spine MRIs in the Fifth affiliated Hospital of Sun Yat-sen University from January 2015 to May 2019. Before, 143 patients were excluded based on the exclusion criteria. We screened studies based on the following inclusion criteria: patients undergoing lumbar MR imaging because of LBP were suitable to participate in this study. Exclusion criteria for the study were as follows: (1) vertebral fractures and/or active inflammation at lumbar MRIs; (2) history of concomitant malignancy; (3) previous spine surgery; (4) severe artifacts at lumbar MRIs. The patients of our internal data set were split into training (n = 710), validation (n = 152) and test sets (n = 153). In addition, external validation was performed on the external test dataset, which contains 1273 axial T2W MRIs from 100 patients who received lumbar spine MRIs in the Third Affiliated Hospital of Southern Medical University, from June 2016 to December 2017. All patients received a lumbar MRI scan using a 3.0-T unit (Magnetom Verio; Siemens, Erlangen, Germany) with T2-weighted turbo spin echo sequence (T2W TSE). The characteristics of T2W TSE in the datasets varied: Repetition time: 3500 to 3775 ms. Echo time: 94 to 120 ms. Field of view: 153 × 153 mm^2. Slice thickness: 4 to 4.5 mm. Bandwidth: 250 kHz. The lumbar MRI images were stored as DICOM files (Digital Imaging and Communications in Medicine). The patients' demographics of the two datasets are summarized in **Table 1**, and a flowchart of the data selection processes is illustrated in **Figure 1**.

Dataset Labeling

As regions of interest (ROIs), Bounding boxes were drawn at all images by one expert surgeon with MRIcro software. Grading on these three lumbar spinal diseases was then performed for this study, with the three classification systems, which were done using well-established criteria for LDH (7, 19), LCCS (9, 20) and LNRC (10, 11).

TABLE 1 | Patients' demographic.

Characteristics	All Internal Datasets (n=1015)	External Test Dataset (n=100)
Age (y)*	49 ± 14 (13-88)	53 ± 16 (17-84)
Men	523 (51.5)	49 (49.0)
Women	492 (48.5)	51 (51.0)

Unless otherwise stated, data are numbers of patients, with percentages in parentheses.
**Data are means ± standard deviations, with ranges in parentheses.*

The three classification systems are described in the following: the classification system of LDH is divided into four grades, according to the size of disc herniation: Grade 0, Grade 1, Grade 2 and Grade 3 (**Figure 2**); the classification system of LCCS is divided into four grades based on the space of anterior cerebrospinal fluid: grade 0, grade 1, grade 2 and grade 3 (**Figure 3**); the classification system of LNRC is also divided into four grades, grade 0, grade 1, grade 2 and grade 3 (**Figure 4**). Two clinicians independently analyzed each axial T2W TSE MR image of the internal dataset and graded it using the above classification systems. In cases of agreement, these grading results of two clinicians served as the reference standard; in cases of disagreement, these grading results were adjudicated by an experienced spinal surgeon to establish the reference standard. Gwet k was used to assess inter-reader reliability between both clinicians for each classification system (21, 22). The external test dataset was graded by two clinicians independently, using the same method. In cases of agreement, these grading results of two clinicians served as the reference standard; in disagreement, these grading results were adjudicated by an experienced spinal surgeon to establish the reference standard.

Multi-Task Classification Model

The multi-task classification model consists of a backbone network for feature extraction and three fully-connected (FC) networks for classification, as shown in **Figure 5**. The backbone network is a ResNet-50 framework (23), usually used to extract image features, excluding the fully-connected network. A 2048-dimension feature is extracted by the backbone network and then is put into the three parallel FC networks, whose outputs denote the classification result of LDH, LCCS and LNRC. Cross entropy is used as the loss function. The network is capable of capturing the implicit correlation between LDH, LCCS and LNRC since the three classification tasks share a backbone network. The

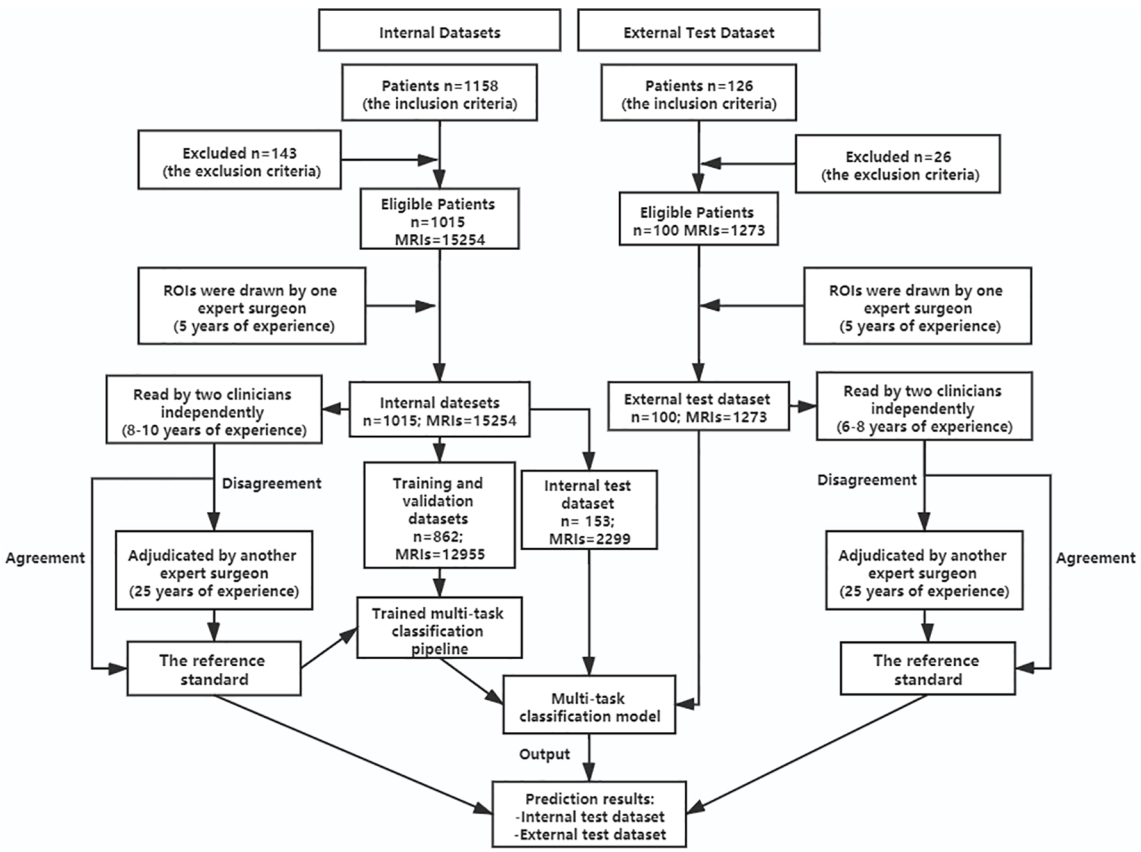

FIGURE 1 | Flowchart showing patients' selection for the datasets and the process of training multi-task classification model. n, number of patients; MRIs, MRI images; ROIs, regions of interest.

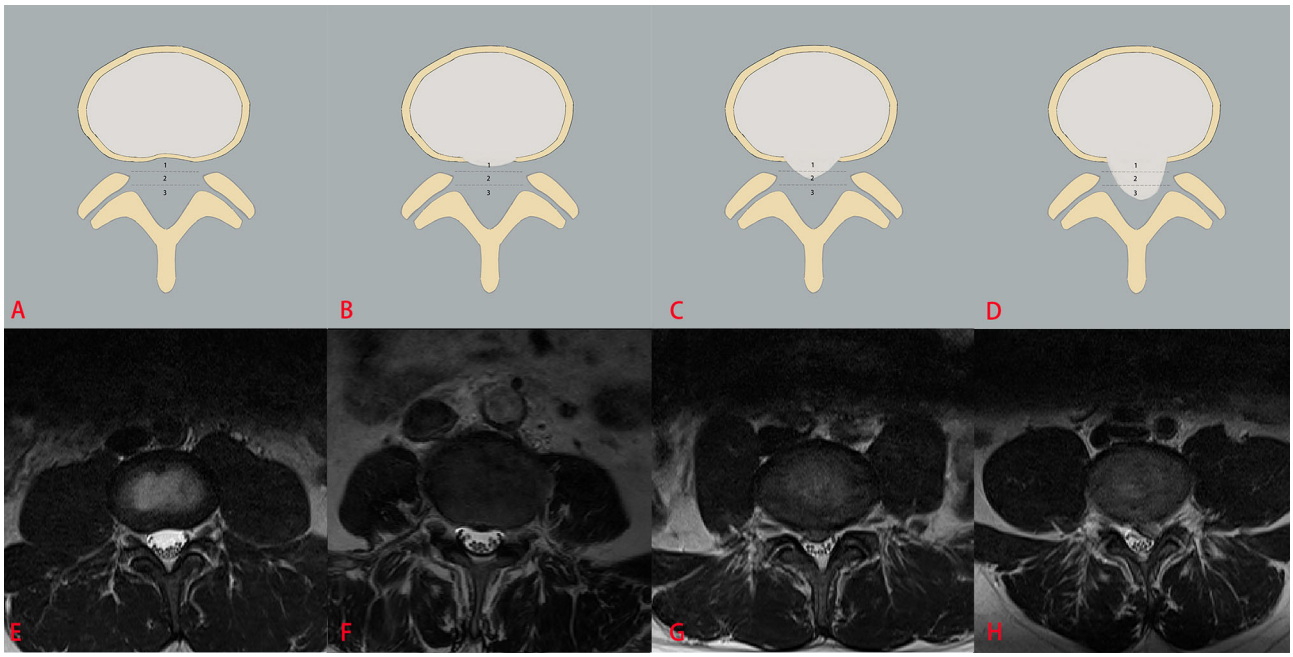

FIGURE 2 | The classification system of the lumbar disc herniation (LDH). The top column is a schematic diagram of four grades with LDH, and the bottom column is the corresponding axial T2W TSE images of four grades with LDH. The size of disc herniation is measured with reference to a single intra-facet line drawn transversely across the lumbar canal, to and from the medial edges of the right and left facet joint articulations. Grade 0 **(A, E)** no disc herniation; Grade 1 **(B, F)** the disc herniation extends up to or less than 50% of the distance from the non-herniated posterior aspect of the disc to the intra-facet line (size-1), Grade 2 **(C, G)** the disc herniation extends up to or more than 50% of the distance from the non-herniated posterior aspect of the disc to the intra-facet line (size-2), Grade 3 **(D, H)**, the herniation extends altogether beyond the intra-facet line (size-3).

multitask classification network was trained with a batch size of 16 for 100 epochs using the Adam optimizer with a weight decay of 0.0001. The learning rate was set to 0.001 initially. The training data was online augmented by random rotation of -15° to 15° and random cropping to improve the generalization of the model. All the networks were implemented by Pytorch (https://pytorch.org), and codes ran in a server with an RTX 2080Ti GPU. Training the multitask classification network took about 2.5 hours. Testing an image only took 11 ms.

Statistical Analysis

Quantitative evaluation metrics including precision, accuracy, sensitivity, specificity, F1 scores, confusion matrices, receiver-operating characteristics (ROC) were applied to assess the diagnostic performance of the multi-task classification network on the two test datasets. Gwet k values with 95% confidence intervals (CIs) were used to evaluate the inter-readers reliability and this model's clinical reliability. The model was trained and assessed by an information technology engineer.

RESULTS

Patient Characteristics in Datasets

A total of 15254 lumbar axial T2W TSE MRIs in 1015 patients in the internal datasets were evaluated. Overall, the mean age of all 1015 patients was 49 years ± 14 (age range, 13-88 years), and the mean age of 492 women was 51 years ± 14 (age range, 15-84 years). (**Table 1**). For the external test dataset, a total of 1273 lumbar spine axial T2W TSE MRIs in 100 patients were evaluated. The mean age of all 100 patients was 53 years ±16 (age range, 17-84 years), and the mean age of 51 women was 56 years ± 15 (age range, 23-84 years). (**Table 1**). The detailed information on reference standard grading at axial MRIs within the two datasets is shown in **Table 2**. The detailed information on reference standard grading from patients within the two datasets is shown in **Supplementary Material**.

A high inter-reader agreement with the reference standard was reached on the internal datasets and the external test dataset. For LDH, the k values of the four-grades were 0.93 (95% CI: 0.92, 0.95) for the internal datasets and 0.88 (0.86, 0.90) for the external test dataset. For LCCS, the k values of the four-grades were 0.95 (0.95, 0.96) for the internal dataset and 0.96 (0.94, 0.97) for the external test dataset. For LNRC, the k values of the four-grades were 0.93 (0.92, 0.94) for the internal datasets and 0.91 (0.89, 0.93) for the external test dataset.

Multi-Task Classification Network Performance on the Internal Test Dataset

After training, there was a similar agreement between the multi-task classification model and the reference standard in the internal test dataset, with *k* values of 0.80 (0.78, 0.82) for the

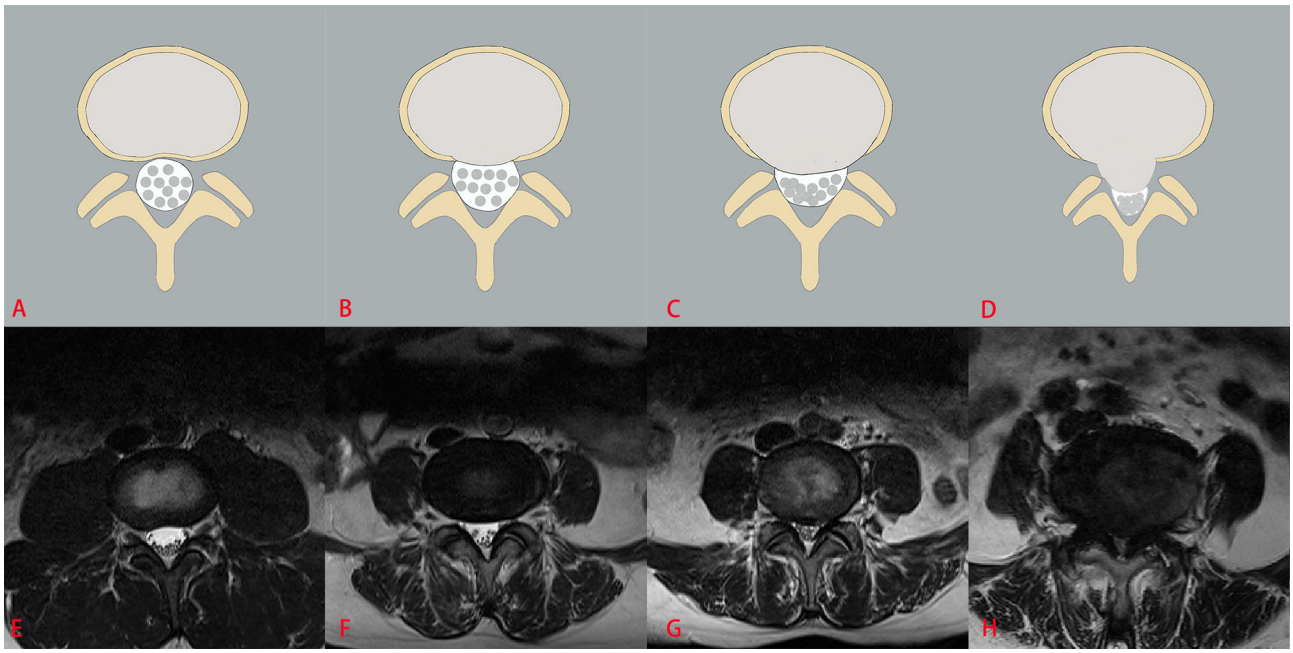

FIGURE 3 | The classification system of lumbar central canal stenosis (LCCS). The top column is a schematic diagram of four grades with LCCS, and the bottom column is the corresponding axial T2W TSE images of four grades with LCCS. LCCS is divided into four grades according to the obliterated severity of anterior cerebrospinal fluid space: Grade 0 **(A, E)** normal; Grade 1 **(B, F)** minor stenosis with clear separation of each cauda equina nerve roots; Grade 2 **(C, G)** moderate stenosis with some cauda equina nerve roots combination; Grade 3 **(D, H)** severe stenosis with all cauda equina nerve roots as a bundle.

four grades of LDH; 0.86 (0.84, 0.87) for the four grades of LCCS; and 0.78 (0.76, 0.80) for the four grades of LNRC. Using the DL algorithm based on ResNet 50 to assess overall grade 0 and the other grades of each classification system, the overall accuracy was as follows: 84.17% (1935 of 2299) for LDH, 86.99% (2000 of 2299) for LCCS, 81.21% (1867 of 2299) for LNRC. Detailed statistics for the four grades of the three classification systems at axial MRIs are summarized in **Figures 6A, C, E**. And detailed statistics for the four grades of the three classification systems at lumbar MRI levels are summarized in **Figures 7A, C, E**. An overview of the results with precision, F1 score, accuracy, k values, sensitivity and specificity are shown in **Table 3**. The area under the ROC curve of the dichotomous classification (grade 0 or grade 1 vs. grade 2 or grade 3) was as follows: 0.97 for LDH, 0.98 for LCCS, 0.95 for LNRC (**Figure 8A**).

Multi-Task Classification Network Performance on the External Test Dataset

The outstanding robustness of this multi-task classification model was obtained in the external test dataset. Reading grades between the reference standard and the multi-task classification model had a strong correlation with *k* values of 0.67 (0.64, 0.70) for the four grades of LDH; 0.77 (0.75, 0.80) for the four grades of LCCS; and 0.69 (0.66, 0.72) for the four grades of LNRC. The overall accuracy was as follows: 74.16% (944 of 1273) for LDH, 79.65% (1014 of 1273) for LCCS, and 74.16% (944 of 1273) for LNRC. And the F1 scores were 81.3% for LDH, 83.5% for LCCS and 84.2% for LNRC. Detailed statistics for the four-grades of the three classification systems at axial MRIs are summarized in **Figures 6B, D, F**. And detailed statistics for the four grades of the three classification systems at lumbar MRI levels are summarized in **Figures 7B, D, F**. An overview of the results with precision, F1 score, accuracy, k values, sensitivity and specificity are shown in **Table 4**. The area under the ROC curve of the dichotomous grading (grade 0 or grade 1 vs. grade 2 or grade 3) was as follows: 0.95 for LDH, 0.98 for LCCS, 0.87 for LNRC (**Figure 8B**).

DISCUSSION

In this study, we developed and validated a multi-task classification network in the automated grading of LDH, LCCS and LNRC at lumbar axial MRIs. This study is the first comprehensive study of multi-task classification for grading LDH, LCCS and LNRC at axial MRIs. The multi-task classification network demonstrated good performance in the automated grading of LDH, LCCS and LNRC.

MRI plays an important role in the assessment of LBP and accurate grading of LDH (7), LCCS (9) and LNRC (10, 11). However, detailing such assessment information, which may be beneficial to clinicians in providing more effective treatment strategies for patients with LBP, is repetitive and time-consuming and subjective for clinicians (12). A multi-task classification network that reliably classifies the severity of

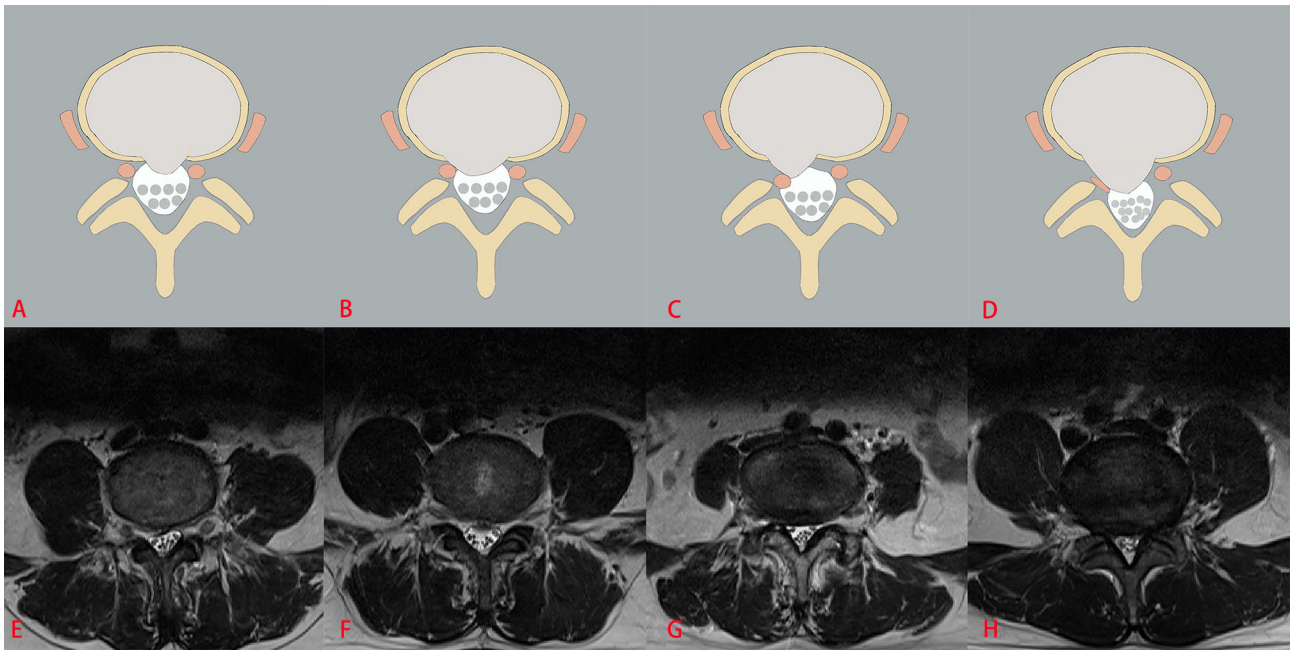

FIGURE 4 | The classification system of lumbar nerve root compromise (LNRC). The top column is a schematic diagram of four grades with LNRC, and the bottom column is the corresponding axial T2W TSE images of four grades with LNRC. Grade 0 **(A, E)** No compromise of the nerve root is seen (normal). There is no evident contact of disk material with the nerve root and the epidural fat layer between the nerve root and the disc material is preserved. Grade 1 **(B, F)** There is visible contact of disc material with the nerve root and the normal epidural fat layer between the two is not evident (contact). The nerve root has a normal position and there is no dorsal deviation. Grade 2 **(C, G)** The nerve root is displaced dorsally by disc material (deviation). Grade 3 **(D, H)** The nerve root is compressed between disc material and the wall of the spinal canal; it may appear flattened or be indistinguishable from disc material (compression).

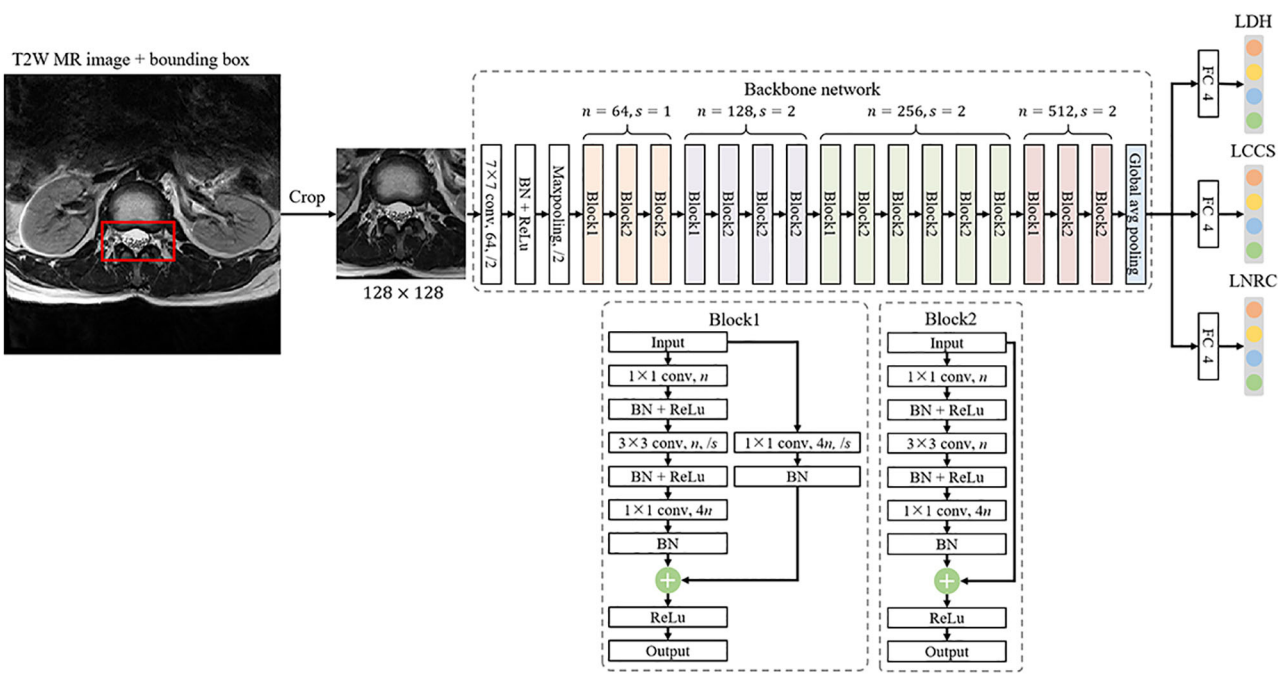

FIGURE 5 | The framework of a multi-task classification network consists of a backbone network for feature extraction and three fully-connected (FC) networks for classification, where n denotes the number of output channels and s is the stride of convolution.

TABLE 2 | Reference standard classifications of the three lumbar diseases at axial T2W MRIs.

Data Set and Diseases Severity	Lumbar Disc Herniation (LDH)	Lumbar Central Canal Stenosis (LCCS)	Lumbar Nerve Roots Compromise (LNRC)
Internal training and validation dataset			
Grade 0	6450 (49.8)	10770 (93.1)	9403 (72.6)
Grade 1	4933 (38.1)	1836 (14.2)	2227 (17.2)
Grade 2	1435 (11.1)	226 (1.7)	648 (5.0)
Grade 3	137 (1.1)	123 (0.9)	677 (5.2)
Total	12955	12955	12955
Internal test dataset			
Grade 0	1121 (48.8)	1902 (82.7)	1616 (70.3)
Grade 1	864 (37.6)	343 (14.9)	424 (18.4)
Grade 2	287 (12.5)	40 (1.7)	127 (5.5)
Grade 3	27 (1.2)	14 (0.6)	132 (5.7)
Total	2299	2299	2299
External test dataset			
Grade 0	550 (43.2)	1105 (86.8)	866 (68.0)
Grade 1	499 (39.2)	105 (8.2)	305 (24.0)
Grade 2	196 (15.4)	42 (3.3)	44 (3.5)
Grade 3	28 (2.2)	21 (1.6)	58 (4.6)
Total	1273	1273	1273

Unless otherwise stated, data are numbers of patients, with percentages in parentheses.

lumbar degenerative diseases may be desired and useful in clinical practice.

Previous studies (14, 24) have shown the potential of the DL algorithm to classify spinal diseases shown on lumbar MRIs. They validated the feasibility of using the DL algorithm to grade LCCS or LDH automatically. However, these automated grading models based on the DL algorithm were only used to classify a single lumbar disease and failed to realize the automated grading of multiple lumbar diseases. Therefore, researchers explored the potential of a multi-task classification network to evaluate multiple lumbar diseases. Jamaludin et al. (25) proposed a multi-task classification network: SpineNet, which was developed for the automated classification of several pathological spinal features, including Pfirrmann grading (26), intervertebral disc stenosis, lumbar central canal stenosis, bone marrow changes and endplate defects. Lu et al. (18) developed the DeepSpine model, which could be used to diagnose lumbar central canal stenosis and neural foraminal stenosis automatically at axial and sagittal T2W MRIs. More recently, in 2021, a multi-task classification model was developed to automatically detect and classify lumbar central canal, neural foraminal stenosis and lateral recess at axial and sagittal T2W MRIs (27). It can be used to evaluate lumbar spinal stenosis in clinical practice quickly. Overall, these studies suggest the efficacy of multi-task classification models in the automated grading of spinal stenosis on lumbar MRIs. To date, Lewandrowski et al. (28) have made a preliminary attempt and demonstrated that a multi-task classification model based on the DL algorithm is feasible for automated grading of disc bulging, disc herniation, and lumbar stenosis at routine MRIs. But they failed to diagnose the severity of disc herniation and lumbar stenosis, which may not be enough to help surgeons make clinical decisions.

The classification systems of these three diseases in our model correlate with surgical treatment modalities. Mysliwiec et al. (7) suggest that patients with grade 1 should be excluded from surgical consideration, and patients with grade 2 or grade 3 should be considered for performing micro discectomies. This classification system is currently widely used in the clinical setting (29, 30). In addition, the classification system of LCCS, a valuable method for clinicians and radiologists to use in clinical practice, is defined by the degree of separation of the cauda equina related to the severity of the clinical signs (9, 31). Moreover, the classification system of LNRC is decided by the spatial relationship between herniated disc material and nerve roots, and this system is proven to be relevant to surgical grading (10, 11). Notably, our model achieved superior performance for the dichotomous classification (grade 0 or grade 1 vs. grade 2 or grade 3). Each result of the area under the ROC curve on the internal test dataset (external test dataset) was as follows: LDH: 0.97 (0.95); LCCS: 0.98 (0.98); and LNRC: 0.95 (0.87). This superior performance demonstrates that our model is a promising tool to be used in clinical practice to assess LDH, LCCS and LNRC.

The model proposed in our study achieves good performance for grading LDH, LCCS and LNRC at axial MRIs. Firstly, on the internal test dataset, our model showed substantial to the almost perfect levels of agreement for the three classification systems with four grades. Especially in the grading of LCCS, our model had a k value of 0.86 for the four grades, which is higher than the k value of 0.82 reported by Hallinan et al. (27). Our model also showed substantial levels of agreement on the external test dataset. In addition, the model has high accuracy for the automated classification of LDH, LCCS and LNRC. The average classification accuracy rates (grade 0, grade 1, grade 2 and grade 3) of LDH, LCCS and LNRC were 84.17%, 86.99% and 81.21%, respectively. Among these, the average classification accuracy of LCCS is higher than that reported in previous studies (14, 18, 27).

Although this multi-task classification network shows considerable consistency and good performance in the automated grading of LDH, LCCS and LNRC, our study has several limitations. First, we selected the international classification systems relevant for surgical selection as the reference standard, although there remains controversy concerning LDH, LCCS and LNRC classification at MRI (31, 32). Second, the diagnostic accuracy of grade 2 and grade 3 for the three lumbar diseases was low in our study, which may be the potential to be associated with a data class imbalance. Increasing the data sample size would be one way to improve the diagnostic accuracy and will be completed in our future work. Using only axial MRIs for grading LDH, LCCS and LNRC may be another limitation, although the grading of three systems is taken from the axial T2W MRIs. In addition, automated grading of multiple lumbar diseases such as Pfirrmann grading and osteoporotic vertebral fractures using multiple MRI sequences should be integrated into our model in the future. Finally, we did not

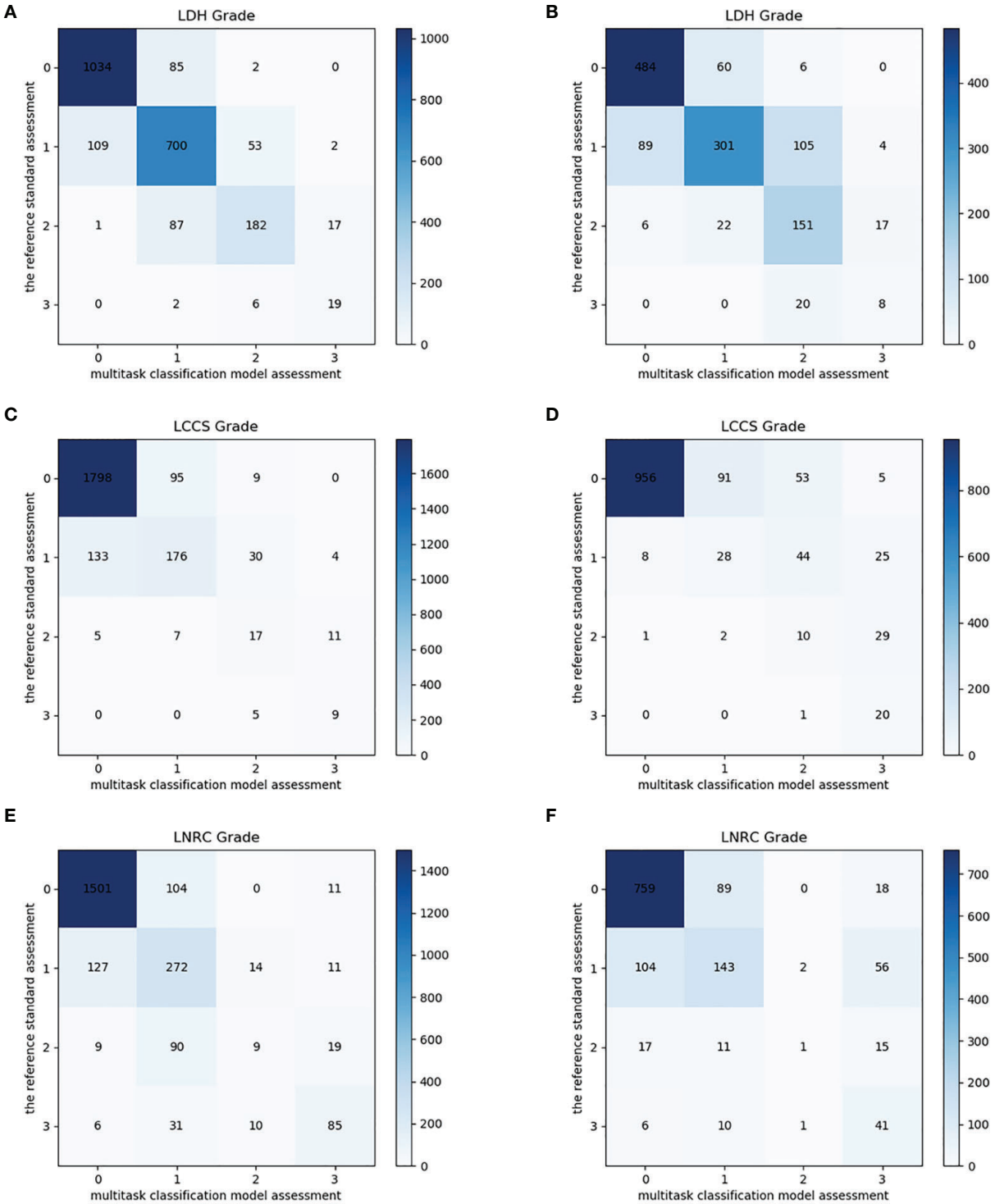

FIGURE 6 | Confusion matrix of the multi-task classification model at axial MRIs. Confusion matrix of the multi-task classification model for grading lumbar disc herniation LDH **(A)**, lumbar central canal stenosis LCCS **(C)** and lumbar nerve roots compression LNRC **(E)** on the internal test dataset. Confusion matrix of the multi-task classification model for grading LDH **(B)**, LCCS **(D)** and LNRC **(F)** on the external test dataset.

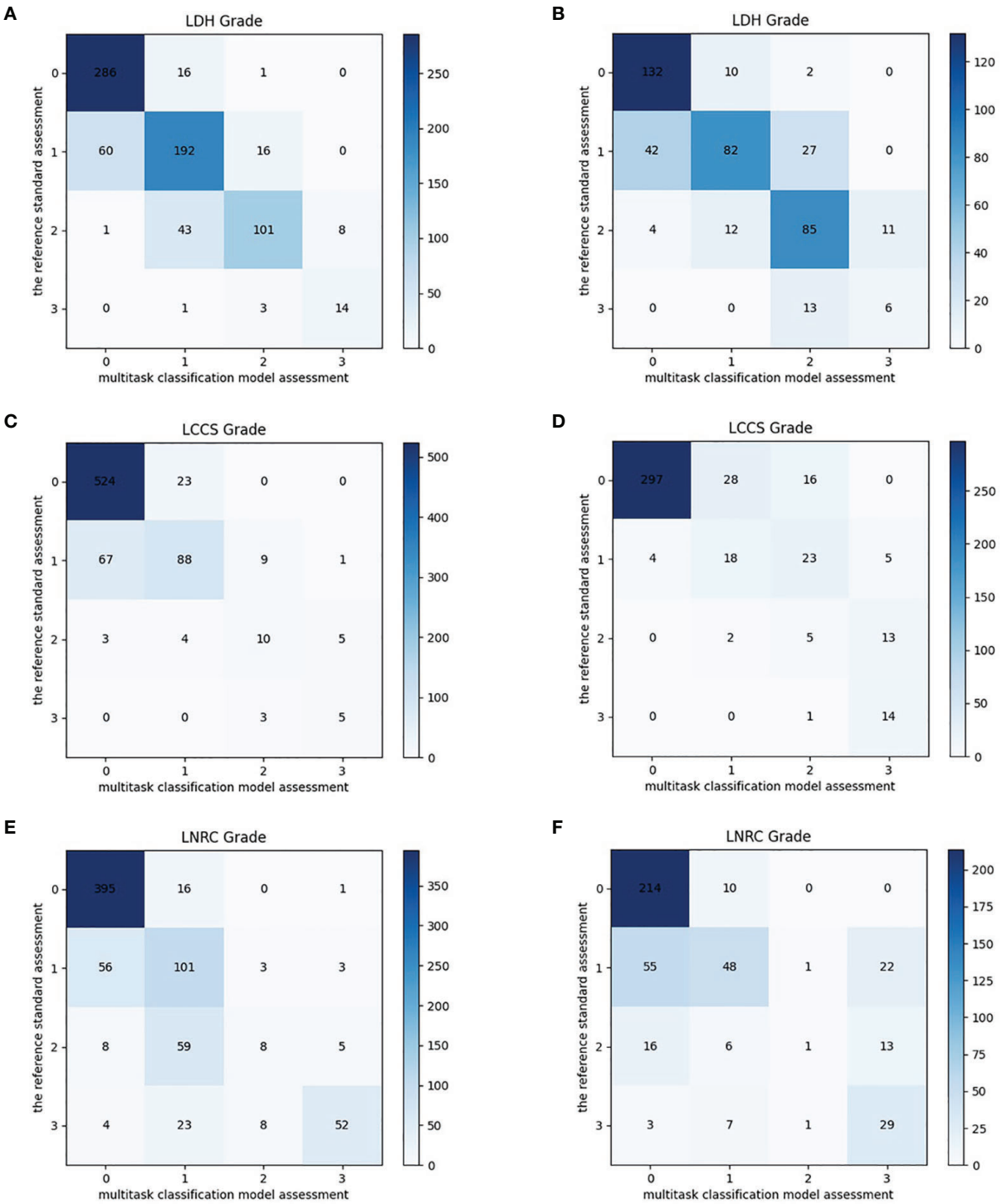

FIGURE 7 | Confusion matrix of the multi-task classification model at lumbar MRI levels. Confusion matrix of the multi-task classification model for grading lumbar disc herniation LDH **(A)**, lumbar central canal stenosis LCCS **(C)** and lumbar nerve roots compression LNRC **(E)** on the internal test dataset. Confusion matrix of the multi-task classification model for grading LDH **(B)**, LCCS **(D)** and LNRC **(F)** on the external test dataset.

TABLE 3 | The accuracy performance of the multi-task classification model on the internal test dataset.

Predicted Grading	Precision (%)	F1 Score (%)	Accuracy (%)	Sensitivity (%)	Specificity (%)	Gwet *k*
LDH	84.1	84.1	84.2	90.7	92.2	0.80
Grade 0	90.4	91.3				
Grade 1	80.1	80.6				
Grade 2	74.9	68.7				
Grade 3	50.0	58.5				
LCCS	87.0	86.8	87.0	65.2	94.5	0.85
Grade 0	92.9	93.7				
Grade 1	63.3	56.7				
Grade 2	27.9	33.7				
Grade 3	37.5	47.4				
LNRC	79.7	80.0	81.2	79.2	92.9	0.78
Grade 0	91.4	92.1				
Grade 1	54.7	59.1				
Grade 2	27.3	11.2				
Grade 3	67.5	65.9				

LDH, lumbar disc herniation; LCCS, lumbar central canal stenosis; LNRC, lumbar nerve roots compromise.

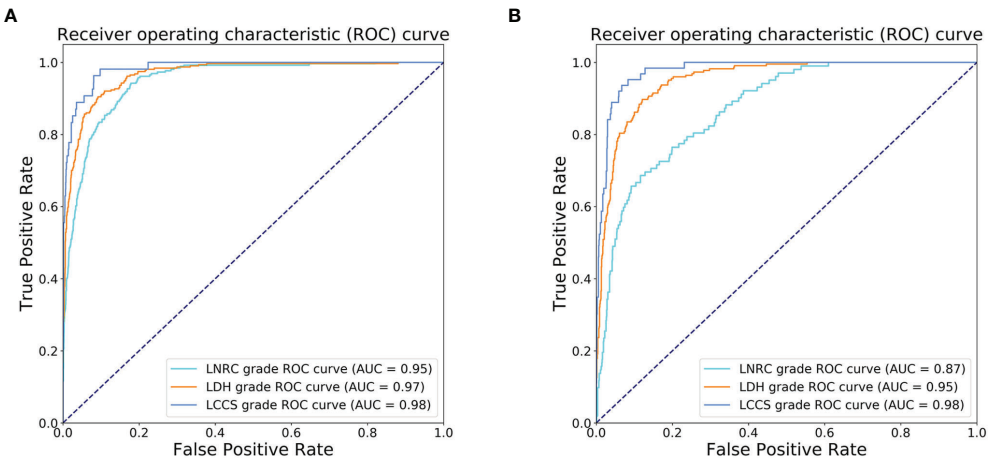

FIGURE 8 | Receiver operating characteristic (ROC) curves of dichotomous grading (grade 0 or grade 1 vs. grade 2 or grade 3) for the three spine diseases. **(A)** ROC curves for the automated grading of three diseases: lumbar disc herniation (LDH), lumbar central canal stenosis (LCCS) and lumbar nerve roots compression (LNRC) on the internal test dataset. **(B)** ROC curves for the automated grading of three diseases: LDH, LCCS and LNRC on the external test dataset.

TABLE 4 | The accuracy performance of the multi-task classification model on the external test dataset.

Predicted Grading	Precision (%)	F1 Score (%)	Accuracy (%)	Sensitivity (%)	Specificity (%)	Gwet *k*
LDH	75.8	74.1	74.2	86.9	88.0	0.67
Grade 0	83.6	85.7				
Grade 1	78.6	68.3				
Grade 2	53.5	63.2				
Grade 3	27.6	28.1				
LCCS	88.6	83.3	79.7	94.6	86.5	0.77
Grade 0	99.1	92.4				
Grade 1	23.1	24.8				
Grade 2	9.1	13.3				
Grade 3	25.3	40.0				
LNRC	74.1	73.4	74.2	68.8	87.6	0.69
Grade 0	85.7	86.6				
Grade 1	56.5	51.3				
Grade 2	25.0	4.2				
Grade 3	31.5	43.6				

LDH, lumbar disc herniation; LCCS, lumbar central canal stenosis; LNRC, lumbar nerve roots compromise.

explore the relationship between clinical symptoms and the grading of three systems. This relationship may play an essential role in clinical decision-making and will be completed in our future work.

In conclusion, we proposed a multi-task classification network for automated grading of LDH, LCCS and LNRC at lumbar axial MRIs. The current study found that automated grading of LDH, LCCS and LNRC at lumbar axial MRIs using a multi-task classification network is feasible with moderate to high accuracy. Additionally, our model showed comparable agreement with clinicians in classifying LDH, LCCS and LNRC.

DATA AVAILABILITY STATEMENT

The original contributions presented in the study are included in the article/**Supplementary Material**. Further inquiries can be directed to the corresponding author.

ETHICS STATEMENT

The studies involving human participants were reviewed and approved by Institutional Review Board of the Fifth Affiliated Hospital of Sun Yat-Sen University. Written informed consent to participate in this study was provided by the participants' legal guardian/next of kin.

AUTHOR CONTRIBUTIONS

Z-HS and JL designed the study, collected and analyzed the data, and revised the manuscript for intellectual content. M-SY and KY conceptualized, analyzed and interpreted the data, and drafted the manuscript. Z-YC analyzed the data. JS and C-JH reanalyzed the data and drafted the manuscript. Q-HZ and E-QL collected and analyzed and interpreted the data. Q-JF contributed to the methods (model training) and revised the manuscript for intellectual content. LZ contributed to the deep-learning algorithms. S-MP analyzed and interpreted the data, developed the multi-task classification model, and drafted and revised the manuscript for intellectual content. S-LL and HL conceptualized and designed the study, interpreted the data, contributed to the discussion, reviewed and edited the manuscript. All authors contributed to the article and approved the submitted version.

FUNDING

Study supported by Zhuhai City Innovation and Innovation Team Project, Guangdong Province, China (ZH0406190031PWC), Zhuhai City Industry-University-Research Cooperation Project, Guangdong Province (ZH0406190031PWC), China and supported by the National Natural Science Foundation of China (No. 62001207 and No. 12126603).

ACKNOWLEDGMENTS

The authors thank AiMi Academic Services (www.aimieditor.com) for the English language editing and review services.

SUPPLEMENTARY MATERIAL

The Supplementary Material for this article can be found online at: https://www.frontiersin.org/articles/10.3389/fendo.2022.890371/full#supplementary-material

REFERENCES

1. Knezevic NN, Candido KD, Vlaeyen JWS, Van Zundert J, Cohen SP. Low Back Pain. *Lancet* (2021) 398(10294):78–92. doi: 10.1016/s0140-6736(21)00733-9
2. C. Global Burden of Disease Study. Global, Regional, and National Incidence, Prevalence, and Years Lived With Disability for 301 Acute and Chronic Diseases and Injuries in 188 Countries, 1990-2013: A Systematic Analysis for the Global Burden of Disease Study 2013. *Lancet (London England)* (2015) 386(9995):743–800. doi: 10.1016/s0140-6736(15)60692-4
3. Rydevik B, Brown MD, Lundborg G. Pathoanatomy and Pathophysiology of Nerve Root Compression. *Spine (Phila Pa 1976)* (1984) 9(1):7–15. doi: 10.1097/00007632-198401000-00004
4. Qaseem A, Wilt TJ, McLean RM, Forciea MA. Noninvasive Treatments for Acute, Subacute, and Chronic Low Back Pain: A Clinical Practice Guideline From the American College of Physicians. *Ann Intern Med* (2017) 166 (7):514–30. doi: 10.7326/m16-2367
5. Zaina F, Tomkins-Lane C, Carragee E, Negrini S. Surgical Versus non-Surgical Treatment for Lumbar Spinal Stenosis. *Cochrane Database Syst Rev* (2016) 2016(1):Cd010264. doi: 10.1002/14651858.CD010264.pub2
6. Kim HS, Wu PH, Jang IT. Lumbar Degenerative Disease Part 1: Anatomy and Pathophysiology of Intervertebral Discogenic Pain and Radiofrequency Ablation of Basivertebral and Sinuvertebral Nerve Treatment for Chronic Discogenic Back Pain: A Prospective Case Series and Review of Literature. *Int J Mol Sci* (2020) 21(4):1483. doi: 10.3390/ijms21041483
7. Mysliwiec LW, Cholewicki J, Winkelpleck MD, Eis GP. MSU Classification for Herniated Lumbar Discs on MRI: Toward Developing Objective Criteria for Surgical Selection. *Eur Spine J* (2010) 19(7):1087–93. doi: 10.1007/s00586-009-1274-4
8. Kaliya-Perumal AK, Luo CA, Yeh YC, Tsai YF, Chen MJ, Tsai TT. Reliability of the Michigan State University (MSU) Classification of Lumbar Disc Herniation. *Acta Ortop Bras* (2018) 26(6):411–4. doi: 10.1590/1413-785220182606201444
9. Lee GY, Lee JW, Choi HS, Oh KJ, Kang HS. A New Grading System of Lumbar Central Canal Stenosis on MRI: An Easy and Reliable Method. *Skeletal Radiol* (2011) 40(8):1033–9. doi: 10.1007/s00256-011-1102-x
10. Pfirrmann CW, Dora C, Schmid MR, Zanetti M, Hodler J, Boos N. MR Image-Based Grading of Lumbar Nerve Root Compromise Due to Disk Herniation: Reliability Study With Surgical Correlation. *Radiology* (2004) 230(2):583–8. doi: 10.1148/radiol.2302021289
11. Sung J, Jee WH, Jung JY, Jang J, Kim JS, Kim YH, et al. Diagnosis of Nerve Root Compromise of the Lumbar Spine: Evaluation of the Performance of Three-Dimensional Isotropic T2-Weighted Turbo Spin-Echo SPACE Sequence at 3T. *Korean J Radiol* (2017) 18(1):249–59. doi: 10.3348/kjr.2017.18.1.249
12. McDonald RJ, Schwartz KM, Eckel LJ, Diehn FE, Hunt CH, Bartholmai BJ, et al. The Effects of Changes in Utilization and Technological Advancements of Cross-Sectional Imaging on Radiologist Workload. *Acad Radiol* (2015) 22 (9):1191–8. doi: 10.1016/j.acra.2015.05.007

13. Hosny A, Parmar C, Quackenbush J, Schwartz LH, Aerts H. Artificial Intelligence in Radiology. *Nat Rev Cancer* (2018) 18(8):500–10. doi: 10.1038/s41568-018-0016-5
14. Won D, Lee HJ, Lee SJ, Park SH. Spinal Stenosis Grading in Magnetic Resonance Imaging Using Deep Convolutional Neural Networks. *Spine (Phila Pa 1976)* (2020) 45(12):804–12. doi: 10.1097/brs.0000000000003377
15. Yabu A, Hoshino M, Tabuchi H, Takahashi S, Masumoto H, Akada M, et al. Using Artificial Intelligence to Diagnose Fresh Osteoporotic Vertebral Fractures on Magnetic Resonance Images. *Spine J* (2021) 21(10):1652–8. doi: 10.1016/j.spinee.2021.03.006
16. Tsai JY, Hung IY, Guo YL, Jan YK, Lin CY, Shih TT, et al. Lumbar Disc Herniation Automatic Detection in Magnetic Resonance Imaging Based on Deep Learning. *Front Bioeng Biotechnol* (2021) 9:708137. doi: 10.3389/fbioe.2021.708137
17. Han Z, Wei B, Leung S, Nachum IB, Laidley D, Li S. Automated Pathogenesis-Based Diagnosis of Lumbar Neural Foraminal Stenosis *via* Deep Multiscale Multitask Learning. *Neuroinformatics* (2018) 16(3-4):325–37. doi: 10.1007/s12021-018-9365-1
18. Lu J-T, Pedemonte S, Bizzo B, Doyle S, Andriole KP, Michalski MH, et al. Deep Spine: Automated Lumbar Vertebral Segmentation, Disc-Level Designation, and Spinal Stenosis Grading Using Deep Learning, in: Lawrence Neil, editor. *Proceedings of Machine Learning Research. PMLR 2018: Proceedings of the 3rd Machine Learning for Healthcare Conference*. Palo Alto, California: PMLR., (2018) 85:403-19.
19. Zhu K, Su Q, Chen T, Zhang J, Yang M, Pan J, et al. Association Between Lumbar Disc Herniation and Facet Joint Osteoarthritis. *BMC Musculoskelet Disord* (2020) 21(1):56. doi: 10.1186/s12891-020-3070-6
20. Park HJ, Kim SS, Lee YJ, Lee SY, Park NH, Choi YJ, et al. Clinical Correlation of a New Practical MRI Method for Assessing Central Lumbar Spinal Stenosis. *Br J Radiol* (2013) 86(1025):20120180. doi: 10.1259/bjr.20120180
21. Gwet KL. Computing Inter-Rater Reliability and its Variance in the Presence of High Agreement. *Br J Math Stat Psychol* (2008) 61(Pt 1):29–48. doi: 10.1348/000711006x126600
22. Wongpakaran N, Wongpakaran T, Wedding D, Gwet KL. A Comparison of Cohen's Kappa and Gwet's AC1 When Calculating Inter-Rater Reliability Coefficients: A Study Conducted With Personality Disorder Samples. *BMC Med Res Methodol* (2013) 13:61. doi: 10.1186/1471-2288-13-61
23. Jian S, ed. Deep Residual Learning for Image Recognition. In: IEEE Conference on Computer Vision and Pattern Recognition. CVPR 2016: IEEE Conference on Computer Vision and Pattern Recognition. Las Vegas, NV: IEEE. (2016) 770-8.
24. He X, Landis M, Leung S, Warrington J, Shmuilovich O, Li S. Automated Grading of Lumbar Disc Degeneration *via* Supervised Distance Metric Learning. In: International Society for Optics andPhotonics. SPIE 2017: Proceedings Volume 10134, Medical Imaging: Computer-Aided Diagnosis. Orlando, Florida: SPIE. (2017) 10134:1013443.
25. Jamaludin A, Kadir T, Zisserman A. SpineNet: Automated Classification and Evidence Visualization in Spinal MRIs. *Med Image Anal* (2017) 41:63–73. doi: 10.1016/j.media.2017.07.002
26. Pfirrmann CW, Metzdorf A, Zanetti M, Hodler J, Boos N. Magnetic Resonance Classification of Lumbar Intervertebral Disc Degeneration. *Spine (Phila Pa 1976)* (2001) 26(17):1873–8. doi: 10.1097/00007632-200109010-00011
27. Hallinan J, Zhu L, Yang K, Makmur A, Algazwi DAR, Thian YL, et al. Deep Learning Model for Automated Detection and Classification of Central Canal, Lateral Recess, and Neural Foraminal Stenosis at Lumbar Spine MRI. *Radiology* (2021) 300(1):130–8. doi: 10.1148/radiol.2021204289
28. Lehnen NC, Haase R, Faber J, Rüber T, Vatter H, Radbruch A, et al. Detection of Degenerative Changes on MR Images of the Lumbar Spine With a Convolutional Neural Network: A Feasibility Study. *Diagn (Basel)* (2021) 11 (5):902. doi: 10.3390/diagnostics11050902
29. d'Ercole M, Innocenzi G, Ricciardi F, Bistazzoni S. Prognostic Value of Michigan State University (MSU) Classification for Lumbar Disc Herniation: Is It Suitable for Surgical Selection? *Int J Spine Surg* (2021) 15 (3):466–70. doi: 10.14444/8068
30. Beyaz SG, Ülgen AM, Kaya B, İnanmaz ME, Ergönenç T, Eman A, et al. A Novel Combination Technique: Three Points of Epiduroscopic Laser Neural Decompression and Percutaneous Laser Disc Decompression With the Ho: YAG Laser in an MSU Classification 3ab Herniated Disc. *Pain Pract* (2020) 20 (5):501–9. doi: 10.1111/papr.12878
31. Ko YJ, Lee E, Lee JW, Park CY, Cho J, Kang Y, et al. Clinical Validity of Two Different Grading Systems for Lumbar Central Canal Stenosis: Schizas and Lee Classification Systems. *PloS One* (2020) 15(5):e0233633. doi: 10.1371/journal.pone.0233633
32. Li Y, Fredrickson V, Resnick DK. How Should We Grade Lumbar Disc Herniation and Nerve Root Compression? *A Systematic Rev Clin Orthop Relat Res* (2015) 473(6):1896–902. doi: 10.1007/s11999-014-3674-y

Conflict of Interest: The authors declare that the research was conducted in the absence of any commercial or financial relationships that could be construed as a potential conflict of interest.

Publisher's Note: All claims expressed in this article are solely those of the authors and do not necessarily represent those of their affiliated organizations, or those of the publisher, the editors and the reviewers. Any product that may be evaluated in this article, or claim that may be made by its manufacturer, is not guaranteed or endorsed by the publisher.

frontiers | Frontiers in Endocrinology

TYPE Original Research
PUBLISHED 11 November 2022
DOI 10.3389/fendo.2022.958151

OPEN ACCESS

EDITED BY
Bing Wu,
GE Healthcare, China

REVIEWED BY
Hadassa Degani,
Weizmann Institute of Science, Israel
Katrien Vandoorne,
Technion Israel Institute of Technology, Israel

*CORRESPONDENCE
Jinliang Niu
sxlscjy@163.com

SPECIALTY SECTION
This article was submitted to Bone Research, a section of the journal Frontiers in Endocrinology

RECEIVED 31 May 2022
ACCEPTED 25 October 2022
PUBLISHED 11 November 2022

CITATION
Wu W, Gong T, Niu J, Li W, Li J, Song X, Cui S, Bian W and Wang J (2022) Study of bone marrow microstructure in healthy young adults using intravoxel incoherent motion diffusion-weighted MRI. *Front. Endocrinol.* 13:958151. doi: 10.3389/fendo.2022.958151

Study of bone marrow microstructure in healthy young adults using intravoxel incoherent motion diffusion-weighted MRI

Wenqi Wu[1], Tong Gong[2], Jinliang Niu[1]*, Wenjin Li[3], Jianting Li[1], Xiaoli Song[1], Sha Cui[1], Wenjin Bian[4] and Jun Wang[1]

[1]Departments of Radiology, The Second Hospital, Shanxi Medical University, Taiyuan, China, [2]Departments of Radiology, People's Hospital, Sichuan, China, [3]Department of stomatology, The Second Hospital, Shanxi Medical University, Taiyuan, China, [4]Department of Medical Imaging, Shanxi Medical University, Taiyuan, China

Bone marrow is one of the most important organs in the human body. The evaluation of bone marrow microstructure and gender-related cellular and capillary networks in healthy young adults can help to better understand the process of bone metabolism. Intravoxel incoherent motion (IVIM) provides both diffusion and perfusion quantifications without requiring intravenous contrast agent injection. In this prospective study, 60 healthy young age-matched volunteers (30 men and 30 women) underwent MRI scans at 1.5 T using multi–b-value diffusion-weighted imaging on sagittal planes covering the lumbar bone marrow. The apparent diffusion coefficient (ADC), true ADC (*D*), pseudo-ADC (*D**), and perfusion fraction (*f*) were calculated from the diffusion-weighted images using the mono- and bi-exponential models. Lumbar cancellous bone (L2–L4) was selected as the region of interest. An independent *t*-test was used to detect significant differences in ADC values and IVIM parameters between men and women. The differences in IVIM parameters among the L2, L3, and L4 groups were compared with analysis of variance. The *D* and *f* values in women were significantly higher than that in men (p = 0.001, 0.026). However, *D** was significantly lower in women than that in men (p = 0.001). Furthermore, there was no significant gender difference for the conventional ADC value (p = 0.186). Moreover, there were no significant differences in the *D*, *f*, and *D** values among the L2, L3, and L4 vertebras of women or men. IVIM parameters can show differences in bone marrow between young women and men. As a non-invasive method, it can assess bone marrow microstructure, such as cellularity and perfusion.

KEYWORDS

marrow, intravoxel incoherent motion (IVIM), diffusion-weighted imaging, genders, microstructure

Introduction

The bone marrow is the fourth largest organ of the human body. The primary microstructure comprises cellular structure and blood capillary (1). The factors that regulate the content of bone marrow microstructure include development, age, and gender (2). Anemia can change the pathological state of the bone marrow microstructure, causing an increase in bone marrow cell composition and blood capillary. Malignant blood system diseases can cause bone marrow pathological hyperplasia (3). Moreover, physiological changes have been reported in disease and normal bone marrow (4). The bone composition differs between men and women. Increasing age also thins the trabecular structure of the bone, increases fat content, and reduces local perfusion, resulting in bone marrow water–fat imbalance (5, 6). Therefore, it is important to determine bone marrow values in normal populations to understand the impact of physiological factors (such as gender) on quantitative and functional parameters so that we can better characterize and assess the pathogenesis, pathophysiology, and prognosis of bone marrow diseases.

Magnetic resonance imaging (MRI) is more commonly used than other imaging modalities when evaluating marrow compositions (7). Although conventional MRI can assess the cellularity of bone marrow based on signal intensity, it does not provide a quantitative evaluation (8–10). The apparent diffusion coefficient (ADC) represents a positive correlation with the cellularity of the marrow (11) and shows a linear decrease with age (more yellow marrow and less red marrow) (12). However, the ADC value overlaps neoplastic and normal marrow (13), which is controversial when assessing vertebral body lesions (12). MR spectroscopy is widely used to quantify the marrow fat fraction (14); however, different ranges of marrow fat fraction have been reported (15, 16). Dynamic contrast-enhanced MRI (DCE-MRI) has been applied to analyze the marrow perfusion of the capillary network in patients with osteoporosis, diagnose malignant lesions, and monitor tumor treatment response (17–21). However, it is not widely used in clinical practice because of the need for intravenous injection of an MRI tracer, especially in patients with renal malfunctions.

Intravoxel incoherent motion (IVIM) is a diffusion-weighted imaging (DWI) method that uses multiple b-values and a bi-exponential signal model to calculate quantitative parameters that can separately reflect tissue microcapillary perfusion and diffusivity (22–24). The low b-values (<200 s/mm^2), pseudoperfusion fraction (f), and pseudodiffusion coefficient (D^*) represent the characteristics of perfusion, whereas the high b-values (200 to 1,000 s/mm^2) and the diffusion coefficient (D) can reflect water diffusion that is related to tissue cellularity (25).

Gender difference is one of the factors affecting the microstructure content of bone marrow, with men and women having different performances (2, 26). The quantification of the cellular structure and blood capillary of marrow can be obtained by invasive iliac crest biopsy, which is an invasive method and subject to sampling errors (21). IVIM provides diffusion and perfusion quantification information without requiring intravenous contrast agent injection (24). It has been applied to evaluate various diseases and body organs (23, 24, 27–29) and recently for bone marrow disorders (30, 31). As a baseline study, we aim to evaluate the vertebral bone marrow microstructure of healthy young people through changes in IVIM and tissue diffusion parameters and gender differences in vertebral bone marrow cellularity and capillary perfusion capacity.

Materials and methods

Selection of volunteers

This cross-sectional study was approved by the ethics committee of performing site. Informed consent was obtained from all the participants included in this study. Sixty healthy volunteers were recruited: 30 men and 30 women (age range, 22 to 25 years; average age, 23 years). The inclusion criteria were as follows: (a) no lesions in the spine (e.g., spinal deformity or spinal tuberculosis); (b) no hematologic disease (e.g., leukemia, anemia, or aplastic anemia); and (c) no contraindication to MRI examination at 1.5 T. All women were in the same period of the menstrual cycle.

Magnetic resonance imaging

MRI of the lumbar vertebral bone marrow was performed on a GE Signa 1.5-T MRI scanner (GE Healthcare, Waukesha, WI, USA) using an eight-channel MR cervical/thoracic/lumbar coil. The imaging protocol included routine fast spin echo sagittal T1-weighted (repetition time (TR), 400.0 ms; echedelaytime (TE), 9.3 ms; section thickness, 5.0 mm; spacing, 0.0 mm; number of excitation (NEX), 4; field of view (FOV), 36 × 36 cm; matrix, 320 × 192; acquisition time, 2 min 29 s). The IVIM sequence was on the basis of standard diffusion-weighted single-shot spin-echo-planar imaging with 11 b-values (b = 0, 10, 25, 50, 100, 200, 400, 600, 800, 1,000, and 1,200 s/mm^2; TR, 2000 ms; TE, 91 ms; NEX, 4; slice thickness, 5.0 mm; FOV, 36 × 36 cm; matrix, 128 × 128; diffusion gradient directions, 3; spatial resolution, 2.8 × 2.8; acquisition time, 8 min 45 s). Fat suppression of a spectral-spatial excitation pulse was used with the IVIM sequence.

Image analysis

The post-processing software (Functool MADC software, Advantage Windows Workstation 4.4, GE Healthcare, WI, USA) was used to analyze the IVIM parameters of vertebral marrow. The traditional ADC was calculated with the mono-exponential model using b = 0 and 600 s/mm^2 from the multi–b-value DWI. As the main IVIM parameters, the f, D^*, and D values were calculated using the bi-exponential logarithmic signal fitting equation (1), and the corresponding parameter maps were generated automatically.

$$S_b/S_0 = (1-f) \times e^{-bD} + f \times e^{-bD^*} \quad (1)$$

where S_b is the signal intensity in different b-values, and S_0 is the signal intensity when b is 0.

The b = 0 images of the vertebral marrow, as the clearest anatomic structure among the multiple b-value images, served as a location map in the sagittal plane. The regions of interest (ROIs) were selected centrally in the lumbar vertebral cancellous bone (L2–L4) (21), which were intended to minimize the effect of vertebral end-plate changes, vertebral venous plexus, and cerebrospinal fluid. The vertebral bodies with an irregular shape, such as wedging of the vertebra, vertebrae with Schmorls node, and vertebral growth deformity, were not included in the analysis. The mean ROI size was 214 mm^2 (range, 187–261 mm^2) (Figure 1). We adopted the average value of three lumbar vertebrae (L2, L3, and L4) to compare the parameters of women and men.

Statistical analysis

An independent t-test or Mann–Whitney U-test was used to detect significant differences in ADC values and IVIM parameters between men and women. Whisker plots visually describe the difference. The differences in IVIM parameters among the L2, L3, and L4 groups were compared with analysis of variance. Statistical analyses were performed using SPSS software (SPSS 19 Chicago, IL, USA). A P-value<0.05 was considered a significant difference.

Results

Comparison of parameters on women and men

The ADC value of women was 0.60 ± 0.04 × 10^{-3} mm^2/s, whereas that of men was 0.58 ± 0.07 ×10^{-3} mm^2/s, without statistically significant differences (Table 1 and Figures 2, 3). The D value of IVIM, representing tissue water diffusivity, was 0.28 ± 0.04 × 10^{-3} mm^2/s in women and significantly higher than the 0.20 ± 0.04 × 10^{-3} mm^2/s in men (t = −8.653, p = 0.001; Table 1 and Figures 2, 3). In the perfusion-related parameters, f was significantly higher in women (31.70% ± 3.65%) compared with that in men (28.94% ± 5.52%) (t = −2.286, p = 0.026). However, the D^* value was significantly lower in women (41.65 × 10–^{3} mm^2/s) than that in men (95.07 × 10^{-3} mm^2/s) (Z = −7.387, p = 0.001; Table 1 and Figures 2, 3).

The logarithmic plot of signal intensity decay and bi-exponential fitting curves revealed differences between women and men (red and green lines, respectively), as illustrated in Figure 4. The ROI was in the L4 vertebral bone marrow. When b< 200 s/mm^2, the signal intensity of men decayed faster. When b > 200 s/mm^2, the signal decay rate of men was slower than that of women. Therefore, the bi-exponential fit curves for women and men were crossed and not parallel (Figure 4).

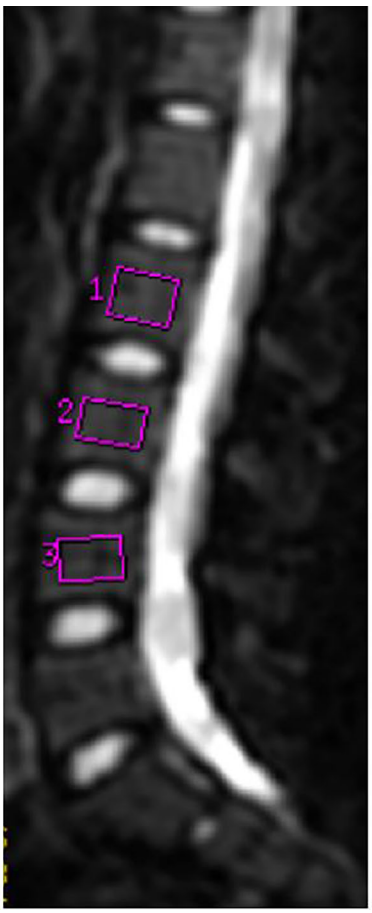

FIGURE 1
MR image in a 24-year-old woman. On the median sagittal image with b = 0, L2–L4 vertebrae were selected to delineate ROI.

10.3389/fendo.2022.958151

TABLE 1 Comparison of MRI parameters of women and men.

MRI parameter	Females (n = 30)	Males (n = 30)	t/Z	p
ADC	0.60 ± 0.04	0.58 ± 0.07	−1.337	0.186
(10^{-3} mm^2/s)	0.60 (0.57, 0.63)	0.58 (0.52, 0.63)		
D	0.28 ± 0.04	0.20 ± 0.04	−8.653	0.001
(10^{-3} mm^2/s)	0.28 (0.25, 0.31)	0.19 (0.17, 0.22)		
f (%)	31.70 ± 3.65	28.94 ± 5.22	−2.286	0.026
	31.76 (29.71, 34.24)	29.74 (24.73, 32.93)		
*D**	46.72 ± 12.90	91.78 ± 30.83	−5.544	0.001[#]
(10^{-3} mm^2/s)	41.65 (38.09, 51.95)	95.07 (66.16, 109.69)		

Data are shown as mean ± standard deviation, mean (interquartile range). The independent t-test was applied to compare the two treatment response groups, unless otherwise specified.
[#]Determined with the Mann–Whitney U-test.
Pseudodiffusion coefficient (D*) represent the characteristics of perfusion.

Parameters on different vertebral segments

The *D*, *f*, and *D** values were not significantly different among the L2, L3, and L4 vertebras in women (p = 0.978, 0.642, and 0.397, respectively; Table 2). Likewise, there were no significant differences in men (p = 0.691, 0.533, and 0.723, respectively; Table 2).

Discussion

Multi–b-value DWI (including a large range of b-values) reference with analysis of IVIM reflects tissue perfusion and tissue cellularity. The current study did not conduct a correlational study on bone marrow histology and IVIM in healthy volunteers. However, our previous research depicted that the *f* value was positively correlated with microvessel density in the marrow, which can be used as an alternative imaging marker of marrow angiogenesis in patients with acute leukemia and anemia (30–32). Therefore, IVIM may reflect the histology of the bone marrow in healthy people. Our current study demonstrated that the *D* and *f* values of women were significantly higher than those of men. As a non-invasive examination method, there are significant differences in IVIM parameters of bone marrow between young women and men, which provides a baseline for the evaluation of bone marrow microstructure (cellularity and perfusion).

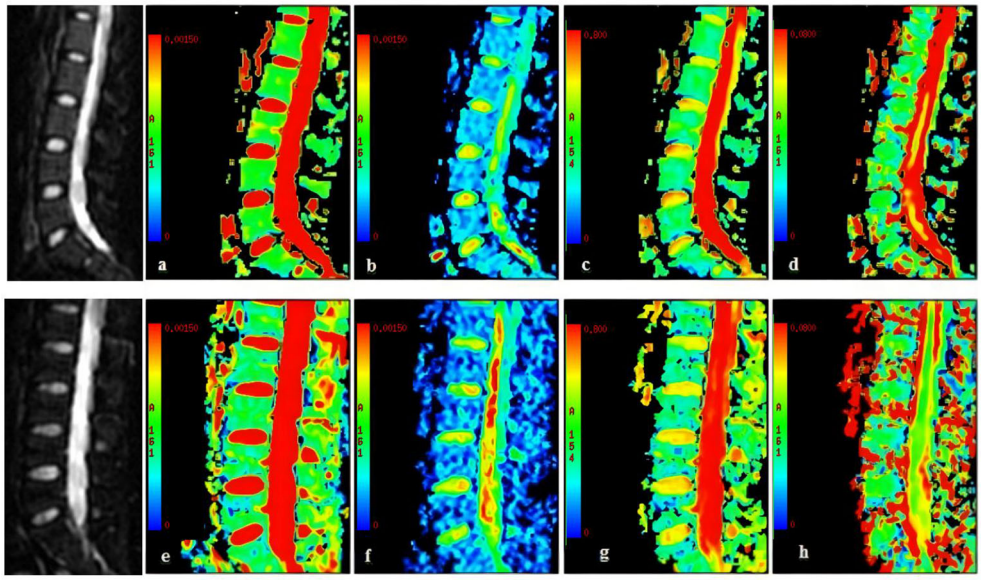

FIGURE 2
A 24-year-old woman **(A–D)**. **(A)** ADC map, ADC = 0.653 × 10^{-3} mm^2/s; **(B)** *D* map, *D* = 0.308 × 10^{-3} mm^2/s; **(C)** *f* map, *f* = 0.327; **(D)** *D** map, *D** = 46.0 × 10^{-3} mm^2/s. A 25-year-old healthy man **(E–H)**. **(E)** ADC map, ADC = 0.588 × 10^{-3} mm^2/s; **(F)** *D* map, *D* = 0.236 × 10^{-3} mm^2/s; **(G)** *f* map, *f* = 0.294; **(D)** *D** map, *D** = 85.3 × 10^{-3} mm^2/s. The two gray images on the left are images with b = 0.

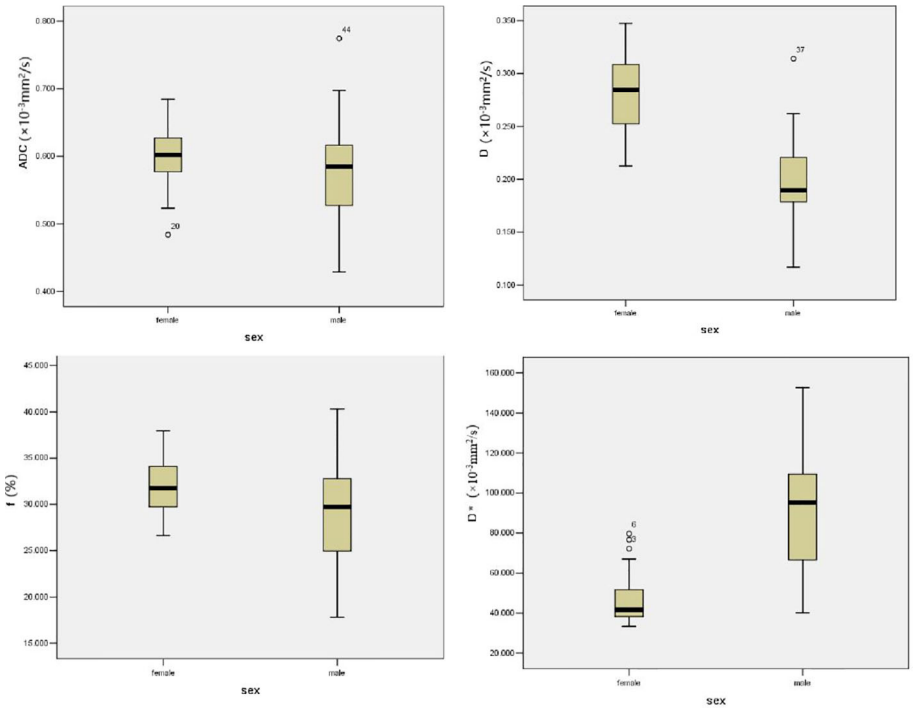

FIGURE 3
Graph shows the mean ADC, *D*, *D**, and *f* values of L2–L4 for two gender groups. The horizontal bar shows the median for each group.

The research on gender-related marrow composition demonstrated that women exhibited lower values of fat fraction and more cellularity compared with men of similar age (16). Although the ADC value has been correlated with the cellularity of the bone marrow (11), our study demonstrated no significant differences in the ADC values between men and women of similar ages. However, the *D* value (diffusion-related IVIM parameters) was statistically different. It suggested that the *D* value was more accurate than the ADC value in reflecting the variety of cellularity in the bone marrow.

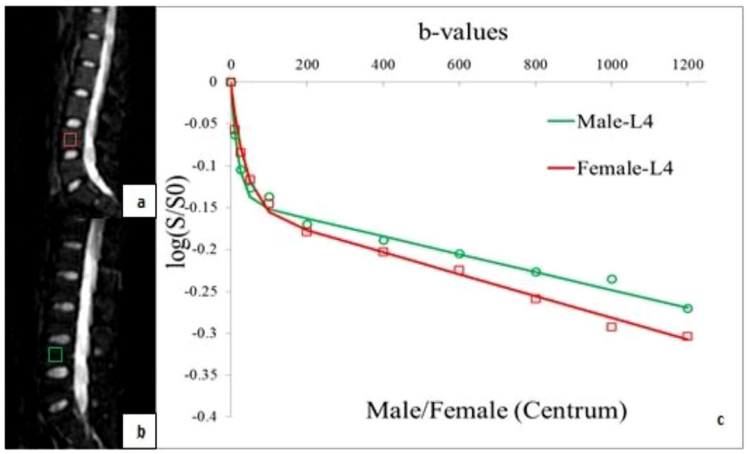

FIGURE 4
ROIs of the fourth vertebral bone marrow in a healthy 24-year-old woman **(A)** and in a healthy 24-year-old man **(B)**. The combination of their logarithmic plot of signal intensity decay and bi-exponential fitting curves **(C)**, the signal intensity decays more quickly in men than that in women within b< 200 s/mm^2. The bi-exponential fitting curves for women (red line) and men (green line) are cross instead of parallel.

10.3389/fendo.2022.958151

TABLE 2 MRI parameter of women and men in different vertebral segments.

MRI	Females (n = 30)					Males (n = 30)				
parameter	L2	L3	L4	f	p	L2	L3	L4	f	p
D (10^{-3} mm^2/s)	0.29 ± 0.05	0.28 ± 0.04	0.28 ± 0.04	0.022	0.978	0.21 ± 0.04	0.20 ± 0.04	0.20 ± 0.05	0.37	0.691
f (%)	32.10 ± 3.80	30.99 ± 6.12	32.00 ± 4.95	0.445	0.642	29.13 ± 6.35	29.84 ± 6.41	27.85 ± 7.87	0.634	0.533
*D** (10^{-3} mm^2/s)	45.98 ± 16.19	44.44 ± 8.80	49.73 ± 19.22	0.942	0.397	87.97 ± 28.32	95.03 ± 34.81	92.35 ± 38.59	0.326	0.723

Data are shown as means ± standard deviations. L, lumbar. Determined with the analysis of variance.
Pseudodiffusion coefficient (D*) represent the characteristics of perfusion.

The ADC value based on a mono-exponential model was between the measured signal intensity and diffusion-weighting (b-value); however, the bone marrow was not homogeneous, and the trabeculae and fat content may cause structural tortuosity. The signal attenuation of the bone marrow was non-linear with the increasing b-value, and the ADC values included the content of tissue microcirculation perfusion (33). In previous studies, the bone marrow ADC values in young women decreased with age (34–36), but there was no significant correlation between the two in men (37, 38). The possible reason is that, with the increase in bone marrow cells in young women, the effective diffusion length is longer (37, 38).

The *f* (perfusion-related IVIM parameters) value in the bone marrow of younger women significantly increased compared with men of similar age. As the *f* value reflects the fractional volume of capillary blood flow in each voxel (25), our study depicted that the marrow perfusion and intra-medullary blood flow of younger women were higher than that of men. DCE-MRI with contrast enhancement has been useful for evaluating bone marrow perfusion (20) and has shown that the marrow perfusion of younger women (age ≤50 years) was significantly higher than that of men of similar age. This difference became less obvious in older men (age >50 years) and women (1, 39). The menstrual cycle and sex hormones of younger women were important factors for the higher bone marrow perfusion as the blood loss from menstruation may activate the hematopoietic marrow and promote red marrow (39). In our previous study, the *f* value in bone marrow was positively correlated with microvessel density, and it can be used as an alternative imaging marker of angiogenesis in the marrow in patients with acute leukemia and anemia (32). Furthermore, the *f* value can show the difference in vascularity between benign and malignant marrow disease (32). Thus, the *f* value may be a biological marker to assess the characteristics of marrow perfusion in healthy people.

The *D** value was another perfusion parameter of IVIM, which was considered proportional to the mean capillary segment length and average blood velocity. A theoretical relationship between the IVIM perfusion parameter and classical perfusion parameters showed that the *D** value was inversely proportional to the mean transit time (MTT) (27, 40). Our results showed that the *D** value of marrow in men was significantly higher than that of women, which may suggest that the blood velocity of microcirculation in marrow was different between men and women. In men, yellow marrow is more abundant and consists of sparse capillaries, venules, and thin-walled veins. Women have more red bone marrow, which is composed of abundant dendrosinuses. The blood flow in the capillaries may be faster than the sinusoidal flow. These results suggested that the *D** value could be used as an index to assess the MTT of bone marrow.

Our results indicated no significant differences in IVIM parameters among the L2, L3, and L4 vertebrae in women and men. Compared with the upper lumbar spine, the lower lumbar sustain greater stress, which may increase the pathophysiologic aging process (red to yellow marrow conversion) and decrease the perfusion inside the lower vertebral body (20, 41). DCE-MRI research reported increased perfusion of the upper lumbar spine (L2 and L3) compared with the lower (L3, L4, and L5) lumbar spine (20). The aging process of marrow alterations related to spinal level in our study was not obvious as we only investigated individuals younger than 25 years old.

We compared several previous studies using a similar approach (34, 35, 42, 43). According to the differences in DWI protocol, population, and results, we summarized the limitations of this study and areas that need to be improved in the future. First, although sex-related marrow perfusion in DCE-MRI has been reported (20), the relationship of the IVIM parameter with the microstructure of the capillary network in bone marrow can be explained if histological contrast is available, such as bone mineral density, bone markers, and sex hormone level analysis. Second, fat cells can impede water movement to a greater extent than hematopoietic cells (33). Although the red marrow was present before yellow marrow in the spine of younger volunteers (approximately 20 years old) (44), evaluating the fat fraction (FF %) could offer more information to explain our results (35). Third, limiting the study to very young volunteers reduced its clinical relevance. In the next step, we will investigate age-related bone marrow differences. Finally, compared with other IVIM parameters, the *D** value map showed a low signal-to-noise ratio, especially in men. Using more b-values (0–50 s/mm^2) may

provide a more accurate estimation, whereas the decreased high b-values would improve image quality. The FOCUS-IVIM may improve its reliability (43). However, it requires high equipment and needs to be studied at 3.0 T.

Conclusion

In conclusion, as a non-invasive imaging method, IVIM parameters can distinguish the bone marrow microstructure of young people of different gender by evaluating cellularity, vascular volume, and blood velocity of bone marrow compared with the ADC value.

Data availability statement

The original contributions presented in the study are included in the article/supplementary material. Further inquiries can be directed to the corresponding author.

Ethics statement

The studies involving human participants were reviewed and approved by Ethics Committee of the Second Hospital of Shanxi Medical University. The patients/participants provided their written informed consent to participate in this study.

Author contributions

WW and TG made equal contributions to the paper and were joint first authors. All authors contributed to the article and approved the submitted version.

Funding

This work was supported, in part, by the General project of National Natural Science Foundation of China, 82071898.

Conflict of interest

The authors declare that the research was conducted in the absence of any commercial or financial relationships that could be construed as a potential conflict of interest.

Publisher's note

All claims expressed in this article are solely those of the authors and do not necessarily represent those of their affiliated organizations, or those of the publisher, the editors and the reviewers. Any product that may be evaluated in this article, or claim that may be made by its manufacturer, is not guaranteed or endorsed by the publisher.

References

1. Sollmann N, Löffler MT, Kronthaler S, Böhm C, Dieckmeyer M, Ruschke S, et al. MRI-Based quantitative osteoporosis imaging at the spine and femur. *J magnet resonance Imaging JMRI* (2021) 54:12–35. doi: 10.1002/jmri.27260

2. Colombo A, Bombelli L, Summers PE, Saia G, Zugni F, Marvaso G, et al. Effects of sex and age on fat fraction, diffusion-weighted image signal intensity and apparent diffusion coefficient in the bone marrow of asymptomatic individuals: A cross-sectional whole-body MRI study. *Diagn (Basel Switzerland)* (2021) 11:913. doi: 10.3390/diagnostics11050913

3. Chramiec A, Vunjak-Novakovic G. Tissue engineered models of healthy and malignant human bone marrow. *Adv Drug delivery Rev* (2019) 140:78–92. doi: 10.1016/j.addr.2019.04.003

4. Coleman RE, Croucher PI, Padhani AR, Clézardin P, Chow E, Fallon M, et al. Bone metastases. *Nat Rev Dis Primers* (2020) 6:83. doi: 10.1038/s41572-020-00216-3

5. Hardouin P, Pansini V, Cortet B. Bone marrow fat. *Joint Bone Spine* (2014) 81:313–9. doi: 10.1016/j.jbspin.2014.02.013

6. Veldhuis-Vlug AG, Rosen CJ. Mechanisms of marrow adiposity and its implications for skeletal health. *Metab: Clin Exp* (2017) 67:106–14. doi: 10.1016/j.metabol.2016.11.013

7. Moulopoulos LA, Dimopoulos MA. Magnetic resonance imaging of the bone marrow in hematologic malignancies. *Blood* (1997) 90:2127–47. doi: 10.1182/blood.V90.6.2127

8. Alyas F, Saifuddin A, Connell D. MR imaging evaluation of the bone marrow and marrow infiltrative disorders of the lumbar spine. *Magn Reson Imaging Clin N Am* (2007) 15:199–219. doi: 10.1016/j.mric.2007.03.002

9. Daldrup-Link HE, Henning T, Link TM. MR imaging of therapy-induced changes of bone marrow. *Eur Radiol* (2007) 17:743–61. doi: 10.1007/s00330-006-0404-1

10. Subhawong TK, Jacobs MA, Fayad LM. Insights into quantitative diffusion-weighted MRI for musculoskeletal tumor imaging. *Am J Roentgenol* (2014) 203:560–72. doi: 10.2214/AJR.13.12165

11. Nonomura Y, Yasumoto M, Yoshimura R, Haraguchi K, Ito S, Akashi T, et al. Relationship between bone marrow cellularity and apparent diffusion coefficien. *J Of Magnet Resonance Imaging* (2001) 13:757–60. doi: 10.1002/jmri.1105

12. Herrmann J, Krstin N, Schoennagel BP, Sornsakrin M, Derlin T, Busch JD, et al. Age-related distribution of vertebral bone-marrow diffusivity. *Eur J Radiol* (2012) 81:4046–9. doi: 10.1016/j.ejrad.2012.03.033

13. Dietrich O, Biffar A, Reiser MF, Baur-Melnyk A. Diffusion-weighted imaging of bone marrow. *Semin musculoskeletal Radiol* (2009) 13:134–44. doi: 10.1055/s-0029-1220884

14. Liney GP, Bernard CP, Manton DJ, Turnbull LW, Langton CM. Age, gender, and skeletal variation in bone marrow composition: A preliminary study at 3.0 Tesla. *J magnet resonance Imaging JMRI* (2007) 26:787–93. doi: 10.1002/jmri.21072

15. Howe BM, Johnson GB, Wenger DE. Current concepts in MRI of focal and diffuse malignancy of bone marrow. *Semin musculoskeletal Radiol* (2013) 17:137–44. doi: 10.1055/s-0033-1343069

16. Dieckmeyer M, Ruschke S, Cordes C, Yap SP, Kooijman H, Hauner H, et al. The need for T(2) correction on MRS-based vertebral bone marrow fat quantification: Implications for bone marrow fat fraction age dependence. *NMR biomed* (2015) 28:432–9. doi: 10.1002/nbm.3267

17. Biffar A, Dietrich O, Sourbron S, Duerr HR, Reiser MF, Baur-Melnyk A. Diffusion and perfusion imaging of bone marrow. *Eur J Radiol* (2010) 76:323–8. doi: 10.1016/j.ejrad.2010.03.011

18. Xing D, Zha Y, Yan L, Wang K, Gong W, Lin H. Feasibility of ASL spinal bone marrow perfusion imaging with optimized inversion time. *J magnet resonance Imaging JMRI* (2015) 42:1314–20. doi: 10.1002/jmri.24891

19. Shih TT, Liu HC, Chang CJ, Wei SY, Shen LC, Yang PC. Correlation of MR lumbar spine bone marrow perfusion with bone mineral density in female subjects. *Radiology* (2004) 233:121–8. doi: 10.1148/radiol.2331031509

20. Savvopoulou V, Maris TG, Vlahos L, Moulopoulos LA. Differences in perfusion parameters between upper and lower lumbar vertebral segments with dynamic contrast-enhanced MRI (DCE MRI). *Eur Radiol* (2008) 18:1876–83. doi: 10.1007/s00330-008-0943-8

21. Shih TT, Hou HA, Liu CY, Chen BB, Tang JL, Chen HY, et al. Bone marrow angiogenesis magnetic resonance imaging in patients with acute myeloid leukemia: peak enhancement ratio is an independent predictor for overall survival. *Blood* (2009) 113:3161–7. doi: 10.1182/blood-2008-08-173104

22. Le Bihan D, Breton E, Lallemand D, Grenier P, Cabanis E, Laval-Jeantet M. MR imaging of intravoxel incoherent motions: application to diffusion and perfusion in neurologic disorders. *Radiology* (1986) 161:401–7. doi: 10.1148/radiology.161.2.3763909

23. Koh DM, Collins DJ, Orton MR. Intravoxel incoherent motion in body diffusion-weighted MRI: reality and challenges. *AJR Am J roentgenol* (2011) 196:1351–61. doi: 10.2214/AJR.10.5515

24. Takahara T, Kwee TC. Low b-value diffusion-weighted imaging: emerging applications in the body. *J magnet resonance Imaging JMRI* (2012) 35:1266–73. doi: 10.1002/jmri.22857

25. Le Bihan D, Turner R. The capillary network: a link between IVIM and classical perfusion. *Magnet resonance Med* (1992) 27:171–8. doi: 10.1002/mrm.1910270116

26. Ruschke S, Syväri J, Dieckmeyer M, Junker D, Makowski MR, Baum T, et al. Physiological variation of the vertebral bone marrow water T2 relaxation time. *NMR biomed* (2021) 34:e4439. doi: 10.1002/nbm.4439

27. Federau C, O'Brien K, Meuli R, Hagmann P, Maeder P. Measuring brain perfusion with intravoxel incoherent motion (IVIM): initial clinical experience. *J magnet resonance Imaging JMRI* (2014) 39:624–32. doi: 10.1002/jmri.24195

28. Lee Y, Lee SS, Kim N, Kim E, Kim YJ, Yun S-C, et al. Intravoxel incoherent motion diffusion-weighted MR imaging of the liver: effect of triggering methods on regional variability and measurement repeatability of quantitative parameters. *Radiology* (2015) 274:405–15. doi: 10.1148/radiol.14140759

29. Federau C, Meuli R, O'Brien K, Maeder P, Hagmann P. Perfusion measurement in brain gliomas with intravoxel incoherent motion MRI. *AJNR Am J neuroradiol* (2014) 35:256–62. doi: 10.3174/ajnr.A3686

30. Niu J, Li W, Wang H, Wu W, Gong T, Huang N, et al. Intravoxel incoherent motion diffusion-weighted imaging of bone marrow in patients with acute myeloid leukemia: a pilot study of prognostic value. *J magnet resonance Imaging JMRI* (2017) 46:476–82. doi: 10.1002/jmri.25600

31. Li J, Li W, Niu J, Song X, Wu W, Gong T, et al. Intravoxel incoherent motion diffusion-weighted MRI of infiltrated marrow for predicting overall survival in newly diagnosed acute myeloid leukemia. *Radiology* (2020) 295:155–61. doi: 10.1148/radiol.2020191693

32. Fan R, Zhu H, Niu J, Li J, Zheng R, Song X. Correlation of histological marrow characteristics and intravoxel incoherent motion-derived parameters in benign and malignant hematological disorders. *Eur J Radiol* (2020) 123:108745. doi: 10.1016/j.ejrad.2019.108745

33. Khoo MM, Tyler PA, Saifuddin A, Padhani AR. Diffusion-weighted imaging (DWI) in musculoskeletal MRI: a critical review. *Skeletal Radiol* (2011) 40:665–81. doi: 10.1007/s00256-011-1106-6

34. He J, Fang H, Na Li X. Vertebral bone marrow diffusivity in normal adults with varying bone densities at 3T diffusion-weighted imaging. *Acta radiol (Stockholm Sweden 1987)* (2018) 59:89–96. doi: 10.1177/0284185117704235

35. Lavdas I, Rockall AG, Castelli F, Sandhu RS, Papadaki A, Honeyfield L, et al. Apparent diffusion coefficient of normal abdominal organs and bone marrow from whole-body DWI at 1.5 T: The effect of sex and age. *AJR Am J roentgenol* (2015) 205:242–50. doi: 10.2214/AJR.14.13964

36. Chen YY, Wu CL, Shen SH. High signal in bone marrow on diffusion-weighted imaging of female pelvis: Correlation with anemia and fibroid-associated symptoms. *J magnet resonance Imaging JMRI* (2018) 48:1024–33. doi: 10.1002/jmri.26002

37. Cui FZ, Cui JL, Wang SL, Yu H, Sun YC, Zhao N, et al. Signal characteristics of normal adult bone marrow in whole-body diffusion-weighted imaging. *Acta radiol (Stockholm Sweden 1987)* (2016) 57:1230–7. doi: 10.1177/0284185115626477

38. Zhang CY, Rong R, Wang XY. Age-related changes of bone marrow of normal adult man on diffusion weighted imaging. *Chin Med Sci J* (2008) 23:162–5. doi: 10.1016/S1001-9294(09)60032-8

39. Chen W-T, Shih TT-F, Chen R-C, Lo S-Y, Chou C-T, Lee J-M, et al. Vertebral bone marrow perfusion evaluated with dynamic contrast-enhanced MR imaging: significance of aging and sex. *Radiology* (2001) 220:213–8. doi: 10.1148/radiology.220.1.r01jl32213

40. Le Bihan D, Breton E, Lallemand D, Aubin ML, Vignaud J, Laval-Jeantet M. Separation of diffusion and perfusion in intravoxel incoherent motion MR imaging. *Radiology* (1988) 168:497–505. doi: 10.1148/radiology.168.2.3393671

41. Gardner-Morse MG, Stokes IAF. Structural behavior of human lumbar spinal motion segments. *J Biomech* (2004) 37:205–12. doi: 10.1016/j.jbiomech.2003.10.003

42. Marchand AJ, Hitti E, Monge F, Saint-Jalmes H, Guillin R, Duvauferrier R, et al. MRI Quantification of diffusion and perfusion in bone marrow by intravoxel incoherent motion (IVIM) and non-negative least square (NNLS) analysis. *Magn Reson Imaging* (2014) 32:1091–6. doi: 10.1016/j.mri.2014.07.009

43. Cao J, Zhu J, Sun W, Cui L. Comparison of field-of-view optimized and constrained undistorted single shot with conventional intravoxel incoherent motion diffusion-weighted imaging for measurements of diffusion and perfusion in vertebral bone marrow. *J Comput Assist Tomogr* (2021) 45(1):98–102. doi: 10.1097/RCT.0000000000001111

44. Ricci C, Cova M, Kang YS, Yang A, Rahmouni A, Scott WWJr, et al. Normal age-related patterns of cellular and fatty bone marrow distribution in the axial skeleton: MR imaging study. *Radiology* (1990) 177:83–8. doi: 10.1148/radiology.177.1.2399343

Frontiers in Endocrinology

Explores the endocrine system to find new therapies for key health issues

The second most-cited endocrinology and metabolism journal, which advances our understanding of the endocrine system. It uncovers new therapies for prevalent health issues such as obesity, diabetes, reproduction, and aging.

Discover the latest Research Topics

See more →

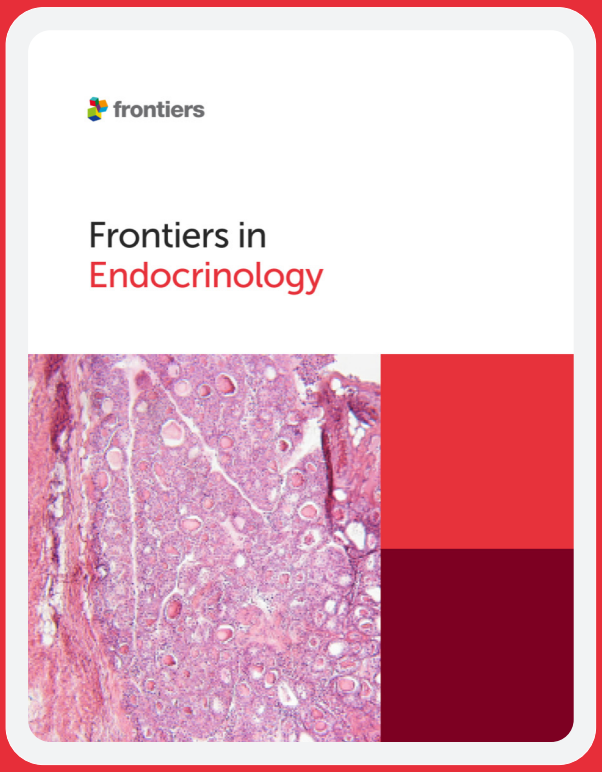

Frontiers

Avenue du Tribunal-Fédéral 34
1005 Lausanne, Switzerland
frontiersin.org

Contact us

+41 (0)21 510 17 00
frontiersin.org/about/contact